FABRICATION, NUMERICAL MODELING, AND TESTING OF SILICON MICROPYRAMID ARRAYS AND RETROREFLECTORS

by

Grant W. Bidney

A dissertation submitted to the faculty of
The University of North Carolina at Charlotte
in partial fulfillment of the requirements
for the degree of Doctor of Philosophy in
Optical Science & Engineering

Charlotte

2024

Approved by:

_____
Dr. Vasily N. Astratov

_____
Dr. Glenn D. Boreman

_____
Dr. Thomas J. Suleski

_____
Dr. Donald J. Jacobs

_____
Dr. Yuri A. Godin

ABSTRACT

GRANT W. BIDNEY. Fabrication, Numerical Modeling, and Testing of
Silicon Micropyramid Arrays and Retroreflectors.
(Under the direction of DR. VASILY N. ASTRATOV)

This dissertation is devoted to the optical properties of mesoscale and nanoscale photonic arrays, specifically regarding two different areas: i) silicon (Si) micropyramidal photonics aimed at enhancing photodetectors and emitters, and ii) plasmonic Littrow retroreflectors in the optical regime.

In the first area, it was shown that Si anisotropic wet etching is attractive for the fabrication of large-scale arrays of micropyramids, or microvoids, with an extraordinary level of uniformity over centimeter-scale wafers. This is related to the self-terminating nature of the etching process when two (111)-type planes meet under the conditions when a surfactant is used to slow down the undercutting rate of the SiO_2 layer. Although this technology is generally well studied by the microelectromechanical (MEMS) community, it seems that this particular property did not receive sufficient attention in previous studies. However, it is this property which enables the fabrication of uniform micropyramid arrays suitable for integration with detector and emitter arrays in optoelectronics applications. The optical properties of such arrays are studied by 3-D finite-difference time-domain (FDTD) numerical modeling in two realms represented by different boundary conditions (BCs). Periodic BCs result in Talbot self-images experimentally observed in this work. Perfectly matched layer BCs describe mesoscale interference effects resulting in the subwavelength focusing properties of individual micropyramids. It is proposed that integration with micropyramid arrays can enhance the collection of photons, signal-to-noise ratio, and

operational temperatures of mid-wave infrared photodetector focal plane arrays (FPAs). It is also proposed that Si micropyramid arrays can be used to enhance light extraction and directionality of quantum sources and infrared scene projectors. Additionally, micropyramids were monolithically integrated with silicon-platinum silicide (PtSi/p-Si) Schottky barrier photodetectors to experimentally demonstrate an improved signal obtained by these micropyramid arrays. These results were compared with 3-D FDTD numerical modeling, as well as the modeling of a novel resonator cavity micropyramid structure as a way to further increase the enhancement capabilities of these micropyramids based on using a silicon-on-insulator (SOI) wafer. This structure demonstrated increased absorption of up to 11× compared to a planar reference device of the same size.

In the second area devoted to Littrow grating retroreflectors, the problem of simultaneous and efficient TE and TM polarization retroreflection was undertaken and guidelines for designing such retroreflectors were developed. Optimized performance at wavelengths in the vicinity of λ = 633 nm is expected for top metal slot arrays with thickness in the 20 - 40 nm range. However, this can vary for different metals such as Au, Ag, Al, and Cu. The most interesting development is the proposal to use experimentally measured index values for thin films with different thicknesses to study and optimize the performance of real physical retroreflector devices. To the best of our knowledge this approach was proposed for the first time in our work. Using this approach, it was shown that there is potentially plasmonic enhancement mechanisms involved, caused by their confinement in the metal stripes of the arrays. It was demonstrated that, despite the presence of absorption, such Au Littrow retroreflectors reached simultaneous ~0.2 and ~0.6 efficiency levels for the TE and TM polarizations, respectively, in the same structure.

ACKNOWLEDGEMENTS

I extend my deepest gratitude to my advisor, Dr. Vasily N. Astratov. Over the past several years, he has supported my research with remarkable patience, offering invaluable knowledge and thought-provoking discussions. Throughout this time, he guided me through both my master's defense and doctoral dissertation with enthusiasm. His dedication to preparing me for numerous scientific presentations helped me convey information with clarity and impact. It has been a privilege to learn from his wealth of experience, often shared through his insightful and memorable stories.

I would also like to thank my committee members, Dr. Glenn D. Boreman, Dr. Thomas J. Suleski, Dr. Donald J. Jacobs, and Dr. Yuri A. Godin for their valuable time and patience towards me finishing this dissertation, as well as providing me with advice and support regarding my future career opportunities.

I am very thankful to the Summer Faculty Fellowship Program for enabling the four summer internships at the Air Force Research Laboratory (AFRL) located at Wright-Patterson Air Force Base. I am also thankful for the National Science Foundation supported IUCRC Phase III University of North Carolina at Charlotte: Center for Metamaterials internship, which made it possible to spend an additional five months at AFRL during the academic year. Throughout these experiences, I had the pleasure to learn from great minds such as Dr. Gamini Ariyawansa, Dr. Joshua M. Duran, Dr. Igor Anisimov, Dr. Dennis E. Walker Jr., Dr. Nicholaos I. Limberopoulos, and everyone who has helped me in the AFRL cleanroom.

My graduate research assistantships in Dr. Vasily Astratov's Mesophotonics Laboratory were supported through the Center for Metamaterials at UNCC by AFRL, Jet

Propulsion Laboratory, and Georgia Tech Research Institute (GTRI). I thank Dr. Kenneth W. Allen, Dr. David R. Reid, and Dr. Christopher W. Peterson from GTRI for useful discussions related to numerical modeling methodology.

My initial work in the Mesophotonics Laboratory was devoted to microwave imaging using an advanced inverse scattering algorithm in collaboration with Dr. Michael V. Klibanov's group from the Mathematical Department at UNCC. This work was not included in my dissertation, but I learned greatly about microwave experimental techniques from Steven Kitchin and about the inverse scattering problem in general from Dr. Michael V. Klibanov, Dr. Vo A. Khoa, and Dr. Loc H. Nguyen. I appreciate Steven Kitchin's patience and Dr. Michael V. Klibanov's support during my first two years in the program obtained through his grant from the Army Research Office.

I am grateful to Dr. Aaron Brettin and Dr. Boya Jin, fellow members of the Mesophotonics Laboratory, for their guidance early in my graduate studies. I am grateful to Dr. Lou Deguzman, and Scott Williams for their patience while teaching me how to operate the equipment in the UNCC Optics center. I was supported by the GASP award throughout my graduate studies. I am thankful for the Department of Physics and Optical Sciences for supporting me with teaching assistantships.

DEDICATION

I dedicate this dissertation to my...

...parents for their persistent love, guidance, and support.

...girlfriend for her understanding, encouragement, and patience.

"Last but not least, I want to thank me. I want to thank me for believing in me. I want to thank me for doing all this hard work. I want to thank me for having no days off. I want to thank me for never quitting. I want to thank me for always being a giver and trying to give more than I receive. I want to thank me for trying to do more right than wrong. I want to thank me for just being me at all times."

- *Snoop Dogg*

TABLE OF CONTENTS

LIST OF FIGURES xi

LIST OF ABBREVIATIONS xxviii

CHAPTER 1: INTRODUCTION

1.1. Outline and Overview of the Dissertation 1

1.2. Infrared Photodetector Focal Plane Arrays 5

1.2.1. Fundamentals of Photon Detectors 8

1.2.2. Focal Plane Array Integration Techniques 11

1.2.3. FPA Enhancement with Light Concentration Techniques 14

1.3. Light Manipulation with Mesoscale Structures 22

1.3.1. Photonic Nanojets 24

1.3.2. The Talbot Effect 32

1.4. Si Anisotropic Wet Etching as a Major Tool for MEMS Fabrication 36

1.4.1. The Crystalline Structure of Si 38

1.4.2. Types of Etchants: Wet & Dry 40

1.4.3. TMAH Anisotropic Wet Etching of Si 44

1.5. Retroreflectors 50

1.5.1. Metasurface Retroreflectors 54

1.5.2. Littrow Retroreflectors 60

1.6. Plasmonics 63

1.6.1. Plasmon Resonance Fundamentals 65

1.6.2. Plasmonic Effects on Transmission, Reflection, and Absorption 71

1.7. Statement of Goals 76

CHAPTER 2: SI ANISOTROPIC WET ETCHING FOR PHOTONIC APPLICATIONS

2.1. Introduction 80

2.2. Si Mesophotonic Array Fabrication Protocol 83

2.3. Si Mesophotonic Arrays Fabricated with 25% TMAH 86

2.4. Introduction TMAH with Triton X-100: Utilization Considerations 92

2.5. Conclusions 96

CHAPTER 3: NUMERICAL MODELING THE OPTICAL PROPERTIES OF SI MICROPYRAMID ARRAYS

3.1. Introduction 99

3.2. Role of the Boundary Conditions in 3-D FDTD Numerical Modeling 103

3.3. Periodic BCs: Talbot Effect 106

3.4. Perfectly Matched Layer BCs: Photonic Jets for Photodetector Applications 113

3.5. Emitter Applications 119

3.6. Conclusions 123

CHAPTER 4: PHOTODETECTOR FOCAL PLANE ARRAYS ENHANCED WITH SI MICROPYRAMID ARRAYS

4.1. Introduction 126

4.2. Fabrication of Monolithically Integrated Photodetectors with Si Micropyramids 129

4.3. MWIR Micropyramidal Photodetector Characterization 136

4.4. Silicon-on-Insulator Micropyramids: Further Signal Enhancement 145

4.5. Conclusions 155

CHAPTER 5: NUMERICAL MODELING THE OPTICAL PROPERTIES OF LITTROW RETROREFLECTORS

5.1. Grating Concept and Polar Angle Performance 159

5.2. Suppression of the Specular Beam 161

5.3. Describing the Model in 3-D FDTD Numerical Modeling Software 163

5.4. Azimuthal Dependence 168

5.5. Transition from PEC Model to Real Metals: Au, Ag, Al, and Cu 170

5.6. From Bulk Metal to Real Au Thin Films 175

5.7. Conclusions and Guidance for Fabrication 179

CHAPTER 6: SUMMARY OF THE MAIN RESULTS AND CONCLUSIONS 181

REFERENCES 188

APPENDIX A: PUBLICATIONS SO FAR 222

LIST OF FIGURES

FIGURE 1.1. Diagram depicting the imaging system for IR detectors and their important sub-systems [1, 10]. 6

FIGURE 1.2. Diagram depicting the diversity of IR detector technologies at their respective operating temperatures and wavelengths [1]. 8

FIGURE 1.3. (a) Optical excitation mechanisms in semiconductors: i) intrinsic absorption, ii) extrinsic absorption, iii) free carrier absorption. (b-f) Diagrams showing a few types of photon detectors, as well as their operating principles: (b) p-n junction photodiode, (c) Schottky barrier photodiode, (d) metal-insulator-semiconductor photodiode, (e) blocked impurity band detector, and (f) photoconductor [1]. 9

FIGURE 1.4. Diagram depicting four different monolithic FPAs and different interconnect techniques for hybrid FPAs. Monolithic FPAs include (a) CCD array, (b) CMOS array, (c) heteroepitaxy-on-silicon, or the growth of a crystalline film on Si, and (d) microbolometer. Interconnect techniques for hybrid FPAs include (e) layered-hybrid design, (f) loophole technique, and (g) indium bump technique [1]. 12

FIGURE 1.5. HgCdTe photodiode band diagrams for (a) n^+-on-p and (b) p-on-n. (c) Numerical modeling of mercury vacancy dark current for n-on-p HgCdTe photodiodes [1, 31, 33]. 14

FIGURE 1.6. (a) Diagram of a HgCdTe MWIR photodiode integrated with a metalens. (b) Power flux distribution on the x-z cross section of the device with the active region outlined by dashed white lines. (c) Absorptance of the HgCdTe detector's active region with and without the metalens for two different photosensitive square areas. (d) Relative detectivity as a function of incident wavelength for two different photosensitive areas [14]. 15

FIGURE 1.7. (a) Diagram of a microlens incident on a photodetector which concentrates light from area A_0 to A_s. (b) Schematic of the microlens integrated with an IR FPA, describing its parts. (c) Microscope image of pixels integrated with a microlens and without a microlens. (d) Raw pixel output responses to a pulsed beam, showing a measured enhancement of 7.4 times [17]. 17

FIGURE 1.8. (a) Virtual imaging by a microsphere integrated with a photodetector. (b) Optical micrograph of a microsphere on top of 18

a photodetector mesa. (c) Photocurrent measured at different bias voltages for microspheres of different material and diameter. (d) Photocurrent enhancement factors obtained by dividing the photocurrent the microsphere integrated detector with the photocurrent spectra of the isolated detector, showing up to 100 times enhancement [22].

FIGURE 1.9. (a-e) Normal micropyramidal Al-silicide and (f-i) inverted micropyramidal Cu-silicide Schottky barrier photodetectors in the SWIR depicting plasmonic enhancement effects. (a) I-V measurements of the micropyramid compared to the flat device, showing current enhancement of ~100 times. (b), (d) Numerically modeled electromagnetic field intensities superimposed on 3-D Si models. (c), (e) SEM images of the fabricated devices [23]. (f) Energy band diagram for a Cu-based Schottky barrier photodetector. (g) Diagram showing direction light is incident on the array. (h-i) Electromagnetic field map for Cu-based Schottky barrier photodetector at two different polarizations [24]. 20

FIGURE 1.10. (a) Electromagnetic field distribution inside a 4 μm small base, 14 μm large base free-floating Si microcone calculated at normal incidence with a 1 μm thick Pt mirror at the bottom base. Weak absorption effects of the Schottky barrier were modeled by introducing a 1% absorption effect in the lowest 1 μm thick section of microcone closest to the small base. (b) Power enhancement factor spectra calculated for 0 - 30° incidence angles at both TE and TM polarizations [25]. 21

FIGURE 1.11. (a) Diagram depicting the characteristics of a photonic nanojet. (b-e) Numerical modeling of photonic nanojets emerging from a cylinder with diameter D and refractive index n_p, where the background medium consists of refractive index n_{bg}. The cylinder is illuminated with a plane wave of wavelength λ. (b) D=6 μm, n_p=2.3275, n_{bg}=1.33, and λ=300 nm. (c) D=10 μm, n_p=2.3275, n_{bg}=1.33, and λ=300 nm. (d) D=5 μm, n_p=2.5, n_{bg}=1, and λ=500 nm. (e) D=5 μm, n_p=1.7, n_{bg}=1, and λ=500 nm [57, 59]. 25

FIGURE 1.12. (a) Diagram depicting the 3-D FDTD numerical modeling simulation region. The incident plane wave propagates upwards with λ = 532 nm, the substrate consists of index n_1 = 1.4, the glass particles consists of index n_2 = 1.6, and the surrounding air consists of index n = 1. (b-d) Optical field intensity B in proximity to glass microparticles buried in polymer of thickness s marked by the red horizontal line for (b) normal microcones, (c) inverted microcones, and (d) microspheres [67]. 26

FIGURE 1.13. Phase diffraction gratings with their optical intensity profile B calculated by 3-D FDTD numerical modeling, depicting the formation of photonic nanojets. The plane wave source of $\lambda = 532$ nm propagates upwards. (a) Saw-tooth grating with $h = \lambda$, $d = 2\lambda$, and $\alpha = 45°$. (b) Rectangular grating with $h = \lambda$, $d = 2\lambda$, and $D = 1.5\lambda$. (c) Hemispherical grating with $h = \lambda$, $d = 3\lambda$, and $D = 1.5\lambda$ [84]. 27

FIGURE 1.14. (a) Diagram depicting the illuminating wavelength λ, the dimensions of the resulting photonic nanojet, the height of the sawtooth $h = 2.5$ μm, the peak-to-peak separation distance $d = 2.5$ μm, and the angle of the pyramid formed $\alpha = 45°$. (b) FDTD power flow map for a sawtooth grating with $\lambda = 405$ nm compared to (c) experiment. (d) FDTD power flow map for a sawtooth grating with $\lambda = 532$ nm compared to (e) experiment [85]. 28

FIGURE 1.15. (a) Diagram depicting the composition of the bilayer micropyramid array inside the 3-D FDTD numerical modeling simulation region when illuminated by a plane wave with $\lambda = 640$ nm. (b) Numerical model with $L_b = 7.60$ μm, $L_t = 3.80$ μm, $h_1 = 2.00$ μm, $h_2 = 1.30$ μm, $n_1 = 2.02$, and $n_2 = 1.458$. (c) Experiment with $L_b = 7.61$ μm, $L_t = 3.81$ μm, $h_1 = 2.03$ μm, $h_2 = 1.32$ μm, $n_1 = 2.04$, and $n_2 = 1.462$ [88]. 29

FIGURE 1.16. (a) Diagram depicting the Talbot effect and example imaging distances z_1, and z_2 based on the wavelength of the plane wave source λ and the period of the diffraction grating Λ. (b) 3-D diagram depicting the Talbot effect and the allowable imaging interval around the Talbot plane that can be considered a part of the Talbot image [117]. 33

FIGURE 1.17. (a) Diagram depicting Talbot imaging with a stepped phase layer. (b) Numerically modeled electric field with different phase layer thicknesses [117]. 34

FIGURE 1.18. (a) Diagram depicting the ability to expose different regions of photoresist through Talbot imaging with an array of cones where the incident light is an unpolarized plane wave with $\lambda = 365$ nm, $H = D = 300$ nm, $\Lambda_x = 500$ nm, and $\Lambda_y = 866$ nm. The time-averaged numerically modeled intensity patterns at different depths z are shown [144] (b) Diagram depicting the ability to expose different regions of photoresist through Talbot imaging with an array of nanospheres where the incident light is a UV laser, and d is the propagation distance. SEM images of a structure fabricated with this method are shown [145]. 35

FIGURE 1.19. (a) The face centered cubic (FCC) crystalline structure of Si. Diagrams depicting the (b) (100), (c) (110), and (d) (111) crystalline planes. 39

FIGURE 1.20. Diagram depicting a (100) Si wafer. The surface is a (100) plane, and the wafer flat is along the <110> direction. Additionally, the (110) plane and the (100) plane are shown. 39

FIGURE 1.21. Diagram depicting the categorization of wet and dry etching [150]. Both methods of etching have the ability to etch either isotropically or anisotropically, depending on the chemicals and methods utilized [150]. 41

FIGURE 1.22. (a) Etch rates along the (100) plane for TMAH and KOH as a function of concentration at three different temperatures. (b) Etch rate ratios for the (111) plane etch rate divided by the (100) plane etch rate for TMAH and KOH as a function of concentration at three different temperatures. SEM photos of a Si wafer etched at 70° C where the wafer was (c) not patterned and etched with 5 wt% TMAH for 20 min, (d) not patterned and etched with 5 wt% KOH for 11 min, (e) patterned and etched with 5 wt% TMAH for 20 min, (f) patterned and etched with 5 wt% KOH for 25 min, (g) patterned and etched with 25 wt% TMAH for 15 min, and (h) patterned and etched with 25 wt% KOH for 7 min [164]. 45

FIGURE 1.23. (a) Pyramidal hillocks formed when etched in 5 wt%, 10 wt%, 15 wt%, 22 wt%, and 40 wt% TMAH [165]. (b) The number and size of pyramidal hillocks etched at 90° C for 5, 15, and 30 minutes [166]. (c) The height of the pyramidal hillocks as a function of etching time at different temperatures when etched with 25 wt% TMAH [167]. 46

FIGURE 1.24. (a) Diagram depicting undercutting of a mask used to define the etched geometry. (b) The undercut rate as a function of etchant concentration at three different temperatures for KOH and TMAH [164]. 47

FIGURE 1.25. (a) SEM images of micropyramids etched with pure 25 wt% TMAH and TMAH with added Triton X-100, showing the reduced undercutting by the solution with added Triton X-100 plotted in (b) [174]. (c) The (100)-Si etch rate as a function of temperature for three different concentrations of Triton X-100 added to 25 wt% TMAH [150]. (d) The (110)-Si etch rate as a function of temperature for pure 25 wt% TMAH and 25 wt% TMAH with 0.1% Triton X-100 added [174]. (e) SEM images showing the surface roughness of the (100) plane and the (110) plane when 48

etched with pure TMAH and five different concentrations of Triton X-100 [175].

FIGURE 1.26. Various corner compensation structures at each of the four corners [158]. 49

FIGURE 1.27. Various retroreflective devices. (a) Cat's eye retroreflector [187]. (b) Corner cube retroreflector. Specifically, one with cantilevers to adjust the bottom mirror [188]. (c) Luneburg lens with a metallic mirror on the bottom surface [189]. (d) Van Atta array, a phased antenna array, that redirects light back towards the direction it came [190]. (e) Example of a metasurface retroreflector [190]. (f) Diffraction grating retroreflector, following the Littrow configuration [191]. 52

FIGURE 1.28. (a) Flat retroreflector (FRR) based on a metasurface doublet, which consists of vertically stacked metasurfaces MS1 and MS2. (b) Detected retroreflected optical power at θ_{in} = 0°, 10°, 15°, and 25° [220]. 55

FIGURE 1.29. (a) Adaptive reconfigurable spin-locked metasurface retroreflector, based on utilization of meta-atoms with rotational mechanical control to process either right or left circularly polarized light. Experimental and simulation results of left circularly polarized light incident on 2-D scattering patterns at 4 GHz for (b) θ_{in} = 11° and φ_{in} = 0°, (c) θ_{in} = 24° and φ_{in} = -27°, (d) θ_{in} = 31° and φ_{in} = 135°, and (e) θ_{in} = 42° and φ_{in} = -146° [190]. 56

FIGURE 1.30. (a) Hyperbolic plasmonic metasurface (HPM) retroreflector design, where the diameter is d, period is p, and the separation between the HPMs and the metal cylinder array is h. (b) Photo of the experimental setup, where the retroreflector is covered by an absorber except where the metal cylinder array is located. (c) Diagram showing the top-down view of the experimental setup. (d) Experimentally measured retroreflection efficiency as a function of frequency shown for incident angles θ [221]. 57

FIGURE 1.31. Huygens' metasurface retroreflectors at 24 GHz are shown. (a) TE retroreflector shown in 2-D and 3-D. The dimensions of the components are P_{x1} = 2.16 mm, P_{x2} = 2.35 mm, P_y = 1.5 mm, U_x = U_y = 3.149 mm, and S_z = 1.575 mm. (b) Monostatic radar cross section (RCS) simulation for the TE retroreflector, shown in blue, and for the theoretical RCS of an ideal mirror placed normal to the incident radiation, shown in red. (c) TM retroreflector shown in 2-D and 3-D. The dimensions of the components are P_{x1} = 0.8 mm, P_{x2} = 3.149 mm, P_y = 1.5 mm, U_x = U_y = 3.149 mm, and S_z = 3.175 59

mm. (d) Monostatic RCS simulation for the TM retroreflector, shown in blue, and for the theoretical RCS of an ideal mirror placed normal to the incident radiation, shown in red [191].

FIGURE 1.32. (a) Diagram depicting a diffraction grating's cross-section. (b) Numerically modeled TE polarization diffraction efficiency of a diffraction grating in the Littrow configuration, with the horizontal line corresponding to the $f = 0.045$ plot shown in (c), which plots the diffraction efficiency as d varies for $\varepsilon_d = 2.08541$ and $\varepsilon_a = 1$. (d) Numerically modeled TM polarization diffraction efficiency of a diffraction grating in the Littrow configuration, with the horizontal line corresponding to the $f = 0.45$ plot shown in (e), which plots the diffraction efficiency as d varies for $\varepsilon_d = 2.08541$ and $\varepsilon_a = 1$ [225]. 61

FIGURE 1.33. Diagram depicting the basics of surface plasmonic resonance. (a) At the interface of a dielectric and a metal, surface plasmons have a combined electromagnetic wave and surface charge. The generation of surface charge requires an electric field normal to the metal's surface. (b) The surface plasmon dispersion curve, displaying the momentum mismatch between the light, $\hbar k_0$, and the surface plasmon modes, $\hbar k_{SP}$. (c) The field component perpendicular to the surface can be enhanced near the surface, but decays exponentially with distance, where the decal length in the medium above the metal is δ_d, and the skin depth into the metal is δ_m [226]. (d-h) Diagrams depicting how the plasmon resonance of a metal nanostructure is affected by the field distribution. (d) Metallic nanospheres incased in different dielectric materials, (e) metallic nanoshells with a symmetric plasmon mode, (f) metallic nanoshells with an antisymmetric plasmon mode, (g) metallic nanorods with field polarization parallel to the nanorods, and (h) metallic nanorods with field polarization perpendicular to the nanorods [248]. 66

FIGURE 1.34. (a-f) Numerically modeled spherical nanoparticle dimers with varying gap sizes, exhibiting plasmonic coupling. (a) Light polarized perpendicular to the dimer axis, displaying destructive interference. (b) Light polarized parallel to the dimer axis, displaying constructive interference. Electric field maps showing (c) destructive interference and (d) constructive interference for 20 nm diameter Ag spherical nanoparticles separated by 5 nm. Extinction spectra for the same nanoparticles with light polarized (e) perpendicular to the dimer axis, and (f) parallel to the dimer axis. The gap sizes are 1, 2, 3, 4, 5, 10, 20, 30, 40, and 50 nm from lightest color to darkest color [263]. Experimentally measured extinction spectra for nanodisk arrays with labeled particle sizes 70

for (g) Au, and (h) Al. The separation between nanodisks were random, with the smallest center-to-center distance of 6 nanodisk diameters [272].

FIGURE 1.35. Numerically modeled monolayer of hexagonal close packed arrays consisting of 20 nm diameter nanoparticles in a dielectric medium with n = 1.33. The arrays were illuminated at normal incidence, and the separation between the particles d was varied. (a) Transmittance, (b) reflectance, and (c) absorptance data for Au nanoparticles. (d) Transmittance, (e) reflectance, and (f) absorptance data for Ag nanoparticles [285]. 72

FIGURE 1.36. Numerically modeled Au nanobar absorption spectrum for width w = 60 nm, length l = 100 nm, and varying thickness t. Absorption plots as a function of wavelength where incident light is either (a) longitudinally or (b) transversely polarized. (c) Plot depicting the peak resonance wavelength as a function of thickness for both polarizations, as well as the impact rounded corners have on the peak resonance wavelength [291]. 74

FIGURE 2.1. Diagram depicting the universal Si mesophotonic array fabrication protocol, where each fabrication step corresponds to a column, and each row corresponds to a point-of-view. The example structures are truncated Si micropyramids with θ = 54.74˚ sidewall angles formed along the (111) crystalline planes through anisotropic wet etching a (100) Si wafer with 25% TMAH. Row (a) depicts a top-down perspective. Row (b) depicts a sideview perspective. Row (c) depicts an arial view. Step 1, depicted in the first column, is to perform photolithography shown in red to define the structure's geometry on a (100) Si wafer shown in grey with a thermal SiO_2 layer shown in blue. Step 2, depicted in column 2, is to transfer the photolithography pattern to the SiO_2 layer through a buffered oxide etchant (BOE) etch. Step 3, depicted in column 3, is to remove the photoresist in order to prevent changing the etching characteristics of TMAH. Step 4, shown in column 4, is to anisotropically wet etch the mesophotonic arrays. Step 5, shown in column 5, is to remove the leftover SiO_2 layer with a second BOE etch. The final result is a mesophotonic array which, in this case, is a truncated Si micropyramid array. 83

FIGURE 2.2. SEM images of truncated Si micropyramid arrays with θ = 54.74˚, 15 μm pitch, and a square cross section fabricated by anisotropic wet etching in 25% TMAH with added Triton X-100, as depicted in Fig. 2.1. Row (a) consists of SEM images from a top-down perspective. Row (b) consists of the corresponding cross-sectional side view. Row (c) consists of SEM images from an arial view to 87

display their 3-D nature. Column 1 contains SEM images corresponding to truncated Si micropyramids with ~11.0 μm small base. Column 2 contains SEM images corresponding to truncated Si micropyramids with ~6.0 μm small base. Column 3 contains SEM images corresponding to truncated Si micropyramids with ~2.5 μm small base. A stir bar was used to mix the TMAH and Triton X-100 solution, but no stir bar was utilized during the etch.

FIGURE 2.3. SEM images of truncated Si microcone arrays with $\theta = 45^{\circ}$, 30 μm pitch, and an octagonal cross section fabricated by anisotropic wet etching in 25% TMAH at 80° C without added Triton X-100, as depicted in Fig. 2.1. Row (a) consists of SEM images from a top-down perspective. Row (b) consists of the corresponding cross-sectional side view. Row (c) consists of SEM images from an arial view to display their 3-D nature. Column 1 contains SEM images corresponding to microcones with ~23.0 μm small base. Column 2 contains SEM images corresponding to microcones with ~16.0 μm small base. Column 3 contains SEM images corresponding to microcones with ~6.0 μm small base. A stir bar was used to mix the TMAH and Triton X-100 solution, but no stir bar was utilized during the etch. 88

FIGURE 2.4. SEM images of three types of inverted Si mesophotonic arrays fabricated by anisotropic wet etching in 25% TMAH, as depicted in Fig. 2.1. Each column is associated with a unique mesophotonic array, and each row corresponds to images of the same type. Row (a) consists of SEM images from a top-down perspective. Row (b) consists of the corresponding cross-sectional side view. Row (c) consists of SEM images from an arial view to display their 3-D nature. Column 1 contains SEM images corresponding to inverted micropyramids with $\theta = 54.74^{\circ}$, 30 μm pitch, nanometer scale small base, and a square cross section. Column 2 contains SEM images corresponding to inverted micropyramids with $\theta = 45^{\circ}$, 30 μm pitch, 14.7 μm small base, and a square cross section. Column 3 contains SEM images corresponding to inverted triangular micropyramids with different sidewall angles θ. One side of the equilateral triangular photomask was aligned to the <110> direction which resulted in $\theta = 54.74^{\circ}$ and is ~21.8 μm long, while the other two sides of the photomask were aligned to a different direction which resulted in $\theta = \sim 48^{\circ}$ and are ~14.3 μm long. A stir bar was used to mix the TMAH and Triton X-100 solution, but no stir bar was utilized during the etch. 89

FIGURE 2.5. Series of confocal microscope images illustrating the ability to precisely control the geometry of the fabricated structures. The shown example is for 30 μm pitch truncated Si micropyramids 91

with 54.74˚ sidewall angles. (a-k) Truncated Si micropyramid's small base size equal to 20.0, 18.1, 15.8, 13.5, 12.1, 10.9, 9.1, 8.4, 5.6, 3.3, and 1.0 μm respectively. (l) Si micropyramid with nanometer scale top. This fabrication control can be generalized to other mesophotonic structures. A stir bar was used to mix the TMAH and Triton X-100 solution, but no stir bar was utilized during the etch.

FIGURE 2.6. Series of confocal microscope images depicting the undercutting of a 100 nm thick thermal SiO_2 square mask layer, represented by the white squares located atop the truncated Si micropyramids. The truncated Si micropyramids were fabricated through anisotropic wet etching with 25% TMAH and 0.3% v/v Triton X-100 for 50 minutes at 80°C. A stir bar was used to mix the TMAH and Triton X-100 solution, but no stir bar was utilized during the etch. The calculated undercutting ratio *l/d* of the <110> direction was ~0.29 *l/d*, where *l* is the undercutting along the <110> direction of the SiO_2 mask, and *d* is the total depth of the etch [314]. (a-d) Undercutting of 30 μm pitch truncated Si micropyramids. (e, f) Undercutting of 15 μm pitch truncated Si micropyramids. 94

FIGURE 2.7. (a-f) Series of confocal microscope images depicting the surface deformations that develop if too much Triton X-100 is added to a 25% TMAH etch at 80° C for 50 minutes. The surface topology is seen in the plots below the images in (d-f), located along the red dotted line. Here, 0.4% v/v Triton X-100 was added to the etchant bath, as seen in Fig. 1.21. A stir bar was used to mix the TMAH and Triton X-100 solution, but no stir bar was utilized during the etch. 95

FIGURE 3.1. 3-D FDTD numerical modeling simulations. Two methodologies for accessing different optical properties of periodic arrays under plane wave illumination at λ = 3, 4, and 5 μm based on two types of BCs: (a) perfectly matched layer BCs at the left and right most plane of the simulation region, and periodic BCs on the four *z*-planes of the simulation region, describing grating-type diffraction and interference effects leading to the formation of the Talbot images at further distances from the truncated Si micropyramids, and (b) perfectly matched layer BCs on all six planes of the simulation region, describing the concentration of light and the formation of photonic jets close to the truncated Si micropyramids. Both (a) and (b) display electromagnetic (EM) field distributions calculated at normal incidence on truncated Si micropyramids with refractive index n = 3.43. The truncated Si micropyramids shown 104

have the same small base size, D_S = 5 μm, and same large base size D_L = 15 μm.

FIGURE 3.2. 3-D FDTD numerical modeling simulations to demonstrate the impact truncated Si micropyramid height has on the Talbot effect. EM field distributions calculated at normal incidence for truncated Si micropyramids with index n = 3.43 at λ = 2.94 μm. Three different truncated Si micropyramids depicted in the three rows all have the same small base size, D_S = 4 μm, and different large base size, D_L = 5, 8, and 11 μm, respectively. PML BCs along the x-direction and periodic BCs along z-directions describe grating-type diffraction and interference effects leading to the formation of the Talbot images at further distances from the truncated Si micropyramids [363]. 108

FIGURE 3.3. Experimental study of Talbot effect and comparison with a 3-D FDTD numerical modeling simulation. (a) Experimental setup where imaging of intensity distributions at different distances z from the tops of the truncated Si micropyramids was provided by a Ge IR lens with f = 12.7 mm attached to a micrometer translation stage. The illumination was provided with an Er:YAG laser at wavelength λ = 2.94 μm and the Talbot images were captured by a MWIR Spiricon beam profiler. (b) Typical examples of experimental Talbot self-images belonging to the "Talbot Length" subset obtained at distances $z_T(m)$ and the "Half Talbot Length" subset obtained at distances $z_T(m + 0.5)$ where m = 0, 1, 2, …, etc., respectively. In the cross-sectional xy planes, the peaks in the "Talbot Length" subset are aligned with the truncated Si micropyramids whereas the peaks in the "Half Talbot Length" occupy positions between the truncated Si micropyramids. (c) EM field distribution numerically modeled along the propagation direction in a plane passing through centers of the truncated Si micropyramids which illustrate properties of the "Talbot Length" subset. (d) Experimentally determined positions of the self-imaging Talbot planes and relative intensities of the peaks in these Talbot planes depicted by grey and red bars for the "Talbot Length" and "Half Talbot Length" subsets, respectively [363]. 110

FIGURE 3.4. 3-D FDTD numerical modeling simulation study on the optical properties of truncated Si micropyramids at λ = 3 μm by utilizing perfectly matched layer BCs. (a) EM field map defining the parameters studied; specifically, the peak intensity enhancement factor (IEF), FWHM, and light concentration distance d of the photonic jets, as well as the truncated Si micropyramid's large base size D_L and small base size D_S. In this EM field map, D_L = 30 μm and D_S = 10 μm. (b-d) Plots showing how the peak IEF, 115

FWHM, and d of the photonic jets change depending on D_L, and D_S [363].

FIGURE 3.5. 3-D FDTD numerical modeling simulation study on the optical properties of truncated Si micropyramids at λ = 4 μm by utilizing perfectly matched layer BCs. (a) EM field map defining the parameters studied; specifically, the peak intensity enhancement factor (IEF), FWHM, and light concentration distance d of the photonic jets, as well as the truncated Si micropyramid's large base size D_L and small base size D_S. In this EM field map, D_L = 30 μm and D_S = 10 μm. (b-d) Plots showing how the peak IEF, FWHM, and d of the photonic jets change depending on D_L, and D_S [363]. 116

FIGURE 3.6. 3-D FDTD numerical modeling simulation study on the optical properties of truncated Si micropyramids at λ = 5 μm by utilizing perfectly matched layer BCs. (a) EM field map defining the parameters studied; specifically, the peak intensity enhancement factor (IEF), FWHM, and light concentration distance d of the photonic jets, as well as the truncated Si micropyramid's large base size D_L and small base size D_S. In this EM field map, D_L = 30 μm and D_S = 10 μm. (b-d) Plots showing how the peak IEF, FWHM, and d of the photonic jets change depending on D_L, and D_S [363]. 117

FIGURE 3.7. 3-D FDTD numerical modeling simulation performed for a dipole source embedded at 1 μm depth in a Si slab. Comparison of the light extraction and directionality of the dipole sources embedded in Si slabs for the following cases: (a-c) bare Si wafer and (d-f) dipole positioned close to the small base D_S of the truncated Si micropyramid. The dipole source oscillates perpendicular to the xz plane at λ = 3 μm. The dimensions of the truncated Si micropyramid in (d-f) are D_L = 15 μm and D_S = 6.4 μm. Efficient coupling of the dipole's emission into the truncated Si micropyramid is depicted by comparing EM field profiles portrayed in (b, e). An order of magnitude higher extraction efficiency was obtained in the case of using a truncated Si micropyramid, where a more structured far-field emission profile is apparent by comparing the far-field EM field distributions shown in (c, f). 120

FIGURE 4.1. Diagram depicting the fabrication protocol to create 10 × 10 arrays of monolithically integrated Si micropyramids with MWIR PtSi/p-Si Schottky barrier photodetectors fabricated on the small based of these truncated micropyramids. The top row depicts microscope images of the top-down view, and the bottom row depicts 130

diagrams of the corresponding side-view. (a) The device fabrication begins with the micropyramids previously fabricated, as described in Chapter 2. (b) The mesa fabrication steps first requires the mesa size to be defined with photolithography. (c) The mesa fabrication step ends with the deposition of Pt and the excess Pt is lifted off by removing the photoresist. (d) The passivation step begins by depositing a uniform 300 nm thick layer of SiO_2 and performing photolithography to prepare for the next step. (e) The passivation step ends when the SiO_2 undergoes a BOE etch to create through-holes in the SiO_2 layer, where the remaining photoresist is removed. (f) The metal step is where the 5 nm thick Cr and 300 nm thick Au layers are deposited, in order to electrically connect all 100 detectors together for characterization.

FIGURE 4.2. Microscope images showing the fabrication step for MWIR PtSi detectors corresponding to Fig. 4.1(c). (a) An entire die is shown, where the top eight detectors are planar reference devices and the bottom eight detectors are fabricated on top of micropyramids. (b, e) 10 × 10 PtSi detector array with 21 μm squares fabricated on top of 60 μm pitch micropyramids. (c, f) 10 × 10 PtSi reference detector array of the same size as the detectors on the micropyramids. (d, g) 10 × 10 PtSi detector array with a large fill-factor of 58 μm squares with 60 μm pitch. 132

FIGURE 4.3. Microscope images showing the fabrication step for MWIR PtSi detectors corresponding to Fig. 4.1(e). (a) An entire die is shown, where the top eight detectors are planar reference devices and the bottom eight detectors are fabricated on top of micropyramids. (b, e) 10 × 10 PtSi detector array with 21 μm squares fabricated on top of 60 μm pitch micropyramids. (c, f) 10 × 10 PtSi reference detector array of the same size as the detectors on the micropyramids. (d, g) 10 × 10 PtSi detector array with a large fill-factor of 58 μm squares with 60 μm pitch. 133

FIGURE 4.4. Microscope images showing the fabrication step for MWIR PtSi detectors corresponding to Fig. 4.1(f) before the 5 nm of Cr and 300 nm of Au were deposited. (a) An entire die is shown, where the top eight detectors are planar reference devices and the bottom eight detectors are fabricated on top of micropyramids. (b, e) 10 × 10 PtSi detector array with 21 μm squares fabricated on top of 60 μm pitch micropyramids. (c, f) 10 × 10 PtSi reference detector array of the same size as the detectors on the micropyramids. (d, g) 10 × 10 PtSi detector array with a large fill-factor of 58 μm squares with 60 μm pitch. 134

FIGURE 4.5. Microscope images showing the fabrication step for MWIR PtSi detectors corresponding to Fig. 4.1(f) after the 5 nm of Cr and 300 nm of Au were deposited. (a) An entire die is shown, where the top eight detectors are planar reference devices and the bottom eight detectors are fabricated on top of micropyramids. (b, e) 10 × 10 PtSi detector array with 21 μm squares fabricated on top of 60 μm pitch micropyramids. (c, f) 10 × 10 PtSi reference detector array of the same size as the detectors on the micropyramids. (d, g) 10 × 10 PtSi detector array with a large fill-factor of 58 μm squares with 60 μm pitch. 135

FIGURE 4.6. (a) Top-down microscope image and (c) corresponding cross-sectional view depicting monolithic integration of Si micropyramid arrays with MWIR PtSi/p-Si Schottky barrier photodetectors. These detectors have 21 μm square mesas fabricated on the small bases of the micropyramids. (b, d) Complimentary images depicting planar reference devices with identical photodetector mesa size. The device diagrams in (c, d) illustrate that, in both cases, the 5 nm thick Cr layer with 300 nm thick Au layer is electrically connected to the ~2 nm thick PtSi layer (n-contact) via a tiny ~3 μm opening in the 300 nm thick SiO_2 layer. (e) Measurement setup for the photoresponse spectra using a Vertex 80v Fourier transform infrared spectrometer (FTIR) by Bruker. (f) Measurement setup for determining the quantum efficiency (QE) of PtSi Schottky barrier detectors with a calibrated blackbody system heated to 1000° C. (g) Plot showing the transmission characteristics of the three optical filters used in the QE setup shown in (f). 138

FIGURE 4.7. Spectral response plots for the four 10 × 10 detector arrays in the center of the dies shown in Figs 4.2(a)-4.5(a) measured at 80 K in reverse bias with a Ge window installed on the dewar, where the inset shows the corresponding Fowler plots used to optically determine the PtSi barrier height. 139

FIGURE 4.8. (a) Barrier height as a function of voltage and (b) dark current density as a function of voltage for the four 10 × 10 detector arrays in the center of the dies shown in Figs 4.2(a)-4.5(a) measured at 80 K in reverse bias with a Ge window installed on the dewar. These devices all were fabricated on the same Si wafer and were all exposed to the same annealing conditions, yet the large planar reference device shows different barrier height values. 140

FIGURE 4.9. (a) Comparison of the QE spectra from two 10 × 10 micropyramidal photodetector arrays, shown by the red and black curves, to the corresponding 10 × 10 planar reference 142

photodetector array fabricated on the same Si wafer, shown by the blue curve. The detector mesas were 21 μm squares with ~2 nm thick PtSi. The insert shows that the dark current density-voltage (I-V) relationships in these three cases were identical. (b) PEF spectra showing ~1.25× signal enhancement due to the micropyramids. This PEF spectra were smaller, potentially due to edge leakage current effects. This is apparent in Fig. 4.2(e) where the corners of the mesa on the micropyramid are over the edge of the micropyramid.

FIGURE 4.10. (a) By using this same process for the previous die shown in Fig. 4.9, PEF spectra showing ~1.5× signal enhancement due to these micropyramids were obtained. This is in relatively close agreement with what numerical modeling predicts at PEF ≈ 1.7× signal enhancement, shown by the blue curve. This device doesn't have the issue of the mesa hanging over the edge, and therefore gave larger PEF ≈ 1.5×. The numerical modeling curve was calculated by dividing the absorption spectra of the detector integrated with a micropyramid shown in (b) by the absorption spectra of a planar detector shown in (c). 144

FIGURE 4.11. The optical absorption characteristics of two micropyramids monolithically integrated with weak absorbers are depicted via ray tracing and 3-D FDTD numerical modeling EM field maps. In both cases the Si micropyramids have identical dimensions where D_L = 15 μm and D_S = 9 μm. (a) The PEF spectra were obtained by calculating the absorption spectra with a micropyramid (as shown in (b) and (c)) and dividing them by the absorption spectra of the planar reference structure (as depicted in Fig 4.10(c)). The resulting PEF spectra are presented for two designs: the red curve corresponds to a design utilizing a silicon-on-insulator (SOI) wafer, while the blue curve represents a monolithic all-Si structure. (b, d) Ray tracing diagram and corresponding EM field map for a SOI micropyramid. (c, e) Ray tracing diagram and corresponding EM field map for an all-Si micropyramid. Both are coated with a 300 nm thick SiO_2 layer and a 300 nm thick Au layer. To model the absorption behavior of PtSi Schottky barrier photodetectors, a simplified approach was used, with a weakly absorbing square structure (8 μm in size, 50 nm thick) positioned at the interface between the small base of the micropyramid and the SiO_2 layer. The Au mirror was included to enhance MWIR radiation absorption [363]. 147

FIGURE 4.12. The optical absorption characteristics of two micropyramids monolithically integrated with weak absorbers are depicted via ray tracing and 3-D FDTD numerical modeling EM field maps. In 150

both cases the Si micropyramids have identical dimensions where D_L = 30 μm and D_S = 18 μm. (a) The PEF spectra were obtained by calculating the absorption spectra with a micropyramid (as shown in (b) and (c)) and dividing them by the absorption spectra of the planar reference structure (as depicted in Fig 4.10(c)). The resulting PEF spectra are presented for two designs: the red curve corresponds to a design utilizing a silicon-on-insulator (SOI) wafer, while the blue curve represents a monolithic all-Si structure. (b) EM field map for a SOI micropyramid. (c) EM field map for an all-Si micropyramid. Both are coated with a 300 nm thick SiO_2 layer and a 300 nm thick Au layer. To model the absorption behavior of PtSi Schottky barrier photodetectors, a simplified approach was used, with a weakly absorbing square structure (17 μm in size, 50 nm thick) positioned at the interface between the small base of the micropyramid and the SiO_2 layer. The Au mirror was included to enhance MWIR radiation absorption.

FIGURE 4.13. The optical absorption characteristics of two micropyramids monolithically integrated with weak absorbers are depicted via ray tracing and 3-D FDTD numerical modeling EM field maps. In both cases the Si micropyramids have identical dimensions where D_L = 60 μm and D_S = 22 μm. (a) The PEF spectra were obtained by calculating the absorption spectra with a micropyramid (as shown in (b) and (c)) and dividing them by the absorption spectra of the planar reference structure (as depicted in Fig 4.10(c)). The resulting PEF spectra are presented for two designs: the red curve corresponds to a design utilizing a silicon-on-insulator (SOI) wafer, while the blue curve represents a monolithic all-Si structure. (b) EM field map for a SOI micropyramid. (c) EM field map for an all-Si micropyramid. Both are coated with a 300 nm thick SiO_2 layer and a 300 nm thick Au layer. To model the absorption behavior of PtSi Schottky barrier photodetectors, a simplified approach was used, with a weakly absorbing square structure (21 μm in size, 50 nm thick) positioned at the interface between the small base of the micropyramid and the SiO_2 layer. The Au mirror was included to enhance MWIR radiation absorption. 153

FIGURE 5.1. Sketch illustrating the 3-D geometry of the retroreflector structure, as well as the experimental geometry. It shows the main parameters such as the period (Λ) and width of the metallic stripes (a) in the surface square slot array. Plane waves are incident at an angle of Θ_{in}. A specularly reflected zero-order beam and diffracted beam corresponding to m = -1 in the grating equation are illustrated. 160

FIGURE 5.2. Wavelength dependence of the diffraction angle calculated for several angles of incidence in the 60 - 80° range. The dependencies coincide for TE and TM polarizations of incident light. The design wavelength λ = 633 nm is shown by the vertical dashed line. 164

FIGURE 5.3. Retroreflection spectra normalized to the intensity of the incident beam. The spectra were calculated for (a) TE and (b) TM polarizations incident at Θ_{in} = 70° for different stripe widths, a = 60, 80, 100, 120, and 140 nm. The vertical dashed line shows the design wavelength of λ = 633 nm. 165

FIGURE 5.4. Intensity of the diffracted (m = -1) beam normalized to the intensity of the incident beam calculated at different angles of incidence, Θ_{in} = 65°, 70°, and 80° for TE and TM polarizations. 166

FIGURE 5.5. (a) Diagram depicting the azimuthal performance of the Littrow retroreflector, showing light incident in a plane rotated by angle ϕ relative to the symmetry plane passing through x-axis. (b) Polar plot showing both the polar and azimuthal angles for the incident, specular, and diffracted beams. The diffracted beam is indicated as retro in this plot [369]. 168

FIGURE 5.6. Retroreflection spectra normalized to the intensity of the incident beam and calculated for (a) TE and (b) TM polarizations at a polar incidence angle of Θ_{in} = 70° and for different azimuthal angles ϕ = 0°, 5°, 10°, and 15°, measured from the symmetry plane. The design wavelength of λ = 633 nm is shown by the vertical dashed line. 169

FIGURE 5.7. Retroreflection spectra normalized to the intensity of the incident beam for an Au slot array. Retroreflection calculated for (a) TE and (b) TM polarizations of incident light at Θ_{in} = 70° for thicknesses in the 20 - 70 nm range. The vertical dashed line represents the design wavelength of λ = 633 nm. 172

FIGURE 5.8. Retroreflection spectra normalized to the intensity of the incident beam for an Ag slot array. Retroreflection calculated for (a) TE and (b) TM polarizations of incident light at Θ_{in} = 70° for thicknesses in the 20 - 70 nm range. The vertical dashed line represents the design wavelength of λ = 633 nm. 173

FIGURE 5.9. Retroreflection spectra normalized on the intensity of the incident beam for a Cu slot array calculated at (a) TE and (b) TM polarizations of incident light for Θ_{in} = 70° with the thicknesses in 174

the 20 - 70 nm range. The design wavelength of λ = 633 nm is shown by the vertical dashed line.

FIGURE 5.10. Retroreflection spectra normalized on the intensity of the incident beam for an Al slot array calculated at (a) TE and (b) TM polarizations of incident light for Θ_{in} = 70° with the thicknesses in the 20 - 70 nm range. The design wavelength of λ = 633 nm is shown by the vertical dashed line. 175

FIGURE 5.11. Retroreflection spectra normalized to the intensity of the incident beam for an Au slot array with thicknesses of 11.7, 21, 25, 44, 53, and 117 nm. Calculations for real Au thin films with experimentally determined index values are shown by solid curves whereas similar calculations for the bulk Au index values for the same thicknesses are shown by dashed lines. The results were obtained at (a) TE and (b) TM polarizations of incident light at Θ_{in} = 70°. The design wavelength of λ = 633 nm is shown by the vertical dashed line. 177

FIGURE 5.12. Absorption spectra normalized to the intensity of the incident beam for an Au slot array for thin films with thicknesses of 11.7, 21, 25, 44, 53, and 117 nm indicated by the same colors as in Fig. 5.11. Calculations for real Au thin films with experimentally determined index values are shown by solid curves whereas similar calculations for the bulk Au index values for the same thicknesses of the slot arrays are shown by dashed lines. The results were obtained at (a) TE and (b) TM polarizations of incident light at Θ_{in} = 70°. The design wavelength of λ = 633 nm is shown by the vertical dashed line. 178

LIST OF ABBREVIATIONS

Abbreviation	Word or Phrase
1-D	one-dimensional
2-D	two-dimensional
3-D	three-dimensional
AFRL	Air Force Research Laboratory
AOV	angle-of-view
BIB	blocked impurity band
BOE	buffered oxide etchant
BSI	back-side illumination
CCD	charge-coupled device
CMOS	complementary metal oxide semiconductor
DSP	double-side polished
EM	electromagnetic
FCC	face-centered cubic
FDTD	finite-difference time-domain
FPA	focal plane array
FRR	flat retroreflector
FTIR	Fourier transform infrared
FWHM	full-width at half-maximum
GTRI	Georgia Tech Research Institute
HMDS	hexamethyldisilazane

HPM	hyperbolic plasmonic metasurface
IC	integrated circuit
IEF	intensity enhancement factor
IPA	isopropyl alcohol
IR	infrared
KOH	potassium hydroxide
LED	light-emitting diode
LSPR	localized surface plasmon resonances
MEMS	micro-electro-mechanical
MIS	metal-insulator-semiconductor
MWIR	mid-wave infrared
NEP	noise-equivalent power
PEC	perfect electric conductor
PECVD	plasma-enhanced chemical vapor deposition
PEF	power enhancement factor
PML	perfectly matched layer
PS	polystyrene
PSP	propagating surface plasmons
QE	quantum efficiency
QWIP	quantum well infrared photodetectors
RCS	radar cross-section
RF	radiofrequency
RFID	radiofrequency identification

RIE	reactive ion etching
ROIC	readout integrated circuit
RPM	revolutions per minute
SB	Schottky barrier
SEM	scanning electron microscope
SIL	solid immersion lens
SLG	soda-lime glass
SLR	surface lattice resonance
SNR	signal-to-noise
SOI	silicon-on-insulator
SP	surface plasmon
SPP	surface plasmon polariton
SWIR	short-wave infrared
TE	transverse electric
TM	transverse magnetic
TMAH	tetramethylammonium hydroxide
UV	ultraviolet

CHAPTER 1: INTRODUCTION

1.1. Outline and Overview of the Dissertation

In this dissertation, methods for enhancing infrared (IR) photodetector focal plane arrays (FPAs) through integration with silicon (Si) micropyramidal arrays are investigated, as well as investigate novel metamaterial retroreflecting arrays designed to optimize the retroreflection of both transverse electric (TE) and transverse magnetic (TM) polarizations simultaneously in the visible wavelength regime. In the former, to enhance FPAs with Si micropyramidal arrays, first a general understanding of IR photodetector FPAs and their limitations are necessary in order to comprehend how to enhance them. Second, the means by which these light-concentrating mesoscale structures actually enhance the signal need to be understood, as well as their optical properties. Third, Si anisotropic wet etching typically used in micro-electro-mechanical systems (MEMS) must be understood in order to fabricate the Si micropyramidal arrays. These are all introduced in sections 1.2, 1.3, and 1.4, respectively. In the latter, different retroreflector methodologies need to be understood in order to comprehend their limitations. Additionally, many of these retroreflectors utilize plasmonic contributions to enhance their retroreflectivity, and therefore an understanding of plasmonic effects needs to be understood as well. These are introduced in sections 1.5 and 1.6, respectively.

A FPA is a crucial component of imaging systems and is formed by arranging individual photodetectors in a grid-like array. Modern FPAs for mid-wave IR (MWIR, λ = 3–5 μm) imaging systems feature progressively smaller pixels to improve spatial sampling and enhance the spatial resolution of the captured images [1-5]. High-performance MWIR FPAs are typically cooled to cryogenic temperatures to reduce the dark current noise. This cooling is essential to prevent thermal generation of charge carriers, as thermal transitions compete with optical transitions, resulting in significant noise in non-cooled devices [1-11]. This noise can be reduced by shrinking the photodetector area. Reducing the dimensions of the photodetectors decreases the dark current, thereby enhancing sensitivity [1-5]. However, this downsizing can also reduce quantum efficiency (QE) due to less effective light coupling, potentially hindering detection performance [1-5]. The light collection efficiency can be improved using light-concentrating structures such as metalenses, microlenses, microspheres, or micropyramids which are placed over individual pixels [12-25]. This allows light to be collected from a larger area and concentrated into a much smaller area that can be aligned with the photodetector's mesa to maintain or enhance the signal-to-noise ratio (SNR) in order to increase the operating temperature of FPAs.

In Chapter 2, anisotropic wet etching of Si for photonic applications was explored by fabricating micropyramidal arrays with different geometries, sidewall angles, and number of sidewalls. The key advantage of Si in MEMS is its compatibility with IC fabrication processes, enabling the integration of mechanical, electrical, and computational functionalities onto a single chip [156, 157]. MEMS fabrication involves a series of processes such as lithography, deposition, and etching. Among these, wet etching is a crucial step that selectively removes material from Si wafers, allowing the formation of

intricate structures with high precision [150-160]. This chapter will discuss the role the wafer orientation has in the sidewall angle of the fabricated structure. It will discuss over etching and the role of surfactant, how the orientation of the photoresist patterns affects the final fabricated structure, and will depict several examples of fabricated mesophotonic arrays for optical applications.

In Chapter 3, applications arising from the unique optical properties of anisotropically wet etched Si micropyramids in the mesoscale regime were investigated by employing Ansys/Lumerical's three-dimensional (3-D) finite-difference time-domain (FDTD) numerical modeling software. Mesoscale denotes objects, like micropyramids, with geometric dimensions on the order of the incident wavelength of light. These objects exhibit different optical properties through light-matter interactions as their geometry varies [46-56]. When micropyramids are much larger than the wavelength of light, the properties of these micropyramids follow the laws of geometrical optics. The diverse properties of mesoscale objects offer a wide array of applications. The focus in this Chapter lies on exploring the optical characteristics and potential uses of micropyramidal structures featuring mesoscale dimensions. The ability of micropyramids to concentrate light stems from the reflections facilitated by their sidewalls. These characteristics are commonly termed as non-imaging light concentration properties, distinguishing them from the focusing effects of lenses. The light-concentration ability typically exhibits a non-resonant nature. However, the optical properties of a micropyramidal array can also lead to various interference effects. Such arrays can be treated as a transmission grating [115-147]. The optical properties of mesoscale structures depend on their geometry, and the properties of

truncated pyramids have been relatively unstudied. From an application development perspective, mesoscale structures of this nature hold considerable promise and appeal.

In Chapter 4, the light-concentration ability of Si micropyramids were experimentally investigated by monolithically integrating MWIR PtSi photodetectors directly on top of truncated micropyramids. This was done to determine if reducing the dimensions of the photodetectors to decrease the dark current, while enhancing the light collection efficiency through using light-concentrating micropyramids will increase the SNR [25, 94-114]. This allows light to be collected from a larger area and concentrated into a much smaller area that can be aligned with the photodetector's mesa to maintain or enhance the SNR in order to increase the operating temperature of FPAs [1-11]. This required an extensive fabrication effort, which is discussed. Additionally, a detailed analysis of the micropyramid FPA was conducted through characterizing the fabricated devices' spectral response and QE in order to determine the enhancement obtained through integration with micropyramids.

In addition to extensive research conducted on enhancing FPAs through integration with truncated Si micropyramid arrays, metasurface retroreflectors were designed for visible wavelengths in this dissertation. Retroreflectors are optical devices designed to reflect an electromagnetic wave back towards its source, irrespective of the angle of incidence [179-223]. Metasurfaces are structures with periodicity smaller than the wavelength of incident light and are designed to have electromagnetic properties beyond what can be found in nature [196-217]. These structures can consist of either dielectric or metallic materials, or some combination thereof. Metasurfaces are able to have a low profile and can be an inexpensive solution to retroreflect light at specific designed angles

for wavelengths of light longer than the visible spectrum. However, they consist of sizes on the order of λ or smaller. Therefore, fabrication of metasurface retroreflectors in the visible spectrum can significantly increase costs and reduce fabrication uniformity. Additionally, it remains rare to achieve a combination of a flat profile, high reflection efficiency, and a wide range of incidence angles in an ultrathin metasurface retroreflector capable of operating for both TE and TM modes [185, 190, 191, 198-203].

In Chapter 5, extensive FDTD numerical modeling was completed for a Littrow configuration metamaterial retroreflector studied with FDTD numerical modeling designed for a HeNe wavelength of 632.8 nm in order to develop fabrication guidelines for retroreflectors operating in the visible regime. Additionally, numerical modeling was extended to real metals with real thicknesses in order to study the impact the type of metal has on retroreflection, as well as how the thickness of the metal layer impacts retroreflection efficiency [264, 305, 306]. The retroreflector has nanometer scale dimensions, and thus plasmonic effects are expected. Real metals at optical frequencies display substantial plasmonic effects, which can drastically affect retroreflector performance [226-237].

1.2. Infrared Photodetector Focal Plane Arrays

A FPA is a crucial component of imaging systems and is formed by arranging individual photodetectors in a grid-like array. Generally, each pixel has its own independent contact while sharing a common contact with other pixels in the array. The layout of these shared contacts affects both electrical performance and readout speed. Modern FPAs for IR imaging systems feature progressively smaller pixels to improve

spatial sampling and enhance the spatial resolution of the captured images. In the MWIR, typical pixel sizes have reached approximately 10 μm [1-3]. High-performance MWIR FPAs are typically cooled to cryogenic temperatures to reduce the dark current noise. Increasing the operating temperature is possible by minimizing the detector's active volume, which decreases the dark current. IR photodetectors are extensively used across numerous scientific and technical fields, including remote sensing, meteorological monitoring, military target detection, and biomedical sensing. To meet the rapidly growing demands, there is a strong pursuit for high-performance IR detectors that offer high responsivity and low dark current [1, 4-9].

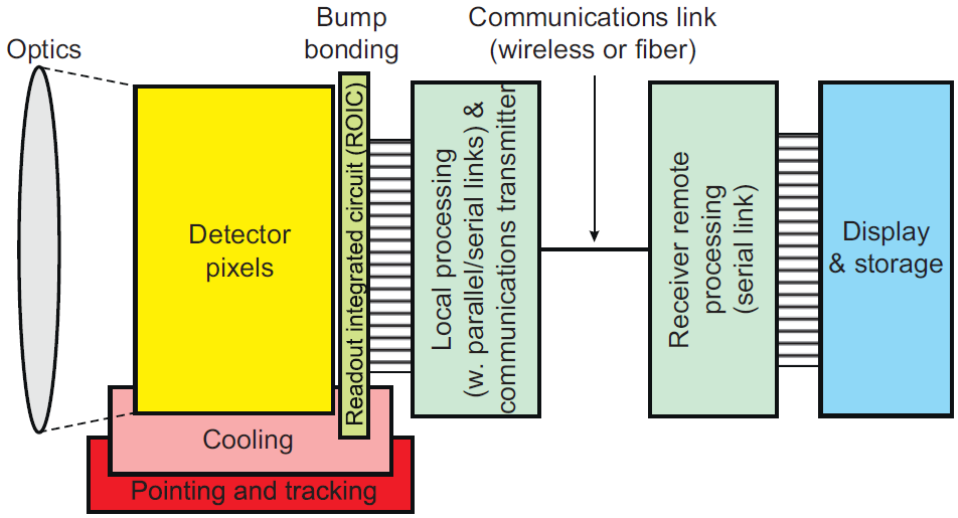

Figure 1.1: Diagram depicting the imaging system for IR detectors and their important sub-systems [1, 10].

Detectors are just one component of functional sensor systems. Military sensor systems also include numerous other components such as optics, coolers, pointing and tracking systems, electronics, communication, processing and information-extraction subsystems, and displays, as seen in Fig. 1.1. Therefore, developing a complete sensor system is significantly more challenging than simply fabricating a detector array [1, 5].

For IR photodetection, materials with large absorption coefficients and high quantum efficiencies, such as HgCdTe, incident photons are almost entirely converted into electronic signals, making further increases in responsivity challenging. Therefore, reducing the active volume to lower the dark current, while maintaining light collection efficiency through light concentration methods, presents a promising approach to enhance detectivity [1, 11].

The light collection efficiency can be enhanced by utilizing light concentrating structures such as metalenses [12-16], microlenses [17-19], microspheres [20-22], or micropyramids [23-25], to name a few, where the light concentrating structures are placed over individual pixels. However, commercial microlens arrays typically have long focal distances ($f \sim 200$ μm), resulting in a narrow angle-of-view of only a few degrees. In contrast, microspheres with an index of refraction $n \sim 1.6–1.8$ can focus light near their shadow-side surface, creating "photonic jets" with subwavelength transversal widths [21, 22]. This enables the collection of light from a larger area where it is concentrated into a much smaller area that can be aligned with the photodetector's mesa.

In general, detectors fall into two primary categories: cooled and uncooled. Cooled detectors necessitate cooling below ambient temperature. While uncooled sensors present notable benefits in terms of cost, longevity, size, weight, and power consumption, cooled sensors offer notably improved range, resolution, and sensitivity due to their operation at lower noise levels [1, 4-9, 11]. Fig. 1.2 illustrates the range of operating temperatures and wavelength regions covered by various IR detector technologies. Operating temperatures typically span from 4K to slightly below room temperature, depending on the specific detector technology employed. Most modern cooled detectors function within a

temperature range of below 10K to 150K, varying according to the type of detector and desired performance level. A temperature of 77K is quite common, as it can be relatively easily achieved using liquid nitrogen. Despite their name, uncooled detectors typically include some form of temperature control, maintaining temperatures of approximately 250–300 K to minimize noise, optimize resolution, and ensure stable operation [1, 4-9, 11].

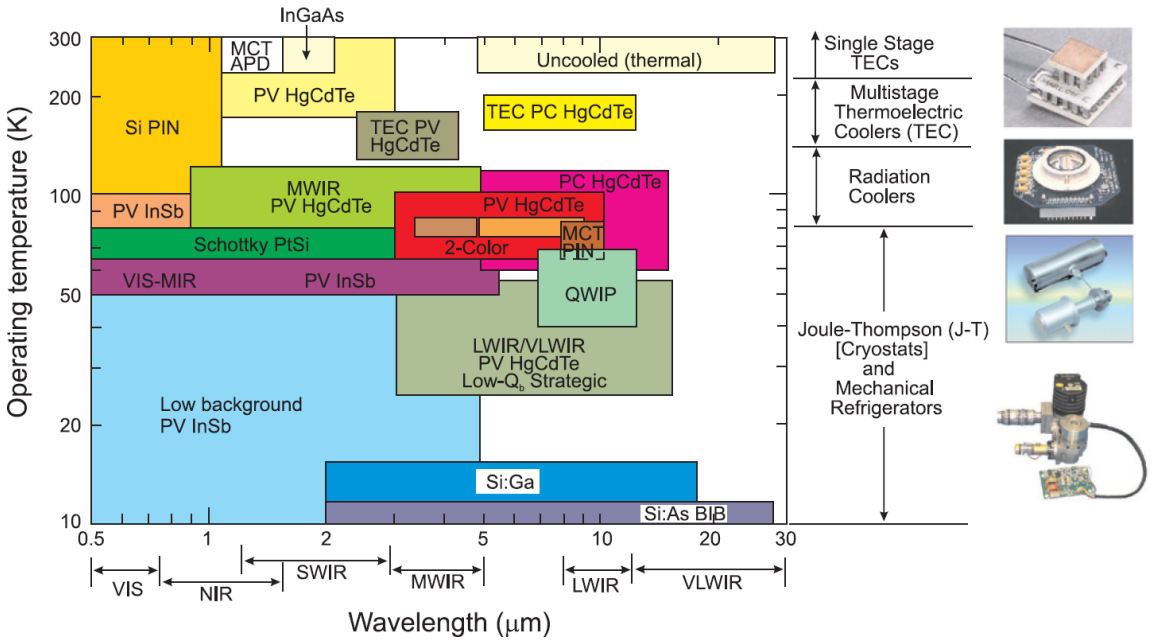

Figure 1.2: Diagram depicting the diversity of IR detector technologies at their respective operating temperatures and wavelengths [1].

1.2.1. Fundamentals of Photon Detectors

In photon detectors, radiation is absorbed within the material through interactions with electrons, either bound to lattice atoms, impurity atoms, or free electrons. The resulting electrical output signal arises from the altered electronic energy distribution [1, 11]. The fundamental optical excitation processes in semiconductors are seen in Fig. 1.3(a). Photon detectors demonstrate a wavelength-dependent response per unit incident radiation power. They offer excellent SNR performance and rapid response. However, achieving this

requires cryogenic cooling for IR detectors. This cooling is essential to prevent thermal generation of charge carriers, as thermal transitions compete with optical transitions, resulting in significant noise in non-cooled devices. Based on the nature of the interaction, the category of photon detectors is divided into various types. The most significant among these are intrinsic detectors, extrinsic detectors, and photoemissive detectors such as Schottky barrier photodetectors [1, 5, 11]. A few of these are shown in Fig. 1.3(b-f).

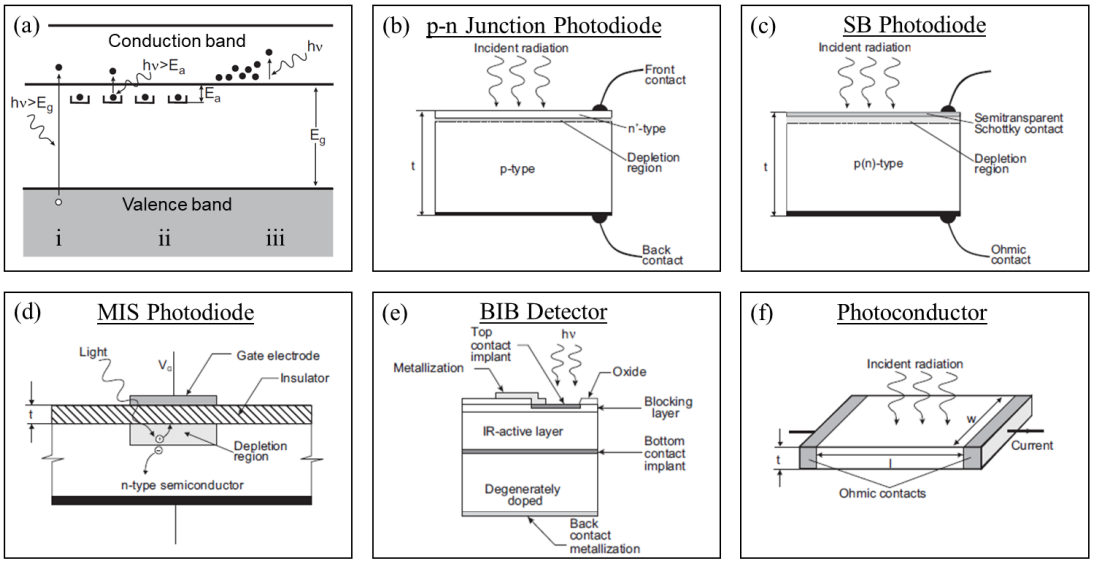

Figure 1.3: (a) Optical excitation mechanisms in semiconductors: i) intrinsic absorption, ii) extrinsic absorption, iii) free carrier absorption. (b-f) Diagrams showing a few types of photon detectors, as well as their operating principles: (b) p-n junction photodiode, (c) Schottky barrier photodiode, (d) metal-insulator-semiconductor photodiode, (e) blocked impurity band detector, and (f) photoconductor [1].

The p–n junction photodiode shown in Fig. 1.3(b) is the most commonly employed photovoltaic detector, characterized by a robust internal electric field spanning the junction. When photons strike the junction, they generate free hole–electron pairs that become separated by this internal electric field. This separation leads to a voltage alteration across the open-circuit cell or induces a current flow in the short-circuited scenario. Because recombination noise is absent, the inherent noise level of the p–n junction can ideally be $\sqrt{2}$ times less compared to a photoconductor [1, 11].

Schottky barrier (SB) photodiodes shown in Fig. 1.3(c) offer several advantages over p–n junction photodiodes. These include a simplified fabrication process, the absence of high-temperature diffusion steps, and a rapid response speed. As a majority carrier device, SB photodiodes do not encounter issues with minority carrier storage and removal, allowing for higher expected bandwidths. Moreover, the thermionic emission process is significantly more efficient than diffusion, resulting in a saturation current of several orders of magnitude higher than that in p–n junctions for a given built-in voltage [1, 11].

The metal-insulator-semiconductor (MIS) photodiode shown in Fig. 1.3(d) contains a semiconductor and a metal gate electrode separated by an insulator. Electrons are repelled from the insulator-semiconductor interface when a negative voltage is applied to the metal electrode, creating a depletion region. The minority carriers drift to the depletion region after incident photons generated hole-electron pairs, causing the depletion region to become smaller. The photogate's total charge collection capability is influenced by the gate bias, insulator thickness, electrode area, and the semiconductor's doping [1, 26, 27].

The blocked impurity band (BIB) detector structure shown in Fig. 1.3(e) has the active region positioned between an undoped blocking layer and a highly doped degenerate substrate electrode. The active layer is doped sufficiently to initiate an impurity band, ensuring high quantum efficiency for impurity ionization. The device exhibits a diode-like characteristic, except that electron photoexcitation occurs between the donor impurity and the conduction band [1, 11].

Photoconductors shown in Fig. 1.3(f) are basically resistors sensitive to radiation. They either rely on the excitation of electrons from the valence to the conduction band and are termed intrinsic detectors, or function by elevating electrons to the conduction band or

moving holes to the valence band from impurity states within the band and are termed extrinsic detectors. The electrical conductivity increases when a photon releases an impurity-bound charge carrier or an electron-hole pair, and this change is measured with ohmic contacts attached to either side of the photosensitive material [1, 4-9, 11].

A significant distinction between intrinsic and extrinsic detectors is that extrinsic detectors necessitate extensive cooling to achieve high sensitivity at a specific spectral response cutoff, compared to intrinsic detectors. Operating at low temperatures is crucial for longer-wavelength sensitivity to mitigate noise arising from thermally induced transitions between closely spaced energy levels [1, 11].

Photodiodes can be assembled into two-dimensional (2-D) arrays containing a very large number of pixels. They have exceptionally low power dissipation, inherently high impedance, negligible 1/f noise, and easy signal readout through a readout integrated circuit (ROIC). Additionally, the photoresponse of photodiodes remains linear for significantly higher photon flux levels compared to photoconductors, primarily due to higher doping levels in the photodiode absorber layer and the rapid collection of photogenerated carriers by the junction [1, 4, 5, 11].

1.2.2. Focal Plane Array Integration Techniques

Progress in integrated circuit (IC) design and fabrication techniques have led to ongoing, rapid advancements in the size and performance of detectors integrated with electronic readouts to create detector arrays. The term focal plane array describes a collection of individual detector elements situated at the focal plane of an imaging system. Typically, the optical component of an optoelectronic imaging device is responsible solely

for focusing the image onto the detector array. Various photodetector integration methods with a ROIC, such as monolithic or hybrid shown in Fig. 1.4, are employed in the creation of FPAs [1, 4, 5, 11]. The key design considerations revolve around balancing performance advantages with manufacturability. Depending on the specific technical requirements, projected costs, and timelines, different applications may lean towards one approach.

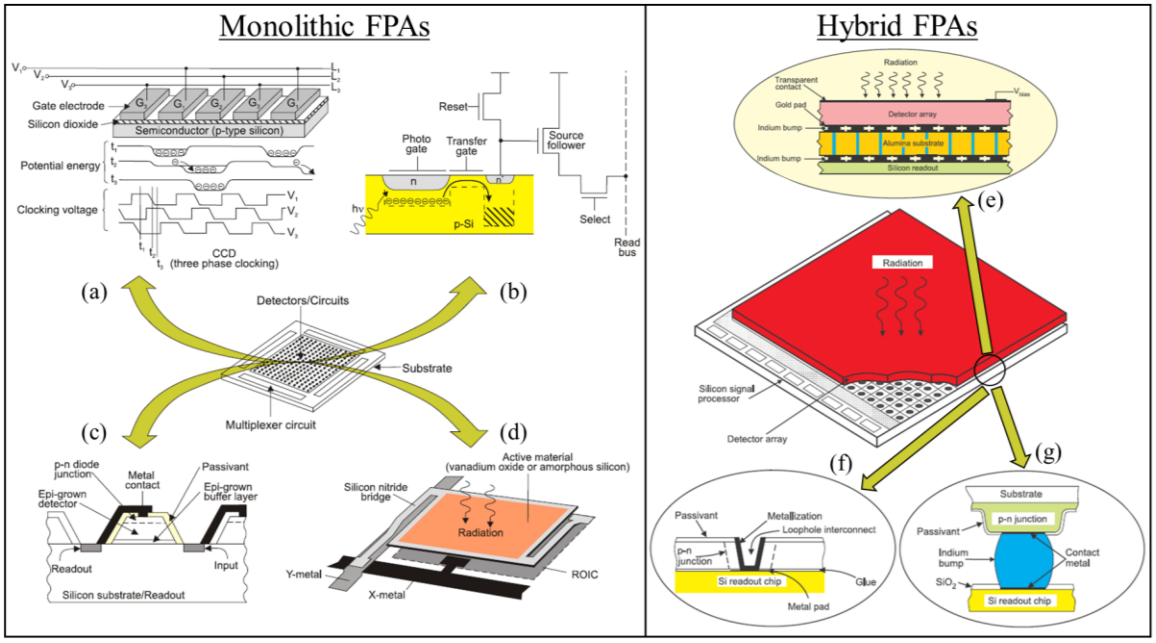

Figure 1.4: Diagram depicting four different monolithic FPAs and different interconnect techniques for hybrid FPAs. Monolithic FPAs include (a) CCD array, (b) CMOS array, (c) heteroepitaxy-on-silicon, or the growth of a crystalline film on Si, and (d) microbolometer. Interconnect techniques for hybrid FPAs include (e) layered-hybrid design, (f) loophole technique, and (g) indium bump technique [1].

In the monolithic approach, both light detection and signal readout occur within the detector material itself, rather than relying on an external readout circuit. Integrating the detector and readout functions onto a single monolithic piece reduces the number of processing steps, enhances yields, and lowers costs. A few examples of monolithic integration are shown in Fig. 1.4(a-d). Despite efforts to cultivate monolithic structures utilizing diverse IR detector materials, only a handful have progressed to a stage of

practical application. These include PtSi, and more recently PbS, PbSe, and PbTe. The PtSi detector stands out as the most widely utilized Schottky barrier detector, offering detection capabilities within the 3 - 5 μm spectral range [1, 4-6, 11, 28, 29].

Other IR material systems such as InGaAs, InSb, HgCdTe, GaAs/AlGaAs QWIP, and extrinsic Si are employed in hybrid configurations. The hybrid approach, shown in Fig. 1.4(e-g), enables the ability to optimize both the detector material and the signal readout independently [1, 7, 11]. These FPAs offer several advantages, including near-100% fill factors and an increased signal-processing area on the chip.

Various hybridization methods are utilized today, with the most prevalent being flip-chip interconnect using bump bonding shown in Fig. 1.4(g). In this technique, indium bumps are created on both the detector array and the ROIC chip. The array and the ROIC are aligned, and pressure is applied to induce the indium bumps to cold-weld together. Alternatively, in another approach, indium bumps are exclusively formed on the ROIC; the detector array is aligned and brought into proximity with the ROIC, the temperature is elevated to melt the indium, and contact is established through reflow. This greatly simplifies the interface between the vacuum-enclosed cryogenic sensor and the system electronics [1, 5].

The detector array can receive illumination from either the frontside, with photons traversing the transparent Si signal readout, or the backside, with photons passing through the transparent substrate of the detector array. Typically, the backside illumination approach is more advantageous, as the signal readout often contains metallized areas and other opaque regions that can diminish the effective optical area of the structure [1, 5, 11,

30]. For backside detector illumination, transparent substrates are necessary. However, when using opaque materials, substrates can be thinned to improve performance.

One specific example of a detector material that can operate in either frontside or backside illumination modes is the HgCdTe photodiode hybrid FPA with spectral range from 1 to 20 µm [31, 32]. The spectral cutoff can be customized by adjusting the composition of the HgCdTe alloy. In Fig 1.5(a,b), the schematic band profiles of the most commonly utilized unbiased homo- (n+-on-p) and heterojunction (p-on-n) photodiodes are depicted, while Fig 1.5(c) shows numerical modeling of the mercury vacancy dark current for n-on-p HgCdTe photodiodes [1].

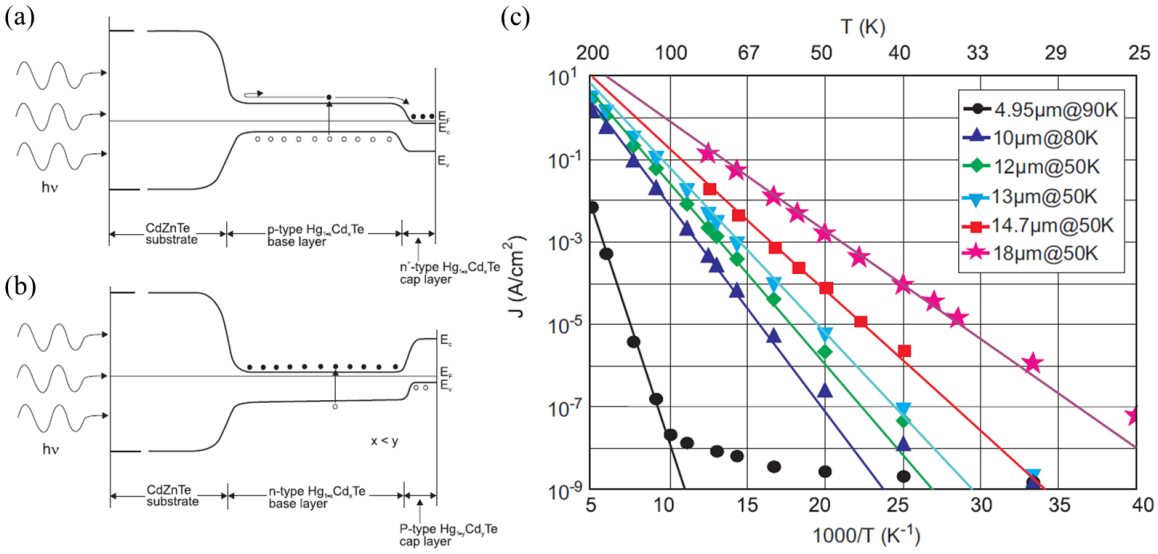

Figure 1.5: HgCdTe photodiode band diagrams for (a) n^+-on-p and (b) p-on-n. (c) Numerical modeling of mercury vacancy dark current for n-on-p HgCdTe photodiodes [1, 31, 33].

1.2.3. FPA Enhancement with Light Concentration Techniques

A fundamental limitation to IR photodetector technology is the large thermal noise of uncooled FPAs [1, 4, 5]. This noise can be reduced by shrinking the photodetector area, and therefore reducing its associated noise. Reducing the dimensions of the photodetectors

decreases both the dark current and junction capacitance, thereby enhancing sensitivity [14]. However, this downsizing can also reduce quantum efficiency due to less effective light coupling, potentially hindering detection performance. The light collection efficiency can be improved using light-concentrating structures such as metalenses, microlenses, microspheres, or micropyramids which are placed over individual pixels. This allows light to be collected from a larger area and concentrated into a much smaller area that can be aligned with the photodetector's mesa to maintain or enhance the SNR in order to increase the operating temperature of FPAs.

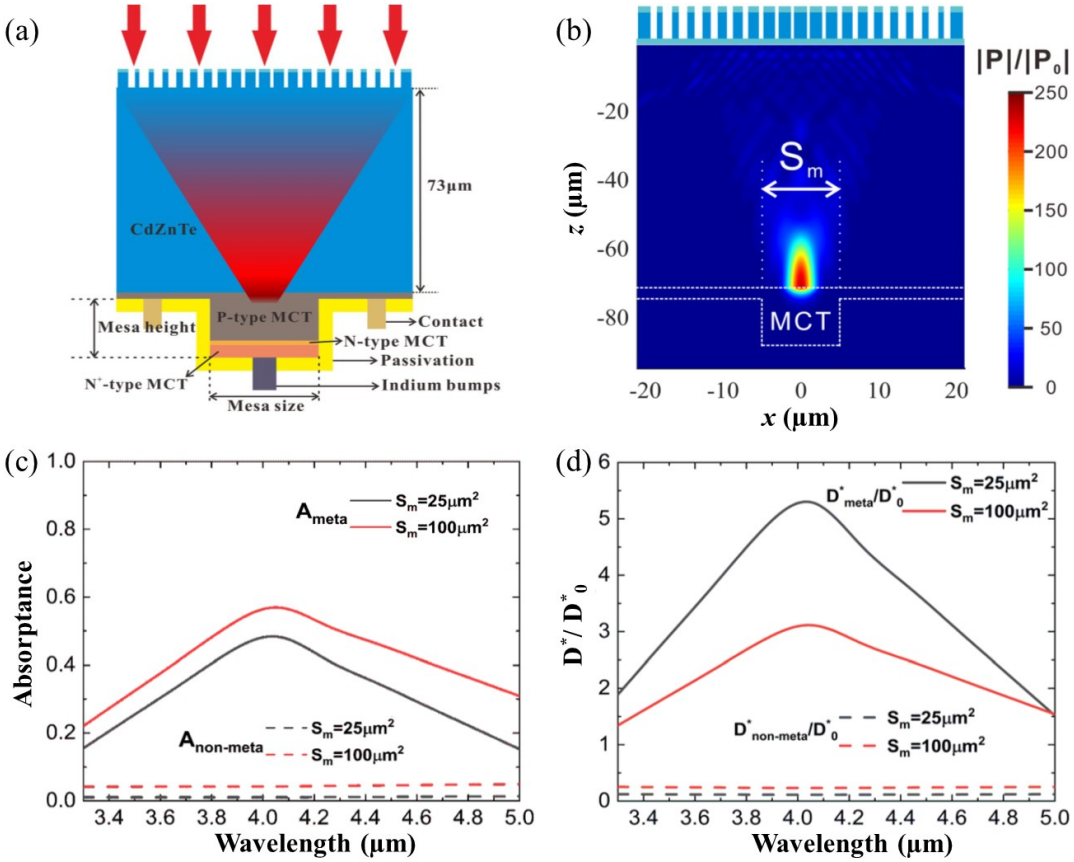

Figure 1.6: (a) Diagram of a HgCdTe MWIR photodiode integrated with a metalens. (b) Power flux distribution on the x-z cross section of the device with the active region outlined by dashed white lines. (c) Absorptance of the HgCdTe detector's active region with and without the metalens for two different photosensitive square areas. (d) Relative detectivity as a function of incident wavelength for two different photosensitive areas [14].

Fig. 1.6 depicts a polarization-independent dielectric metalens design integrated with a HgCdTe IR photodetector aimed at concentrating power flux into a reduced photosensitive area to enhance performance. The metalens, comprised of an array of nano-pillars with varying sizes, was created in the CdZnTe substrate of the detector, with an additional SiO_2 layer added to enhance transmission. It focused incident light through the CdZnTe substrate onto the HgCdTe detector with a focal spot of λ, and a focusing efficiency of ~63%. While reducing the photosensitive area simultaneously reduces the dark current, it also decreases light absorption, therefore degrading the specific detectivity D*. With a HgCdTe detector pitch size of 40 μm × 40 μm, the metalens maintained light absorptance of 50% or 58% for photosensitive regions of 25 μm^2 or 100 μm^2, as shown in Fig. 1.6(c). Additionally, D* was enhanced by up to 5.5 times for a 25 μm^2 photosensitive area, as seen in Fig. 1.6(d) [14].

The metalens demonstrated good dispersion tolerance over a wavelength range from 3.3 μm to 5.0 μm, with an average detectivity enhancement of ~3 times for a 25 μm^2 photosensitive area. The angular response was contingent on the focal length, with an angle of view (AOV) of 4.0° for a 25 μm^2 detector at a focal length of 73 μm. A reduction of the focal length to 38 μm increased the AOV to 7.7° for the 25 μm^2 detector, and to 15.4° for a 100 μm^2 detector [14].

While flat optics has garnered considerable interest and yielded intriguing outcomes compared to traditional refractive lenses, metasurface lenses still encounter challenges related to relatively low focusing efficiency and inherent limitations to narrow wavelength band operation. However, a microlens assembly enables broad-band operation among other benefits.

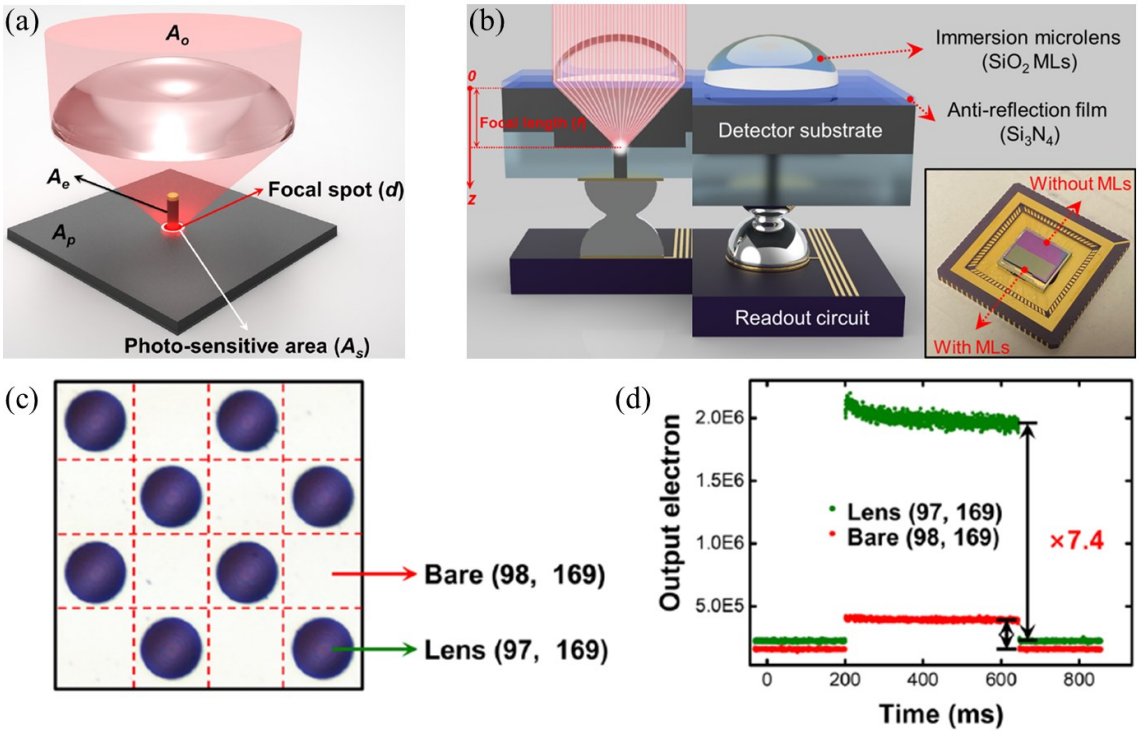

Figure 1.7: (a) Diagram of a microlens incident on a photodetector which concentrates light from area A_0 to A_s. (b) Schematic of the microlens integrated with an IR FPA, describing its parts. (c) Microscope image of pixels integrated with a microlens and without a microlens. (d) Raw pixel output responses to a pulsed beam, showing a measured enhancement of 7.4 times [17].

Fig. 1.7(a) depicts an immersion microlens that is adaptable to various types of IR FPAs, regardless of the substrate material, and concentrates light from area A_0 to A_S on the photodetector to enhance performance. To enhance the sensitivity of IR FPAs, it is essential to concurrently optimize the performance of both the photodetectors and the immersion microlens. Fig. 1.7(b) shows diagram of the immersion microlens integrated with an IR FPA. In this setup, the immersion microlens was created from SiO_2 due to its broad-band transparency, wide etch selectivity, and capability to be deposited on any detector substrate. Moreover, a Si_3N_4 layer was interposed between the SiO_2 immersion microlens and the substrate to serve as a broad-band antireflection coating [17].

Notably, minimal performance degradation occurred across a wide range of wavelengths. Additionally, experimental characterization of a short-wave IR (SWIR) FPA integrated with the immersion microlens resulted in a 7.4 times enhancement in quantum efficiency, as shown in Fig. 1.7(c-d). Furthermore, accounting for size, weight, and power consumption considerations in imaging systems, the optimal FPA design was found to align with diffraction-limited pixel sizes [17]. In this context, integrating microlenses with IR photodetectors has gained significant attention. However, practical application is hindered by limited numerical aperture, complex packaging and alignment processes, and challenges in forming curved surfaces [34-36]. Several of these limitations are alleviated by utilizing a microsphere array instead.

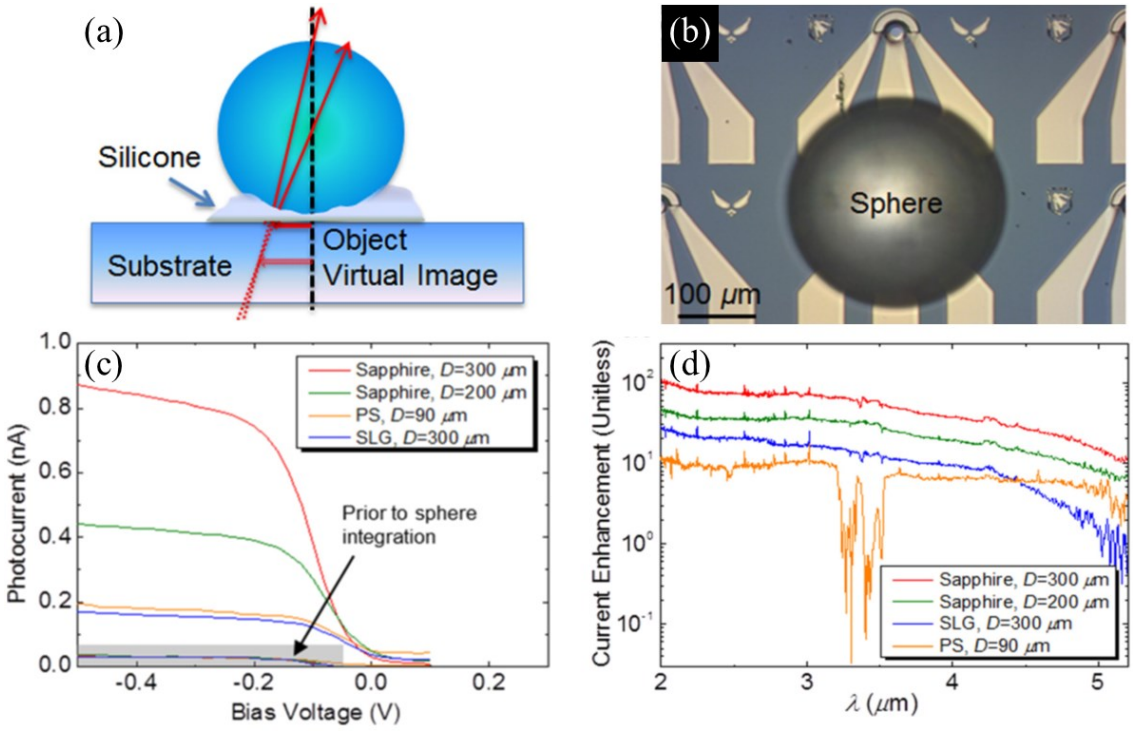

Figure 1.8: (a) Virtual imaging by a microsphere integrated with a photodetector. (b) Optical micrograph of a microsphere on top of a photodetector mesa. (c) Photocurrent measured at different bias voltages for microspheres of different material and diameter. (d) Photocurrent enhancement factors obtained by dividing the photocurrent the microsphere integrated detector with the photocurrent spectra of the isolated detector, showing up to 100 times enhancement [22].

Fig. 1.8 depicts an enhanced photodetector through the utilization of photonic jets facilitated by dielectric microspheres fabricated from sapphire with n = 1.71, polystyrene (PS) with n = 1.56, and soda-lime glass (SLG) with n = 1.47, where the diameters ranged from 90 to 300 μm. The enhancement factors were determined by dividing the Fourier transform infrared (FTIR) photocurrent spectra of the microsphere integrated detector with the photocurrent spectra of the isolated detector. Enhancement factors of up 100 times were experimentally measured for the 35 μm diameter mesa integrated with a 300 μm diameter sapphire sphere at λ = 2 μm, as illustrated in Fig. 1.8(d) [22]. Additionally, through FDTD numerical modeling, a notable combination of enhanced sensitivity and AOV of up to 20° for backside illuminated photodetectors was demonstrated, with the potential for even greater AOVs in frontside illuminated configurations [22].

This combination of properties holds great promise for imaging applications, but is limited in its manufacturability and ease of integration with FPAs. Extending this technology to FPAs necessitates the development of assembly techniques capable of arranging dielectric microspheres into large-scale arrays. Various technologies can facilitate this, but the uniformity of microspheres integrated with individual photodetectors is low, and therefore a technology with the ability to maintain high uniformity across a pixel array is necessary. Such a technology exists through utilizing Si anisotropic wet etching to fabricate Si micropyramids.

Fig. 1.9 depicts two monolithically integrated SWIR photodetectors on top of normal (Fig. 1.9(a-e)) or inverted (Fig. 1.9(f-i)) Si micropyramids. Both of these configurations utilized pyramidally shaped plasmonic concentrators. In the case of normal micropyramids, an Al-silicide SB photodetector monolithically integrated with nanoscale

top micropyramids of 18 µm pitch displayed elevated responsivity and an enhanced SNR. These pyramids collected light from a wide area corresponding to their base, where light was then concentrated towards the nano-scale three-dimensional (3-D) pyramid apex, such that the light was absorbed in the metal to generate hot electrons. Through the internal photoemission process, these electrons surmounted the Schottky barrier and were captured as a photocurrent. By utilizing this approach, a photocurrent enhancement of ~100 times was obtained with ~50 nm pyramid tops in the SWIR [23].

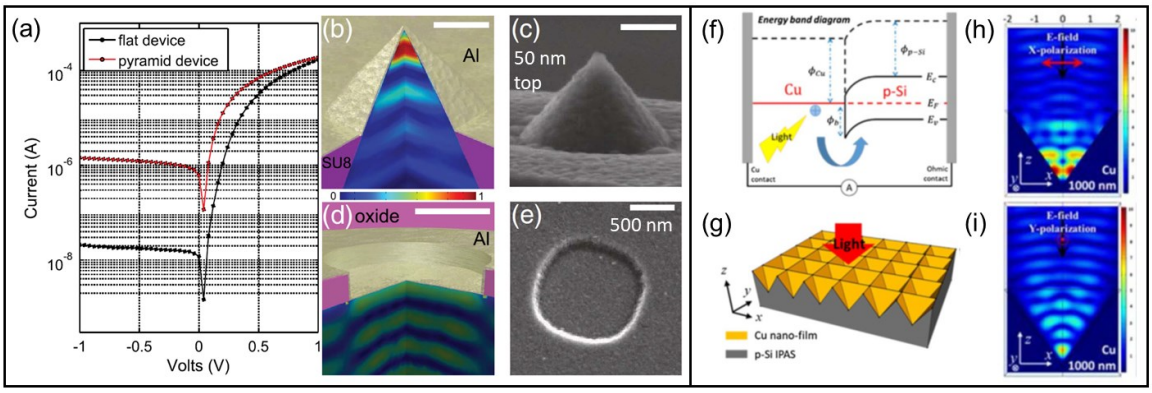

Figure 1.9: (a-e) Normal micropyramidal Al-silicide and (f-i) inverted micropyramidal Cu-silicide Schottky barrier photodetectors in the SWIR depicting plasmonic enhancement effects. (a) I-V measurements of the micropyramid compared to the flat device, showing current enhancement of ~100 times. (b), (d) Numerically modeled electromagnetic field intensities superimposed on 3-D Si models. (c), (e) SEM images of the fabricated devices [23]. (f) Energy band diagram for a Cu-based Schottky barrier photodetector. (g) Diagram showing direction light is incident on the array. (h-i) Electromagnetic field map for Cu-based Schottky barrier photodetector at two different polarizations [24].

On the other hand, the inverted Si micropyramids with 4 µm pitch shown in Fig. 1.9(f-i) utilized a Cu-silicide SB photodetector and reported an enhancement of ~40 times in the SWIR. Both of these approaches utilized the conversion of photons into plasmons, and adiabatic compressions of the plasmons towards the nanoscale tips [24].

Structures capable of employing plasmon resonance have found widespread application in enhancing the photoresponse across a variety of photoactive devices. However, in the case of FPAs, obtaining uniform pixel performance from individual pixels

enhanced by normal or inverted micropyramids with plasmonic absorption effects proves a difficult task. The aforementioned monolithically integrated micropyramidal SB photodetectors have performance which depends on Si's crystalline planes, its dopant concentrations, as well as the surfaces' smoothness and uniformity [29, 36-45]; all of which can be affected during the micropyramid fabrication process. Additionally, these light concentrators can only be monolithically integrated with IR detectors, limiting their usefulness.

However, truncated Si micropyramids facilitates the preservation of the micropyramids' planar small bases, therefore preserving the uniform doping concentrations and, consequentially, the performance of planar monolithically integrated photodetectors fabricated on the truncated micropyramids' small base. Furthermore, truncated Si micropyramids supports heterogeneous integration to create a hybrid array, further increasing its utility.

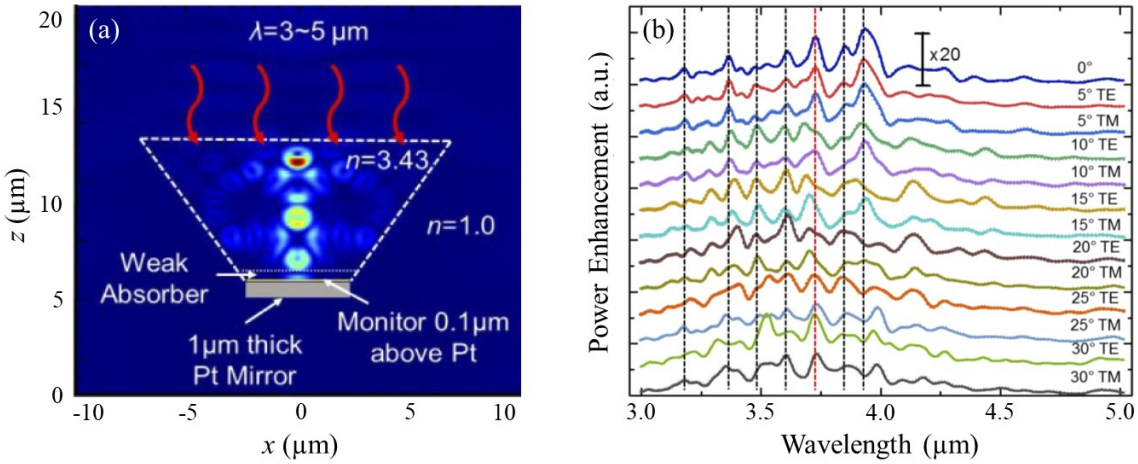

Figure 1.10: (a) Electromagnetic field distribution inside a 4 μm small base, 14 μm large base free-floating Si microcone calculated at normal incidence with a 1 μm thick Pt mirror at the bottom base. Weak absorption effects of the Schottky barrier were modeled by introducing a 1% absorption effect in the lowest 1 μm thick section of microcone closest to the small base. (b) Power enhancement factor spectra calculated for 0 - 30° incidence angles at both TE and TM polarizations [25].

Fig. 1.10 depicts the enhancement capability of a free-floating Si microcone with 4 μm small base and 14 μm large base. The Si microcone has a circular cross-section while a Si micropyramid has a square cross-section. The incident light is a 3-5 μm plane wave, and the microcone has a 1 μm thick Pt mirror with a weak absorbing layer at the small base to mimic a PtSi SB photodetector, as seen in Fig. 1.10(a). The power enhancement factors (PEFs) are defined as the ratio of the photon flux detected with the microcones to the photon flux detected by the same detector without the microcones. Fig. 1.10(b) demonstrates the PEF reached up to 25 times with omnidirectional resonance capabilities for both TE and TM polarizations with AOVs up to 30°. These Si microcones illustrate multispectral imaging with approximately 100 nm bands and expansive AOVs for both polarizations. Additionally, Si microcones function akin to single-pass optical components, such as dielectric microspheres, generating sharply focused photonic nanojets [25].

The integration of Si technology with high collection efficiency and nanoscale confinement renders the Si pyramids optimal for enhancing photodetectors. Moreover, small planar square photodetectors can be integrated with truncated Si micropyramids, and these detectors will exhibit significantly reduced dark current compared to large planar detectors, resulting in an improved SNR. Furthermore, these detectors can be configured into pixel arrays, thereby serving as FPAs. Therefore, a better understanding of the light concentrators' optical properties is necessary.

1.3. Light Manipulation with Mesoscale Structures

In this dissertation, applications arising from the unique optical properties of anisotropically wet etched truncated Si micropyramids are investigated in the mesoscale

regime. Mesoscale denotes objects, like micropyramids, with geometric dimensions on the order of the incident wavelength of light. These objects exhibit different optical properties through light-matter interactions as their geometry varies. When the micropyramids are much larger than the wavelength of light, the properties of the micropyramids follow the laws of geometrical optics, which is well understood. Since the onset of the 2000s, the photonics community has redirected its focus towards mesoscale and nanoscale designs, owing to the emergence of innovative fabrication methods [46-56].

The diverse properties of mesoscale objects offer a wide array of applications. In this dissertation, the focus lies on exploring the optical characteristics and potential uses of micropyramidal structures featuring mesoscale dimensions. The functionality of single truncated Si micropyramidal structures share similarities with adiabatically tapered fibers. Their ability to concentrate light stems from the significant reflections facilitated by their sidewalls. These characteristics are commonly termed as non-imaging light concentration properties, distinguishing them from the focusing effects of lenses [56]. The light-concentration ability typically exhibits a non-resonant nature.

However, the optical properties of a truncated Si micropyramidal array can also lead to various interference effects due to its mesoscale and light-concentrating nature. Such arrays can be treated as a transmission grating. The optical properties of mesoscale structures depend on their geometry, and the properties of truncated Si micropyramids have been relatively unstudied. From an application development perspective, mesoscale structures of this nature hold considerable promise and appeal. Two important effects are necessary to be introduced in regard to the light-concentrating ability of truncated Si micropyramids: photonic nanojets and the Talbot effect.

1.3.1. Photonic Nanojets

Photonic nanojets are a fascinating phenomenon in the field of optics and nanotechnology. These are highly focused light beams that emerge when a transparent or dielectric microscale or nanoscale particle is illuminated by a plane wave or a focused laser beam. The phenomenon was first observed and studied in the early 2000s, and since then, it has garnered significant interest due to its unique properties and potential applications [57, 58] The nanojets typically exhibit a narrow and intense focal spot that extends beyond the diffraction limit, enabling subwavelength focusing of light. This ability to confine light to extremely small volumes makes photonic nanojets promising for various applications, including optical microscopy, lithography, sensing, and particle manipulation [56, 59].

The term "photonic nanojets" was initially coined to describe the exceptional focusing ability of dielectric microspheres. This was evidenced by the discovery that, under specific conditions, they could generate light beams with dimensions smaller than the diffraction limit. Dielectric micro or nano scale particles can create photonic nanojets by concentrating incident light in a nearby proximity. The emergence of photonic nanojets is attributed to the interference between diffracted and refracted light waves that impinge upon a particle. These concentrated electromagnetic beams are extremely narrow and emerge from the opposite side of the particle. Typically, the diameter of the particle is greater than the incident wavelength. It's important to highlight that the photonic nanojet emerges within the spatial domain where the influence of near-field scattering, particularly evanescent fields, is substantial and the focused beam can exhibit unique phenomena [56, 59-61]. However, the spectral analysis of the photonic jets conducted in [62] led to the conclusion that the contribution of the evanescent field to the structure of photonic jets is

minimal. Instead, the main factor influencing their structure is attributed to a specific phase distribution.

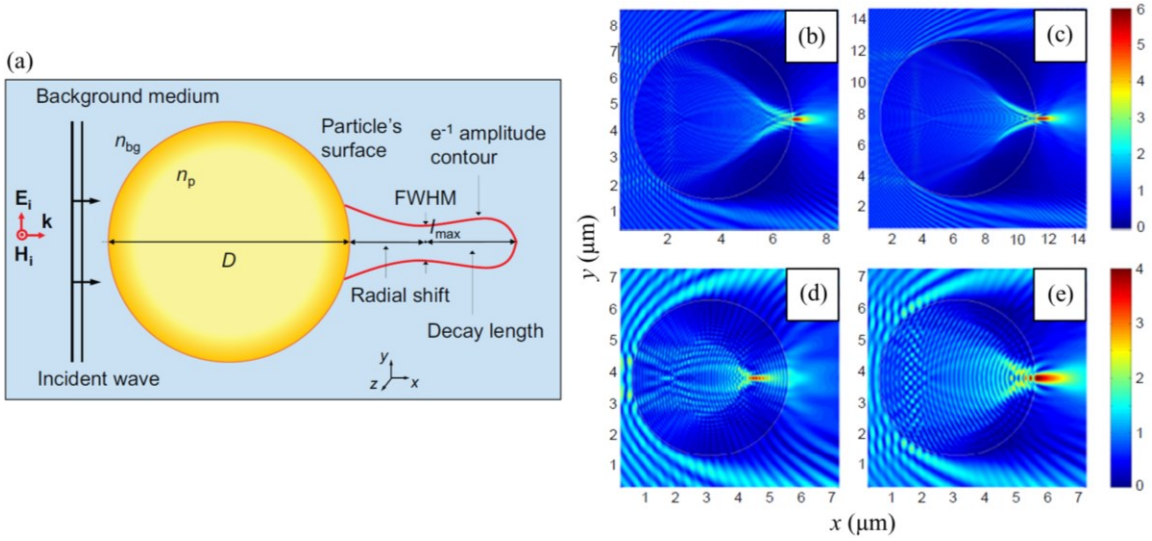

Figure 1.11: (a) Diagram depicting the characteristics of a photonic nanojet. (b-e) Numerical modeling of photonic nanojets emerging from a cylinder with diameter D and refractive index n_p, where the background medium consists of refractive index n_{bg}. The cylinder is illuminated with a plane wave of wavelength λ. (b) D=6 μm, n_p=2.3275, n_{bg}=1.33, and λ=300 nm. (c) D=10 μm, n_p=2.3275, n_{bg}=1.33, and λ=300 nm. (d) D=5 μm, n_p=2.5, n_{bg}=1, and λ=500 nm. (e) D=5 μm, n_p=1.7, n_{bg}=1, and λ=500 nm [57, 59].

The photonic nanojet can be characterized by the beam's full-width at half-maximum (FWHM), peak intensity, decay length, and location, as depicted in Fig. 1.11(a). These characteristic parameters can be modified by changing the refractive index of the particle and background medium, the particle's geometry, as well as the wavelength of the incident source, as shown in Fig. 1.11(b-e). Additionally, the characteristics of the photonic nanojet also depends on the polarization of the incident light, as well as its phase distributions. Photonic nanojets display interesting properties such as exhibiting a FWHM smaller than the diffraction limit, with concentrated intensities up to 1000 times the intensity of the incident light source [57, 58, 63, 64]. Photonic nanojets are non-resonant phenomena [64, 65]. However, when the wavelength of the incident plane wave aligns with

the resonant wavelength of the particle, the photonic nanojets display an enhanced intensity and reduced FWHM [66].

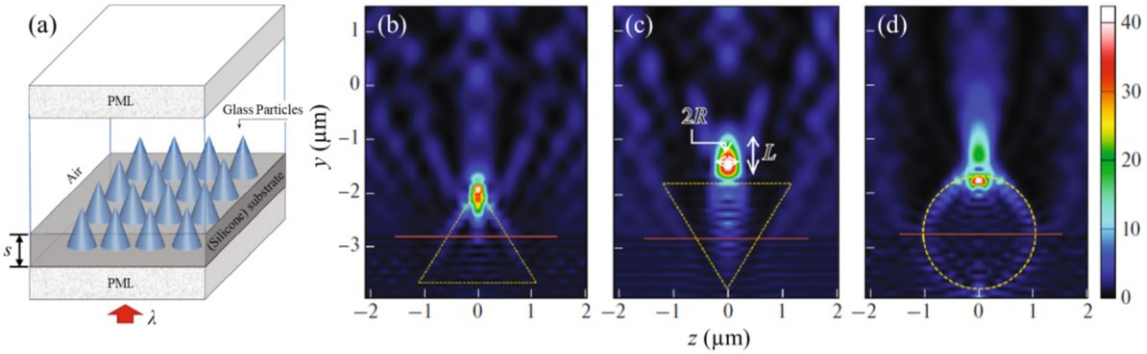

Figure 1.12: (a) Diagram depicting the 3-D FDTD numerical modeling simulation region. The incident plane wave propagates upwards with λ = 532 nm, the substrate consists of index n_1 = 1.4, the glass particles consists of index n_2 = 1.6, and the surrounding air consists of index n = 1. (b-d) Optical field intensity B in proximity to glass microparticles buried in polymer of thickness s marked by the red horizontal line for (b) normal microcones, (c) inverted microcones, and (d) microspheres [67].

More recently, the term photonic nanojet has been applied to various nonspherical mesoscale objects like microcones as shown in Fig. 1.12, and other shapes including pyramids, axicons, cuboids, among others [68-83]. Like spherical dielectric particles, nonspherical dielectric particles also modify the spatial structure of light and can exhibit photonic nanojets. Additionally, in some cases, photonic nanojets can be produced through reflections instead of only through transmission.

It was demonstrated that various spatial arrangements of the assembly of microcones enabled the generation of a collection of photonic nanojets possessing specific parameters that could not be achieved by individual isolated microcones [67]. Furthermore, it was found that a collection of normal microcones resulted in photonic nanojets with the most stable spatial parameters. However, their power parameters exhibit significant sensitivity to the degree of particle immersion and spatial distribution of particles within the substrate. As the interparticle spacing increases, the collective interference effects

weaken. This indicates the existence of highly subtle collective effects, which are linked to the focusing properties produced by these particles. When normal microcones are fully immersed in a material with differing refractive index, the resulting photonic nanojets exhibit reduced decay lengths but still maintain high intensity and small transverse dimensions.

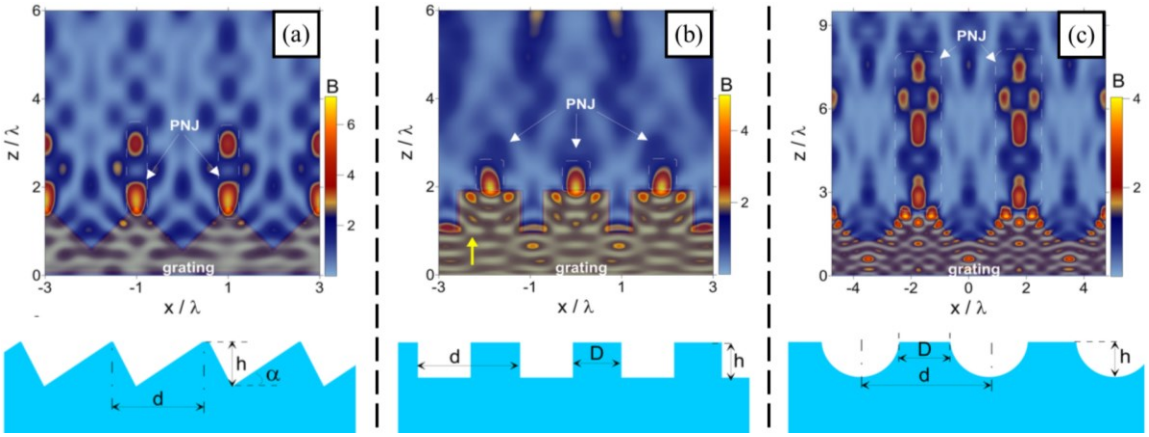

Figure 1.13: Phase diffraction gratings with their optical intensity profile *B* calculated by 3-D FDTD numerical modeling, depicting the formation of photonic nanojets. The plane wave source of $\lambda = 532$ nm propagates upwards. (a) Saw-tooth grating with $h = \lambda$, $d = 2\lambda$, and $\alpha = 45°$. (b) Rectangular grating with $h = \lambda$, $d = 2\lambda$, and $D = 1.5\lambda$. (c) Hemispherical grating with $h = \lambda$, $d = 3\lambda$, and $D = 1.5\lambda$ [84].

Additionally, as seen in Fig. 1.13, the variations in the intensity can cause an initially continuous photonic nanojet to fragment into individual segments along the optical axis because of interference effects between the electromagnetic fields of neighboring photonic nanojets. Specific arrangements of dielectric particles within a cluster can yield photonic nanojets with parameters notably superior to those generated by isolated particles. Therefore, the emerging electromagnetic fields can be engineered to have elongated nanojets or reduced transverse size with an enhanced intensity through modulating the spatial separation of the particles and the resulting interference [84].

Another particle shape a photonic nanojet can emerge from is a micropyramid. The first time photonic nanojets emitted from micropyramids were published was in 2014 [86]. Afterwards, preliminary numerical modeling via the FDTD method was utilized to study how the geometry impacts the optical field distribution, showing that the resulting photonic nanojets depends on the angle of incident on the micropyramid [86, 87]. The first experimental observation of photonic nanojets emerging from micropyramids was reported in 2018 by a saw-tooth diffraction grating, as seen in Fig. 1.14 [85]. These investigations predominantly involved micropyramids composed of one material.

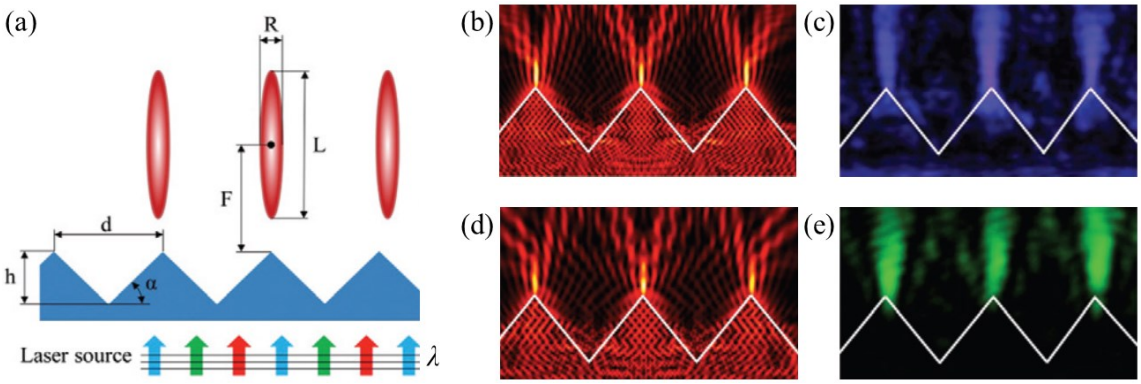

Figure 1.14: (a) Diagram depicting the illuminating wavelength λ, the dimensions of the resulting photonic nanojet, the height of the sawtooth h = 2.5 μm, the peak-to-peak separation distance d = 2.5 μm, and the angle of the pyramid formed α = 45°. (b) FDTD power flow map for a sawtooth grating with λ = 405 nm compared to (c) experiment. (d) FDTD power flow map for a sawtooth grating with λ = 532 nm compared to (e) experiment [85].

However, experiments have been performed with micropyramids composed of multiple materials in a bilayer fashion to engineer the resulting photonic nanojet to have superior light concentration, as shown in Fig. 1.15. The bilayer micropyramid array was numerically modeled with 3-D FDTD simulations when illuminated by a plane wave of λ = 640 nm, as shown in Fig. 1.15(a). The model was compared to a fabricated bilayer micropyramid with nearly identical geometry, where the results are compared in Fig. 1.15(b,c). The bilayer micropyramidal array created photonic nanojets with intensity

reaching 33.8 times that of the incident light's intensity with a FWHM of 0.6λ [88]. Clearly, micropyramids can be useful to create highly concentrated beams with large intensities, useful for applications in high-resolution imaging, nanolithography, optical trapping, and enhancing focal plane arrays.

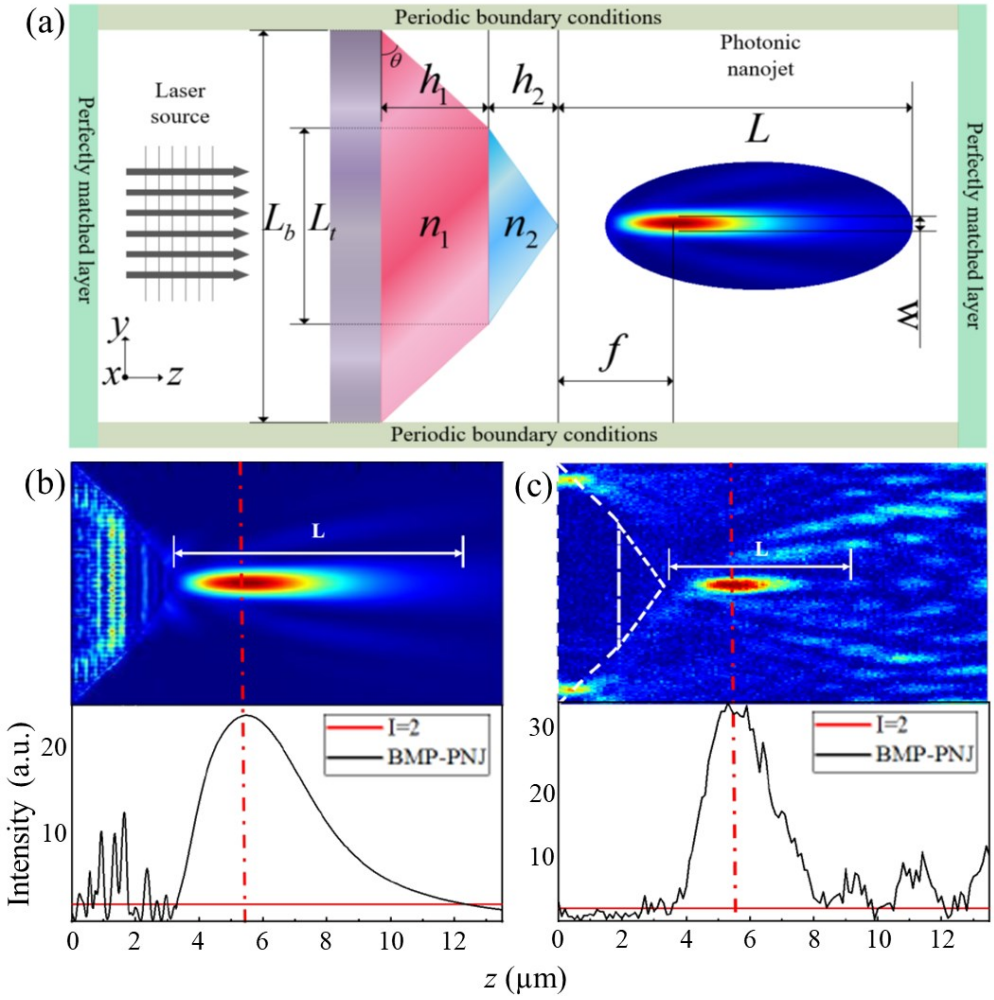

Figure 1.15: (a) Diagram depicting the composition of the bilayer micropyramid array inside the 3-D FDTD numerical modeling simulation region when illuminated by a plane wave with λ = 640 nm. (b) Numerical model with L_b = 7.60 μm, L_t = 3.80 μm, h_1 = 2.00 μm, h_2 = 1.30 μm, n_1 = 2.02, and n_2 = 1.458. (c) Experiment with L_b = 7.61 μm, L_t = 3.81 μm, h_1 = 2.03 μm, h_2 = 1.32 μm, n_1 = 2.04, and n_2 = 1.462 [88].

Due to their intense light concentrating ability and localized nature, photonic nanojets have found applications across numerous fields. These applications include microsphere-assisted microscopy, nano-photolithography, nanostructuring, Raman

spectroscopy, detection and manipulation of nanoparticles, fluorescent sensing, high-density optical data-storage disks, innovative optical waveguides, photovoltaics, photodiodes, and more.

Regarding microscopy, photonic nanojets can enhance imaging resolution beyond the diffraction limit, enabling researchers to observe subcellular structures and nanoscale features with unprecedented clarity. In lithography, nanojets can be utilized to achieve high-resolution patterning for the fabrication of nanoscale devices and structures. Additionally, in sensing applications, nanojets can enhance the detection sensitivity by concentrating light around target analytes, thereby improving the SNR. Moreover, photonic nanojets can exert strong optical forces on nearby particles, enabling precise manipulation and trapping of micro- and nanoparticles [64, 89-92]. This property has implications in fields such as optofluidics, biophotonics, and nanomanipulation.

Regarding enhancing optical devices, photonic nanojets can be utilized to concentrate light onto a small device area. Optically active devices, such as solar cells or detectors, convert light into electrical energy. A key design obstacle lies in enhancing their efficiency while preserving their minimal thickness. One method to accomplish this is to utilize photonic nanojets to concentrate light onto a small device area. FDTD simulations with a 6.5 μm diameter microsphere with $n = 1.59$ demonstrated formation of the photonic nanojet into a photodiode volume of 0.0045 μm^3 with resulting enhancement of the electric field by 26 times, irrespective of the initial polarization of light [93]. Additionally, it was demonstrated with a photonic nanojet emitting Si microcone that an enhanced signal of up to 21 times is capable at $\lambda = 3.73$ μm, with omnidirectional resonance and angle-of-view of up to 10° [25].

The formation of photonic nanojets involves an intricate interplay between diffracted and scattered fields, influenced by the interference of light waves transmitted through and refracted by the photonic nanojet creating particle. Because of the multifaceted characteristics of the photonic nanojet phenomenon, customizing their properties are essential for maximizing their utility in each application. Given the mesoscale nature of photonic nanojets, optimization must be conducted for every application to determine the optimal combination of parameters including the index of refraction and geometry of the photonic nanojet emitting particle, and the illumination conditions necessary to yield the most effective results for that particular application.

In this dissertation, optimization for Si micropyramids is performed in order to find the conditions necessary to maximize the photoresponse of MWIR FPAs used in imaging devices such as IR cameras [25, 94-114]. It is important to note that direct comparison between focusing and imaging is typically not feasible with such light-concentrating objects. The reciprocity principle in optics forms the foundation for such comparisons, which is only applicable to identical optical modes. When different optical modes govern the focusing and imaging properties, the reciprocity principle cannot be utilized. These mesoscale objects are rather complex and require numerical methods to understand these properties.

Overall, photonic nanojets represent a promising avenue for advancing optical technologies and exploring novel applications in various scientific and engineering disciplines. Continued research into their properties and capabilities is expected to uncover new opportunities for harnessing their potential in diverse fields.

1.3.2. The Talbot Effect

Diffraction and interference phenomena arise from the wave nature of light, and an example of this effect is seen in diffraction gratings. Each diffraction order propagates at a specific angle and can interfere with other orders while propagating along the optical axis. This coherent interference effect leads to the generation of self-images, and was originally discovered by Talbot in 1836, which was later deemed the Talbot effect [115]. These self-images also follow a periodic pattern along the optical axis, where an analytical description was derived by Rayleigh in 1881 in order to define the Talbot length as the separation distance between these self-images [116].

The Talbot length is defined by equation (1):

$$z_T(m) = \frac{\frac{m\lambda}{n}}{1 - \sqrt{1 - \left(\frac{\lambda}{n\Lambda}\right)^2}} \tag{1}$$

where z_T is the Talbot length of order m (where the mth Talbot image is located), λ is the wavelength of light, n is the index of refraction of the propagating medium, and Λ is the period of the diffraction grating. If the wavelength of the coherent light source or the period of the diffraction grating varies, the Talbot length changes. Fig. 1.16(a) shows the Talbot effect, with sequential Talbot lengths labeled. The planes positioned at a distance equal to the Talbot length from the grating are commonly referred to as Talbot planes.

Currently, the Talbot effect has numerous applications in various industrial sectors, encompassing encoders, photolithography, microscopy, spectrometry, optical trapping, and more [118-141]. For all these applications, the sequential Talbot images need to be highly resolved. Fig. 1.16(b) displays the Talbot effect's imaging interval, such that there

is contrast between the image and the surrounding diffracted intensity to resolve the Talbot image. The contrast of the Talbot images peaks at the Talbot planes and diminishes gradually as it moves away from these planes. Therefore, a range of focus can be established and used to determine the self-imaging depth, useful for applications in optical encoders and photolithography [117, 139-147].

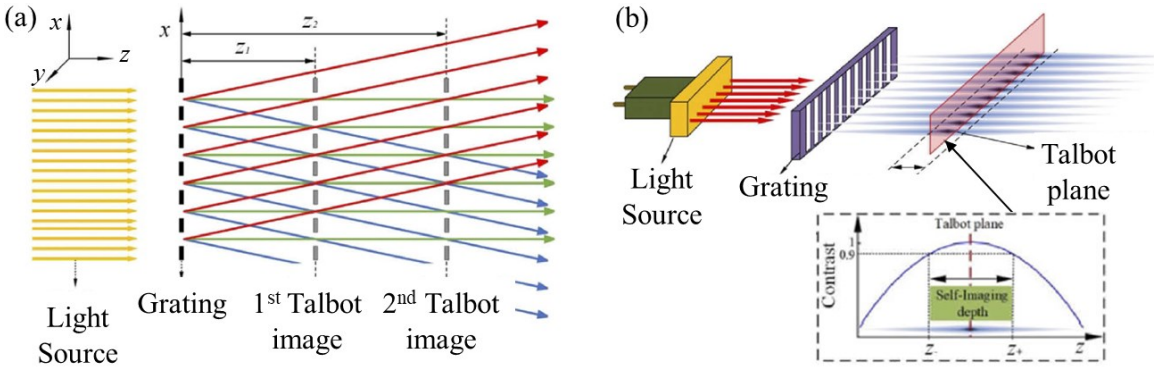

Figure 1.16: (a) Diagram depicting the Talbot effect and example imaging distances z_1, and z_2 based on the wavelength of the plane wave source λ and the period of the diffraction grating Λ. (b) 3-D diagram depicting the Talbot effect and the allowable imaging interval around the Talbot plane that can be considered a part of the Talbot image [117].

One type of image alteration arises from harmonic distortion due to superimposed spatial harmonics, which can occur from the 3-D nature of certain diffraction gratings. The Talbot length can be modulated by introducing an index of refraction variation at locations around the diffraction grating, shown in Fig. 1.17. This effect can be utilized to either reduce harmonic distortion or further increase it, through modifying the non-uniform phase layers' index and geometry. Additionally, these spatial harmonics can be engineered by designing 3-D structures with the parameters necessary to achieve the desired effect. Therefore, the Talbot effect can be utilized in a wide variety of applications [117].

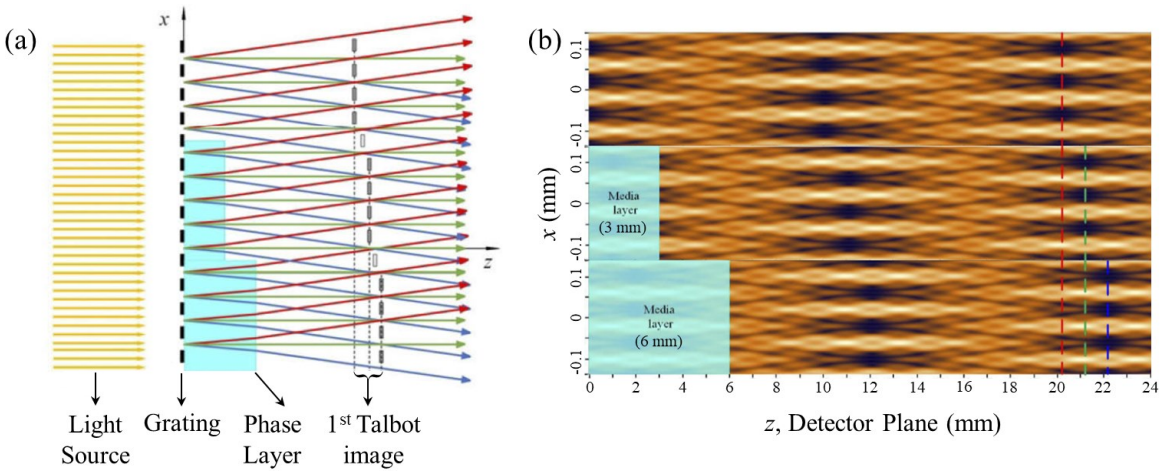

Figure 1.17: (a) Diagram depicting Talbot imaging with a stepped phase layer. (b) Numerically modeled electric field with different phase layer thicknesses [117].

The Talbot effect can also be employed in 3-D photolithography to support recent developments in nanotechnology by creating unique 3-D nanostructures in photoresist. Fig.1.18(a) shows photolithography completed with a periodic conical phase mask, such that the photoresist is exposed at different depths according to the Talbot length corresponding to the phase mask and the wavelength of light used. Unlike traditional Talbot photolithography, which utilizes only one image in the photoactive layer, this method generates two periodic images of the phase mask where the second periodic image consists of the phase-shifted periodic image corresponding to the lateral locations of the holes in the phase mask. The depth of these repeated patterns depends on the energy of light. Conical symmetry is essential for creating only two periodic patterns of the phase mask by effectively suppressing higher orders of diffraction [144].

Another example of 3-D photolithography due to the Talbot effect is through utilizing a periodic array of nanospheres to expose photoresist at various depths, as shown in Fig. 1.18(b). The Talbot effect projects a pattern onto the photoresist underneath to capture the 3-D intensity distribution. This method was able to produce features with 80

nm sizes, approximately four times smaller than the wavelength used to expose the resist [145]. However, 3-D Talbot photolithography is limited by the flexibility of the resulting geometry, the ability to create the initial phase mask, and the cost to develop these unique phase masks useful for only specific applications. Nonetheless, there is potential in developing this field to fabricate diverse microstructures for photonics and optoelectronics applications.

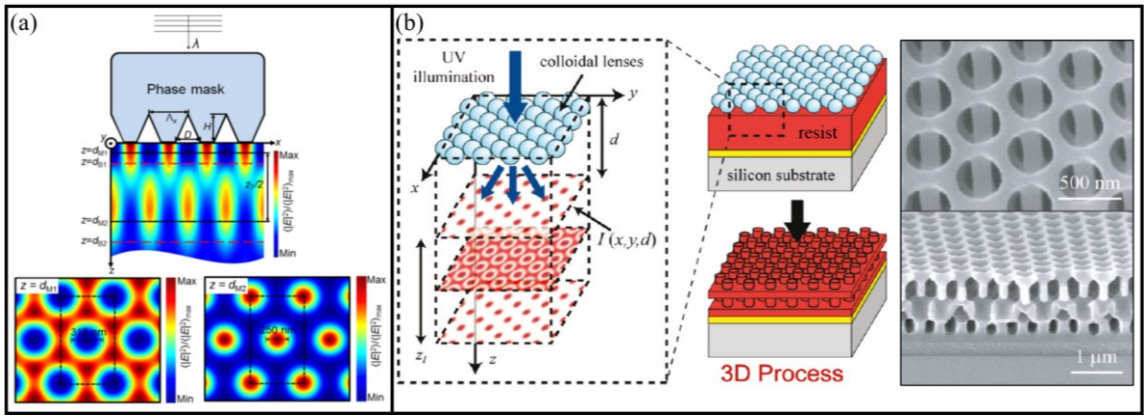

Figure 1.18: (a) Diagram depicting the ability to expose different regions of photoresist through Talbot imaging with an array of cones where the incident light is an unpolarized plane wave with λ = 365 nm, $H = D$ = 300 nm, Λ_x = 500 nm, and Λ_y = 866 nm. The time-averaged numerically modeled intensity patterns at different depths z are shown [144] (b) Diagram depicting the ability to expose different regions of photoresist through Talbot imaging with an array of nanospheres where the incident light is a ultraviolet (UV) laser, and d is the propagation distance. SEM images of a structure fabricated with this method are shown [145].

In this dissertation, the Talbot effect resulting from Si micropyramids that were illuminated by coherent MWIR light is discussed. Since Si micropyramids consist of a unique 3-D geometry, the resulting Talbot images contain harmonic distortions due to the superimposed spatial harmonics [146]. This effect depends on the period of the micropyramid arrays, as well as their relative heights to the wavelength of light. These mesoscale objects are rather complex and require numerical methods to understand these properties.

1.4. Si Anisotropic Wet Etching as a Major Tool for MEMS Fabrication

Si anisotropic etching with TMAH was utilized to fabricate micropyramidal arrays with light-concentrating ability in order to experimentally demonstrate an enhanced FPA integrated with a micropyramidal array. An understanding of Si's role in MEMS is necessary.

MEMS have emerged as a revolutionary technology with diverse applications in various fields, from aerospace to healthcare, and telecommunications to consumer electronics. MEMS devices are characterized by their miniature size, low power consumption, and ability to interact with the physical world, making them indispensable in today's rapidly evolving technological landscape. At the heart of MEMS fabrication lies a myriad of intricate processes, and among them, anisotropic wet etching of Si has risen as an important tool playing a pivotal role in shaping the MEMS landscape [148].

MEMS are miniature devices typically composed of Si and other materials, and they can include sensors, actuators, and microstructures. The key advantage of Si in MEMS is its compatibility with IC fabrication processes, enabling the integration of mechanical, electrical, and computational functionalities onto a single chip. This integration has led to the development of a wide range of MEMS applications, including accelerometers, gyroscopes, pressure sensors, microfluidic devices, and more.

To create these complex microsystems, MEMS fabrication involves a series of processes such as lithography, deposition, and etching. Among these, wet etching is a crucial step that selectively removes material from Si wafers, allowing the formation of intricate structures with high precision.

Si is the dominant material in MEMS fabrication for several reasons:

- **Compatibility with Semiconductor Processing:** Si is compatible with the same fabrication processes used in the semiconductor industry, allowing for the integration of MEMS and microelectronics on a single chip. This compatibility is essential for achieving compact and multifunctional MEMS devices.
- **Material Properties:** Si exhibits desirable material properties for MEMS, such as high mechanical strength, thermal stability, and excellent electrical conductivity. These properties enable the development of MEMS devices that can withstand harsh operating conditions.
- **Ease of Micromachining:** Si can be easily micromachined using various techniques, including wet etching, dry etching, and deposition. Among these techniques, wet etching stands out for its ability to create precise and controlled features on Si substrates.

Wet etching has been a fundamental process in MEMS fabrication since its inception. Over the years, it has evolved in response to the growing demand for more complex and miniaturized devices. Anisotropic wet etching can be tailored to selectively remove specific materials or layers, enabling the creation of complex MEMS structures with multiple integrated components. As MEMS devices continue to shrink in size, anisotropic wet etching has become essential for achieving these challenging geometries.

Proven techniques in microfabrication, commonly employed for fabricating microstructures and circuits, can be adapted to fabricate 3-D structures for interfacing with the nanoscale domain. In microfabrication, bulk materials are sculpted into microstructures through processes such as lithography and etching. Various chemical solutions, including acids and bases, have historically been utilized to selectively remove substantial amounts

of Si via chemical reactions with the etchant, yielding diverse microstructures. Anisotropic wet etching relies on these chemical reactions to selectively remove material from Si wafers. Common etchants include KOH and TMAH. These chemicals etch Si along its crystallographic planes, resulting in well-defined sidewalls. Due to undercutting, the etched shapes typically differ from those of the mask, especially at the corners of structures. The undercutting of convex corners can be mitigated by employing appropriately designed masks. Through the utilization of compensation techniques, sharp corners can be achieved. Various research groups have proposed and validated different designs for corner compensation using solutions such as KOH and TMAH. While alternative methods have been documented, they often involve additional masks and processing steps, rendering them more costly and intricate.

As MEMS technology continues to advance, anisotropic wet etching remains an indispensable tool. Ongoing research in this area aim to push the boundaries of what is achievable in terms of precision, miniaturization, and integration. In this introductory section, an overview of MEMS technology is provided to highlight its unutilized potential.

1.4.1. The Crystalline Structure of Si

In order to grasp the intricacies of Si anisotropic wet etching, it's essential to comprehend its crystalline arrangement. When discussing a (100) Si wafer, it's crucial to understand its crystalline structure and orientation. Si has a diamond cubic crystal structure, meaning it has a face-centered cubic (FCC) lattice arrangement with two atoms per unit cell, characterized by a lattice constant of a = 5.43 Å. Fig. 1.19 depicts the atom lattice of Si along three crucial crystalline planes.

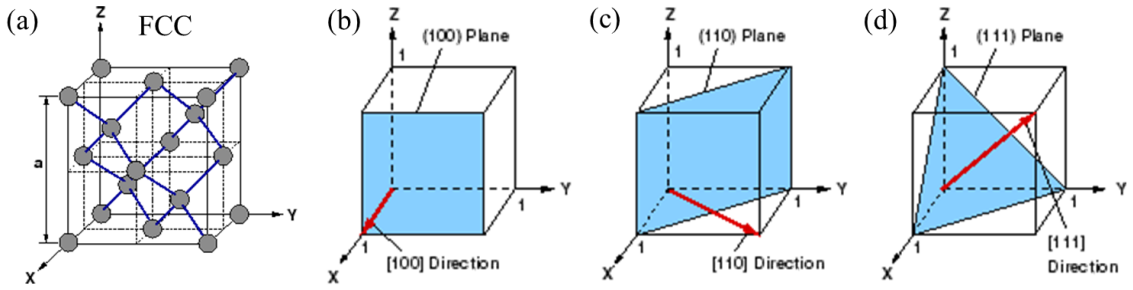

Figure 1.19: (a) The face centered cubic (FCC) crystalline structure of Si. Diagrams depicting the (b) (100), (c) (110), and (d) (111) crystalline planes.

The most common Si wafer used is the (100) Si wafer, as shown in Fig. 1.20. The (100) Si wafer's surface is oriented along the (100) crystal plane. This orientation results in the exposed surface of the wafer being flat and smooth, with atoms arranged in a regular pattern. The (100) plane intersects the wafer surface at right angles, forming a square grid-like pattern.

On a (100) Si wafer, the atomic arrangement exposes the (111) crystal planes along the edges of the square grid. These (111) planes make an angle of 54.74° with the wafer surface. This orientation is significant in various semiconductor processes, including anisotropic wet etching, as it influences the etching behavior and resulting structures [149]. Understanding the crystalline structure of a (100) Si wafer is essential for controlling and manipulating surface properties and for designing and fabricating semiconductor devices.

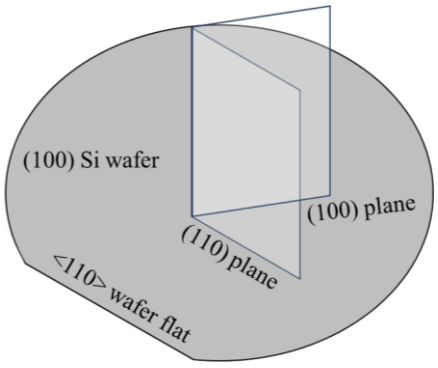

Figure 1.20: Diagram depicting a (100) Si wafer. The surface is a (100) plane, and the wafer flat is along the <110> direction. Additionally, the (110) plane and the (100) plane are shown.

1.4.2. Types of Etchants: Wet & Dry

The inception of microfabrication marked a significant milestone in technology, driven by the exploration of chemical solutions, including acids and bases, to shape Si wafers. In these formative stages, the precision crafting of microstructures relied heavily on the selective removal of Si through chemical reactions with etchants. This transformative process laid the groundwork for modern microfabrication techniques, establishing a foundation where intricate structures could be meticulously engineered at the microscale. Central to this evolution are the two principal categories of etching methods: wet and dry.

These methods, each with their distinct characteristics and applications, have revolutionized the landscape of microfabrication, propelling advancements across a multitude of industries and disciplines. Dry etching presents several drawbacks, including the toxicity and corrosiveness of certain gases involved. Additionally, it necessitates the redeposition of non-volatile compounds and demands specialized, costly equipment. In contrast, wet etching, known for its cost-effectiveness, has been widely adopted for MEMS component fabrication, particularly on (100) Si wafers. Wet etching facilitates the creation of diverse micromechanical devices through either isotropic or anisotropic processes. The distinction lies in whether the solution selectively targets different crystalline planes or etches uniformly in all directions. Key agents utilized in anisotropic wet etching include potassium hydroxide (KOH) and tetramethylammonium hydroxide (TMAH). The differences in wet and dry etching, as well as the differences in isotropic and anisotropic wet etching, are shown in Fig. 1.21.

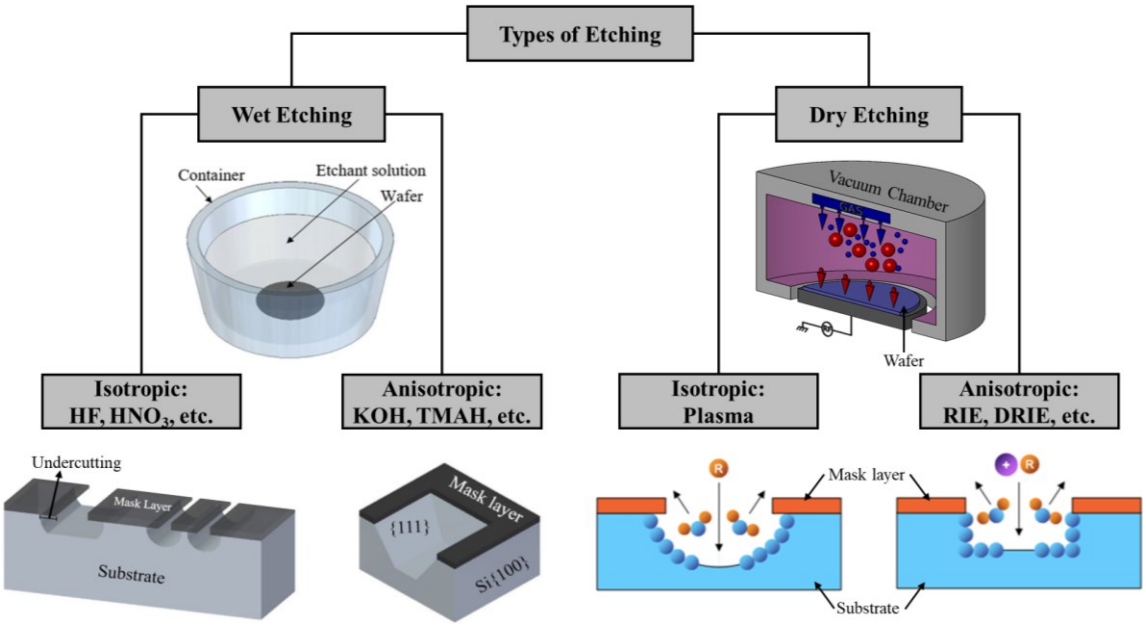

Figure 1.21: Diagram depicting the categorization of wet and dry etching [150]. Both methods of etching have the ability to etch either isotropically or anisotropically, depending on the chemicals and methods utilized [150].

Wet Etching

- Isotropic Wet Etching:

Isotropic wet etching removes material uniformly in all directions, resulting in rounded features and undercutting. This process does not depend on the crystal orientation of the substrate, making it simpler and more versatile for certain applications. However, isotropic etching lacks precision and control over feature shapes and dimensions compared to anisotropic wet etching. Isotropic wet etching is often used for creating simple structures, roughening surfaces, or removing large amounts of material quickly. It is commonly employed in MEMS fabrication for tasks such as shaping, thinning, or roughening Si wafers to achieve desired mechanical or optical properties. Despite its simplicity and versatility, isotropic wet etching has limitations, such as the inability to create precise geometries or vertical sidewalls. Therefore, it is often used in combination with anisotropic etching or other techniques to achieve the desired results in microfabrication processes.

- Anisotropic Wet Etching:

Anisotropic wet etching removes material from a substrate along specific crystallographic planes. Unlike isotropic etching, which removes material uniformly in all directions, anisotropic etching preferentially attacks certain crystal planes, resulting in well-defined structures with distinct geometries and precise features. This selective dissolution of material along certain planes results in the formation of features with smooth sidewalls and high aspect ratios. The etch rate along different crystallographic planes can vary significantly, allowing for precise control over the shape, dimensions, and orientation of the etched structures. As the etching process continues, the slower etched crystalline planes, such as the (111) planes of Si, become increasingly exposed. This enables the creation of complex three-dimensional structures, such as trenches, grooves, and pyramids, with high accuracy and repeatability. Common etchants used in anisotropic wet etching of Si include potassium hydroxide (KOH) and tetramethylammonium hydroxide (TMAH). The choice of etchant, along with process parameters such as temperature and etching time, can be carefully controlled to achieve the desired etch profile and surface finish.

Dry Etching

Dry etching is a process that uses reactive gases in a vacuum environment. Unlike wet etching, which relies on liquid chemical solutions, dry etching operates in a gas phase, making it a highly controlled and precise technique. Additionally, dry etching can either etch isotropically in all directions, such as in plasma etching, or have a directional component based, such as in reactive ion etching. The substrate is placed in a vacuum chamber where it is exposed to reactive gases, such as fluorine-based or chlorine-based gases, along with inert gases like argon or helium. These gases undergo chemical reactions

with the substrate material, breaking molecular bonds and removing material from the surface. Dry etching can be further categorized into two main types: isotropic or anisotropic dry etching.

- Isotropic Dry Etching:

In plasma etching, the reactive gases are ionized into a plasma state using radiofrequency (RF) energy or other sources of energy. Plasma is typically created by introducing a gas, such as oxygen, fluorine-based gases, or chlorine-based gases into the chamber. The plasma contains charged particles, such as ions and electrons, which bombard the substrate surface, causing chemical reactions and material removal. Plasma etching offers high selectivity, control, and uniformity, making it suitable for microfabrication processes.

- Anisotropic Dry Etching:

Reactive ion etching (RIE) is a variation of plasma etching where an additional bias voltage is applied to the substrate. This voltage accelerates the charged particles in the plasma towards the substrate surface, increasing the etch rate with additional directional control. RIE is known for its anisotropic etching capabilities, allowing for precise pattern transfer, high aspect ratio features, and the ability to create vertical sidewalls.

Both dry and wet etching have their respective advantages. Dry etching offers better control over feature shapes, dimensions, and compatibility with more delicate materials. However, it also presents challenges such as equipment complexity, higher costs, and the potential for substrate damage due to ion bombardment. On the other hand, wet etching is cheaper, significantly faster, and anisotropic wet etching enables geometries that can only be fabricated though its ability to etch along crystalline planes. Overall, wet and dry etching

are powerful techniques utilized in microfabrication, offering precise control over feature geometry and enabling the creation of complex, high-performance devices for a wide range of applications.

1.4.3. TMAH Anisotropic Wet Etching of Si

Despite the recent advancements in semiconductor technology, bulk micromachining of Si remains a vital process in microfabrication. This is not only due to its widespread use but also its well-established infrastructure. Compared to dry etching, wet chemical etching offers higher selectivity and is often faster [150]. TMAH, as an anisotropic etchant, offers numerous advantages, such as high selectivity to thermal oxide [151], exceptionally smooth etched surfaces [150, 152-155], and compatibility with ICs [156, 157]. Like other anisotropic etchants such as KOH, TMAH etching yields geometric shapes delineated by precisely defined crystallographic planes. Although these two etchants are similar, the etch rate, surface smoothness, and IC compatibility are three key distinguishing factors.

The etch rate of TMAH varies substantially with the experimental conditions, but it is dominated by the etchant's temperature and concentration, as can be seen in Fig. 1.22. It is worth noting that external agitation, and the relative separation of the neighboring structures also impacts the etch rate [150, 157, 158]. This is due to the reduced or increased availability of the etchant. The rate TMAH etches depends also on which crystalline plane is being etched, but typical etch rates for various concentrations of TMAH and KOH are shown in Fig. 1.22(a,b). The concentration of TMAH used for etching typically ranges between 3 and 40 wt% [151, 154, 159-163]. The etch rate of the (100) plane increases with

lower TMAH concentrations, while the etch rate increases with increasing temperature for both the (100) and (110) planes. Additionally, the ratio of the (111) plane etch rate divided by the (100) plane etch rate increases with higher concentrations. The higher the temperature of TMAH, the increased selectivity the etchant has towards the (100) plane, while the higher the concentration of TMAH, the etch rate of the (100) plane is reduced. However, the resulting etched structures from high TMAH concentrations improves sidewall smoothness, as well as reduces overall roughness. Furthermore, TMAH produces superior smoothness over all crystalline planes, as seen in Fig. 1.22(c-h).

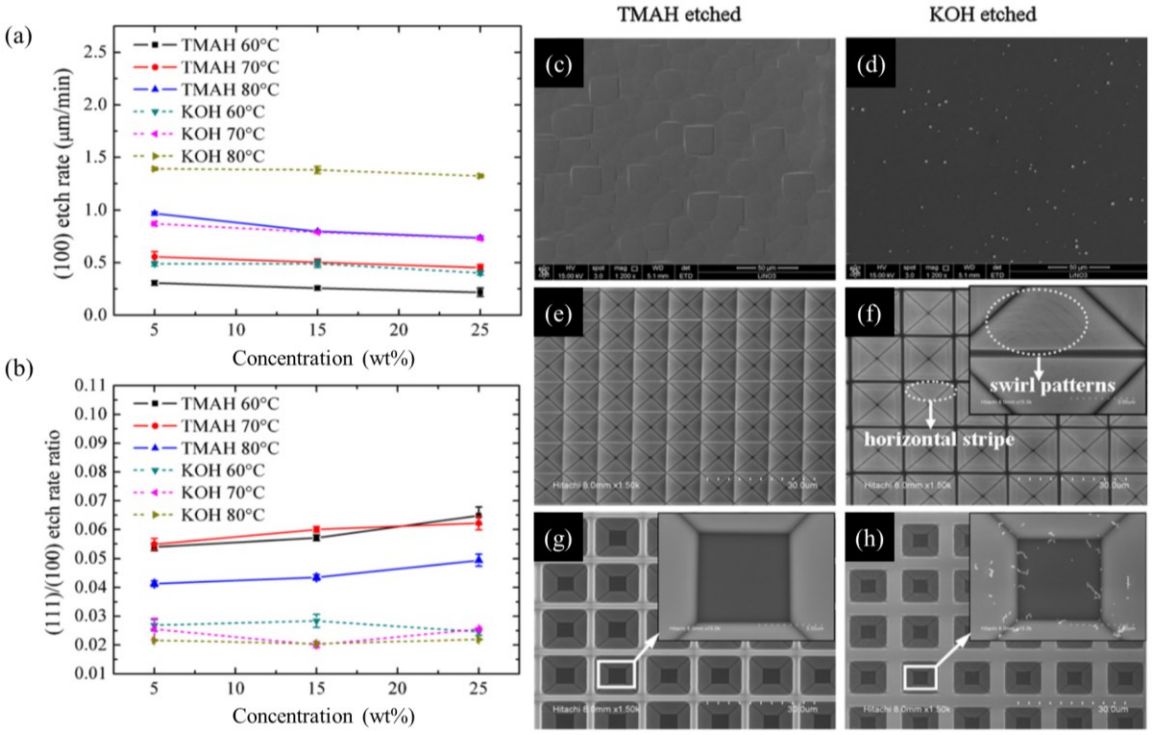

Figure 1.22: (a) Etch rates along the (100) plane for TMAH and KOH as a function of concentration at three different temperatures. (b) Etch rate ratios for the (111) plane etch rate divided by the (100) plane etch rate for TMAH and KOH as a function of concentration at three different temperatures. SEM photos of a Si wafer etched at 70° C where the wafer was (c) not patterned and etched with 5 wt% TMAH for 20 min, (d) not patterned and etched with 5 wt% KOH for 11 min, (e) patterned and etched with 5 wt% TMAH for 20 min, (f) patterned and etched with 5 wt% KOH for 25 min, (g) patterned and etched with 25 wt% TMAH for 15 min, and (h) patterned and etched with 25 wt% KOH for 7 min [164].

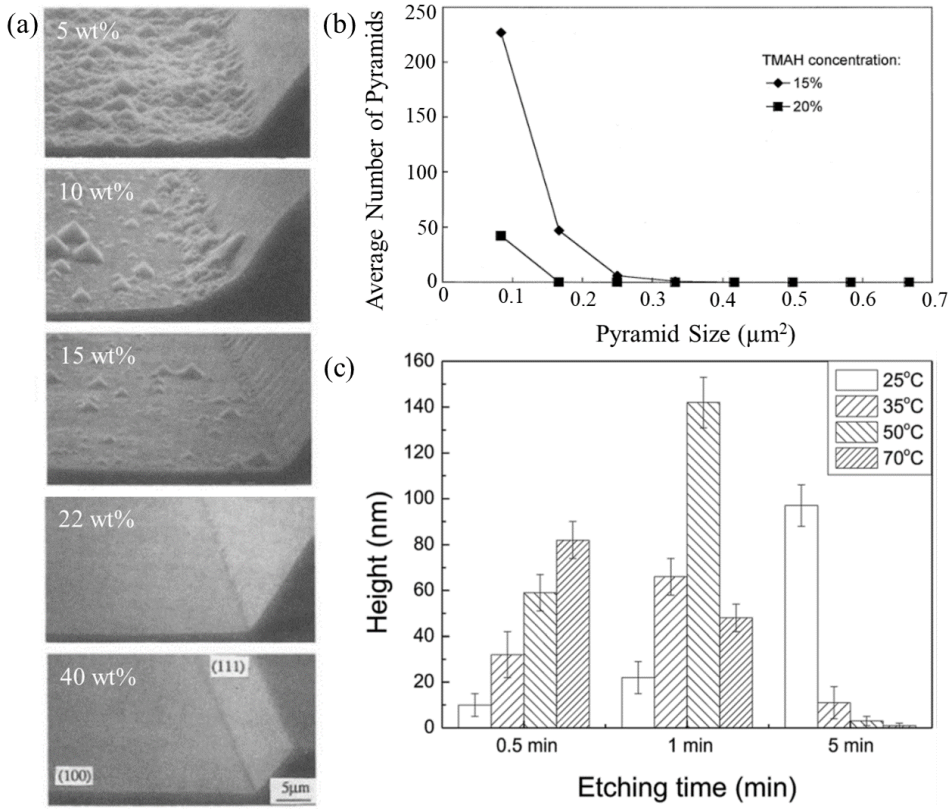

Figure 1.23: (a) Pyramidal hillocks formed when etched in 5 wt%, 10 wt%, 15 wt%, 22 wt%, and 40 wt% TMAH [165]. (b) The number and size of pyramidal hillocks etched at 90° C for 5, 15, and 30 minutes [166]. (c) The height of the pyramidal hillocks as a function of etching time at different temperatures when etched with 25 wt% TMAH [167].

However, the uniformity of the etched structure varies significantly with the concentration but not with temperature. At 5 wt%, the (100) plane has a higher concentration of pyramidal hillocks as shown in Fig. 1.23(a). These pyramidal hillocks are the largest contribution to the surface roughness [150, 166, 168, 169]. As the concentration increases, the number of pyramidal hillocks as well as their size reduces (Fig.1.23(b)). If adjacent (111) planes were etched, the pyramidal hillocks form in the valleys between adjacent structures. At concentrations above 22%, the size of these hillocks were less than 100 nm [165]. Therefore, at higher concentrations, optically smooth surfaces for IR spectrum can be obtained by anisotropically wet etching Si with TMAH, but other factors contribute to the smoothness of the etched surface.

TMAH etching of Si creates hydrogen bubbles as a byproduct of the chemical reaction, which can adhere to the surface and interfere with etching by preventing the TMAH from reaching the Si and therefore increase the surface roughness [150]. Methods to dislodge these hydrogen bubbles include the use of ultrasonic agitation or inclusion of a stir bar which also improve the smoothness of the etched structure, but both of these methods increase the TMAH etch rate in all planes and therefore increase the undercutting rate of the SiO_2 of Si_3N_4 masks [150, 154, 157, 158, 170, 171]. Additionally, various additives to the TMAH solution can be utilized to improve the smoothness of the etched structure, and to reduce undercutting. Isopropyl alcohol (IPA) is typically added to reduce surface roughness of the (100) plane, and it also mitigates undercutting of convex corners [148, 150, 155, 172-175].

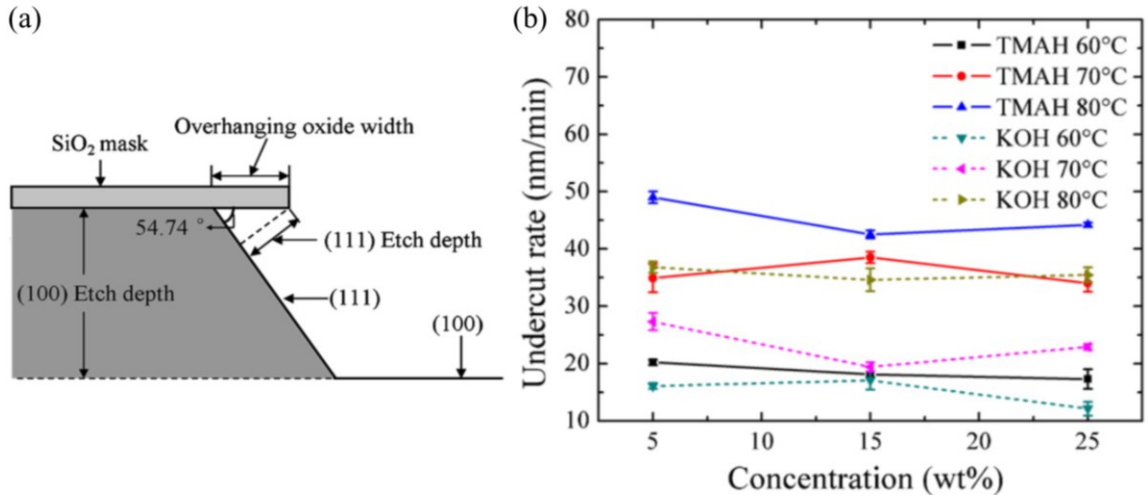

Figure 1.24: (a) Diagram depicting undercutting of a mask used to define the etched geometry. (b) The undercut rate as a function of etchant concentration at three different temperatures for KOH and TMAH [164].

Undercutting of the mask pattern is a severe problem in both TMAH and KOH etching, as seen in Fig. 1.24, but it can be mitigated by the use of additives or corner compensation techniques. One such additive is Triton X-100, which is a surfactant that

reduces the undercut rate and keeps the (111) crystalline planes intact [150, 154, 157, 173, 174, 176]. This is the additive we used when creating the light-concentrating micropyramids. Fig. 1.25(a) shows a square mask pattern aligned to the <110> directions on a (100)-Si wafer. The resulting etched geometry has vastly reduced undercutting when utilizing 0.1% Triton X-100 in 25 wt% TMAH, as seen in Fig. 1.25(b). Additionally, the addition of Triton X-100 minimally impacts the etch rate of the (100) plane, while protecting the (111) and (110) planes, as seen in Fig. 1.25(c-d). Although utilization of this surfactant reduces undercutting substantially, low concentrations can even improve surface smoothness, seen in Fig. 1.25(e).

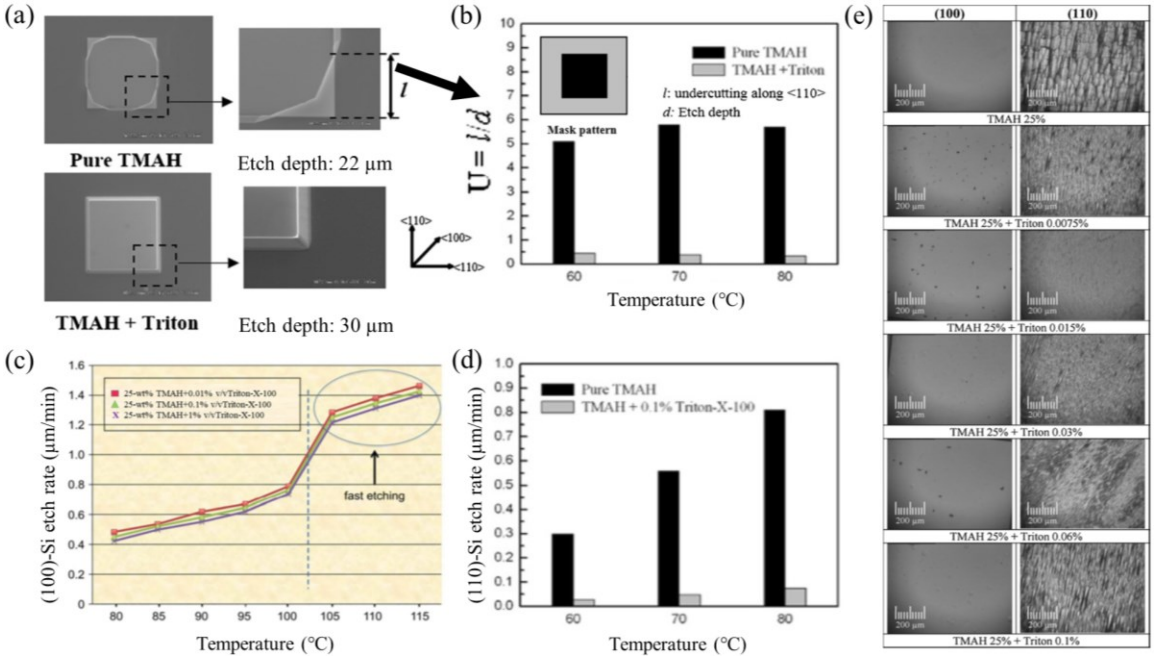

Figure 1.25: (a) SEM images of micropyramids etched with pure 25 wt% TMAH and TMAH with added Triton X-100, showing the reduced undercutting by the solution with added Triton X-100 plotted in (b) [174]. (c) The (100)-Si etch rate as a function of temperature for three different concentrations of Triton X-100 added to 25 wt% TMAH [150]. (d) The (110)-Si etch rate as a function of temperature for pure 25 wt% TMAH and 25 wt% TMAH with 0.1% Triton X-100 added [174]. (e) SEM images showing the surface roughness of the (100) plane and the (110) plane when etched with pure TMAH and five different concentrations of Triton X-100 [175].

Additionally, the implementation of corner compensating structures can effectively reduce or entirely eliminate corner undercutting, which enables the fabrication of nearly perfect 3-D structures [148, 150, 151, 173, 174, 176], as seen in Fig. 1.26. Even so, this approach demands a considerable amount of space on the mask layout to accommodate the compensation structures and permits a structure to be fabricated only to one specific size, as the compensation structure is calculated specifically for this geometry.

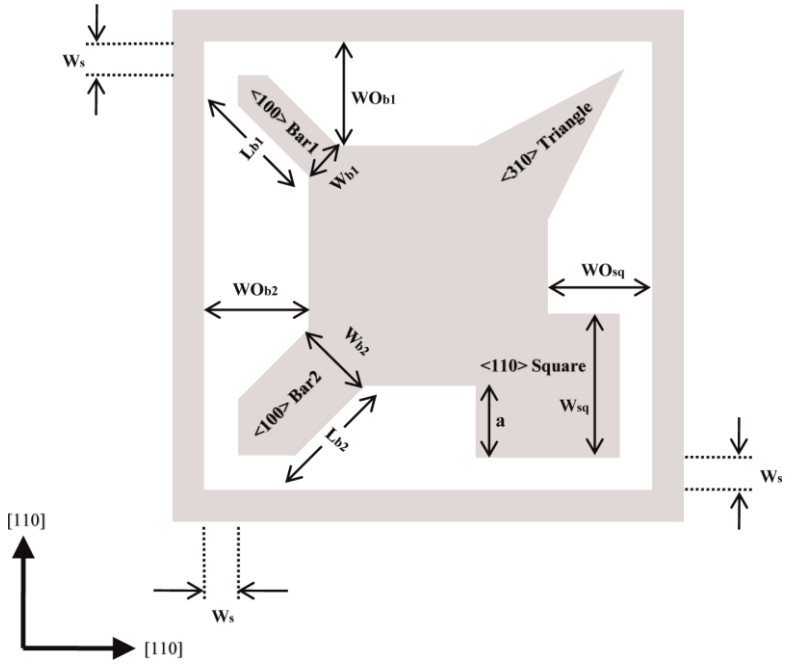

Figure 1.26: Various corner compensation structures at each of the four corners [158].

However, TMAH also etches other materials and special considerations must be taken into account [177]. Akin to KOH, the rate TMAH etches Si is invariable to low levels of dopants required for p-type or n-type Si [150, 158, 178]. However, dissimilarly to KOH, TMAH is CMOS compatible due to the absence of alkali metal ions in the solution, which KOH contains. Therefore, anisotropic wet etching with TMAH enables the fabrication of optical structures which are also compatible with the highly developed IC industry.

1.5. Retroreflectors

Retroreflectors, remarkable optical devices renowned for their unique ability to redirect light or electromagnetic radiation precisely back to its source, have become quintessential components in a multitude of industries. Retroreflectors are optical devices designed to reflect an electromagnetic wave back towards its source, irrespective of the angle of incidence. These remarkable materials have found widespread applications in various fields, ranging from transportation and road safety to astronomy and aerospace engineering. The concept of retroreflection dates back centuries, with early observations of phenomena such as cat's eyes and the Moon's surface exhibiting retroreflective properties. However, it was not until the 20th century that scientists and engineers began to fully understand and harness the potential of retroreflectors for practical applications.

Retroreflectors are typically composed of specialized materials or coatings that possess the unique ability to redirect incident light back towards its source. They have applications in two primary domains: civilian and military. In various applications, there is a frequent need for retroreflectors that possess the following characteristics: capable to efficiently reflect both TE and TM polarizations, functional at large angles of incidence, a minimal profile, cheap, and easy to fabricate.

In civilian applications, it serves purposes such as facilitating RF identification (RFID), enhancing navigation safety, aiding collision avoidance in vehicles, and enabling satellite communications. In transportation, retroreflectors are a cornerstone of road safety, enhancing the visibility of road signs, lane markings, and vehicles during nighttime and adverse weather conditions. Additionally, the use of retroreflectors extends beyond Earth's atmosphere. Aerospace engineering has embraced their capabilities for tracking,

navigation, and communication, showcasing their enduring relevance. For example, the historic Apollo missions established retroreflectors on the Moon's surface, and these devices continue to enable precise measurements between the Earth and the Moon.

In military applications, retroreflectors are primarily used for deception and stealth. Retroreflectors utilized for deception are called decoys, which have a large radar cross-section (RCS) and are easily identifiable by enemy radars. They are designed to send a large wavelength band of light back towards the enemy, but they must also be cheap because they will be destroyed, as in the case of a retroreflective decoy used to trick a guided missile. On the contrary, retroreflectors utilized for stealth must have a narrow band of retroreflected wavelengths in order to minimize the RCS, as well as enable detection by friendly radars designed to operate in that same narrow band. Numerous different types of retroreflectors exist, including the cat's eye retroreflectors, corner cube retroreflectors, Luneberg lens retroreflectors, Van Atta arrays, metasurface retroreflectors, and diffraction grating retroreflectors, as shown in Fig. 1.27. This list is not exhaustive.

The first known structure to retroreflect light was invented by Murray in 1927, and it was the cat's eye retroreflector [179]. This pioneering structure consisted of a plano-convex lens and a concave mirror positioned behind the flat rear surface of the lens, like the cat's eye retroreflector shown in Fig. 1.27(a). Light is focused by the convex lens onto the concave mirror, which then reflects the beam back along its original path. A cat's eye retroreflector with a multistage lens was designed by Biermann et al. [180], and obtained retroreflection with angle of incidence between ±15°. Additionally, a cat's eye retroreflector array consisting of microlenses and micromirrors designed by Lundvall et al. [181] was able to obtain retroreflection with angle of incidence between ±30°.

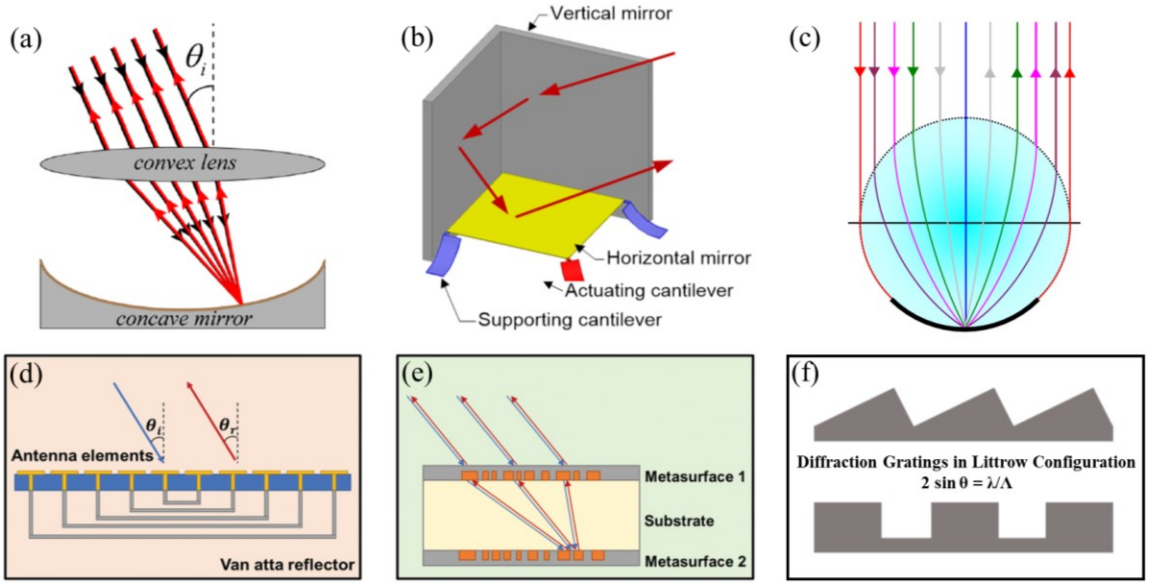

Figure 1.27: Various retroreflective devices. (a) Cat's eye retroreflector [187]. (b) Corner cube retroreflector. Specifically, one with cantilevers to adjust the bottom mirror [188]. (c) Luneburg lens with a metallic mirror on the bottom surface [189]. (d) Van Atta array, a phased antenna array, that redirects light back towards the direction it came [190]. (e) Example of a metasurface retroreflector [190]. (f) Diffraction grating retroreflector, following the Littrow configuration [191].

The next retroreflector is the corner cube retroreflector, originally designed by Duboc [182] in 1943. This structure consists of three reflective perpendicular surfaces fashioned together like the corner of a cube, hence its name. Incoming light bounces off either two or three surfaces, depending on the angle of incidence, and then is returned towards the direction of the incident light. Both theoretical analyses and experiments demonstrate that the corner cube reflector delivers retroreflection at half-power within the range of ±15° [184, 185]. The main disadvantages of the corner reflector is that the structure is large, it can only reflect light incident on the structure from up to 45°, and it can affect the polarization of the incident light [180, 184]. By employing a sheet composed of small trihedral corner cubes, it becomes possible to substantially decrease the depth of the retroreflector and maintain appreciable retroreflection within a ±30° angle of incidence [186]. However, larger angles are still unable to be retroreflected.

A corner cube retroreflector is shown in Fig. 1.27(b). However, this retroreflector was composed of two vertical mirrors fabricated from a Si wafer through anisotropic wet-etching a silicon-on-insulator (SOI) wafer, and a third horizonal mirror that was able to be micro-positioned by piezoelectric micro-cantilevers in order to enhance retroreflection. The corner cube retroreflector demonstrated angular displacement of 1.87° at 5 volts with switching times of 276 μs [188]. However, corner cube retroreflectors are still bulky and have low acceptance angles such that light is retroreflected.

After these more intuitive retroreflectors were discovered, numerous other variants were researched such as the Luneberg lens retroreflector and the Van Atta array. The Luneberg lens was originally designed by Rudolf Luneberg in 1944 [192]. It consists of a spherically symmetric gradient-index lens, such that the index of refraction decreases radially from the center to the outside of the sphere. A modified version of the Luneberg lens with a mirror on the back surface is shown in Fig. 1.27(c), such that light is reflected off the mirror and is reflected towards the incident light [193]. Efficient retroreflection is available in a wide range of incident angles of ±50° [185], but the retroreflector is large, difficult to fabricate, and is expensive. Another less intuitive retroreflector is the Van Atta array shown in Fig. 1.27(d), and was patented by L. C. van Atta in 1959 [194, 195]. It consists of paired antennas connected together by waveguide transmission lines, and is typically used in radio frequencies for wireless communication, and RFIDs.

Lastly, two other retroreflectors worth mentioning are metasurface retroreflectors and diffraction grating retroreflectors shown in Fig. 1.27(e,f). These two types of retroreflectors are closely related to the research in this dissertation, and therefore require a more intensive discussion.

1.5.1. Metasurface Retroreflectors

Not long ago, metasurfaces were developed with the ability to manipulate electromagnetic wavefronts by modifying the phase, amplitude, polarization, and propagation direction of incident light [196-207]. Metasurfaces are structures with periodicity smaller than the wavelength of incident light and are designed to have electromagnetic properties beyond what can be found in nature. These structures can consist of either dielectric or metallic materials, or some combination thereof. Metasurfaces are able to have a low profile and can be an inexpensive solution to retroreflect light at specific designed angles for wavelengths of light longer than the visible spectrum. However, they consist of sizes on the order of λ or smaller. Therefore, fabrication of metasurface retroreflectors in the visible spectrum can significantly increase costs and reduce fabrication uniformity.

Metasurface-based devices using nanoresonators possess dispersion characteristics largely defined by their geometric parameters and structural arrangement, allowing for wavefront manipulation, in contrast to traditional geometrical optics-based components [208-217]. Recently, singlet flat metasurface retroreflectors have been introduced, providing benefits in terms of miniaturization and integration with other optical or electronic devices [218, 219]. However, their limited operational angles remain a challenge. To overcome this, metasurface doublet retroreflectors have been explored.

Fig. 1.28(a) shows a metasurface doublet retroreflector, similar to the metasurface retroreflector shown in Fig. 1.27(e), designed for λ = 1550 nm. The top metasurface, with 480 μm diameter, acts as a Fourier lens with a focal length of 428 μm and performs a spatial Fourier transform on the incident light to focus light with different incident angles

to different locations on to the bottom metasurface. Additionally, the top metasurface also performs the inverse transform for light reflected off the bottom metasurface. The bottom metasurface, with 600 μm diameter, functions as a concave mirror by forcing a spatially varying momentum to retroreflect light back along its incident direction. These surfaces consist of hydrogenated amorphous Si nanopillars and were fabricated with electron beam lithography. Experimental characterization of the metasurface doublet retroreflector show high retroreflection efficiency at any angle up to angle of incidence $\theta_{in} = 25°$ [220].

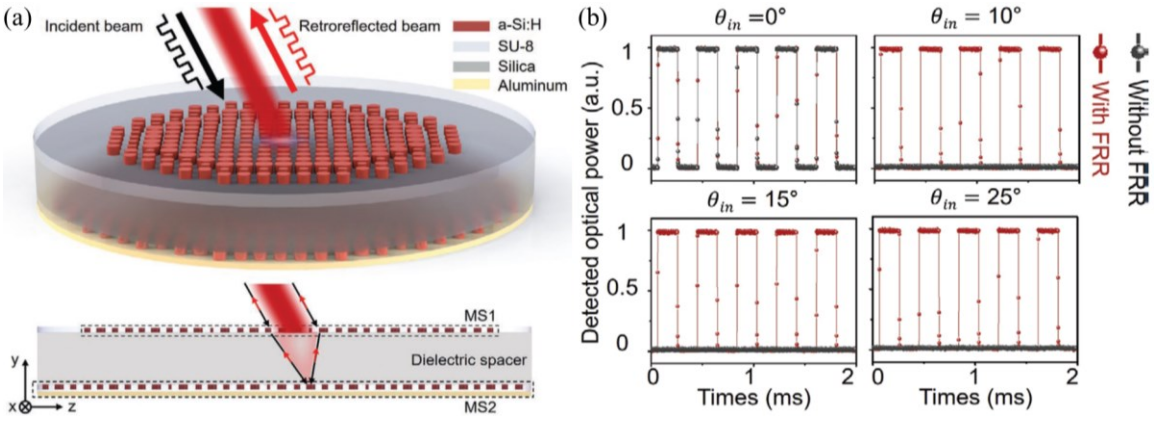

Figure 1.28: (a) Flat retroreflector (FRR) based on a metasurface doublet, which consists of vertically stacked metasurfaces MS1 and MS2. (b) Detected retroreflected optical power at $\theta_{in} = 0°$, 10°, 15°, and 25° [220].

Despite having a planar structure, the retroreflector remains thick overall at ~ 276λ thickness. Additionally, it also has relatively low angle of incidence operation. Furthermore, the retroreflector utilizes nanopillars designed for SWIR operation, and therefore scaling the structure down to visible wavelengths is not a feasible task.

Current metasurface retroreflectors face challenges in achieving wide-angle and omnidirectional operations. Fig. 1.29 depicts an adaptive reconfigurable spin-locked phase gradient metasurface retroreflector designed for 4 GHz with a thickness of 0.07λ. It is capable of high efficiency, wide angle, and omnidirectional retroreflection through

utilizing reconfigurable meta-atoms based on employing micromotors. The top layer consists of copper double-C shaped circular structures designed for rotation on a dielectric substrate. The bottom layer consists of an aluminum plate to prevent any transmission of the incident light. A micromotor is mounted beneath the aluminum plate to control the rotation of each resonator, and to prevent any electromagnetic interference with the resonant structure. An air spacer is placed between the top and bottom layers to accommodate a metallic pedestal that connects the dielectric substrate with the bottom micromotors [190].

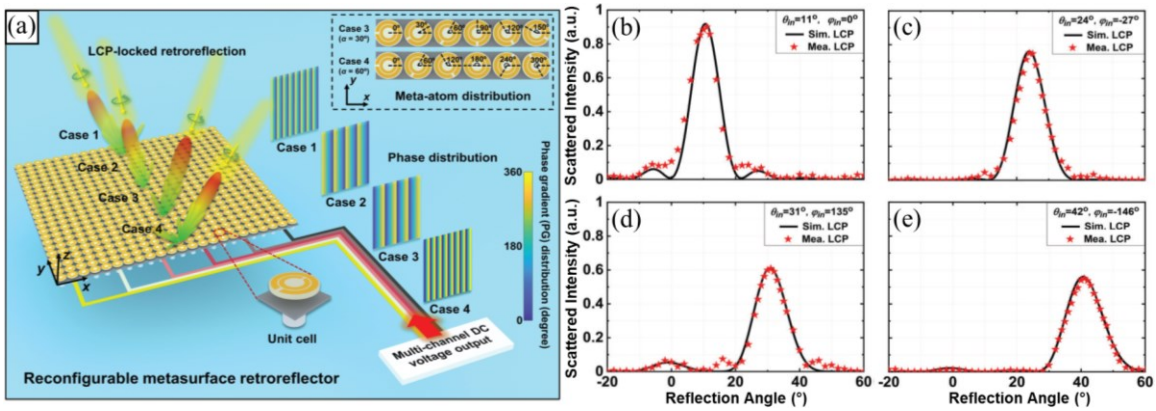

Figure 1.29: (a) Adaptive reconfigurable spin-locked metasurface retroreflector, based on utilization of meta-atoms with rotational mechanical control to process either right or left circularly polarized light. Experimental and simulation results of left circularly polarized light incident on 2-D scattering patterns at 4 GHz for (b) $\theta_{in} = 11°$ and $\varphi_{in} = 0°$, (c) $\theta_{in} = 24°$ and $\varphi_{in} = -27°$, (d) $\theta_{in} = 31°$ and $\varphi_{in} = 135°$, and (e) $\theta_{in} = 42°$ and $\varphi_{in} = -146°$ [190].

The reflection phase of the meta-atoms can be dynamically controlled by adjusting their orientation through mechanically rotating each meta-atom, while maintaining the same reflection handedness as the incident light. This enabled high efficiency retroreflection at up to $\theta_{in} = 47°$, where the performance at a few incident angles are shown in Fig. 1.29(b). To achieve dynamic adaptive retroreflection, the direction of incident light is detected by an antenna array. Next, the detected direction is sent to a computer to

calculate the necessary phase distribution for retroreflection. Lastly, the phase distribution is converted to an electrical signal to control the orientation of each meta-atom [190].

In contrast to retroreflectors reported with bulky structures and restricted retroreflection capabilities within predefined planes, the aforementioned retroreflector offers advantages such as a slim profile, high efficiency, and a wide omnidirectional retroreflection angle. However, this design is complex with numerous moving parts, making the fabrication expensive. Additionally, the retroreflector requires postprocessing, which is time consuming and limits its applicability in real time scenarios. Furthermore, the retroreflector is designed for microwave frequencies and scaling the structure down to visible wavelengths would be difficult to achieve.

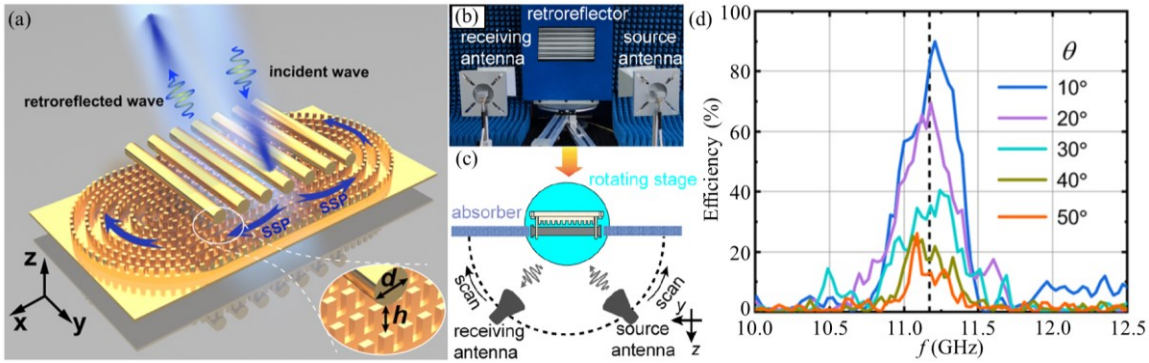

Figure 1.30: (a) Hyperbolic plasmonic metasurface (HPM) retroreflector design, where the diameter is *d*, period is *p*, and the separation between the HPMs and the metal cylinder array is *h*. (b) Photo of the experimental setup, where the retroreflector is covered by an absorber except where the metal cylinder array is located. (c) Diagram showing the top-down view of the experimental setup. (d) Experimentally measured retroreflection efficiency as a function of frequency shown for incident angles θ [221].

Fig. 1.30 depicts a hyperbolic plasmonic metasurface (HPM) retroreflector design capable of real time retroreflection. The key principle behind this technique lies in the orthogonal relationship between the canalized spoof surface plasmons on the hyperbolic plasmonic metasurfaces and the waves propagating in free space, as seen in Fig. 1.30(a). This orthogonality ensures high efficiency and seamless conversion to surface plasmons.

Due to the strong confinement characteristics resulting from the enhanced light-matter interaction, it's possible to effectively direct and retroreflect the canalized spoof surface plasmons using extremely thin structures. Experimental analysis of the retroreflector designed for ~0.92λ thickness at a frequency of 11.2 GHz is shown in Fig. 1.30(b-d), which reveals a half-power field of view reaching up to 53° and a peak efficiency of 83.2% [221]. The primary challenge that constrains both the angular bandwidth efficiency and the efficiency stems from the metal cylinder array's relatively low transmissivity when exposed to incident waves at significant angles, which can be seen in Fig. 1.30(d) where the transmissivity experiences a sharp decline beyond an incidence angle of 40°.

Regardless, this HPM metasurface retroreflector shows great potential for a range of applications such as remote sensing, target detection, and diverse on-chip light control devices. However, its utility in the visible spectrum is not researched and scaling retroreflectors designed for the microwave regime to the visible regime is known to be an arduous task. Additionally, this design is complex, making the fabrication expensive.

Fig. 1.31 depicts a simpler and less expensive retroreflector design; the binary Huygen's metasurface retroreflector. It is designed to retroreflect light according to the Littrow configuration and the Huygens-Fresnel principle, which states that every point on a wavefront can be considered as a source of secondary wavelets, and these secondary wavelets at different locations mutually interfere. The sum of all these wavelets forms a new wavefront. Generally, the Huygens' metasurface retroreflector consists of orthogonal magnetic and electric dipoles which become a series of Huygens' sources when induced by an incident electromagnetic wave [222]. In a retroreflective metasurface, both reflected and incident waves are superimposed and share the same physical space.

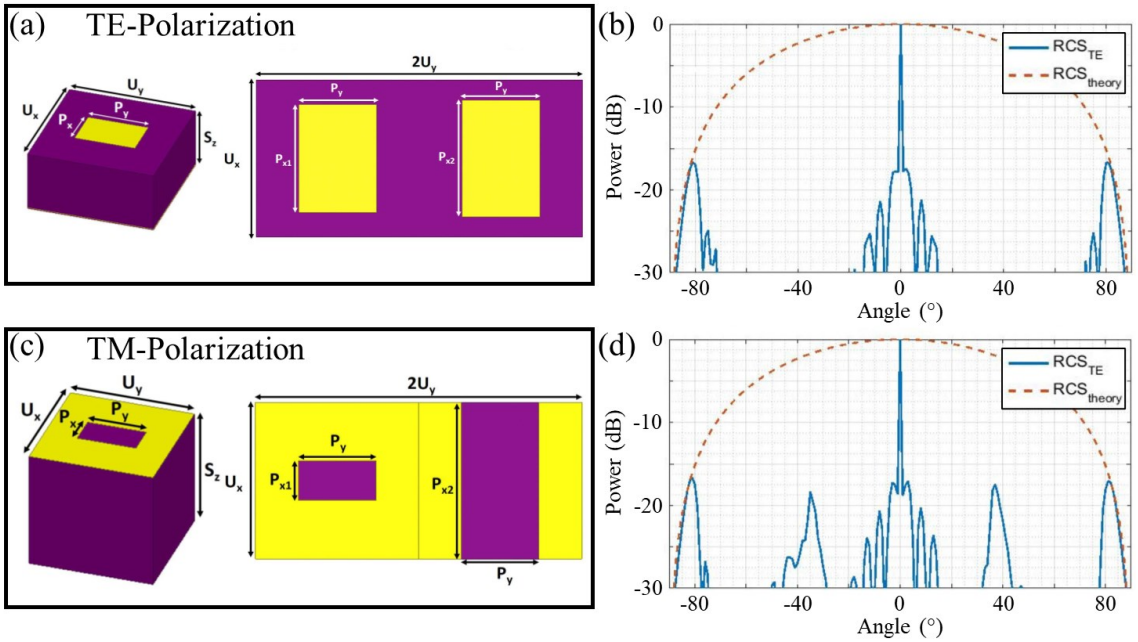

Figure 1.31: Huygens' metasurface retroreflectors at 24 GHz are shown. (a) TE retroreflector shown in 2-D and 3-D. The dimensions of the components are P_{x1} = 2.16 mm, P_{x2} = 2.35 mm, P_y = 1.5 mm, U_x = U_y = 3.149 mm, and S_z = 1.575 mm. (b) Monostatic radar cross section (RCS) simulation for the TE retroreflector, shown in blue, and for the theoretical RCS of an ideal mirror placed normal to the incident radiation, shown in red. (c) TM retroreflector shown in 2-D and 3-D. The dimensions of the components are P_{x1} = 0.8 mm, P_{x2} = 3.149 mm, P_y = 1.5 mm, U_x = U_y = 3.149 mm, and S_z = 3.175 mm. (d) Monostatic RCS simulation for the TM retroreflector, shown in blue, and for the theoretical RCS of an ideal mirror placed normal to the incident radiation, shown in red [191].

This Huygens' metasurface retroreflector was designed to incorporate only two cells per grating period. Resulting from this approach is the binary Huygens' metasurface, which streamlines the design process towards highly efficient, cost-effective, and resilient metasurface retroreflectors. Through this discretization technique, two binary Huygens' metasurfaces were experimentally characterized and found capable of retroreflecting an incident plane wave at 82.87° for TE as seen in Fig. 1.31(a-b), and TM polarized waves, as seen in Fig. 1.31(c-d) [191, 223].

Simulation results for a 2-D infinite retroreflector predicted retroreflection efficiencies of 94% for TE polarization and 99% for TM polarization. The experimental characterizations agreed with numerical modeling and indicated a power efficiency of 93%

for both TE and TM polarizations [191, 223]. This underscores the feasibility of achieving high retroreflection efficiency at a designated angle using a straightforward metasurface design. The proposed design methodology not only facilitates retroreflection but also enables reflection at arbitrary angles with exceptional efficiency, expanding its potential applications.

Consequently, it remains rare to achieve a combination of a flat profile, high reflection efficiency, and a wide range of incidence angles in an ultrathin metasurface retroreflector capable of operating for both TE and TM modes. The binary Huygens' metasurface retroreflector comes close to achieving these goals, but it operates in the microwave regime and therefore scaling the structure down to visible wavelengths can significantly increase fabrication costs. Additionally, it can only have high retroreflection efficiency for either TE or TM modes individually, which limits its usefulness. However, this retroreflector also utilizes the Littrow configuration, which enables downscaling to visible wavelengths.

1.5.2. Littrow Retroreflectors

Littrow retroreflectors take advantage of the diffraction grating equation for a specific scenario called the Littrow configuration shown in Fig. 1.27(f) when the angle of incidence equals the angle of diffraction [224]. The grating equation for a surrounding refractive index of $n = 1$ is $\sin \Theta_r - \sin \Theta_{in} = m\lambda/\Lambda$, where Θ_{in} is the angle of incidence, Θ_r is the angle of diffraction, λ is the wavelength of light, Λ is the periodicity of the diffraction grating, and m is the diffraction order. For $m = -1$ and $\Theta_r = -\Theta_{inc} = \Theta$ the grating equation simplifies to the Littrow configuration; $2 \sin \Theta = \lambda/\Lambda$. For light to be retroreflected, one

needs to design the diffraction grating to satisfy these parameters. For this purpose, maximum optical power is concentrated in the desired direction while the residual power in the other orders is minimized.

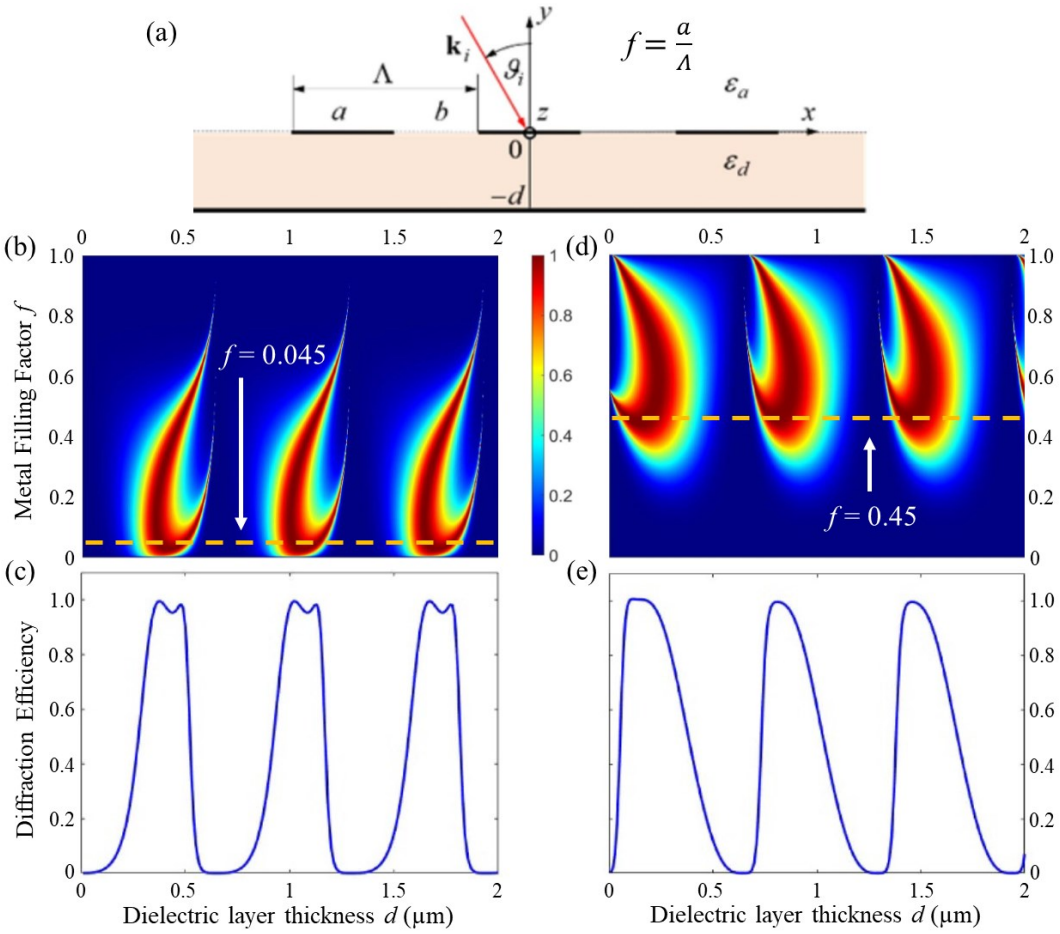

Figure 1.32: (a) Diagram depicting a diffraction grating's cross-section. (b) Numerically modeled TE polarization diffraction efficiency of a diffraction grating in the Littrow configuration, with the horizontal line corresponding to the $f = 0.045$ plot shown in (c), which plots the diffraction efficiency as d varies for $\varepsilon_d = 2.08541$ and $\varepsilon_a = 1$. (d) Numerically modeled TM polarization diffraction efficiency of a diffraction grating in the Littrow configuration, with the horizontal line corresponding to the $f = 0.45$ plot shown in (e), which plots the diffraction efficiency as d varies for $\varepsilon_d = 2.08541$ and $\varepsilon_a = 1$ [225].

Fig. 1.32 depicts a simple yet novel flat metal-dielectric diffraction grating that theoretically achieves 100% retroreflection efficiency through utilizing the Littrow configuration. The diffraction grating consists of a planar dielectric slab with metal on both

sides, where periodic parallel openings exist on the top metal layer, as seen in Fig. 1.32(a). To simplify the analysis, the top metal layer was set to be perfect and infinitely thin with either infinite negative permittivity or infinite conductivity. A variety of grating configurations can achieve very high retroreflection efficiency through an interplay in the metal filling factor $f = a/\Lambda$, which is the ratio of the width of the metal stripes a to the grating period Λ. For light with TE polarization, high retroreflection can be obtained with $f = 0.045$, although $f = 0.5$ can also achieve high retroreflection, albeit with increased sensitivity to the dielectric layer's thickness d. For the TM polarization, $f = 0.45$ yields reduced sensitivity to variations in the thickness of the dielectric slab [225]. These results indicate that 100% retroreflection efficiency can be achieved for both TE and TM polarizations, however with different grating parameters required for each.

Despite the simplicity of the grating's geometry, the wave processes that lead to such high retroreflection efficiency require a more extensive discussion. Achieving 100% retroreflection efficiency requires that specular reflection experiences destructive interference for all waves propagating in the same direction after undergoing multiple diffractions and reflections at the metal layers. The presence of the dielectric layer in between the metal layers exists only to support destructive interference for the specular reflection direction and constructive interference for the retroreflection direction. The primary impact of the lower permittivity is to maintain the required optical path length between the metal layers [225].

Although these results indicate that 100% retroreflection efficiency can be achieved for both TE and TM polarizations, this was shown to only be possible with different grating parameters. Additionally, this analysis of the grating equation explicitly does not consider

the thickness of the metal layer, nor the impact real metals would have on their retroreflection capabilities. Real metals in the visible regime behave quite differently compared to an idealized perfect metal layer. Commonly used metals, such as Ag, Au, and Al, display large negative real dielectric constants and relatively small imaginary dielectric constants.

In this dissertation, retroreflectors were designed in the aforementioned Littrow configuration shown in Fig. 1.32 but extended to real metals with real thicknesses in order to study the impact the type of metal has on retroreflection, as well as how the thickness of the metal layer impacts retroreflection efficiency. Additionally, real metals at optical frequencies display substantial plasmonic effects, which can drastically affect retroreflector performance. Metallic metasurface structures support near-surface electron oscillations known as surface plasmons. In nanostructured metals, localized surface plasmon resonances occur. This results in a wide range of electromagnetic resonant properties.

1.6. Plasmonics

In the realm of nanoscience and nanotechnology, the manipulation of light on the nanoscale has emerged as a profound avenue for scientific inquiry and technological advancement. Plasmonics, a field nestled at the intersection of optics and condensed matter physics, has garnered significant attention for its promise in revolutionizing various domains. At its core, plasmonics revolves around the study of surface plasmons (SPs), collective oscillations of free electrons at metallic-dielectric interfaces, to control and confine light at scales far below its diffraction limit. SPs are being investigated for their

potential in optics, data storage, solar cells, microscopy, for developing sensors, and more [226-228].

The inception of plasmonics can be traced back to the pioneering works of Ritchie, Otto, and others in the mid-20th century, laying the theoretical groundwork for understanding SPs and their implications [229]. However, it was not until the advent of nanofabrication techniques in the late 20th and early 21st centuries that plasmonics truly flourished into a vibrant field of research. The ability to engineer metallic nanostructures with unprecedented precision has unlocked a plethora of opportunities to manipulate light at the nanoscale, enabling functionalities previously deemed unattainable [230-237]. This progress has enabled precise control over SP properties, unveiling new scientific insights and allowing for their customization for specific applications.

A compelling feature of SPs is their capacity to concentrate and direct light within subwavelength structures, offering the potential to create photonic circuits at a scale that exceeds current length constraints [238, 239]. These circuits would begin by converting light into SPs, which would then be subject to processing by logic elements before being transformed back into light. Building such circuits requires various components like switches, waveguides, and couplers. Notably, when incorporated into dielectric materials, the infrastructure facilitating SP propagation can also transmit electrical signals. Advances like these hint at the emergence of a new realm of photonics employing SPPs.

This dissertation aims to provide a comprehensive exploration of the principles, and applications of plasmonics. Beginning with a fundamental overview of plasmonic phenomena, the dissertation will delve into the underlying physics governing surface plasmon resonance, localized surface plasmon resonance, and the role of geometry and

material properties in shaping plasmonic behavior. By explaining the fundamental principles of plasmonics, this work will establish a solid foundation upon which subsequent discussions will build.

1.6.1. Plasmon Resonance Fundamentals

SPs are waves that travel along the surface of a conductor. Essentially, these are coherent free electron oscillations that propagate along the metallic-dielectric interface accompanied by an electromagnetic wave, which are called surface plasmon polaritons (SPPs) [226, 240] and are shown in Fig. 1.33(a). During this interaction, the free electrons collectively oscillate in resonance with the light wave. This resonant interplay between the oscillation of surface charges and the light's electromagnetic field enables unique properties to appear, which results from the frequency-dependent dispersion characteristics of the dielectric and metallic materials [226]. This movement of electrons leads to resonant scattering and absorption of the incident light, as well as significant electric field enhancements on nanoparticles and nanoholes [241-243]. The spectral position of these resonances depends on the material, size of the objects, their geometry [244, 245], and the surrounding environment [246, 247].

The interaction between surface charges and the electromagnetic field that forms the SPP has two key effects. Firstly, this interaction causes the momentum of the SPP mode, $\hbar k_{SP}$, to exceed that of a free-space photon of the same frequency, $\hbar k_0$, as shown in Fig. 1.33(b). For SPPs to exist at an interface, the frequency-dependent permittivity of the metal, ε_m, and the dielectric material, ε_d, must have opposite signs [226]. This causes an increase in momentum caused by the binding of the SPP to the surface, which results in a

momentum mismatch between light and SPPs of the same frequency. The mismatch must be overcome for light to effectively generate SPPs that propagate parallel to the surface of the metal. These are called propagating surface plasmons (PSPs) that can exist at a metallic-dielectric interface [249]. This coherent interaction causes the PSP to have greater momentum than a free photon of the same frequency. They consist of an electromagnetic wave coherently coupled with the collective motion of mobile charges on the metal's surface.

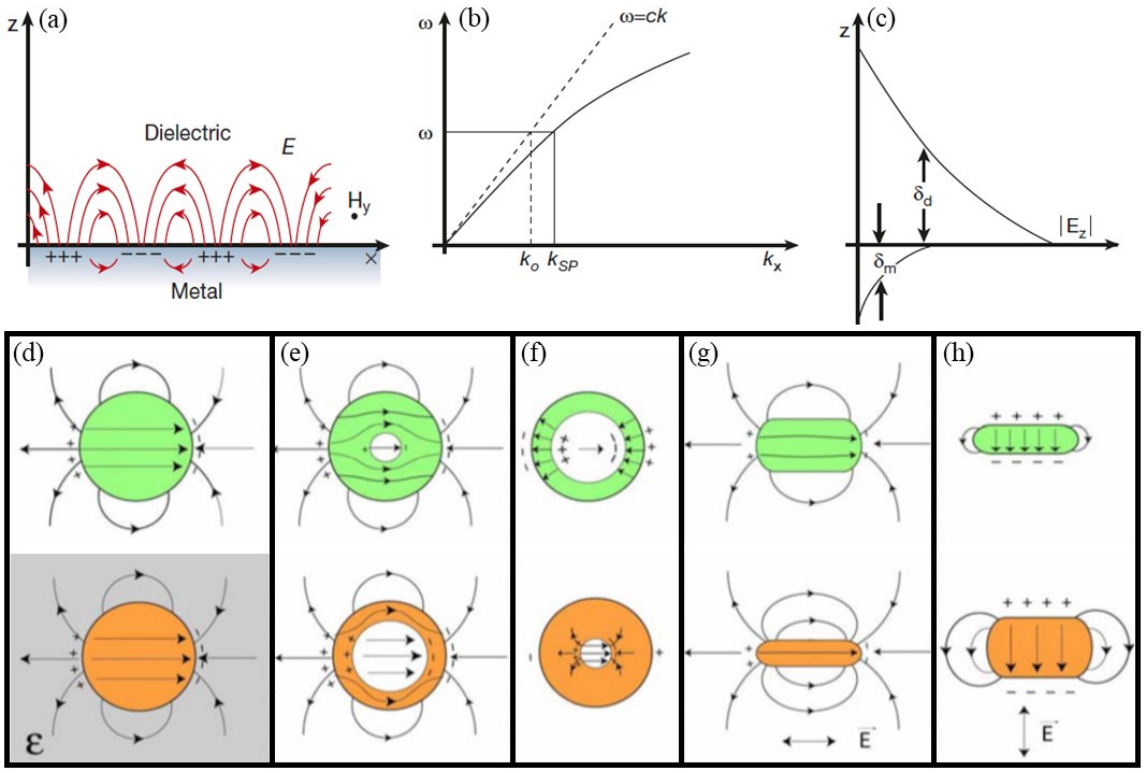

Figure 1.33: Diagram depicting the basics of surface plasmonic resonance. (a) At the interface of a dielectric and a metal, surface plasmons have a combined electromagnetic wave and surface charge. The generation of surface charge requires an electric field normal to the metal's surface. (b) The surface plasmon dispersion curve, displaying the momentum mismatch between the light, $\hbar k_0$, and the surface plasmon modes, $\hbar k_{SP}$. (c) The field component perpendicular to the surface can be enhanced near the surface, but decays exponentially with distance, where the decal length in the medium above the metal is δ_d, and the skin depth into the metal is δ_m [226]. (d-h) Diagrams depicting how the plasmon resonance of a metal nanostructure is affected by the field distribution. (d) Metallic nanospheres incased in different dielectric materials, (e) metallic nanoshells with a symmetric plasmon mode, (f) metallic nanoshells with an antisymmetric plasmon mode, (g) metallic nanorods with field polarization parallel to the nanorods, and (h) metallic nanorods with field polarization perpendicular to the nanorods [248].

Additionally, there exist localized surface plasmons (LSPs) which entail the collective oscillation of free electrons within a metallic nanoparticle, alongside associated oscillations of the electromagnetic field [249]. The resonance frequency is contingent upon the particle's composition, shape, size, and the surrounding optical environment [250, 251], typically falling within the visible to near-infrared region of the spectrum for metal nanostructures (Au, Ag, Cu) field [249].

There are three primary methods to supply the missing momentum to generate SPs. Arguably the most well studied method involves scattering from a defect on the surface, such as nanoparticles or nanoholes [238, 252]. The second method utilizes prism coupling, such as in the Kretschmann configuration, to enhance the momentum of the incident light [253, 254]. The third method employs a periodic corrugation in the metal surface [255]. Wood, over a century ago [256], observed anomalous light diffraction behavior by utilizing metallic diffraction gratings, which some are now understood to result from coupling to SPs. The light scattered by a metallic diffraction grating enables momentum matching and therefore its coupling to SPs [257]. Additionally, the reverse process also facilitates the controlled coupling of non-radiative SP mode with light [258, 259].

After light has been converted into an SP mode, it will gradually decrease with distance due to absorption losses in the metal. This attenuation is dependent on the metal's dielectric function at the SP's oscillation frequency. Secondly, the field perpendicular to the surface decays exponentially with distance and is known as an evanescent or near-field which stems from the non-radiative nature of SPs as shown in Fig. 1.33(c). The decay length of the field into the dielectric medium is δ_d, and the decay length into the metal is δ_m [226].

The ability of SPs to concentrate light within subwavelength structures arises from the dielectric constants of the surrounding non-conductive media and the metals. It has been demonstrated that metal structures can significantly enhance the local electric field by focusing electromagnetic energies into subwavelength volumes. This can be utilized to manipulate light–matter interactions and amplify non-linear phenomena [226, 248, 249, 260]. A few examples of how the field distribution affects the plasmon resonance in metal nanostructures are shown in Fig. 1.33(d-h).

The optical properties of metal nanoparticles rely significantly on their proximity to other nanoparticles. Consequently, they can be intentionally engineered by regulating their environment, arrangement, and symmetry [243, 247, 260-265]. Unique plasmonic effects occur in different spatial regimes via near-field and far-field coupling. When particles are relatively densely packed, they interact through near-field coupling, resulting in substantial spectral shifts of the plasmonic resonances. This interaction also modifies and splits their line-shapes due to the hybridization of the plasmonic modes [266-270]. Significant enhancement in the quality of localized plasmon resonances is achievable through far-field coupling of localized surface plasmons (LSPs) [249, 271]. When particles are randomly distributed, the scattered radiation fields incident upon adjacent particles lack a specific phase relationship, resulting in minimal effects [272].

However, when metallic nanoparticles are arranged in an array with a period that matches the wavelength of the particle plasmon resonance, an additional resonance, termed a surface lattice resonance (SLR), may emerge [247]. By carefully engineering the array period, the quality of the resonance can be improved. When applied to a large array of nanoparticles, these diffractively coupled localized surface plasmon resonances (LSPRs)

can narrow the resonance width to just a few nanometers [273, 274]. The intensity of the LSPR is constrained by the imaginary part of its dielectric constant. This also leads to phenomena such as enhanced absorption, transmission, or reflection of an array. Additionally, if identical particles are arranged in an array, their polarizability changes. This alteration occurs because particles experience driving fields from both the incident light and the light scattered by other particles. These nanoparticle arrays enable engineering of their properties through adjusting interparticle spacing, particle and array shape, particle and array size, or background medium [263].

An example to illustrate the complexity of SPs is shown in Fig. 1.34 with nanoparticle dimers. When the light is polarized transversely to the nanoparticles, Fig. 1.34(a), the dipoles destructively interfere. They produce a less intense electric field in the gap (Fig. 1.34(c)). In this case, the LSPR blue-shifts and decreases in intensity (Fig. 1.34(e)). When the incident field is polarized along the dimer axis where the dipoles are additive (Fig. 1.34(b)), a strongly confined electromagnetic field forms in the gap (Fig. 1.34(d)). This constructive interference between additive dipoles results in a red-shift of the LSPR, which increases as the gap narrows (Fig. 1.34(f)). When the particles are separated by more than $\lambda/2\pi$, static dipolar interactions incur additional retardation effects which can alter and even reverse these trends [263, 272].

Metals like Au, Ag, Cu, and Al are frequently used as plasmonic metals because of their relatively high-quality resonances [250, 272, 275-277]. Fig. 1.34(g,h) depicts how modifying Au and Al nanodisk sizes in arrays with random separation distances affects the extinction efficiency of the incident light. As the sizes increase, the resonance wavelength shifts to longer wavelengths with less energy [272].

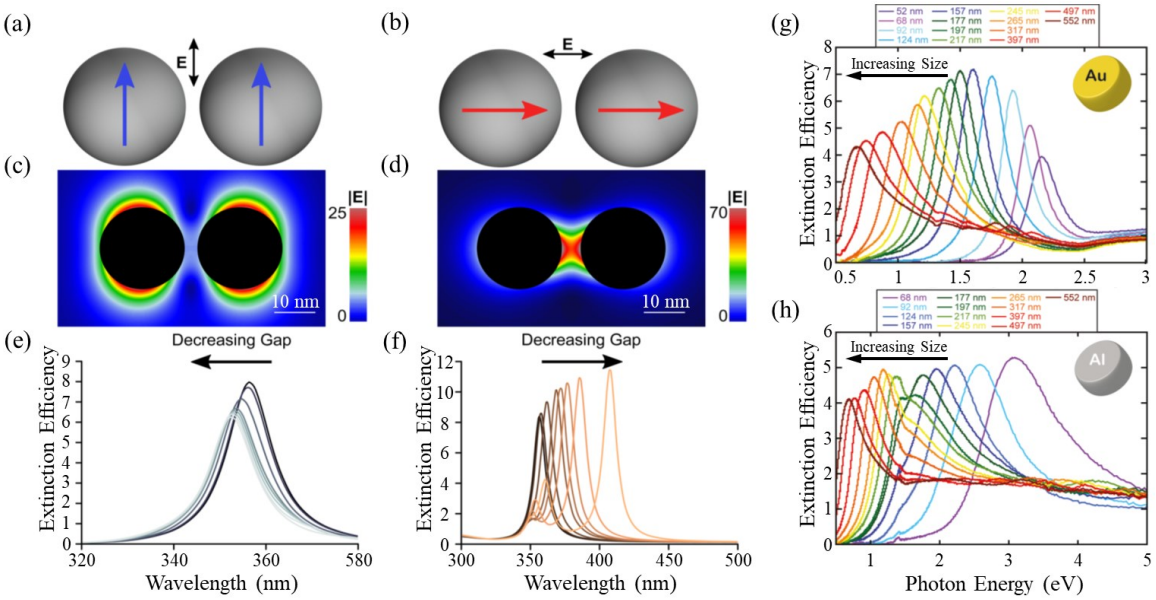

Figure 1.34: (a-f) Numerically modeled spherical nanoparticle dimers with varying gap sizes, exhibiting plasmonic coupling. (a) Light polarized perpendicular to the dimer axis, displaying destructive interference. (b) Light polarized parallel to the dimer axis, displaying constructive interference. Electric field maps showing (c) destructive interference and (d) constructive interference for 20 nm diameter Ag spherical nanoparticles separated by 5 nm. Extinction spectra for the same nanoparticles with light polarized (e) perpendicular to the dimer axis, and (f) parallel to the dimer axis. The gap sizes are 1, 2, 3, 4, 5, 10, 20, 30, 40, and 50 nm from lightest color to darkest color [263]. Experimentally measured extinction spectra for nanodisk arrays with labeled particle sizes for (g) Au, and (h) Al. The separation between nanodisks were random, with the smallest center-to-center distance of 6 nanodisk diameters [272].

Nanoholes in thin metal films can also sustain localized plasmon resonances (LPRs), aligning with Babinet's principle [278-281]. This principle states that the diffraction pattern generated by an opaque body is akin to that produced by a hole of identical shape and size, differing only in the intensity of the forward beam [282]. Consequently, there are parallels between the modes supported by arrays of metallic nanoparticles, and nanohole arrays thin metallic films. Additionally, the existence of a thin metallic layer alters the interaction between adjacent resonators due to the PSP mode supported by the film. Furthermore, hole arrays can demonstrate an alternative form of collective plasmon resonance, in which individual hole resonances are coupled by PSP waves. These resonances typically have broader spectra than standard SLRs [243].

1.6.2. Plasmonic Effects on Transmission, Reflection, and Absorption

Plasmonic effects in nanoparticles and nanoholes also leads to phenomena such as a dramatic enhancement of absorption, transmission, or reflection. Fig. 1.35 displays one such example for numerically modeled 20 nm nanoparticles placed in a hexagonally close packed orientation in a dielectric medium with refractive index n = 1.33. The first row describes these effects for Au nanoparticles, while the second row describes these effects for Ag nanoparticles. The Au nanoparticles plasmonic response is attenuated by interband transitions, attributed to the low interband transition energy of Au at 2.3 eV, aligning with the wavelength range of visible light [283, 284]. However, the interband transition energy of Ag at 3.7 eV necessitates significantly higher energy, aligning with ultraviolet (UV) light. Therefore, the Ag nanoparticles plasmonic response when illuminated with visible light is unaffected by direct interband transition losses, leading to more efficient plasmonic excitation [285].

With an increase in the interparticle gap, the coupling between particles weakens, leading to a decrease in the strength of the lattice resonance. Simultaneously, individual plasmon modes become increasingly prominent. Therefore, the plasmon resonance red-shifts as the nanoparticles move closer together. At small interparticle distances, transmittance is low, but it is primarily the reflectance that increases substantially as the resonance broadens. As the interparticle gap decreases, stronger plasmonic coupling becomes apparent in Ag nanoparticles, as indicated by the broad dips observed in transmittance and broad peaks in reflectance. Additionally, Ag nanoparticles require a greater distance compared to Au nanoparticles to become fully decoupled. This phenomenon is attributed to the far-field coupling of Ag nanoparticles [285].

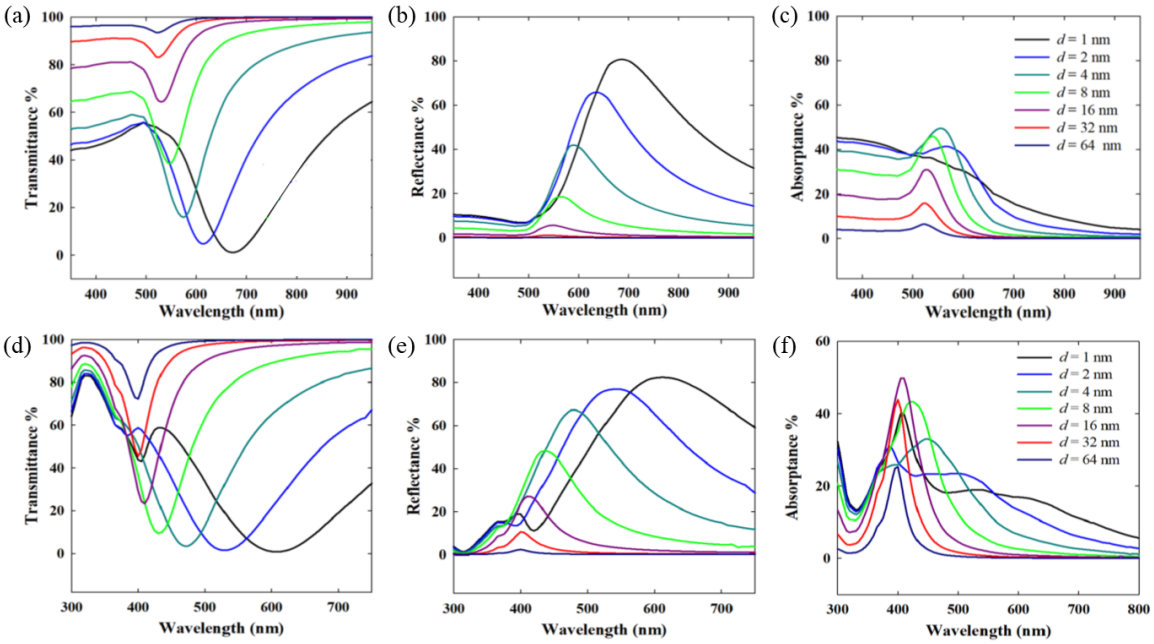

Figure 1.35: Numerically modeled monolayer of hexagonal close packed arrays consisting of 20 nm diameter nanoparticles in a dielectric medium with n = 1.33. The arrays were illuminated at normal incidence, and the separation between the particles d was varied. (a) Transmittance, (b) reflectance, and (c) absorptance data for Au nanoparticles. (d) Transmittance, (e) reflectance, and (f) absorptance data for Ag nanoparticles [285].

When the surrounding medium is a dielectric, the plasmonic nanoparticles and the medium both polarize in response to the incident field, enhancing interparticle coupling [286, 287]. However, in a vacuum with n = 1, the absence of a dielectric environment suppresses interparticle coupling. Therefore, nanoparticles become isolated from interparticle interactions after only a short interparticle distance.

A comparison of Fig. 1.35(d,f) reveals two distinct features in the transmittance and absorptance spectra for interparticle gaps of 1 nm or 2 nm. In the case of a 1 nm interparticle gap, a small shoulder is observed at approximately 400 nm in both the transmittance and reflectance spectra. Additionally, the lowest transmittance dip occurs at 600 nm, while the absorptance exhibits the highest peak at around 400 nm, accompanied by a broad band at 600 nm. Therefore, the absorption peak at 400 nm suggests a strong plasmon resonance

that relaxes non-radiatively. For an interparticle gap of 2 nm, this peak in the transmittance, absorptance, and reflectance spectra is considerably weaker [285].

Clearly, plasmonic properties are influenced by size, shape, material, and the background medium [250, 288], of which significantly impact transmission, reflection, and absorption. Another example of this is shown in Fig. 1.36 regarding the absorption properties of Au nanobars. The polarization of incident light also affects absorption, scattering, and local-field enhancements at resonant wavelengths [251, 289, 290]. Au nanobars demonstrate minimal radiation damping because of their relatively small volume [289], resulting in significant light scattering efficiency. These properties make nanorods particularly appealing for optical applications [289].

COMSOL simulations were used to numerically model the absorption of 3-D Au nanobars with 100 nm length, 60 nm width, and varying thickness from 8 - 60 nm, as shown in Fig. 1.36. The substrate was Si, but the nanobars were modeled by approximating an effective SiO_2 medium surrounding the nanobars with n_{eff} = 1.25 [292-295]. Light was normally incident on the nanobar's surface, with the electric field polarized either longitudinally or transversely, as displayed in the insets of Fig 1.36(a,b).

As the thickness of the nanobars increases, the absorption peaks blue-shift for both polarizations. For transverse polarization, the maximum absorption drops rapidly until a thickness of 20 nm, with minimal change in amplitude afterwards. For longitudinal polarization, the maximum absorption rapidly decreases and stabilizes at higher thicknesses. The dominant peaks in the spectrum are associated with the dipolar resonant plasmonic mode, while the minor peaks at shorter wavelengths arise from higher order modes [291]. Additionally, the spectrum's FWHM shrinks with reducing thickness.

Furthermore, the wavelengths where there exists a resonance peak have significantly differing absorption amplitude locations between the two polarizations for the same Au thickness. In the case of transverse polarization, the absorption exhibits a diminished amplitude compared to longitudinal polarization. This occurs because the plasmonic response relies on the length aligned with the electric field [296].

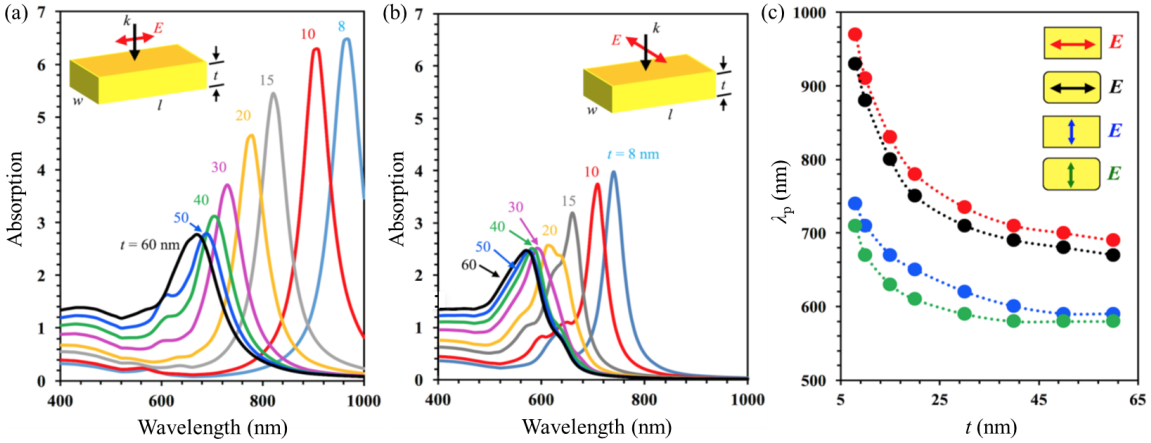

Figure 1.36: Numerically modeled Au nanobar absorption spectrum for width w = 60 nm, length l = 100 nm, and varying thickness t. Absorption plots as a function of wavelength where incident light is either (a) longitudinally or (b) transversely polarized. (c) Plot depicting the peak resonance wavelength as a function of thickness for both polarizations, as well as the impact rounded corners have on the peak resonance wavelength [291].

Numerous studies on nanobars have found that increasing the nanobar length red-shifts the resonance peaks [297, 298]. This shift occurs as a result of the k-vector's direction. When the k-vector is perpendicular to the length, this red-shift occurs. However, when the k-vector is parallel to the length, the resonance peaks blue-shift with increasing thickness [291]. When electrons are polarized along the long axis, they have a bigger area to oscillate in and therefore take an increased time to complete an oscillation. This results in a lower frequency and a longer resonance wavelength compared to polarization along the short axis [299].

It's important to mention that real nanobars will have round corners because of fabrication limitations. Fig. 1.36(c) depicts the impact rounded corners have on the peak resonance wavelength for longitudinal and transverse polarizations as a function of thickness. Round corner nanobars exhibit a resonance wavelength that is blue-shifted by 10 to 40 nm compared to sharp corner nanobars [291]. This blue-shift results from the reduced effective dimension along the rounded sides, as well as the modified charge distribution because the charges are more dispersed in round corner nanobars [300]. For small nanobar thicknesses, the plasmon dipole mode charges are trapped at the corners and edges, which creates localized hot spots. For large thicknesses, the surface charge dipole plasmonic mode are evenly spread across the nanobar's surface. In this situation, the surface charges are weakly confined, which results in a weak enhancement. Round corner nanobars build up less electric charge in the corners than the sharp corner case, which reduces the plasmonic enhancement [291]. This phenomenon is crucial to consider when engineering plasmonic nanobars.

In this dissertation, a basic understanding of plasmonic effects is essential because the retroreflector researched is designed for a HeNe wavelength of 632.8 nm, utilizes thin Au, and has nanometer scale dimensions. Therefore, it operates in the visible regime and plasmonic effects are expected. Additionally, thin metal films display significantly different properties from their bulk counterparts, and thus 3-D FDTD numerical modeling is required in order to understand the impact these thin metal layers have on the retroreflectivity [301-306].

1.7. Statement of Goals

In this dissertation, methods of enhancing IR photodetector FPAs through integration with Si micropyramidal arrays are investigated, as well as novel metamaterial retroreflecting arrays designed to optimize the retroreflection of both TE and TM polarizations simultaneously in the visible wavelength regime. Regarding enhancing FPAs, reducing the dimensions of the photodetectors decreases both the dark current and junction capacitance, thereby enhancing sensitivity. However, this downsizing can also reduce QE due to less effective light coupling, potentially hindering detection performance. The light collection efficiency can be improved using light-concentrating structures such micropyramids which are placed over individual pixels. This allows light to be collected from a larger area and concentrated into a much smaller area that can be aligned with the photodetector's mesa to maintain or enhance the SNR in order to increase the operating temperature of FPAs. In addition to extensive research conducted on enhancing FPAs through integration with truncated Si micropyramid arrays, metasurface retroreflectors designed for visible wavelengths were investigated. These structures can consist of either dielectric or metallic materials, or some combination thereof. Metasurfaces are able to have a low profile and can be an inexpensive solution to retroreflect light at specific designed angles. Additionally, it remains rare to achieve a combination of a flat profile, high reflection efficiency, and a wide range of incidence angles in an ultrathin metasurface retroreflector capable of operating for both TE and TM modes.

In Chapter 2, anisotropic wet etching of Si for photonic applications was explored by fabricating micropyramidal arrays with different geometries, sidewall angles, and number of sidewalls. The key advantage of Si in MEMS is its compatibility with IC

fabrication processes, enabling the integration of mechanical, electrical, and computational functionalities onto a single chip. MEMS fabrication involves a series of processes such as lithography, deposition, and etching. Among these, wet etching is a crucial step that selectively removes material from Si wafers, allowing the formation of intricate structures with high precision. This chapter will discuss the role the wafer orientation has in the sidewall angle of the fabricated structure. It will discuss over etching and the role of surfactant, how the orientation of the photoresist patterns affects the final fabricated structure, and will depict several examples of fabricated mesophotonic arrays for optical applications.

In Chapter 3, the applications stemming from the unique optical properties of anisotropically wet etched Si micropyramids are investigated in the mesoscale regime by employing Ansys/Lumerical's 3-D FDTD numerical modeling software. Mesoscale denotes objects, like micropyramids, with geometric dimensions on the order of the incident wavelength of light. These objects exhibit different optical properties through light-matter interactions as their geometry varies. When micropyramids are much larger than the wavelength of light, the properties of the micropyramids follow the laws of geometrical optics, which is well understood. The diverse properties of mesoscale objects offer a wide array of applications. The focus in this Chapter lies on exploring the optical characteristics and potential uses of micropyramidal structures featuring mesoscale dimensions. The ability of micropyramids to concentrate light stems from the reflections facilitated by their sidewalls. These characteristics are commonly termed as non-imaging light concentration properties, distinguishing them from the focusing effects of lenses. The light-concentration ability typically exhibits a non-resonant nature. However, the optical

properties of a micropyramidal array can also lead to various interference effects. Such arrays can be treated as a transmission grating. The optical properties of mesoscale structures depend on their geometry, and the properties of truncated pyramids have been relatively unstudied. From an application development perspective, mesoscale structures of this nature hold considerable promise and appeal.

In Chapter 4, the light-concentration ability of Si micropyramids are experimentally investigated by monolithically integrating MWIR PtSi photodetectors directly on top of the truncated micropyramids. This was done to experimentally determine if reducing the dimensions of the photodetectors reduces the dark current, while the light collection efficiency can be improved using light-concentrating micropyramids. This allows light to be collected from a larger area and concentrated into a much smaller area that can be aligned with the photodetector's mesa to maintain or enhance the SNR in order to increase the operating temperature of FPAs. This required an extensive fabrication effort that was discussed. Additionally, a detailed analysis of the micropyramid FPA was conducted through characterizing the fabricated devices' spectral response and QE in order to determine the enhancement obtained through integration with micropyramids. Furthermore, a novel way to further enhance the SNR through utilizing a silicon-on-insulator wafer to create a resonator cavity was discussed.

In Chapter 5, extensive FDTD numerical modeling was completed for a Littrow configuration metamaterial retroreflector studied with FDTD numerical modeling designed for a HeNe wavelength of 632.8 nm in order to develop fabrication guidelines for retroreflectors operating in the visible regime. Additionally, numerical modeling was extended to real metals with real thicknesses in order to study the impact the type of metal

has on retroreflection, as well as how the thickness of the metal layer impacts retroreflection efficiency. The retroreflector has nanometer scale dimensions, and thus plasmonic effects are expected. Real metals at optical frequencies display substantial plasmonic effects, which can drastically affect retroreflector performance.

CHAPTER 2: SI ANISOTROPIC WET ETCHING FOR PHOTONIC APPLICATIONS

2.1. Introduction

In this dissertation, methods to enhance IR photodetector FPAs by integrating them with truncated Si micropyramidal arrays are explored. Understanding the intricate fabrication steps for these arrays is crucial. By reducing the photodetector dimensions, the dark current is decreased, and light collection efficiency is improved through light-concentrating structures like truncated Si micropyramids positioned over individual pixels. These structures gather light from a larger area and concentrate it into a much smaller area, aligning with the photodetector's mesa to maintain or enhance the SNR. As dark current noise rises with thermal energy, maintaining SNR through shrinking the photon detectors and integrating light-concentrating structures allows for an increase in the operating temperature of FPAs.

The microelectromechanical systems (MEMS) community has long recognized Si anisotropic wet etching as a significant technique for fabricating micromachined free-standing 3-D structures like beams, membranes, cavities, grooves, through holes, and mesas. MEMS fabrication involves a series of processes such as lithography, deposition, and etching. Among these, wet etching is a crucial step that selectively removes material from Si wafers, allowing the formation of intricate structures with high precision. The key advantage of Si in MEMS is its compatibility with IC fabrication processes, enabling the

integration of mechanical, electrical, and computational functionalities onto a single chip. Using an etchant like tetramethylammonium hydroxide (TMAH), a range of 3-D geometries can be fabricated in Si wafers with different crystallographic orientations, such as (100), (110), and (111) [148, 150, 153, 154, 161, 164, 165, 171, 173]. Interest in this technology has been fueled by its swift etching speed, fabrication reproducibility, and the wide variability of 3-D micromachined geometries that can be constructed in Si wafers. Efforts to leverage the cost-effective and straightforward Si anisotropic wet etching ability for photonics applications have an extensive background, starting with the suggestion to use pyramidally textured surfaces for light trapping to boost the efficiency of solar cells [309, 310]. Numerous other ideas have been proposed, including the development of micromirrors [176] as well as interconnecting components and optical switching [311-313].

This chapter highlights a unique and important fabrication capability of Si anisotropic wet etching technology for creating mesophotonic arrays through utilization of periodically designed photomasks. The primary advantage of this technology lies in its self-terminating nature. Etching through the openings in a transferred square photomask pattern aligned to the <110> crystalline directions enables increasingly deeper V-groove shaped channels in the (100) Si wafer, with sidewalls parallel to the low etch rate (111) crystalline planes, forming a fixed 54.74° sidewall angle with the (100) Si wafer. Notably, the etching process significantly slows when two adjacent low etch rate planes intersect, forming the V-groove. Although the etching can continue by gradually undercutting the transferred square photomask pattern, this process can be substantially slowed down through utilization of various additives, such as a surfactant like Triton X-100 in TMAH etching [148]. This self-terminating property ensures that, even with nonuniform etch rates

at earlier stages, the final geometry remains remarkably uniform, enabling the formation of Si micropyramids or inverted Si micropyramids over large wafer areas. This capability is highly attractive for optics and optoelectronics applications.

Another appealing characteristic is the exceptionally smooth nature of the (111) sidewall surfaces of the fabricated structures; an intrinsic property of Si anisotropic wet etching. This smoothness minimizes incoherent light scattering caused by surface defects. Given the high optical quality of these structures, their optical properties can be accurately numerically modeled for objects with perfect geometries. Therefore, each Si micropyramid can function as a light-concentrating structure in photon detection applications [25, 94-100, 102-104, 109, 110].

In Chapter 2, Si anisotropic wet etching with 25% TMAH for photonic applications is explored by fabricating Si micropyramidal arrays with different geometries, sidewall angles, and number of sidewalls. Section 2.2 discusses the Si mesophotonic array fabrication protocol, as well as the role of the surfactant Triton X-100. Section 2.3 depicts several examples of fabricated Si mesophotonic arrays for optical applications and discusses the role the photoresist patterns orientation plays in the final sidewall angles of the fabricated structures. Additionally, this section will cover the role Triton X-100 plays for each of these structures. Afterwards, section 2.4 discusses Triton X-100 utilization considerations, and the potential defects that arise from excessive usage. This work demonstrates that Si micropyramidal photonics serve as a versatile optoelectronic platform capable of enhancing the SNR and increasing the operational temperature of MWIR FPAs.

2.2. Si Mesophotonic Array Fabrication Protocol

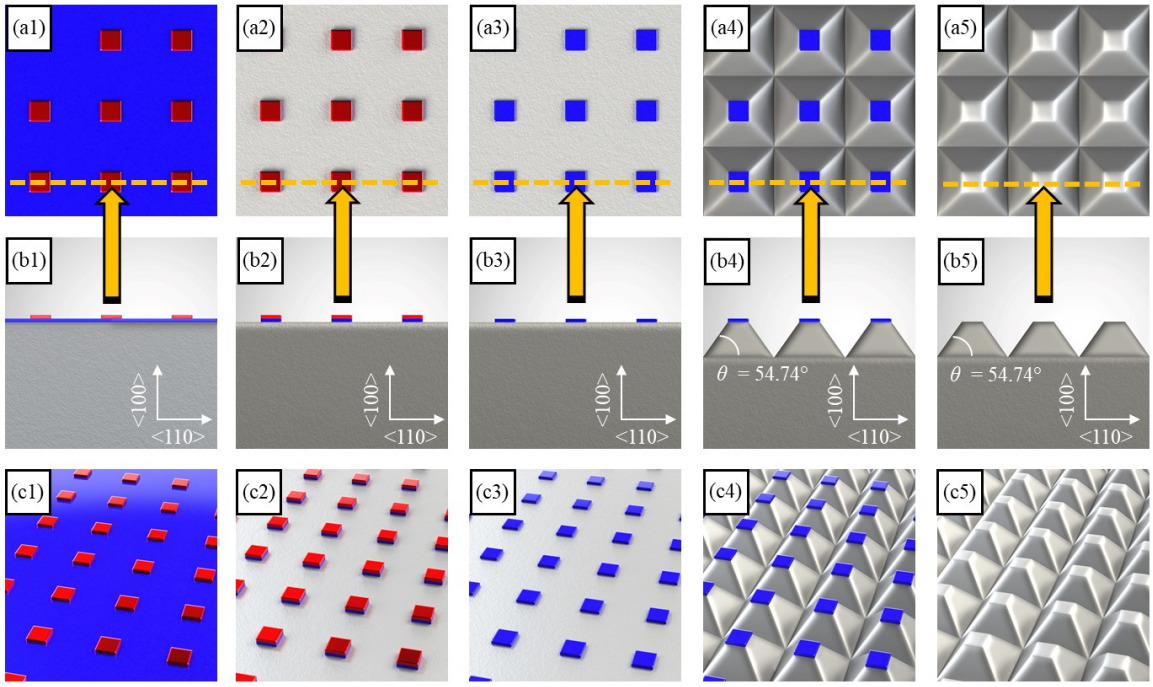

Figure 2.1. Diagram depicting the universal Si mesophotonic array fabrication protocol, where each fabrication step corresponds to a column, and each row corresponds to a point-of-view. The example structures are truncated Si micropyramids with $\theta = 54.74^{\circ}$ sidewall angles formed along the (111) crystalline planes through anisotropic wet etching a (100) Si wafer with 25% TMAH. Row (a) depicts a top-down perspective. Row (b) depicts a sideview perspective. Row (c) depicts an arial view. Step 1, depicted in the first column, is to perform photolithography shown in red to define the structure's geometry on a (100) Si wafer shown in grey with a thermal SiO_2 layer shown in blue. Step 2, depicted in column 2, is to transfer the photolithography pattern to the SiO_2 layer through a buffered oxide etchant (BOE) etch. Step 3, depicted in column 3, is to remove the photoresist in order to prevent changing the etching characteristics of TMAH. Step 4, shown in column 4, is to anisotropically wet etch the mesophotonic arrays. Step 5, shown in column 5, is to remove the leftover SiO_2 layer with a second BOE etch. The final result is a mesophotonic array which, in this case, is a truncated Si micropyramid array.

The utilization of 25% TMAH for Si anisotropic wet etching to create mesophotonic arrays offers numerous advantages and is relatively straightforward to implement in practical fabrication. Si anisotropic wet etching in 25% TMAH allows for the parallel fabrication of numerous identical mesophotonic structures with fixed sidewall angles, facilitated by aligning the photomask pattern with Si's crystalline planes. The process features a rapid etch rate where the resulting (111) sidewalls are atomically smooth,

crucial for optical applications. This method can be employed to create various 3-D light-concentrating Si mesophotonic arrays. While the fabrication protocols for these structures are generally similar, unique mesophotonic arrays are produced depending on whether the surfactant Triton X-100 was used during the Si anisotropic wet etch step, as well as how the mask pattern is aligned to Si's crystalline planes.

Understanding these steps is essential to grasp how the Si mesophotonic arrays depicted in this chapter were fabricated. The universal Si mesophotonic array fabrication protocol is shown in Fig. 2.1. The fabrication process starts with a double-side polished (DSP) (100) Si wafer with thermal SiO_2. The entire wafer underwent thorough cleaning followed by a dehydration bake process. The backside of the wafer was covered with a thick photoresist layer and baked in an oven to safeguard it from the buffered oxide etchant (BOE) utilized subsequently in the second and fourth steps, as depicted in Fig. 2.1 columns 2 and 4. This precaution ensures that the polished surface remains intact and is not etched.

The initial step involves photolithography to define the geometry and orientation of the photoresist pattern, as depicted in Fig. 2.1 column 1, thereby determining the resulting sidewall angles θ after anisotropic wet etching the Si wafer. The sides of the square photoresist caps, in this case, are aligned parallel to the <110> directions of the (100) Si wafer. Following this, the wafer underwent a 4-minute O_2 plasma ash in a plasma asher to ensure complete removal of any residual photoresist that might not have been cleared during the initial development process, promoting uniform etching conditions. Subsequently, the Si wafer was then ready for the isotropic wet etching process, as depicted in Fig. 2.1 column 2. In the second step, the Si wafer undertook a BOE etch to transfer the photoresist pattern onto the thermal SiO_2 layer, as depicted in Fig. 2.1 column 2. This was

followed by stripping the photoresist pattern using a solvent as the third step, depicted in Fig. 2.1 column 3. In the fourth step, the sample was subjected to anisotropic wet etching using 25% TMAH heated to 80° C, as depicted in Fig. 2.1 column 4. This step was conducted on a temperature-controlled hotplate with a temperature probe inside the glass container equipped with a lid containing a small hole to control water evaporation from the TMAH bath. This measure was taken to prevent variations in TMAH concentration, which can affect its etching characteristics. The etch rate of 25% TMAH at 80° C was determined to be ~0.40 μm/minute into the substrate, consistent with values reported in the literature for a (100) Si wafer [150]. In the fifth step, the oxide layers on top of the truncated Si micropyramids were removed through a second BOE etch, depicted in Fig. 2.1 column 5.

Triton X-100 was employed for specific etched geometries to reduce the TMAH undercutting rate of the thermal SiO_2 layer. It was added to the etching bath through a small hole in the lid using a syringe after stabilizing the TMAH's temperature at 80° C. The solution was agitated using a stir bar. However, during the anisotropic wet etch, the stir bar was not used to maintain the effectiveness of Triton X-100 in reducing the undercutting. Typically, concentrations of surfactant added range from 0.1% to 0.3% per volume of TMAH (v/v), with 0.1% v/v being the recommended concentration [150, 154, 173, 174]. The Triton X-100 quantity added was increased to 0.2% v/v, in order to compensate for longer etching times due to water evaporation and subsequent TMAH concentration increase. In practice, this issue can be mitigated using a reflux condenser. Furthermore, the Si wafers were etched upside-down to ensure uniform distribution and prevent excess Triton X-100 from settling on the SiO_2 patterns. If excessive Triton X-100 is added to the 25% TMAH etching bath, various defects can form. These are discussed in section 2.4.

The fabrication steps depicted in Fig. 2.1 outline a standard process for producing mesophotonic arrays of various geometries, including Si micropyramidal arrays with sidewall angles $\theta = 54.74°$, as shown in Fig 2.2.

2.3. Si Mesophotonic Arrays Fabricated with 25% TMAH

By employing the fabrication protocol described in section 2.1, five distinct types of Si mesophotonic arrays were quickly anisotropically wet etched along various crystalline planes, showcasing the technology's usefulness as seen in Fig. 2.2, Fig. 2.3, and Fig. 2.4. Specifically, Fig. 2.2 presents SEM images of truncated Si micropyramids with a square cross-section and sidewall angles $\theta = 54.74°$. Fig. 2.3 shows SEM images of truncated Si microcones with an octagonal cross-section and sidewall angles $\theta = 45°$. In Fig. 2.4, the three columns correspond to different mesophotonic arrays: column 1 features SEM images of inverted Si micropyramids with a square cross-section and sidewall angles $\theta = 54.74°$, column 2 includes SEM images of inverted Si micropyramids with a square cross-section and $\theta = 45°$, and column 3 displays SEM images of inverted triangular micropyramids with varying sidewall angles. For all these structures, a stir bar was used to mix the TMAH and Triton X-100 solution, but no stir bar was utilized during the etch.

The 3-D geometry of the mesophotonic arrays depicted in these figures were controlled by changing and positioning the photoresist patterns to different Si crystalline planes, and through including or not including the surfactant Triton X-100 during the anisotropic wet etching step with 25% TMAH at 80° C. Anisotropic wet etching with 25% TMAH is a versatile technique that facilitates the large-scale fabrication of various types of mesophotonic structures. Specifically, the Si mesophotonic arrays were fabricated

through the following steps, demonstrating how various geometries can be created with minimal adjustments and highlighting the important role of Triton X-100 in forming certain types of arrays.

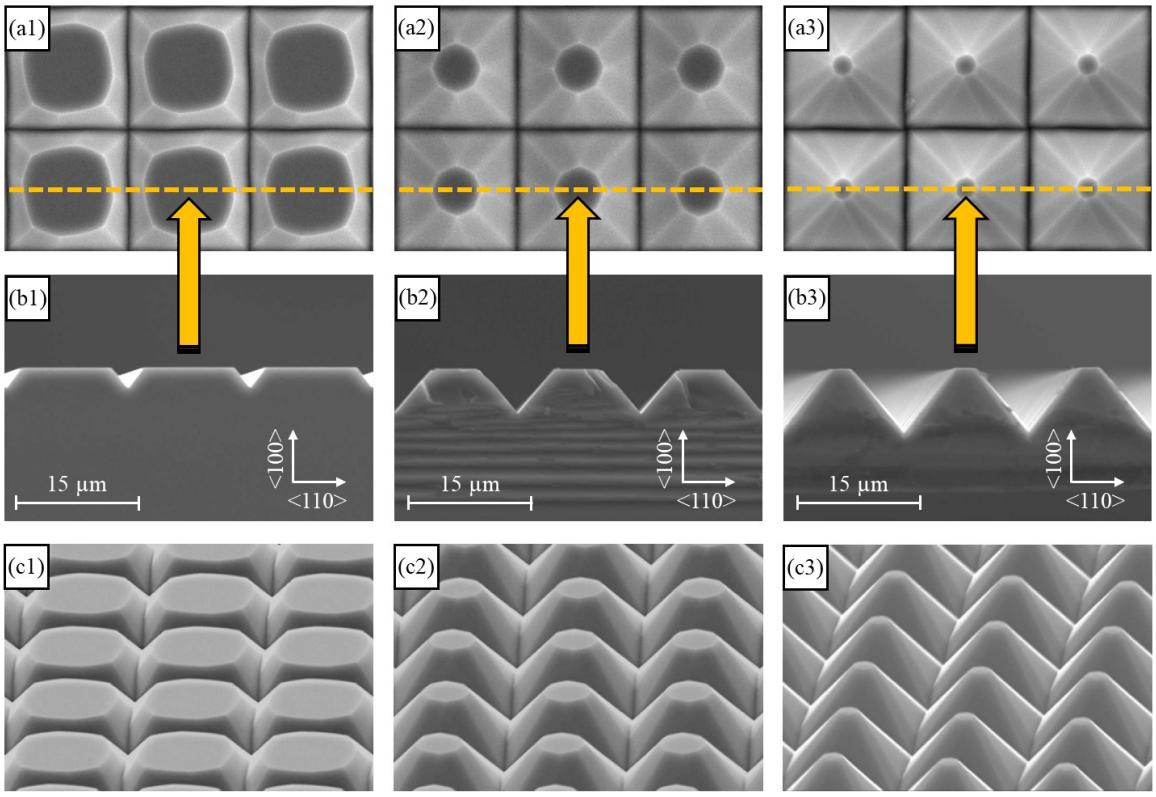

Figure 2.2. SEM images of truncated Si micropyramid arrays with $\theta = 54.74^{\circ}$, 15 µm pitch, and a square cross section fabricated by anisotropic wet etching in 25% TMAH with added Triton X-100, as depicted in Fig. 2.1. Row (a) consists of SEM images from a top-down perspective. Row (b) consists of the corresponding cross-sectional side view. Row (c) consists of SEM images from an arial view to display their 3-D nature. Column 1 contains SEM images corresponding to truncated Si micropyramids with ~11.0 µm small base. Column 2 contains SEM images corresponding to truncated Si micropyramids with ~6.0 µm small base. Column 3 contains SEM images corresponding to truncated Si micropyramids with ~2.5 µm small base. A stir bar was used to mix the TMAH and Triton X-100 solution, but no stir bar was utilized during the etch.

Fig. 2.2 shows SEM images of 15 µm pitch truncated Si micropyramids with sidewall angles $\theta = 54.74^{\circ}$, a square cross-section, and three different small base sizes of ~11.0, 6.0, and 2.5 µm for columns 1, 2, and 3, respectively. These three completely different sized truncated Si micropyramids were created through utilizing the generic

fabrication protocol in Fig. 2.1, with Triton X-100 added to the TMAH bath and the square photoresist patterns aligned to the <110> crystalline directions. Without adding the surfactant Triton X-100, fabrication of such structures becomes difficult due to the severe undercutting of the SiO_2 mask during the anisotropic wet etch step.

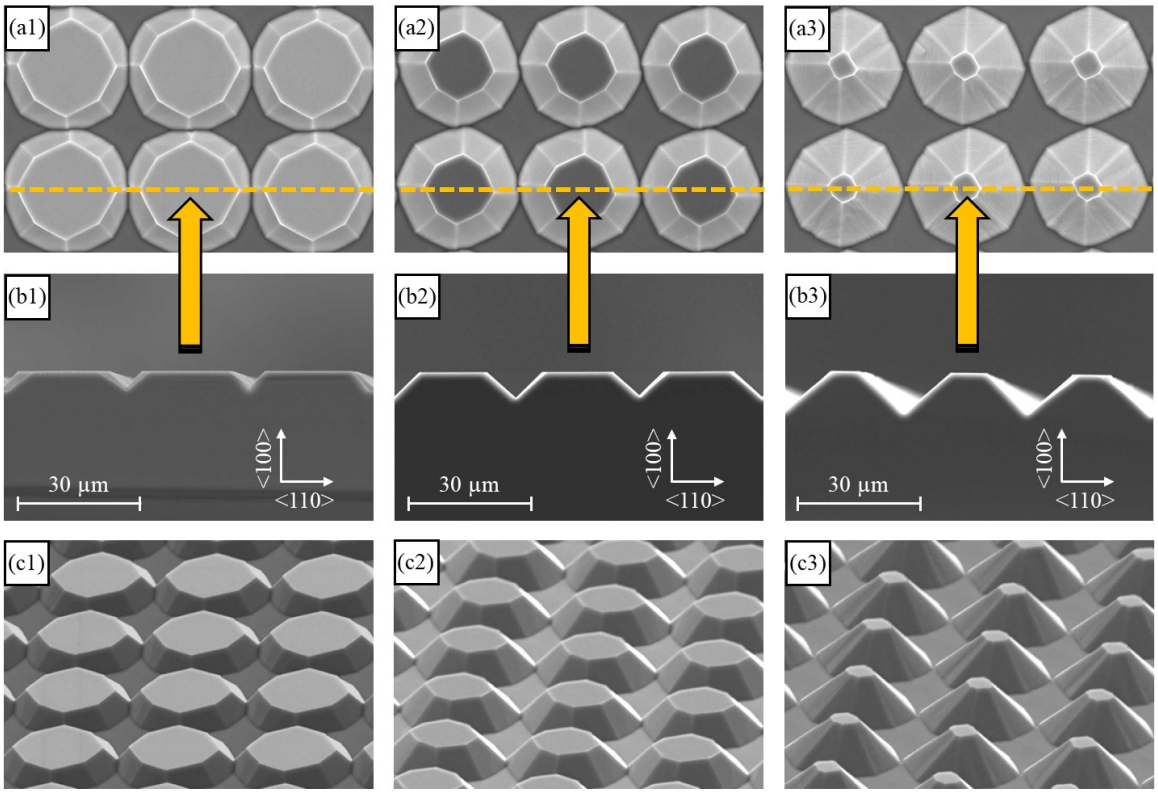

Figure 2.3. SEM images of truncated Si microcone arrays with $\theta = 45^{\circ}$, 30 µm pitch, and an octagonal cross section fabricated by anisotropic wet etching in 25% TMAH at 80° C without added Triton X-100, as depicted in Fig. 2.1. Row (a) consists of SEM images from a top-down perspective. Row (b) consists of the corresponding cross-sectional side view. Row (c) consists of SEM images from an arial view to display their 3-D nature. Column 1 contains SEM images corresponding to microcones with ~23.0 µm small base. Column 2 contains SEM images corresponding to microcones with ~16.0 µm small base. Column 3 contains SEM images corresponding to microcones with ~6.0 µm small base. A stir bar was used to mix the TMAH and Triton X-100 solution, but no stir bar was utilized during the etch.

Fig. 2.3 shows SEM images of 30 µm pitch truncated Si microcones with sidewall angles $\theta = 45^{\circ}$, an octagonal cross-section, and three different small base sizes of ~23.0, 16.0, and 6.0 µm for columns 1, 2, and 3, respectively. These three completely different

sized truncated Si microcones were created through utilizing the generic fabrication protocol in Fig. 2.1 but without the addition of Triton X-100 nor the need for alignment to the <110> directions, resulting in considerable undercutting of the original 25 μm square SiO_2 pattern. This highlights the crucial role of Triton X-100 in reducing the undercut rate of 25% TMAH for structures sticking out from the Si wafer's surface.

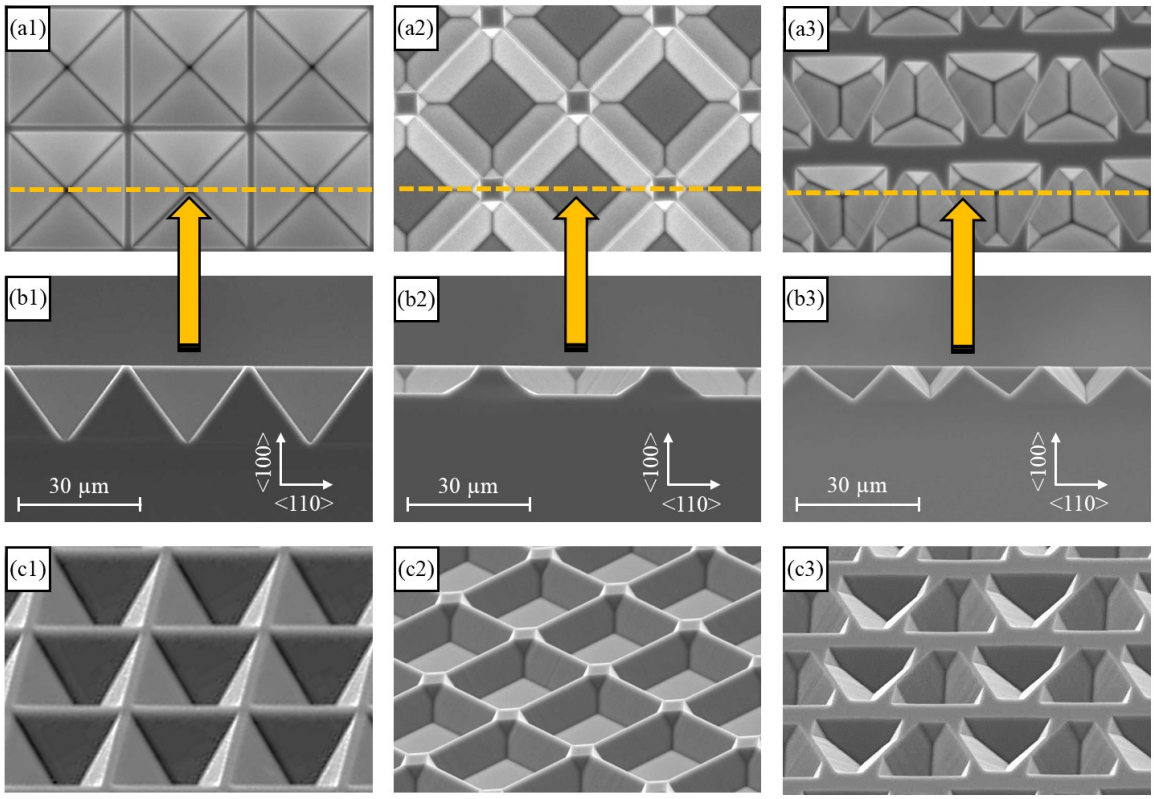

Figure 2.4. SEM images of three types of inverted Si mesophotonic arrays fabricated by anisotropic wet etching in 25% TMAH, as depicted in Fig. 2.1. Each column is associated with a unique mesophotonic array, and each row corresponds to images of the same type. Row (a) consists of SEM images from a top-down perspective. Row (b) consists of the corresponding cross-sectional side view. Row (c) consists of SEM images from an arial view to display their 3-D nature. Column 1 contains SEM images corresponding to inverted micropyramids with θ = 54.74˚, 30 μm pitch, nanometer scale small base, and a square cross section. Column 2 contains SEM images corresponding to inverted micropyramids with θ = 45˚, 30 μm pitch, 14.7 μm small base, and a square cross section. Column 3 contains SEM images corresponding to inverted triangular micropyramids with different sidewall angles θ. One side of the equilateral triangular photomask was aligned to the <110> direction which resulted in θ = 54.74˚ and is ~21.8 μm long, while the other two sides of the photomask were aligned to a different direction which resulted in θ = ~48˚ and are ~14.3 μm long. A stir bar was used to mix the TMAH and Triton X-100 solution, but no stir bar was utilized during the etch.

Fig. 2.4 shows three sets of SEM images in each of the three columns, corresponding to three different types of inverted Si micropyramids capable of being fabricated through utilizing TMAH anisotropic wet etching. The first column shows 30 μm pitch inverted Si micropyramids where the 25 μm photoresist square was aligned with the <110> crystalline directions, resulting in sidewall angles $\theta = 54.74^{\circ}$, a square cross-section, and nanometer scale tips. Whether Triton X-100 was utilized or not in this instance, the resulting structures would maintain a comparable geometry due to the differences between convex and concave undercutting with TMAH [173, 174]. The second column shows 30 μm pitch inverted Si micropyramids where the 25 μm photoresist square was aligned with the <100> crystalline directions, resulting in sidewall angles $\theta = 45^{\circ}$, a square cross-section, and 14.7 μm small base size. Triton X-100 was utilized during this wet etch.

Lastly, the third column in Fig. 2.4 shows inverted triangular micropyramids with different sidewall angles and lengths. One side of the equilateral triangular photomask was aligned to the <110> crystalline direction which resulted in a sidewall angle $\theta = 54.74^{\circ}$ and is ~21.8 μm long, while the other two sides of the photomask were aligned to a different direction which resulted in sidewall angles $\theta = \sim 48^{\circ}$ and are ~14.3 μm long. The utilization of Triton X-100 enabled all three sides to be etched, resulting in the fabrication of the displayed inverted triangular Si micropyramid array. However, if Triton X-100 had not been utilized, the two sides of the triangle not aligned with the <110> direction would have experienced significant undercutting during the TMAH etching process, leading to the formation of horizontal trenches parallel to the <110> crystalline direction.

These last three arrays illustrate the essential role of Triton X-100 in anisotropic wet etching mesophotonic structures that are not aligned with the <110> crystalline

directions. This technology not only facilitates the etching of various geometries, but also allows additional control over the geometry by adjusting the size of the photoresist pattern or changing the etching duration. In the case depicted in Fig. 2.2, precise control over the array geometry is enabled by the self-terminating nature of Si anisotropic wet etching. Here, the etching proceeds slowly along the (111) crystalline planes until they meet. At this stage, the etching speed significantly reduces because the undercutting of the SiO_2 mask is minimized by Triton X-100. Consequently, the sidewall angle is fixed at 54.74°, while the dimensions of the smaller base and the height of the truncated Si micropyramids are primarily determined by the size of the SiO_2 mask.

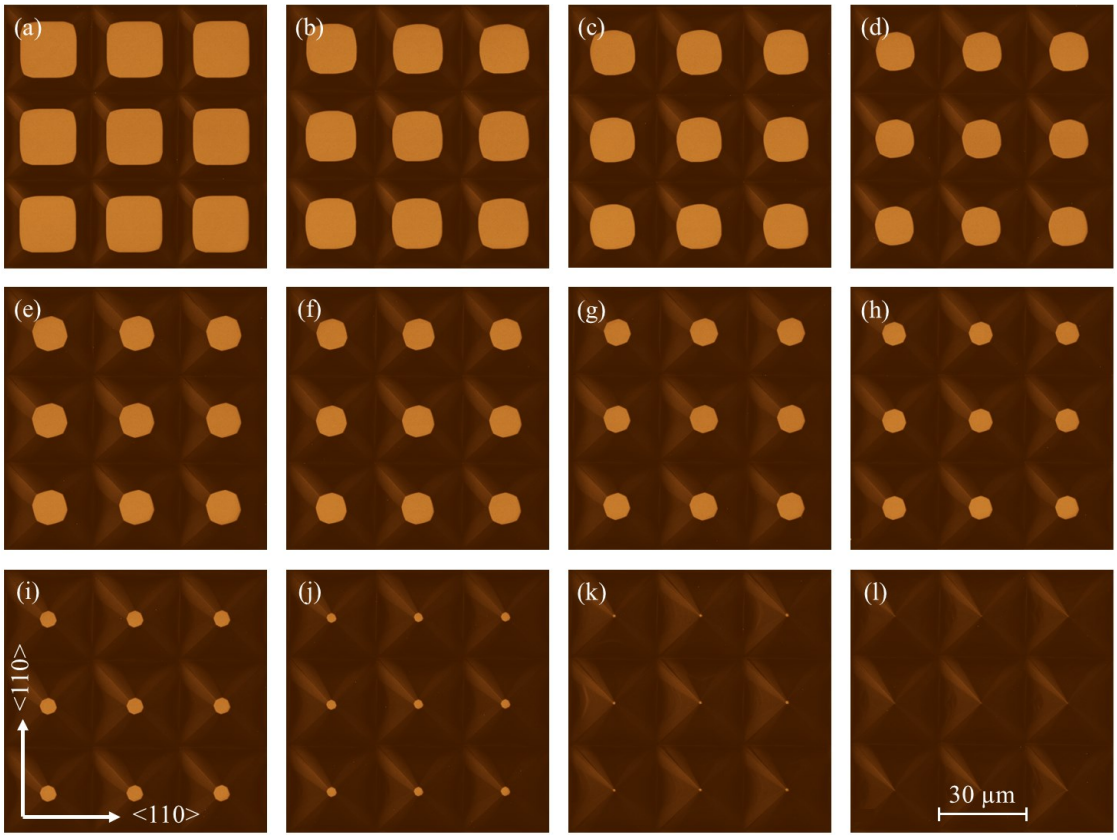

Figure 2.5. Series of confocal microscope images illustrating the ability to precisely control the geometry of the fabricated structures. The shown example is for 30 µm pitch truncated Si micropyramids with 54.74˚ sidewall angles. (a-k) Truncated Si micropyramid's small base size equal to 20.0, 18.1, 15.8, 13.5, 12.1, 10.9, 9.1, 8.4, 5.6, 3.3, and 1.0 µm respectively. (l) Si micropyramid with nanometer scale top. This fabrication control can be generalized to other mesophotonic structures. A stir bar was used to mix the TMAH and Triton X-100 solution, but no stir bar was utilized during the etch.

The ability to control the geometry of Si mesoscale structure can be seen with the example in Fig. 2.5, where twelve square cross-section truncated Si micropyramids with sidewall angles $\theta = 54.74^{\circ}$ are shown in the confocal images. By systematically reducing the size of the original square photoresist patterns with a consistent 30 μm pitch, variations in the geometry of the truncated Si micropyramids were achieved through a two fabrication cycles with two Si wafers. This is possible due to the self-terminating nature of the anisotropic wet etch process. Fig. 2.5(a-l) illustrates that as the size of the photoresist pattern decreases, the corresponding size of the truncated Si micropyramid's small base reduces while simultaneously the micropyramid's height increases, showcasing the range of achievable geometrical variations. These structures are reproducible, and etching with TMAH allows for precise geometry control under well specified etching conditions.

2.4. TMAH with Triton X-100: Utilization Considerations

From an application perspective, three key etching parameters can be used to describe any etchant: the etching rate, the surface morphology, and the corner undercutting. All three of these parameters are affected by the addition of Triton X-100 to TMAH. Triton X-100 is chosen as the added surfactant due to its nonionic nature, which preserves the CMOS compatibility necessary for fabricating monolithically integrated photodetector FPAs [157]. Additionally, Triton X-100 stays a liquid at room temperature, which enables easy measuring of the small quantities added to the TMAH bath.

The extent of undercutting differs between pure 25% TMAH and 25% TMAH with added 0.1% v/v Triton X-100, where the undercutting rate is drastically less when Triton X-100 is included. Geometries with sharp convex corners experience more undercutting

because of the appearance of high-index planes. The addition of a small amount of Triton X-100 to 25% TMAH significantly changes its etching characteristics, particularly regarding undercutting at convex corners and straight edges aligned to other crystalline directions besides the <110> direction on the (100) wafer's top surface [173, 174]. The addition of Triton X-100 drastically reduces the etch rate of orientations near the (110) planes, like the (221), (331), or (441) planes, while having minimal impact the etch rate of orientations near the (100) planes, like the (211), (311), and (411) planes [173, 174, 314]. Furthermore, the etch rate of the (100) Si plane remains nearly identical in both pure TMAH and TMAH with Triton X-100, while the (110) plane etch rate decreases substantially and becomes smoother in TMAH with Triton X-100. Additionally, 0.1% v/v Triton X-100 doesn't remarkably affect the morphology of the (100) Si plane. These etching properties enable a world of mesophotonic arrays capable of being fabricated in Si, all with CMOS compatibility.

However, as mentioned in section 2.2, the Triton X-100 quantity added to the TMAH was increased from 0.1% v/v to 0.2 - 0.3% v/v, in order to compensate for longer etching times because water would evaporate and subsequently the TMAH concentration would increase. Fig. 2.6 depicts the undercutting that occurred with 0.3% v/v Triton X-100. A series of confocal microscope images show the undercutting of a 100 nm thick thermal SiO_2 square mask layer, represented by the white squares on top of the truncated Si micropyramids. These micropyramids were fabricated using 25% TMAH with 0.3% v/v Triton X-100 at 80° C and etched for 50 minutes. The TMAH and Triton X-100 solution was mixed with a stir bar, but no stirring was performed during the etch. Convex undercutting is typically described using the undercutting ratio along the <110> crystalline

direction. The calculated undercutting ratio *l*/*d* along the <110> direction was ~0.29, where *l* represents the undercutting distance along the <110> direction of the SiO_2 mask as seen in Fig. 2.6(c), and *d* is the total etch depth. For 0.1% v/v Triton X-100 added to 25% TMAH heated to 80° C, the undercutting ratio in literature is ~0.30. For 1.0% v/v Triton X-100 added to 25% TMAH heated to 80° C, the undercutting ratio is ~0.27 [314]. Since the undercutting ratio calculated in this work is ~0.29, this indicates that increasing the Triton X-100 concentration from 0.1% v/v to 0.3% v/v does not significantly improve the undercutting ratio. The etching still resulted in large scale uniform arrays at 0.2-0.3% v/v, but at 0.3% v/v and above, surface defects were observed on the mesophotonic arrays after anisotropic wet etching.

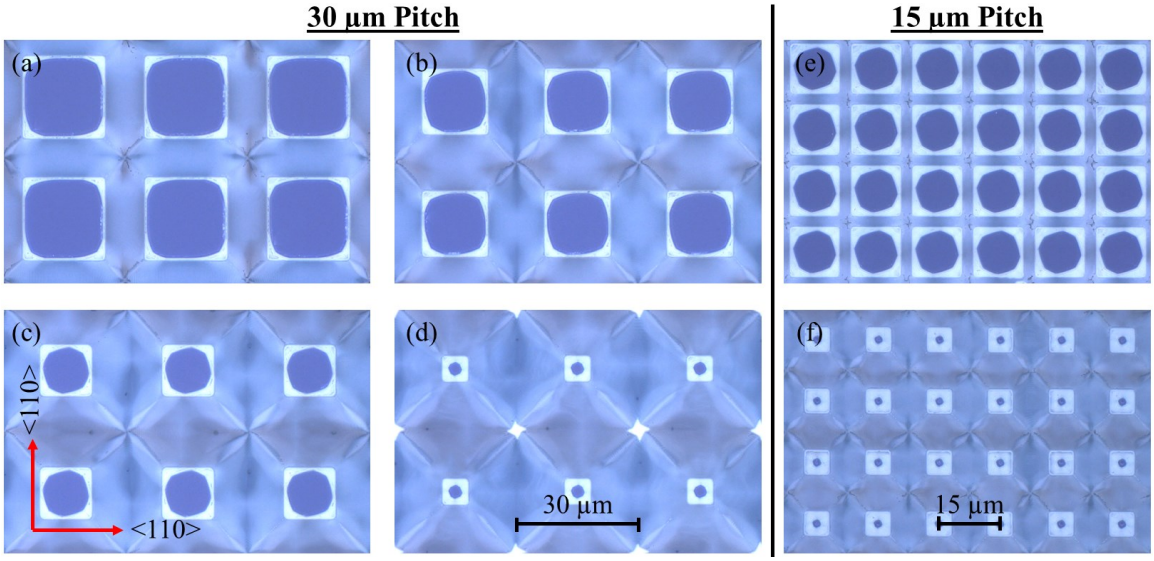

Figure 2.6. Series of confocal microscope images depicting the undercutting of a 100 nm thick thermal SiO_2 square mask layer, represented by the white squares located atop the truncated Si micropyramids. The truncated Si micropyramids were fabricated through anisotropic wet etching with 25% TMAH and 0.3% v/v Triton X-100 for 50 minutes at 80°C. A stir bar was used to mix the TMAH and Triton X-100 solution, but no stir bar was utilized during the etch. The calculated undercutting ratio *l*/*d* of the <110> direction was ~0.29 *l*/*d*, where *l* is the undercutting along the <110> direction of the SiO_2 mask, and *d* is the total depth of the etch [314]. (a-d) Undercutting of 30 µm pitch truncated Si micropyramids. (e, f) Undercutting of 15 µm pitch truncated Si micropyramids.

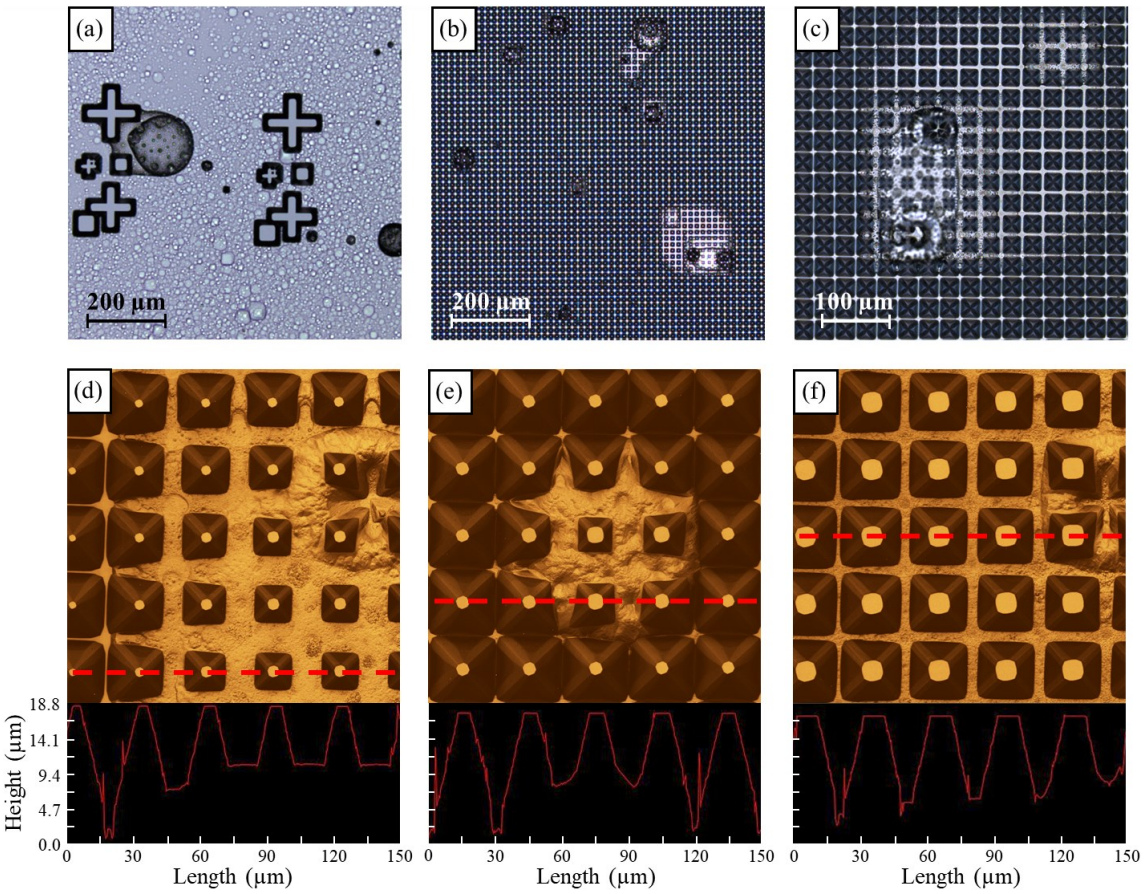

Figure 2.7. (a-f) Series of confocal microscope images depicting the surface deformations that develop if too much Triton X-100 is added to a 25% TMAH etch at 80° C for 50 minutes. The surface topology is seen in the plots below the images in (d-f), located along the red dotted line. Here, 0.4% v/v Triton X-100 was added to the etchant bath, as seen in Fig. 1.21. A stir bar was used to mix the TMAH and Triton X-100 solution, but no stir bar was utilized during the etch.

The uniformity of the surface morphology is impacted when using higher concentrations of Triton X-100, such as 0.3 % v/v or 0.4% v/v, when fabricating truncated Si micropyramid arrays. Both the number and size of these surface morphology defects were rather small when using 0.3% v/v Triton X-100, but both the quantity and the area of these defects increased substantially when utilizing 0.4% v/v Triton X-100. A few confocal images from a sample anisotropically wet etched with 25% TMAH and 0.4% v/v Triton X-100 at 80° C are shown in Fig. 2.7. It appears that regions of the (100) Si wafer had Triton X-100 bubbles attached to the Si surface at some point during the etch, after the

anisotropic wet etching already began, which prevented the TMAH from reaching the Si and therefore interrupted the Si etching. This can be seen over large areas in Fig. 2.7(a-c). The surface topology near Si micropyramids are shown in the plots below the confocal images in Fig. 2.7(d-f), along the red dotted line. In this case, the 0.4% v/v Triton X-100 prevented upwards of 10.5 μm of Si from being etched in certain areas, as seen in Fig. 2.7(d), significantly impacting the uniformity of the fabricated arrays.

To reiterate, all the wafers etched in this dissertation were etched horizontally and upside-down in the TMAH solution. This was done to limit how much Triton X-100 settles on the Si wafer's surface, but could potentially be one of the reasons why these defects occurred. It may be worth placing the wafers vertically in the TMAH bath, which then necessitates significantly more TMAH to be used for each etch. As we were trying to be conservative with our TMAH usage, the wafers were etched horizontally and upside-down. Regardless, utilization of more than 0.1 - 0.2% v/v Triton X-100 does not improve etching characteristics and in fact hinders the overall etch uniformity and surface morphology.

The extent of undercutting varies significantly between pure 25% TMAH and 25% TMAH with the addition of Triton X-100, with the latter showing a drastically reduced undercutting rate. Triton X-100 was selected as the surfactant due to its nonionic nature, maintaining IC compatibility essential for fabricating monolithically integrated photodetector FPAs [157].

2.5. Conclusions

Anisotropic wet etching with 25% TMAH has proven to be a versatile tool, facilitating the large-scale fabrication of various mesophotonic structures in Si. The

fabrication process highlighted several advantages of Si anisotropic wet etching for creating 3-D light-concentrating mesophotonic structures with applications in Si photonics: a) the ability to rapidly produce large-scale arrays of normal or inverted micropyramids simultaneously, b) control over the sidewall angle of light concentrators based on mask orientation for arrays on a (100) wafer, and c) smooth sidewall surfaces at 54.74˚ angles, reducing scattering losses for optical applications. Si anisotropic wet etching is an ideal technique for the rapid and cost-effective fabrication of light-concentrators. In this chapter, it was demonstrated that this technology enables precise control over the geometry of fabricated light-concentrating structures, achieving astonishing uniformity across entire Si wafers. This uniformity is attributed to the self-terminating nature of the etching process, which occurs when two (111) planes converge within a 3-D structure when Triton X-100 is used to slow down the SiO_2 pattern undercutting rate. This combination of properties is highly attractive for developing detector and emitter applications in Si photonics.

Although anisotropic wet etching of Si is extensively studied by the MEMS community, the self-terminating nature of the etching process has not received sufficient attention in previous research. It is this property that enables the creation of truncated Si micropyramid arrays with smooth surfaces and highly uniform characteristics, making them ideal for integration with detector and emitter arrays in optoelectronics applications.

Various methods to control the geometry of micropyramidal arrays were explored, particularly focusing on (100) wafers etched by TMAH with added Triton X-100 as a surfactant. The optimal control of the final structures' shape is achieved by aligning the photoresist patterns parallel to the <110> crystalline directions on (100) wafers and using Triton X-100. This approach results in the formation of exceptionally uniform arrays of Si

micropyramids or microvoids, which can be produced within minutes. These arrays exhibit perfect periodicity, geometry reproducibility, and nearly atomically smooth surfaces—qualities that, to the best of our knowledge, are unattainable with any other technology.

CHAPTER 3: NUMERICAL MODELING THE OPTICAL PROPERTIES OF SI MICROPYRAMID ARRAYS

3.1. Introduction

In this dissertation, methods to enhance IR photodetector FPAs by integrating them with truncated Si micropyramidal arrays are explored. Reducing the dimensions of the photodetectors decreases the dark current, and the light collection efficiency can be improved using light-concentrating structures such as truncated Si micropyramids placed over individual pixels. These structures allow light to be collected from a larger area and concentrated into a much smaller area, which can be aligned with the photodetector's mesa to maintain or enhance the SNR. Since the dark current noise increases with thermal energy, the operating temperature can be increased if the SNR is maintained through shrinking the detectors in the FPA and integrating them with a light-concentrating structure, thereby enabling the operating temperature of FPAs to be increased. In fact, similar concepts for enhancing the SNR have been proposed with the integration of integrated microlenses [17-19, 34-36], microspheres [20-22, 51, 52, 66, 89, 114], and metalenses [12-16].

The focus of this chapter is on utilizing 3-D FDTD simulations to study the optical properties of truncated Si micropyramids in photodetector and emitter applications. Extremely efficient front-illuminated photodetector FPAs can be heterogeneously integrated with truncated Si micropyramids by bringing the micropyramids into contact with the photodetector mesas. The advantage of heterogeneous integration with the

truncated Si micropyramids is that FPAs can be fabricated from detector materials with large absorption in the MWIR, like HgCdTe [4]. On the other hand, FPAs monolithically integrated with truncated Si micropyramids can be achieved by fabricating p-i-n or Schottky barrier photodiodes directly on top of specific individual micropyramids [94-99, 102-104, 363]. The latter approach can be implemented in a back-illuminated configuration, facilitating straightforward integration with a ROIC. As demonstrated in this research, monolithic integration with truncated Si micropyramids can address the longstanding issue of limited quantum efficiency in Si-based photon detectors in the MWIR spectrum.

The monolithic integration of Si micropyramid arrays with SWIR FPAs has been explored previously, utilizing nanoplasmonic effects for large signal enhancement, where arrays of Si micropyramids [23] or inverted Si micropyramids [24] were coated with metal to form a Schottky barrier photodiode. Enhanced photoresponses were observed in both cases. However, the operational mechanisms of these Si micropyramid arrays are quite complex, involving nonlinear processes occurring in the nanoscale regions near the tips of the micropyramids. Ensuring a uniform response across all pixels can be challenging in this scenario. In this work, the strategy for addressing this issue depends primarily on utilizing the dielectric properties of truncated Si micropyramids [25, 94-100, 102-104, 109, 110, 363]. Truncated Si micropyramid arrays are expected to offer a more uniform photoresponse across all pixels. Importantly, these truncated Si micropyramid arrays can significantly enhance the efficiency of MWIR photon detection applications compared to Schottky barrier photodiodes with flat photodetector mesas [5, 44, 363]. This enhancement is achievable through collecting photons over a broader area, increasing the path length of light within the photodetector regions, and resonantly trapping photons [25].

In this chapter, applications stemming from the unique optical properties of anisotropically wet etched truncated Si micropyramids are investigated in the mesoscale regime by using Ansys/Lumerical's 3-D FDTD numerical modeling software. The term mesoscale refers to objects, such as micropyramids, with geometric dimensions comparable to the incident wavelength of light. These objects exhibit varying optical properties through light-matter interactions as their geometry changes. When the truncated Si micropyramids are much larger than the wavelength of light, their properties align with the well-understood principles of geometrical optics. However, the diverse properties of mesoscale objects offer a wide range of applications. In this work, the focus is on exploring the optical characteristics and potential uses of Si micropyramidal structures with mesoscale dimensions.

It has been demonstrated that, contingent on the light's propagation direction, these truncated Si micropyramidal arrays can serve either for integration with MWIR FPAs in photon detection applications or for enhancing the extraction efficiency and directionality of IR photon emitters implanted in high refractive index slabs. The optimization of the truncated Si micropyramid geometry for various optoelectronics applications was guided by 3-D FDTD numerical modeling simulations.

For photon detection applications, the optimization focused on achieving maximum power or intensity enhancement factors offered by truncated Si micropyramids compared to flat mesas. The ability of truncated Si micropyramids to concentrate light results from reflections facilitated by their sidewalls, a property known as non-imaging light concentration, which differentiates them from the focusing effects of lenses. This light-concentration ability is typically non-resonant, but the optical properties of a truncated Si

micropyramidal array can also lead to various interference effects, treating the array as a transmission grating. The optical properties of mesoscale structures depend on their geometry, and the properties of truncated Si micropyramids have been relatively unstudied. From an application development perspective, mesoscale structures of this nature hold considerable promise and appeal.

For IR photon emitters applications, it is shown that the extraction efficiency and directionality of emissions from point sources embedded in truncated Si micropyramids can be significantly enhanced compared to flat mesas. This property enables the integration of such arrays with infrared scene projectors (IRSPs) [308, 315, 363]. Additionally, they can improve the extraction efficiency of single-photon sources created in Si slabs using focused ion beams [316, 363].

Chapter 3 focuses on the optical characteristics of these truncated Si micropyramid arrays. Section 3.2 explores the impact of various boundary conditions (BCs) on the 3-D FDTD numerical modeling of the optical properties of the aforementioned structures. Periodic BCs are utilized to numerically model Talbot images that appear from the diffraction and interference effects within truncated Si micropyramid arrays. On the other hand, perfectly matched layer (PML) BCs are employed to simulate the light-concentrating ability of individual truncated Si micropyramids. In section 3.3, the experimental findings on Talbot images generated by truncated Si micropyramidal arrays are discussed and juxtaposed with 3-D FDTD numerical modeling simulation results. Section 3.4 focuses on the numerical modeling investigation of photonic jets created by mesoscale truncated Si micropyramids, which are pivotal for integrating with MWIR and LWIR FPAs. In section 3.5, the utility of truncated Si micropyramids in enhancing the extraction efficiency and

emission direction of embedded dipole sources are demonstrated. This capability opens up applications for improving the efficiency of extracting single photons from quantum sources within Si slabs and enhancing the directionality of IRSPs. The findings of this research are summarized in section 3.6.

This research demonstrates that truncated Si micropyramidal photonics provides a versatile optoelectronic platform capable of enhancing the SNR and increasing the operational temperature of MWIR FPAs. First, the role of different types of BCs in 3-D FDTD numerical modeling simulations are examined to represent various experimental scenarios and applications of these truncated Si micropyramid arrays.

3.2. Role of the Boundary Conditions in 3-D FDTD Numerical Modeling

The BCs utilized when creating a simulation significantly impact what kind of results will be obtained. For example, the optical properties of an array of truncated Si micropyramids was studied utilizing periodic BCs, and interference effects are observable when illuminated by a coherent source. Additionally, the optical properties of a single truncated Si micropyramid was studied by utilizing perfectly matched layer (PML) BCs and exhibited light-concentrating behavior similar to photonic nanojets. These two BCs are shown in Fig. 3.1.

Periodic BCs, as seen in Fig. 3.1(a), are represented by the plane wave illumination of periodic arrays. While this is not directly related to the imaging applications of such light-concentrating arrays integrated with FPAs, it can be used to observe the diffraction and interference properties of the fabricated structures.

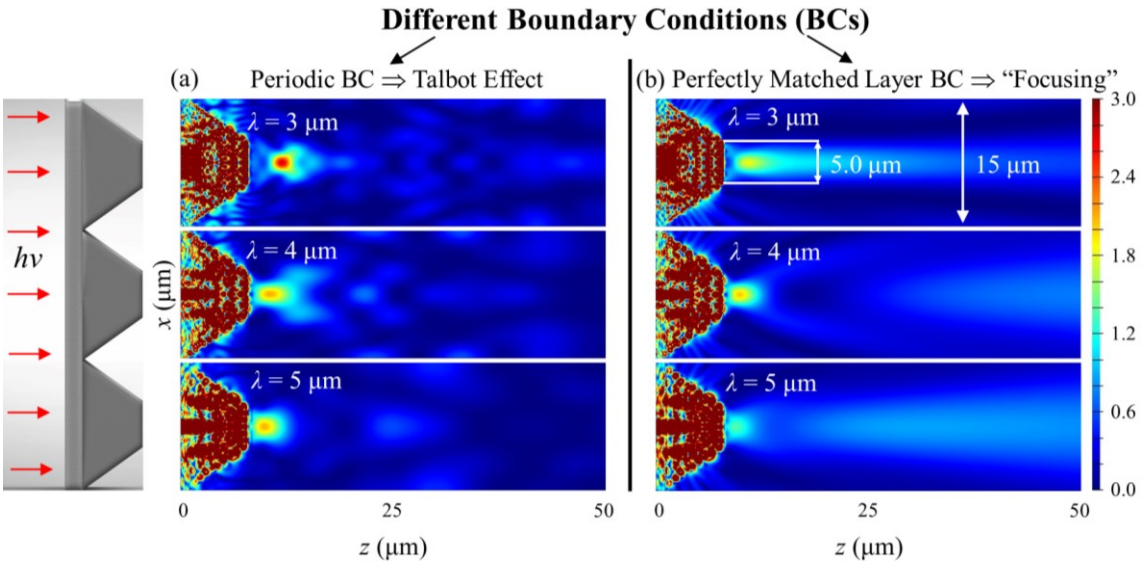

Figure 3.1. 3-D FDTD numerical modeling simulations. Two methodologies for accessing different optical properties of periodic arrays under plane wave illumination at $\lambda = 3$, 4, and 5 μm based on two types of BCs: (a) perfectly matched layer BCs at the left and right most plane of the simulation region, and periodic BCs on the four z-planes of the simulation region, describing grating-type diffraction and interference effects leading to the formation of the Talbot images at further distances from the truncated Si micropyramids, and (b) perfectly matched layer BCs on all six planes of the simulation region, describing the concentration of light and the formation of photonic jets close to the truncated Si micropyramids. Both (a) and (b) display electromagnetic (EM) field distributions calculated at normal incidence on truncated Si micropyramids with refractive index n = 3.43. The truncated Si micropyramids shown have the same small base size, D_S = 5 μm, and same large base size D_L = 15 μm.

To incorporate properties influenced by the array periodicity in the 3-D FDTD numerical modeling simulations, periodic BCs were used along the four z-planes of the simulation region, instead of PML BCs, as shown in Fig. 3.1(a). In the simulations carried out in this study, the period matches the size of the large base of the truncated Si micropyramid, $\Lambda = D_L$. The electromagnetic (EM) field distributions were calculated at much longer distances compared to Fig. 3.1(b) to reveal patterns of periodic maxima along the z-axis, which are shown in Fig. 3.2 and Fig. 3.3. The results for different wavelengths $\lambda = 3$, 4, and 5 μm, are depicted by EM field maps along the three rows of Fig. 3.1(a). In all three cases, the size of the small base is D_S = 5 μm and the size of the large base is D_L = 15 μm. More detailed numerical modeling results in this case are presented in section 3.3.

PML BCs enable us to numerically model the primary intended application of these truncated Si micropyramid arrays, which involves the focusing or light-concentrating capabilities of individual truncated Si micropyramids optically coupled to MWIR photodetectors. In this application, the image is projected onto the entire array using an incoherent structured beam. Interference between adjacent pixels is typically regarded as an undesirable factor in this application. The optical characteristics of individual truncated Si micropyramids can be comprehended through the formation of tightly concentrated beams, analogous to photonic nanojets generated by dielectric microspheres [56, 57].

Fig. 3.1(b) illustrates the 3-D FDTD simulation configuration, where the plane wave source was embedded in the Si wafer with truncated Si micropyramids positioned on the right surface of the wafer. The width of the simulation region along the vertical *x*-axis was equal to the large base of the truncated Si micropyramid, D_L. To assess the optical characteristics of individual truncated Si micropyramids rather than the collective properties influenced by diffraction and interference within periodic arrays, PML BCs along all boundaries of the simulation region were utilized. These conditions enable optical power to exit the computational domain without reflection. By using femtosecond pulses, a sufficiently long calculation time ensured nearly complete decay of the stored energy within the simulation region, leading to convergence of the results. The calculations of photonic jets produced by truncated Si micropyramids for different wavelengths λ = 3, 4, and 5 μm, are illustrated by EM field maps along the three different rows of Fig. 3.1(b). In all three cases, the size of the small base is D_S = 5 μm and the size of the large base is D_L = 15 μm. More detailed numerical modeling results for this case are presented in section 3.4.

3.3. Periodic BCs: Talbot Effect

Diffraction and interference phenomena arise from the wave nature of light, and an example of this effect is seen in diffraction gratings. Each diffraction order propagates at a specific angle and can interfere with other orders while propagating along the optical axis. This coherent interference effect leads to the generation of self-images, and was originally discovered by Talbot in 1836, which was later deemed the Talbot effect [115]. These self-images also follow a periodic pattern along the optical axis, where an analytical description was derived by Rayleigh in 1881 in order to define the Talbot length as the separation distance between these self-images [116].

The Talbot length is defined by equation (1):

$$z_T(m) = \frac{\frac{m\lambda}{n}}{1 - \sqrt{1 - \left(\frac{\lambda}{n\Lambda}\right)^2}} \tag{1}$$

where z_T is the Talbot length of order m (where the mth Talbot image is located), λ is the wavelength of light, n is the index of refraction of the propagating medium, and Λ is the period of the diffraction grating. If the wavelength of the coherent light source or the period of the diffraction grating varies, the Talbot length changes. Fig. 1.16(a) shows the Talbot effect, with sequential Talbot lengths z_T labeled. The planes positioned at a distance equal to the Talbot length from the grating are commonly referred to as Talbot planes. In the results shown in this work, the Talbot length equation can be simplified because the propagating medium is only air, and $n = 1$. Therefore, equation (1) becomes:

$$z_T(m) = \frac{m\lambda}{1 - \sqrt{1 - \left(\frac{\lambda}{\Lambda}\right)^2}} \quad . \tag{2}$$

The theory of the Talbot effect is based on applying the Fresnel-Kirchhoff equation to a plane periodic object under coherent monochromatic light illumination [317, 318]. Recent advancements include the fabrication of 3-D structures [145], application of fractional extreme ultraviolet Talbot lithography [140], generalized Talbot imaging [147], and the study of phase anomalies [142, 143]. The Talbot effect description can be simplified if the periodic object has a weak phase or amplitude variation, as it can then be understood in terms of the interference of the 0th and ±1st diffraction orders [142, 143].

In this dissertation, the Talbot effect resulting from truncated Si micropyramids that were illuminated by coherent MWIR light were discussed. Since truncated Si micropyramids consist of a unique 3-D geometry, the resulting Talbot images contain harmonic distortions due to the superimposed spatial harmonics [146]. This effect depends on the period of the truncated Si micropyramid arrays, as well as their relative heights to the wavelength of light. These mesoscale objects are rather complex and require numerical methods to understand these properties. However, it is important to note that high-index objects with a 3-D pyramid geometry, as shown in Fig. 3.2, differ substantially from planar periodic objects with weak index modulation. The theory of the Talbot effect generated by periodic structures with a pronounced 3-D geometry requires a rigorous electromagnetic approach based on solving Maxwell's equations. This has previously been accomplished either by using FDTD numerical modeling simulations for arrays of microspheres [145], or by employing coupled wave analysis for conical void array in a phase mask [144].

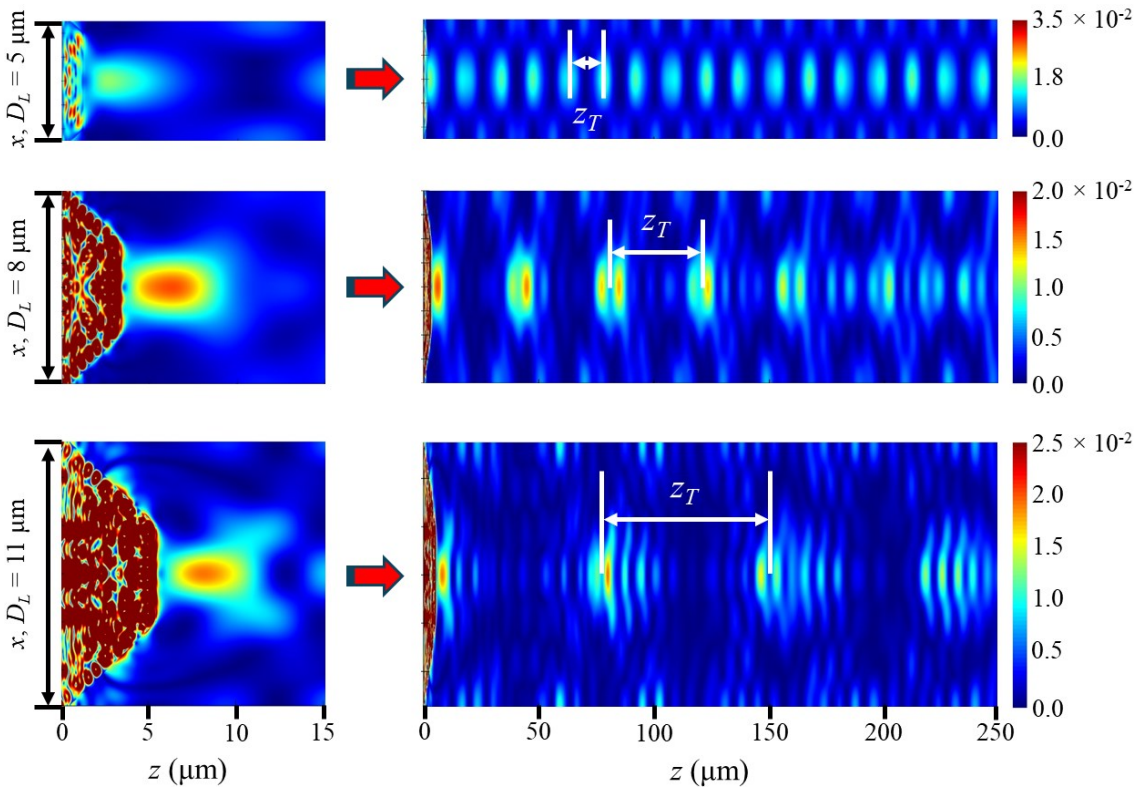

Figure 3.2. 3-D FDTD numerical modeling simulations to demonstrate the impact truncated Si micropyramid height has on the Talbot effect. EM field distributions calculated at normal incidence for truncated Si micropyramids with index n = 3.43 at λ = 2.94 μm. Three different truncated Si micropyramids depicted in the three rows all have the same small base size, D_S = 4 μm, and different large base size, D_L = 5, 8, and 11 μm, respectively. PML BCs along the x-direction and periodic BCs along z-directions describe grating-type diffraction and interference effects leading to the formation of the Talbot images at further distances from the truncated Si micropyramids [363].

The EM field distributions were calculated at much longer distances in Fig. 3.2 compared to Fig. 3.1 to reveal patterns of periodic maxima along the z-axis. The results for different periods $\Lambda = D_L$ = 5, 8, 11 μm, are shown by different EM field maps illustrated in the three different rows of Fig. 3.2. In all three cases, the small base size was D_S = 4 μm. From a geometrical perspective, the results depicted in Fig. 3.2 illustrate a progression from truncated Si micropyramids with a small height of 0.7 μm (top row) to increasingly taller truncated Si micropyramids with heights of 2.8 μm (middle row) and 5.0 μm (bottom row). Although there is extensive literature on the Talbot effect for thin gratings [147, 317, 318],

there are very limited results available for periodic arrays composed of complex 3-D geometries.

It is observed that shallow truncated Si micropyramids with modest heights behave similarly to classical sinusoidal gratings, generating long sequences of Talbot images with a period of z_T = 15.4 μm, described by Eq. (2) with Λ = 5 μm and λ = 2.94 μm. However, for taller truncated Si micropyramids with a more pronounced 3-D geometry, the situation becomes more complex. Each peak splits into several narrower peaks inside an envelope. The centers of the envelope functions are still separated by the Talbot length z_T, which equals 42.0 μm and 80.8 μm in the middle and bottom rows, as expected by Eq. (2). Nevertheless, the number of split components within each envelope increases for truncated Si micropyramids with a more substantial 3-D geometry. This splitting of components can be attributed to the increased vertical extension of the truncated Si micropyramids, indicating that multiple Fourier components contribute to the formation of these patterns.

Furthermore, the Talbot effect was experimentally investigated for truncated Si micropyramidal arrays with D_S = 16.5 μm and D_L = 30 μm, and the findings were compared to numerical modeling simulations. Experimental measurements were conducted using the setup illustrated in Fig. 3.3(a). The backside of the Si wafer was illuminated with an Er:YAG laser at λ = 2.94 μm that was focused to ~0.5 mm spot size on the truncated Si micropyramidal array with a CaF_2 lens of focal length f = 12.7 mm. Because the incident light cone has a small angle (<4°), this type of illumination can be regarded as quasi-plane wave, similar to the plane wave illumination used in the numerical modeling simulation. The light subsequently propagated through the wafer, scattering in various directions as it interacted with the truncated Si micropyramids, resulting in a pattern of Talbot images

caused by constructive and destructive interference effects. Cross-sectional intensity distributions were captured using a MWIR Spiricon beam profilometer with a Ge IR lens of focal length f = 12.7 mm, as depicted schematically in Fig. 3.3(a). The IR lens was moved along the optical axis z with micrometer precision to capture magnified images of various cross-sections of the 3-D pattern of Talbot images.

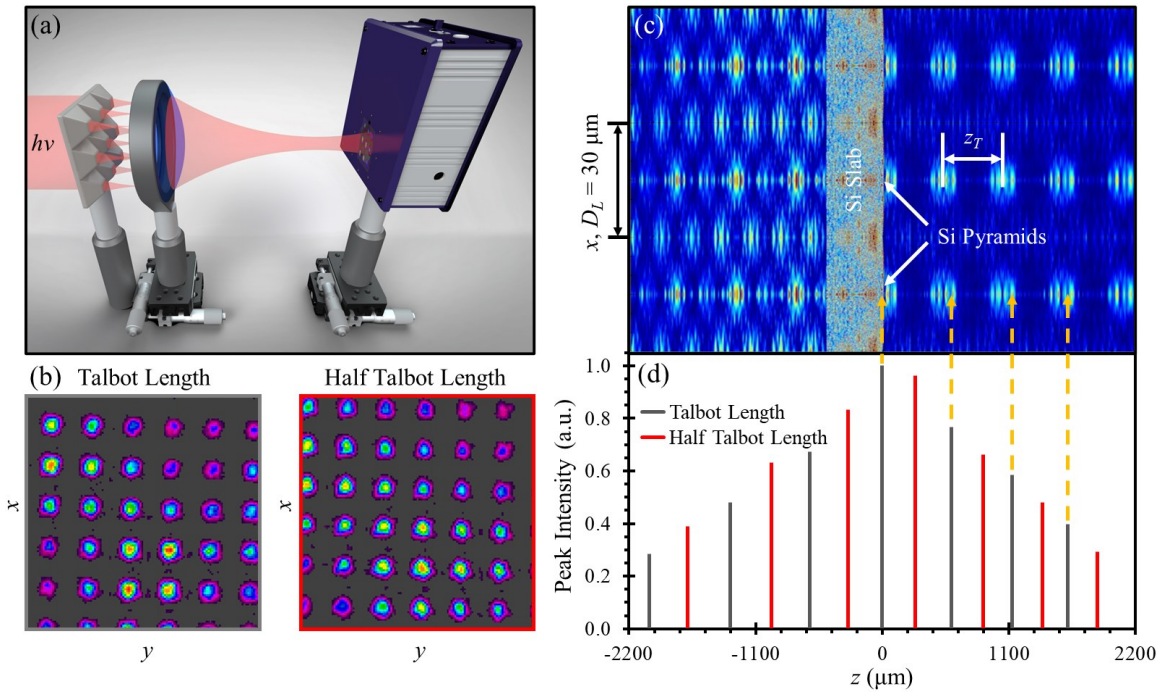

Figure 3.3. Experimental study of Talbot effect and comparison with a 3-D FDTD numerical modeling simulation. (a) Experimental setup where imaging of intensity distributions at different distances z from the tops of the truncated Si micropyramids was provided by a Ge IR lens with f = 12.7 mm attached to a micrometer translation stage. The illumination was provided with an Er:YAG laser at wavelength λ = 2.94 μm and the Talbot images were captured by a MWIR Spiricon beam profiler. (b) Typical examples of experimental Talbot self-images belonging to the "Talbot Length" subset obtained at distances $z_T(m)$ and the "Half Talbot Length" subset obtained at distances $z_T(m + 0.5)$ where m = 0, 1, 2, …, etc., respectively. In the cross-sectional xy planes, the peaks in the "Talbot Length" subset are aligned with the truncated Si micropyramids whereas the peaks in the "Half Talbot Length" occupy positions between the truncated Si micropyramids. (c) EM field distribution numerically modeled along the propagation direction in a plane passing through centers of the truncated Si micropyramids which illustrate properties of the "Talbot Length" subset. (d) Experimentally determined positions of the self-imaging Talbot planes and relative intensities of the peaks in these Talbot planes depicted by grey and red bars for the "Talbot Length" and "Half Talbot Length" subsets, respectively [363].

The study uncovered two distinct subsets of imaging planes (*xy*) exhibiting well-defined interference maxima, separated by the Talbot length of $z_T = 610.8$ μm for a specific period of $\Lambda = D_L = 30$ μm. Examples of typical Talbot images representing each subset are shown in Fig. 3.3(b), labeled as "Talbot Length" and "Half Talbot Length". The Spiricon camera images belonging to the "Talbot Length" subset are aligned with the truncated Si micropyramids' small base D_S in their respective cross-sectional *xy* planes. The locations of the focusing planes, depicting well-defined Talbot self-images and their corresponding intensities, are represented by grey bars in Fig. 3.3(d). These planes are observed not only in front of the structures ($z > 0$) but also deeper into the Si substrate ($z < 0$). The maximum intensity of the peaks (tallest grey bar) is observed near the tops of the truncated Si micropyramids ($z \approx 0$), and the intensity of the corresponding Talbot self-images gradually diminishes for grey bars representing Talbot imaging planes located further away from this plane. Moreover, at half the Talbot length, another set of images occurs, labeled as "Half Talbot Length" in Fig. 3.3(b). These Talbot images are phase-shifted by half a period, meaning that in the corresponding cross-sectional *xy* plane, the maxima occupy positions between the truncated Si micropyramids. The positions of these planes, along with their respective intensities, are denoted by red bars in Fig. 3.3(d).

The 3-D FDTD numerical modeling simulation was completed for a comparable truncated Si micropyramid array with 54.74˚ sidewall angles, refractive index $n = 3.43$, $D_S = 16.5$ μm, and $D_L = 30$ μm, to facilitate comparison with experimental observations. Periodic BCs were applied to this simulation as shown in Fig. 3.1(a), where plane wave illumination of $\lambda = 2.94$ was incident onto the backside of a 500 μm thick Si wafer, where

the truncated Si micropyramidal structures are positioned on the opposing surface, as illustrated in Fig. 3.3(c).

The 3-D FDTD numerical modeling simulation results accurately replicate the characteristics of Talbot images observed experimentally. The distances $z_T(m)$ of the Talbot self-imaging planes labeled "Talbot Length" in Fig. 3.3(b) and the distances $z_T(m + 0.5)$ of the self-imaging planes labeled "Half Talbot Length" in Fig. 3.3(b) where $m = 0, 1, 2, \ldots$, etc., were found to be in very good agreement with the experimental results, represented by the grey and red bars in Fig. 3.3(d), respectively. In a more detailed way this is seen in Figs. 3.3(c) where the calculated EM field distributions are represented along the z-axis propagation direction.

Fig. 3.3(c) depicts such EM field distribution in the xz-plane passing through the centers of the truncated Si micropyramids. It demonstrates that each peak contains multiple split components determined by the complicated Fourier spectrum of a truncated Si micropyramidal array with a pronounced 3-D geometry. However, the corresponding envelope functions of the split components correlate well with the experimental peak positions indicated by the grey bars in Fig. 3.3(d). This correlation is furthermore illustrated by golden arrows connecting different peaks in Figs. 3.3(c, d). Due to a limited axial resolution of the experimental setup, the fine axial structure of the Talbot self-imaging were not resolved. The calculated peaks are located in front ($z > 0$) of the structures, as well as inside it ($z < 0$), in agreement with the experiment. The xy plane FWHM of the calculated peaks are found to be smaller than that for the experimentally observed Talbot self-images which can be explained by a limited lateral resolution of the imaging setup, as well as by some contribution of the incoherent scattering processes.

3.4. Perfectly Matched Layer BCs: Photonic Jets for Photodetector Applications

While the Talbot effect is useful for the optical characterization of fabricated structures and the development of 3-D nanolithography, the primary application of truncated Si micropyramidal arrays lies in their light-concentrating capability, where individual truncated Si micropyramids are optically coupled to photodetectors. As depicted in Fig. 3.1(b), these properties can be numerically modeled when utilizing PML BCs such that the simulation region is enclosed by fully absorbing layers on all sides. These BCs exclude the transmission grating properties arising from the periodicity of the truncated Si micropyramidal arrays, but they permit the examination of the optical properties of individual truncated Si micropyramids as contact microlenses which concentrate light onto the individual pixels of photodetector FPAs. It has long been known that tightly concentrated beams, known as photonic nanojets, can be produced not only by dielectric microspheres [57, 90], but also by mesoscale particles with various shapes, such as disks [81], hemispheres [319], toroids [320], cubes [321], and axicons [56, 70, 85, 88].

The formation of photonic nanojets involves an intricate interplay between diffracted and scattered fields, influenced by the interference of light waves transmitted through and refracted by the photonic nanojet creating particle. Because of the multifaceted characteristics of the photonic nanojet phenomenon, customizing their properties are essential for maximizing their utility in each application. Given the mesoscale nature of photonic nanojets, optimization must be conducted for every application to determine the optimal combination of parameters including the index of refraction and geometry of the photonic nanojet emitting particle, and the illumination conditions necessary to yield the most effective results for that particular application.

In this dissertation, optimization for truncated Si micropyramids were performed in order to find the conditions necessary to maximize the photoresponse of MWIR FPAs used in imaging devices such as IR cameras [25, 94-114, 363]. It is important to note that direct comparison between focusing and imaging is typically not feasible with such light-concentrating objects. The reciprocity principle in optics forms the foundation for such comparisons, which is only applicable to identical optical modes. When different optical modes govern the light-concentrating and imaging properties, the reciprocity principle cannot be utilized. These mesoscale objects are rather complex and require numerical methods to understand these properties.

It can be proposed that in mesoscale particles with characteristic dimensions on the order of several wavelengths, such light-concentrating properties should depend on the interference phenomena occurring within the microparticle. In this context, anisotropically wet etched truncated Si micropyramids serve as an opportune model system for researching these effects [94-104, 363], as the angle of the truncated Si micropyramids is fixed and their geometry is entirely determined by the dimensions of the small and large bases, D_S and D_L, respectively.

As depicted in Figs. 3.4(a), 3.5(a), and 3.6(a) where $\lambda = 3$, 4, and 5 μm, respectively, a truncated Si micropyramid with refractive index $n = 3.43$ and sidewall angles of 54.74° was illuminated with plane waves at normal incidence. The source of the plane waves, with wavelengths ranging from λ = 3-5 μm, was placed inside the bulk Si wafer to streamline and simplify the simulations. The primary characteristics of the concentrated light beam, specifically its FWHM at the narrowest waist, the distance (d) between the concentrated light's most intense position and the smaller base D_S of the truncated Si micropyramid, and

the concentrated light's peak intensity enhancement factor (IEF). This latter parameter (peak IEF) is defined as the ratio of the intensity with a truncated Si micropyramid ($I_{pyramid}$) divided by the uniform intensity measured without a truncated Si micropyramid present (I_{ref}), IEF = $I_{pyramid}$ /I_{ref}. Hence, the peak IEF represents a dimensionless value observed at the position of highest intensity of the concentrated light. For each data point, the field monitor was adjusted along z to capture the location of maximum intensity within the photonic jet.

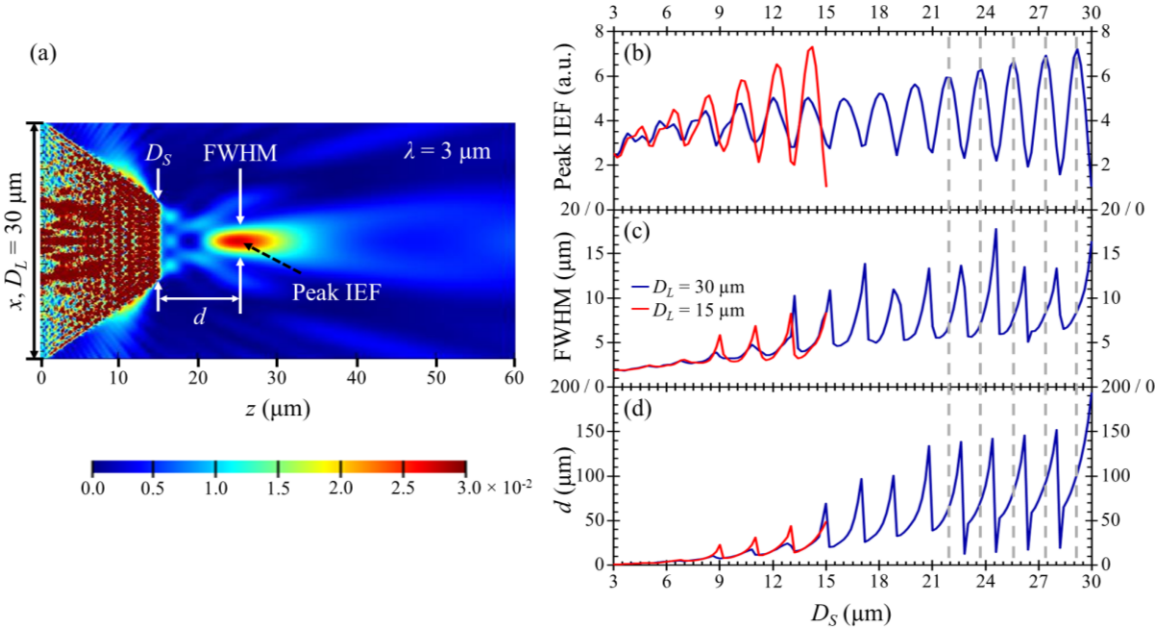

Figure 3.4. 3-D FDTD numerical modeling simulation study on the optical properties of truncated Si micropyramids at $\lambda = 3$ µm by utilizing perfectly matched layer BCs. (a) EM field map defining the parameters studied; specifically, the peak intensity enhancement factor (IEF), FWHM, and light concentration distance d of the photonic jets, as well as the truncated Si micropyramid's large base size D_L and small base size D_S. In this EM field map, $D_L = 30$ µm and $D_S = 10$ µm. (b-d) Plots showing how the peak IEF, FWHM, and d of the photonic jets change depending on D_L, and D_S [363].

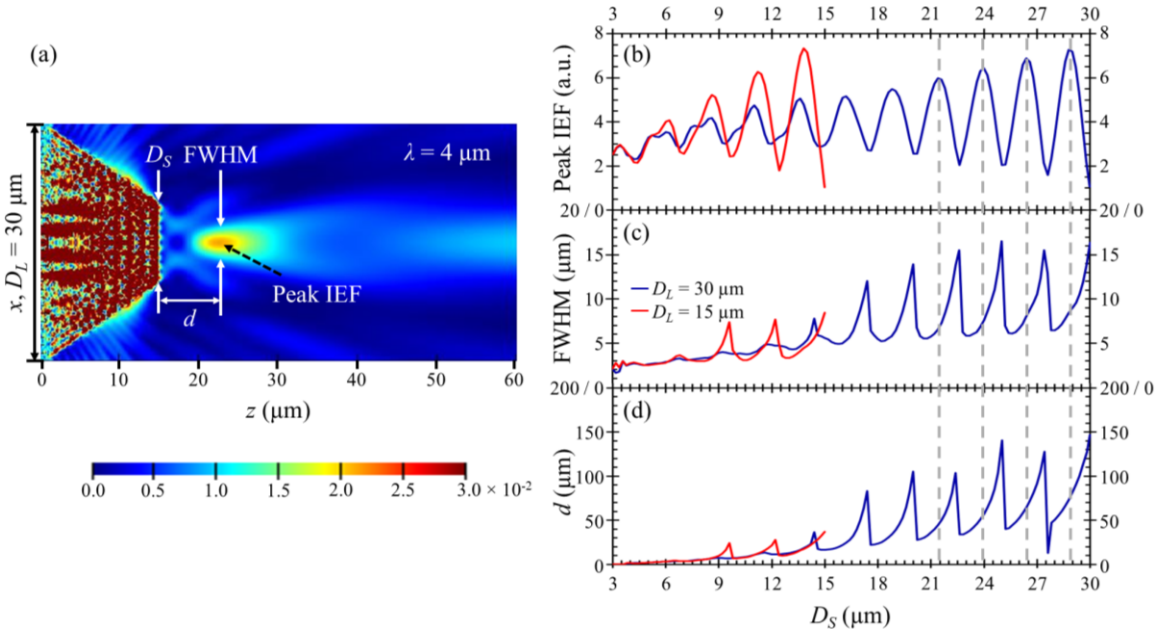

Figure 3.5. 3-D FDTD numerical modeling simulation study on the optical properties of truncated Si micropyramids at $\lambda = 4$ µm by utilizing perfectly matched layer BCs. (a) EM field map defining the parameters studied; specifically, the peak intensity enhancement factor (IEF), FWHM, and light concentration distance d of the photonic jets, as well as the truncated Si micropyramid's large base size D_L and small base size D_S. In this EM field map, $D_L = 30$ µm and $D_S = 10$ µm. (b-d) Plots showing how the peak IEF, FWHM, and d of the photonic jets change depending on D_L, and D_S [363].

The peak IEF, FWHM, and d were studied as a function of D_S for $\lambda = 3$, 4, and 5 µm, as depicted in Figs. 3.4(a), 3.5(a), and 3.6(a), respectively. The effect of the small base size D_S of the truncated Si micropyramid on its light-concentrating ability was investigated for $D_S = 3$ - 15 µm in the case of $D_L = 15$ µm, shown in red, and for $D_S = 3$ - 30 µm in the case of $D_L = 30$ µm, shown in blue. Because the slope of the sidewall surface is fixed during the fabrication process, the height of these truncated Si micropyramids adjusts accordingly for different D_S values. With fixed sidewall angles of 54.74°, this indicates a transition from a slightly truncated Si micropyramidal geometry at $D_S = 3$ µm to a geometry resembling a thin plane-parallel plate as D_S approaches D_L.

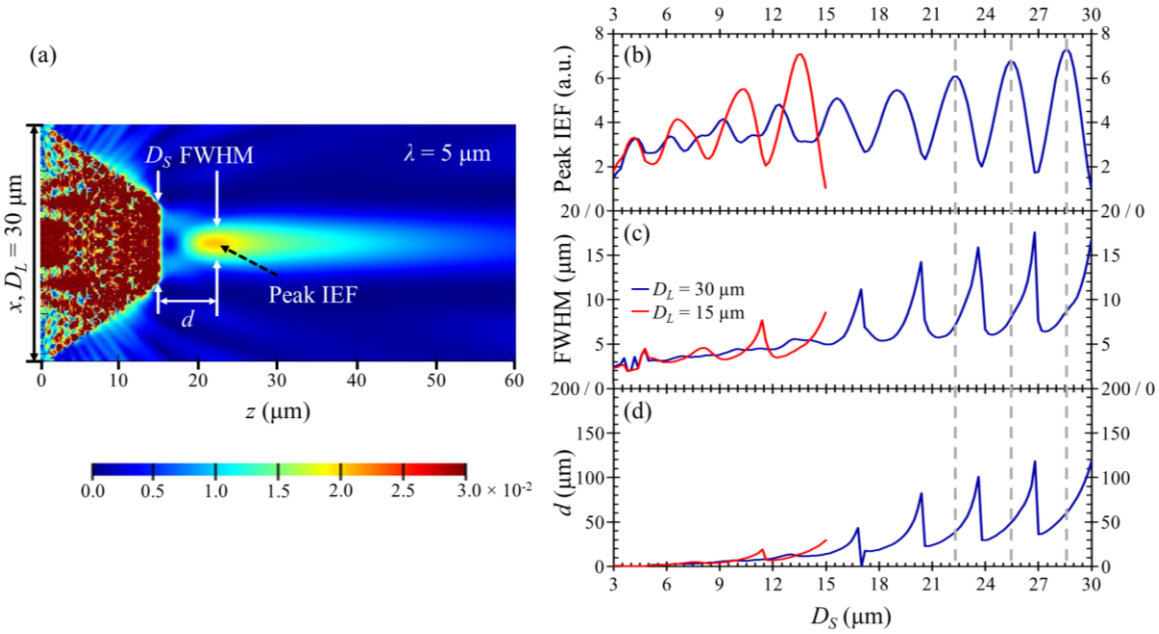

Figure 3.6. 3-D FDTD numerical modeling simulation study on the optical properties of truncated Si micropyramids at λ = 5 µm by utilizing perfectly matched layer BCs. (a) EM field map defining the parameters studied; specifically, the peak intensity enhancement factor (IEF), FWHM, and light concentration distance d of the photonic jets, as well as the truncated Si micropyramid's large base size D_L and small base size D_S. In this EM field map, D_L = 30 µm and D_S = 10 µm. (b-d) Plots showing how the peak IEF, FWHM, and d of the photonic jets change depending on D_L, and D_S [363].

The concentration of light by mesoscale truncated Si micropyramids, as depicted in Figs. 3.4(a), 3.5(a), and 3.6(a), demonstrates the interference nature of this effect through its distinctive properties. The quasi-periodic dependency of the IEF, FWHM, and d on D_S directly highlights the significant role interference effects plays on the light-concentrating ability of truncated Si micropyramids. This is further supported by how these periodic dependencies scale with the wavelength in the range of λ = 3-5 µm. For shorter wavelengths of λ = 3 µm, all extrema depend solely on the D_S values and coincide for D_L = 30 and D_L = 15 µm. This indicates that only a portion of the truncated Si micropyramids immediately next to the small base D_S is accountable for its light-concentrating properties of these truncated Si micropyramids. In contrast, for longer wavelengths of λ = 5 µm, the extrema of the blue curves representing the D_L = 30 µm case do not align with those of the red

curves representing the D_L = 15 μm case, indicating that both D_S and D_L values influence the light-concentrating properties of truncated Si micropyramids.

Furthermore, sharper light-concentration with FWHM ~ 0.6λ can be achieved with taller truncated Si micropyramids that have a reduced small base size D_S. This is a beneficial property for light-concentration onto smaller pixels of front-illuminated photodetectors FPAs. The quality of light-concentration diminishes with increased Si micropyramid truncation, where the FWHM reaches values in the range of ~λ - 2λ. Conversely, the peak IEF increases with greater Si micropyramid truncation, achieving nearly an order of magnitude intensity enhancement. The maximum peak IEF of ~7.5 is observed at $D_S \approx$ 13 μm for D_L = 15 μm, and at $D_S \approx$ 28 μm for D_L = 30 μm. The minima of the FWHM coincide with the minima of d, indicating that sharper light-concentration occurs at closer separation distances to the truncated Si micropyramids. The correlation between the minima of the FWHM and peaks of the IEF is understood by energy conservation through the requirement that the total photon flux is conserved along the light propagation direction.

In summary, integrating truncated Si micropyramidal arrays with photodetectors can offer numerous advantages in the MWIR and LWIR regimes through enhancing the SNR and operational temperature of imaging devices. The monolithic integration of these truncated Si micropyramids with photon detectors can be achieved in the back-illuminated configuration by fabricating p-i-n or Schottky barrier photodiodes, as well as photoconductors like PbSe directly on top of the small base D_S of each individual truncated Si micropyramid [94-99, 102-104, 363]. Alternatively, these truncated Si micropyramidal arrays can be integrated heterogeneously with photon detectors that exhibit high SNR at

sufficiently elevated temperatures, such as HgCdTe based detection materials [4]. These monolithic or hybrid configurations are shown in Fig. 1.4 [1]. Recent innovations in photodetectors with thin absorbing layers include resonant grating-enhanced black phosphorus MWIR photodetectors [322], and avalanche photon-trapping photodiodes [323]. Another potential application of truncated Si micropyramidal arrays is their use as a photolithography tool for patterning photoresists with subwavelength resolution. Photopatterning over a large area can be achieved using truncated Si micropyramid arrays or by surface scanning with individual truncated Si micropyramidal microprobes. Achieving minimal spot sizes in this application requires optimizing the geometry of the truncated Si micropyramids, a task facilitated by employing PML BCs.

3.5. Emitter Applications

Truncated Si micropyramid arrays also have potential emitter applications by addressing the challenges related to light extraction and directionality of light sources embedded in materials with high refractive indices. Enhancing the efficiency of light-emitting diodes (LEDs) involves addressing the challenge of light extraction. One solution to this problem is through utilizing solid immersion lenses (SILs), which are optically transparent truncated microspheres, brought into contact with the samples under investigation [324, 325]. This issue is also crucial for quantum light sources such as quantum dots, color centers, implanted defects, and single ions, where achieving maximum photon flux is essential for measuring correlation effects. This relates to the fact that refraction at the semiconductor-air interface diminishes the solid angle through which light can be extracted from the slab, resulting in less than 1% efficiency for a material with a

refractive index of $n \approx 3.5$. The confinement of light within such a slab is depicted by the field profile and the far-field EM field distribution, as depicted in the 3-D FDTD numerical modeling simulations shown in Fig. 3.7(b, c). These 3-D FDTD numerical modeling simulations are conducted with a dipole source positioned 1 μm beneath the surface of the Si slab, oscillating perpendicularly to the specified cross-section at a wavelength of $\lambda = 3$ μm.

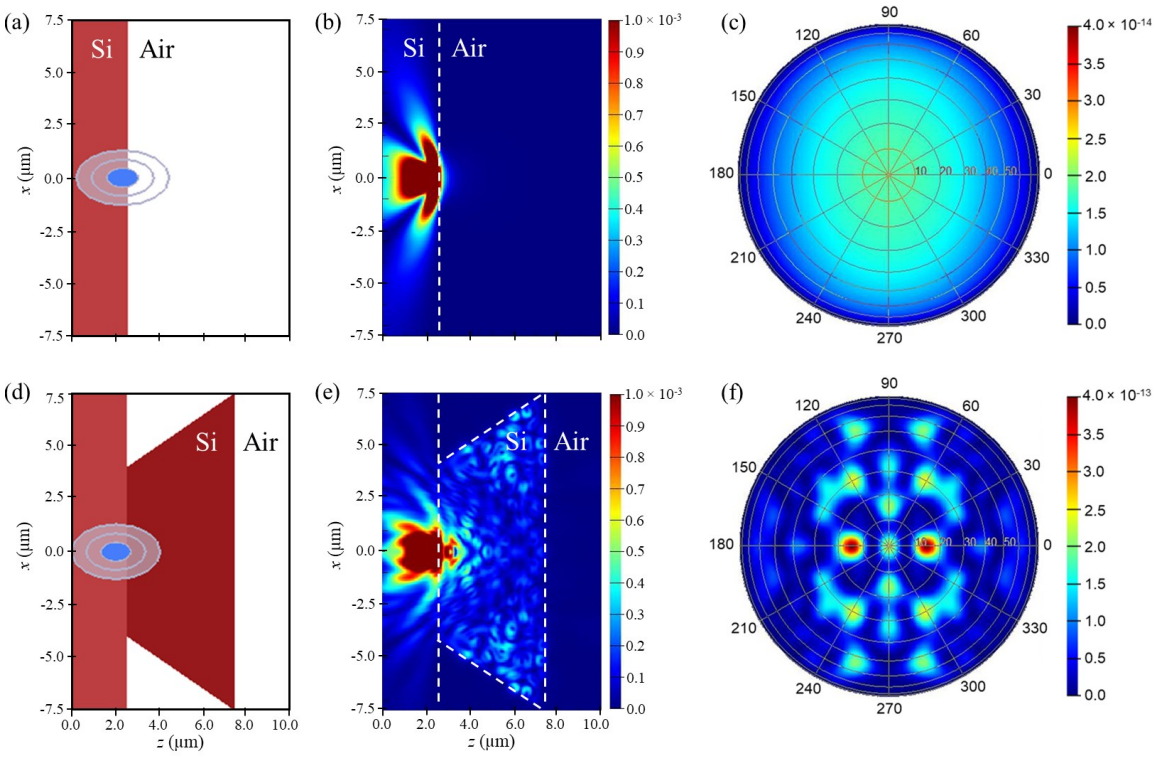

Figure 3.7. 3-D FDTD numerical modeling simulation performed for a dipole source embedded at 1 μm depth in a Si slab. Comparison of the light extraction and directionality of the dipole sources embedded in Si slabs for the following cases: (a-c) bare Si wafer and (d-f) dipole positioned close to the small base D_S of the truncated Si micropyramid. The dipole source oscillates perpendicular to the *xz* plane at $\lambda = 3$ μm. The dimensions of the truncated Si micropyramid in (d-f) are $D_L = 15$ μm and $D_S = 6.4$ μm. Efficient coupling of the dipole's emission into the truncated Si micropyramid is depicted by comparing EM field profiles portrayed in (b, e). An order of magnitude higher extraction efficiency was obtained in the case of using a truncated Si micropyramid, where a more structured far-field emission profile is apparent by comparing the far-field EM field distributions shown in (c, f).

Several microstructures have been suggested to improve the extraction efficiency, such as nanowires [326, 327], micro-pillars [328, 329], dielectric resonators [330, 331], and photonic crystals [332, 333]. All these designs necessitate precise positioning of the quantum sources within the fabricated microstructures alongside spectral alignment of their emission peaks with the resonance peaks of the photonic environment. In this context, using a SIL with an index of refraction n matched to that of the slab is one of the most straightforward methods to enhance extraction efficiency from millimeter-scale areas of the sample [334, 335].

Si photonics plays a crucial role in quantum optics by enabling the monolithic integration of single-photon sources with quantum photonic ICs, thereby facilitating large-scale integration [336]. Several components of these cryogenic photonic ICs are already developed, such as delay lines [337], detectors [338], phase shifters [339], and modulators [340]. Progress in this discipline relies on the accessibility of efficient single-photon sources. Recently, a variety of such emitters have been identified in commercial silicon-on-insulator (SOI) wafers, including G centers with a wavelength of λ_G = 1278 nm [341], T centers [342], W centers [343], and other similar centers. Single W and G centers have been successfully fabricated in Si wafers through utilizing a focused ion beam with large probability [316]. Efficient extraction of single photons in such scenarios is crucial for harnessing quantum correlation effects.

The inherent solution to this challenge is provided by a SIL, typically in the form of a Si hemisphere affixed to the Si slab. However, these micro-dielectric lenses with 3-D geometry cannot be fabricated using conventional nanofabrication methods. While standalone fabrication of such lenses is feasible through micromachining, it does not

address the issue of integrating them on a substantially large scale with quantum photonic ICs. Furthermore, the emission pattern extracted through a SIL exhibits broad directionality, which is suboptimal for such integration purposes.

A straightforward and effective solution to this issue is by utilizing truncated silicon micropyramids as functional equivalents of hemispherical SILs. Anisotropic wet etching of Si enables the fabrication of truncated Si micropyramidal arrays at these aforementioned desired positions. The depicted geometry is exemplified by the results of 3-D FDTD numerical modeling simulations in Fig. 3.7(d-f). These numerical modeling simulations assume the dipole source is at the same position, 1 μm below the surface of the Si slab, as depicted in Fig. 3.7(a-c), and oscillating perpendicular to the specified cross-section at a wavelength of $\lambda = 3$ μm. Although the dipole source in Fig. 3.7(d-f) is located outside the truncated Si micropyramid, similar outcomes can be achieved if the dipole sources are positioned inside the truncated Si micropyramid, particularly near its small base D_S. This suggests that in practical scenarios where single photon sources are embedded within truncated Si micropyramids using a focused ion beam, the emission patterns would closely resemble those depicted in Fig. 3.7(d-f).

The enhanced coupling of the dipole's emission into the truncated Si micropyramid is evident from the comparison of the EM field profiles depicted in Fig. 3.7(b, e). A significant order of magnitude increase in the extraction efficiency is apparent when comparing the far-field emission polar plots depicted in Fig. 3.7(c, f). The emission pattern depicted in Fig. 3.7(f) exhibits a distinct modal structure when compared to Fig. 3.7(c). Additionally, the truncated Si micropyramid enhances the directionality of the extracted light, where the majority of the light is emitted within a 20° half-cone angle. Both the

improvements in extraction efficiency and directionality are crucial in the study of single photon sources in quantum optics.

Another potential application of truncated Si micropyramidal arrays involves their heterogeneous integration with LED arrays to improve their light extraction properties. This integration could prove beneficial in the MWIR spectral range where Si offers transparency, thereby enhancing the efficiency and directionality of IR scene projectors [308, 315].

3.6. Conclusions

This research was motivated by contemporary suggestions for utilizing light-concentrating microstructures to augment the capabilities of MWIR FPAs. The optical properties of truncated Si micropyramids were researched through the utilization of 3-D FDTD numerical modeling simulations based on two types of boundary conditions. By employing periodic BCs, the diffraction and interference characteristics of such truncated Si micropyramid arrays were analyzed, which resulted in the observation of the Talbot effect and the formation of Talbot images. These Talbot images were directly observed and experimentally investigated. Earlier, Talbot lithography was suggested as a potential use for 3-D photolithography, and in theory, truncated Si micropyramidal arrays could serve this purpose. Additionally, if neighboring micropyramids are illuminated, there might be some optical coupling between the modes trapped in individual micropyramids. Somewhat similar coupling effects have been observed between whispering gallery modes in bispheres [364]. Such coupling effects do not play a significant role in this work because of the much larger separations between the modes confined inside individual

micropyramids. Another possibility is based on coupling to the photonic band structures of periodic arrays similar to that studied in photonic crystal waveguides [365, 366]. In this work, however, waveguiding between the individual micropyramids is not possible and only diffraction effects take place. They were included in the 3-D FDTD numerical modeling calculations performed with periodic BCs.

Conversely, through utilizing PML BCs, the light-concentration and focusing characteristics of such truncated Si micropyramidal arrays within the MWIR spectral range were explained. A significant increase in intensity was observed, up to an order of magnitude, due to the concentration of light with subwavelength photonic jet widths. Furthermore, mesoscale optical interference effects were observed in the subwavelength light-concentrating properties exhibited by these truncated Si micropyramids. The intricate connection between their light-concentrating and imaging applications suggests the potential for high-index truncated Si micropyramids to function as contact superlenses when in contact with objects, akin to the behavior of high-index microspheres.

These findings do not signify the boundaries of this technology. Instead, however, these findings highlight the versatility of Si anisotropic wet etching as a versatile tool for creating novel structures designed for various applications in light concentration, diffraction gratings, and other innovative devices. In theory, significantly tighter light concentration can be obtained in analogous micropyramidal structures featuring deeply subwavelength dimensions, thanks to photonic nanojets [344] or photonic funnels [345]. These beams can be directed into photodetector mesas of MWIR photodetector FPAs, enhancing photon collection, SNR, and operational temperature of these devices.

It was demonstrated that the optical characteristics of such structures created through Si anisotropic wet etching, specifically focusing on truncated Si micropyramidal arrays with sidewall angles of 54.74˚, revealed their remarkable ability to concentrate light down to wavelength-scale dimensions. This intriguing property has significant potential for improving the collection of photons with a broad angle-of-view on pixels in MWIR FPAs. It offers the opportunity to decrease the pixel size and therefore reduce the thermal noise of photodetectors while maintaining the optical signal. It can be envisioned that the other fabricated arrays could be utilized for similar applications. The objective of this research was to demonstrate the substantial potential Si anisotropic wet etching has in fabricating low cost, high yield arrays with atomically smooth sidewalls to utilize for optical applications.

Lastly, another promising application of these truncated Si micropyramid arrays was demonstrated, where the micropyramids serve as contact microlenses to enhance the extraction of light as well as directionality from local sources implanted in high-index semiconductor slabs. This introduces a new avenue for utilizing this technology to improve the efficiency of light extraction from single-photon sources fabricated in Si slabs, particularly for applications in quantum photonic ICs. The conventional approach to addressing this issue using hemispherical SILs is not aligned with substantially large-scale integration. It was demonstrated that micropyramidal Si photonics enhances the extraction of single photons by an order of magnitude with highly directional output, which is exceedingly beneficial for leveraging quantum correlation effects in such systems. It was also proposed that integrating truncated Si micropyramidal arrays with LED arrays heterogeneously can enhance the efficiency and directionality of IR scene projectors.

CHAPTER 4: PHOTODETECTOR FOCAL PLANE ARRAYS ENHANCED WITH SI MICROPYRAMID ARRAYS

4.1. Introduction

In this dissertation, methods to enhance IR photodetector FPAs by integrating them with truncated Si micropyramidal arrays are explored. The thermal noise of a photovoltaic detector is proportional to its linear dimensions [1], which can be nearly equivalent to the size of the smaller base of the micropyramid. Reducing the size of the photodetectors lowers their dark current, while the light collection efficiency can be enhanced through using light-concentrating structures, such as truncated Si micropyramids, positioned over individual pixels. These truncated micropyramids gather light from a larger area and concentrate it onto a smaller region aligned with the photodetector's mesa, serving to maintain or improve the signal-to-noise ratio (SNR). Since the dark current noise increases with thermal energy, shrinking the detectors and incorporating light-concentrating structures allows for higher operating temperatures while preserving the SNR. Similar concepts have been proposed using integrated microlenses [17-19, 34-36], microspheres [20-22, 51, 52, 66, 89, 114], and metalenses [12-16] to achieve SNR improvements.

This chapter focuses on the fabrication of truncated Si micropyramidal arrays, as well as the numerical modeling and testing of their optical properties for detector applications. Truncated micropyramidal detector arrays can be integrated with a readout integrated circuit (ROIC) [1]. Heterogeneous integration with highly efficient front-

illuminated photodetector FPAs can be achieved by aligning the truncated micropyramids with photodetector mesas, similar to arrays of tapered microconical waveguides [106, 112]. The advantage of this approach is that FPAs can be made from materials with high MWIR absorption, such as HgCdTe or Type II Strained Layer Superlattice (T2SL) materials. Alternatively, monolithic integration can be realized by fabricating p-i-n or Schottky barrier detectors directly on top of individual truncated micropyramids [94-99, 102-104], which is feasible in a back-illuminated geometry for straightforward ROIC integration.

The main objectives of this research were to fabricate truncated Si micropyramidal arrays, integrate them with platinum/silicide (PtSi) Schottky barrier photodetectors, and conduct optical testing of these devices in comparison with reference planar photodetectors of the same size. This comparison is aimed at evaluating the signal enhancement achieved by the proposed micropyramid designs. In order to make this comparison, determining the quantum efficiency (QE) of these devices is necessary. QE is defined as the ratio of the electrical output divided by the optical input. The QE of conventional planar Si-based photodetectors is limited by Si's indirect band gap, leading to low absorption and inefficient photocarrier collection. However, the light-concentrating properties of the truncated Si micropyramids, once integrated with the photodetectors, offer significant potential for increased absorption, resulting in improved QE and enhanced photoresponse. Another advantage is that the size of the photodetector mesa positioned near the top of the truncated micropyramid can be reduced compared to standard planar devices, which may lead to lower thermal noise in the proposed devices and potentially allow for higher operating temperatures [94-99, 102-104, 363].

A Schottky barrier forms at the interface between a metal like Al, Cu, or Pt and a Si substrate. After annealing, a metal/silicide layer is created, allowing the device to function as a mid-wave infrared (MWIR) or short-wave infrared (SWIR) photodetector by generating and separating electron-hole pairs when a reverse bias is applied. Recently, the ability to rapidly fabricate Si micropyramidal arrays using cost-effective anisotropic wet etching has made it easier to integrate these arrays with photodetectors through either monolithic or heterogeneous methods [94-99, 102-104, 363]. Earlier attempts to use Si micropyramid arrays integrated with photodetectors focused on plasmonic mechanisms to concentrate electromagnetic (EM) power at the pyramid tips [23]. In this case, the sidewalls were metallized with Al, converting incident photons into plasmonic excitations that were adiabatically compressed toward the 50 nm micropyramid tip. The process for generating electron-hole pairs at the tips of these metallized micropyramids was quite complex, but a photoresponse enhancement of up to 100 times at $\lambda = 1.3$ μm was reported [23]. Another approach, using inverted micropyramids with a 4 μm period integrated with Cu/silicide Schottky barrier photodetectors, showed a nearly 40-fold increase in photoresponse [24]. However, these designs required highly precise nanoscale fabrication and component alignment, making them challenging to implement.

In the designs discussed in this Chapter, it is proposed to use appropriately large micropyramids with truncated tops that are optically coupled to photodetectors [94-99, 102-104, 363]. These truncated micropyramids function similarly to "tapered" waveguides or reflective light concentrators used in solar cells. These structures are far easier to fabricate compared to nanoplasmonic counterparts [23, 24], as they only require micron-scale precision, which can be achieved through standard photolithographic techniques.

Chapter 4 focuses on the experimental fabrication and testing of monolithically integrated PtSi detectors with truncated Si micropyramids, as well as a novel way to further improve these detectors. In section 4.2, it cover the fabrication of monolithically integrated MWIR silicon-platinum silicide (PtSi/p-Si) Schottky barrier photodetectors directly on top of the truncated Si micropyramids. This was done to experimentally determine if reducing the dimensions of the photodetectors reduces the dark current, while the light collection efficiency can be improved using light-concentrating truncated micropyramids. This allows light to be collected from a larger area and concentrated into a much smaller area that can be aligned with the photodetector's mesa to maintain or enhance the SNR in order to increase the operating temperature of FPAs. In section 4.3, a detailed analysis of the truncated micropyramid FPA was conducted through characterizing the fabricated devices' spectral response and QE in order to determine the enhancement obtained through integration with truncated micropyramids. Furthermore, in section 4.4, a novel way to further enhance the SNR through utilizing a silicon-on-insulator (SOI) wafer to create a resonator cavity is discussed. This research demonstrates that truncated Si micropyramidal photonics offers a versatile optoelectronic platform capable of improving the SNR and raising the operating temperature of MWIR FPAs.

4.2. Fabrication of Monolithically Integrated Photodetectors with Si Micropyramids

In order to experimentally investigate the light-concentration capabilities of truncated Si micropyramidal arrays, they were monolithically integrated with MWIR photodetectors [94-99, 102-104, 363]. This integration involved fabricating silicon-platinum silicide (PtSi/p-Si) Schottky barrier photodetectors directly atop each truncated

micropyramid, as depicted schematically in Fig. 4.1. In order to focus on studying the signal enhancement of these truncated micropyramids rather than constructing a fully functional camera, Pt was deposited on the tops of individual truncated micropyramids, and 100 PtSi Schottky barrier photodetectors were electrically connected in parallel to streamline the characterization process.

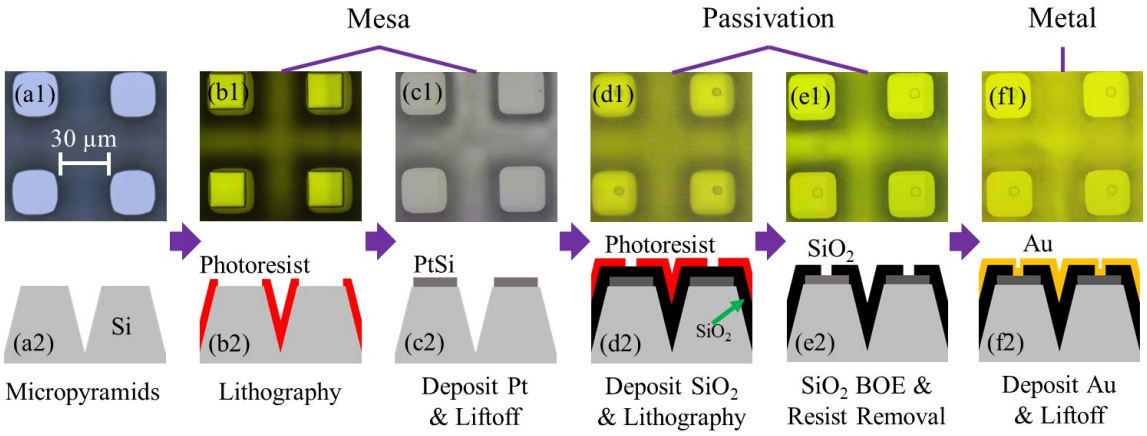

Figure 4.1. Diagram depicting the fabrication protocol to create 10 × 10 arrays of monolithically integrated Si micropyramids with MWIR PtSi/p-Si Schottky barrier photodetectors fabricated on the small based of these truncated micropyramids. The top row depicts microscope images of the top-down view, and the bottom row depicts diagrams of the corresponding side-view. (a) The device fabrication begins with the micropyramids previously fabricated, as described in Chapter 2. (b) The mesa fabrication steps first requires the mesa size to be defined with photolithography. (c) The mesa fabrication step ends with the deposition of Pt and the excess Pt is lifted off by removing the photoresist. (d) The passivation step begins by depositing a uniform 300 nm thick layer of SiO_2 and performing photolithography to prepare for the next step. (e) The passivation step ends when the SiO_2 undergoes a BOE etch to create through-holes in the SiO_2 layer, where the remaining photoresist is removed. (f) The metal step is where the 5 nm thick Cr and 300 nm thick Au layers are deposited, in order to electrically connect all 100 detectors together for characterization.

It is important to mention that a limitation of metal/silicide Schottky barrier photodetectors is their low QE, which is due to their inadequate absorption in the MWIR range. To enhance absorption, the surfaces of the truncated micropyramids were coated with Au, creating a mirror-like configuration that reflects light back toward the active detector region [96-99, 103, 363]. However, photonic jets cannot form in this configuration since the highly reflective mirror obstructs photon transmission through the truncated

micropyramids. Consequently, this monolithic integration with photodetectors represents a different scenario compared to that described in Chapter 3. The experimental objective was to compare the photoresponse of detectors integrated with truncated micropyramidal light concentrators to that of the same detectors in a traditional planar geometry.

The integration of Si micropyramids with the photodetectors involved several steps [96-99, 103, 363], where these steps are described in Fig. 4.1. The device fabrication begins with the fabrication of the truncated Si micropyramids, as described in Chapter 2, but on a 1-10 Ω-cm p-type double side polished (DSP) Si wafer. These truncated Si micropyramids were anisotropically wet etched with 25% TMAH and 0.2% v/v Triton X-100 at 80° C, and resulted in 10 × 10 truncated Si micropyramidal arrays featuring 54.74° sidewall angles, a 60 μm pitch, a 26 μm top size, and a height of 24 μm.

The fabrication of 21 μm square PtSi Schottky barrier photodetectors with ~ 2 nm thickness were created directly on the small bases of these micropyramids, as well as same size planar reference detectors and large 58 μm square planar reference detectors on the same sample, as shown in Fig. 4.2. The wafer was cleaned with 1165 solvent at 95˚ C for 5 minutes, then rinsed with acetone, methanol, and IPA, and then dried with nitrogen gas. A dehydration bake was performed at 110˚ C for 75 seconds, and the wafer was let to cool for 30 seconds. Next, hexamethyldisilazane (HMDS) was spin coated at 2000 RPM with a ramp rate of 200 RPM/second for 30 seconds as an adhesion promoter. It was then baked at 110˚ C for 75 seconds, and left to cool for 30 seconds before the thick photoresist was spin coated on. A thick photoresist is necessary due to the large heights of the micropyramids. AZP4620 positive photoresist was spin coated at 4000 RPM with a ramp rate of 200 RPM/second for 120 seconds, then baked at 110˚ C for 120 seconds, and the

wafer was let to cool for 30 seconds. This low ramp rate was necessary to evenly coat the large topology difference caused by the micropyramids. Afterwards, the photoresist was exposed times with a Heidelberg DWL 66+ laser writer to create the patterns for the mesa and developed with 1:5 351:DI. Next, a 4-minute O_2 ash was completed to remove any residual photoresist. Then a pre-metal BOE dip was performed before 1 nm of Pt was deposited with an electron beam evaporator. Afterwards, liftoff was performed with 1165 solvent at 95˚ C for 5 minutes, then rinsed with acetone, methanol, and IPA, and then dried with nitrogen gas. The PtSi layer was created by annealing in an oven at 400° C in forming gas for 10 minutes.

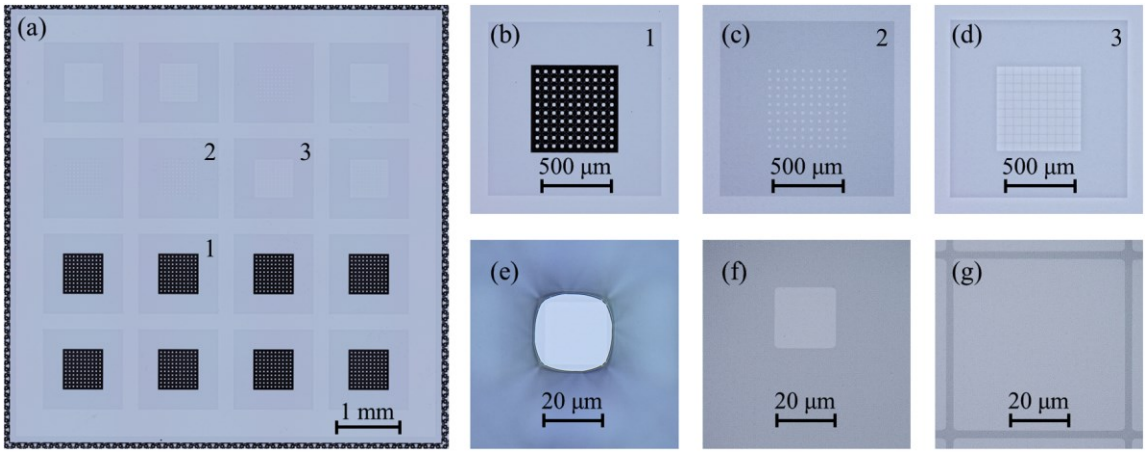

Figure 4.2. Microscope images showing the fabrication step for MWIR PtSi detectors corresponding to Fig. 4.1(c). (a) An entire die is shown, where the top eight detectors are planar reference devices and the bottom eight detectors are fabricated on top of micropyramids. (b, e) 10 × 10 PtSi detector array with 21 µm squares fabricated on top of 60 µm pitch micropyramids. (c, f) 10 × 10 PtSi reference detector array of the same size as the detectors on the micropyramids. (d, g) 10 × 10 PtSi detector array with a large fill-factor of 58 µm squares with 60 µm pitch.

Passivation and isolation of the photodetectors were carried out by first depositing a 300 nm thick SiO_2 layer using plasma-enhanced chemical vapor deposition (PECVD). After deposition, the sample was cleaned with 1165 solvent at 95˚ C for 5 minutes, then rinsed with acetone, methanol, and IPA, and then dried with nitrogen gas. A dehydration

bake was performed at 110˚ C for 75 seconds, and the wafer was let to cool for 30 seconds. Next, HMDS was spin coated at 2000 RPM with a ramp rate of 200 RPM/second for 30 seconds as an adhesion promoter. It was then baked at 110˚ C for 75 seconds and left to cool for 30 seconds. AZP4620 positive photoresist was then spin coated at 4000 RPM with a ramp rate of 200 RPM/second for 120 seconds, then baked at 110˚ C for 120 seconds, and the wafer was let to cool for 30 seconds. Afterwards, the photoresist was exposed times with a Heidelberg DWL 66+ laser writer to create the patterns for the through holes and was developed with 1:5 351:DI. Next, a 4-minute O_2 ash was completed to remove any residual photoresist. Lastly, a BOE etch was completed to etch small ~3 µm holes in the SiO_2 layer to reveal the PtSi detectors underneath, in order to create the n-contact. The remaining photoresist was stripped with 1165 solvent at 95˚ C for 5 minutes, then rinsed with acetone, methanol, and IPA, and then dried with nitrogen gas. At this stage, the devices looked as they do in Fig. 4.3.

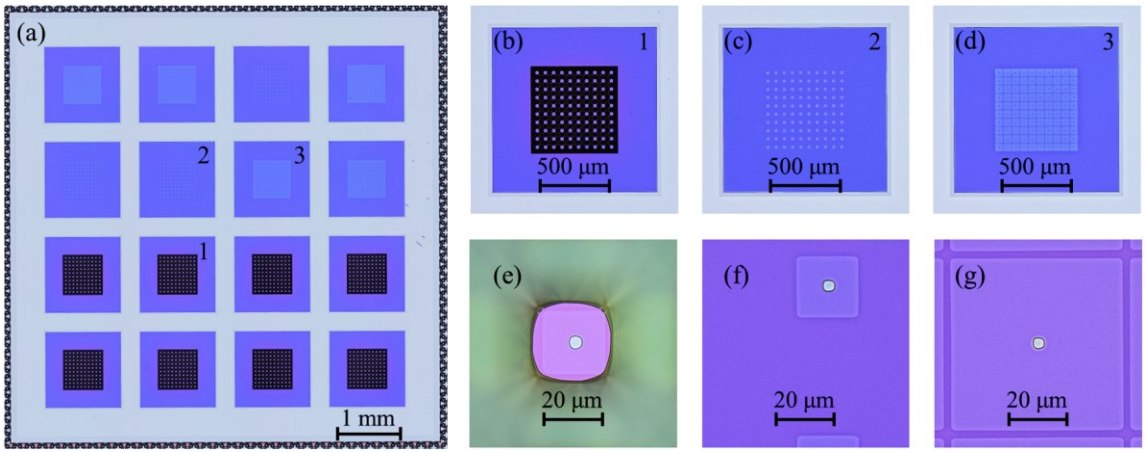

Figure 4.3. Microscope images showing the fabrication step for MWIR PtSi detectors corresponding to Fig. 4.1(e). (a) An entire die is shown, where the top eight detectors are planar reference devices and the bottom eight detectors are fabricated on top of micropyramids. (b, e) 10 × 10 PtSi detector array with 21 µm squares fabricated on top of 60 µm pitch micropyramids. (c, f) 10 × 10 PtSi reference detector array of the same size as the detectors on the micropyramids. (d, g) 10 × 10 PtSi detector array with a large fill-factor of 58 µm squares with 60 µm pitch.

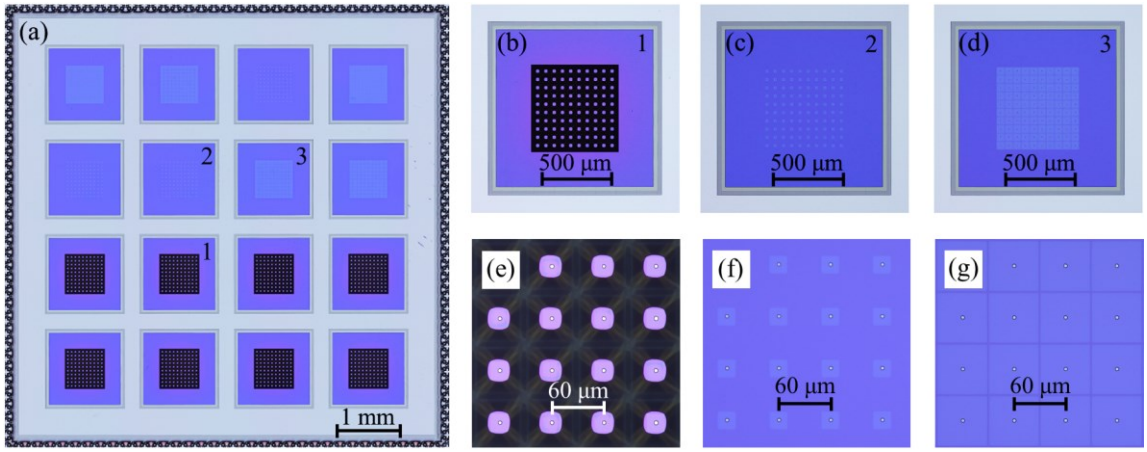

Figure 4.4. Microscope images showing the fabrication step for MWIR PtSi detectors corresponding to Fig. 4.1(f) before the 5 nm of Cr and 300 nm of Au were deposited. (a) An entire die is shown, where the top eight detectors are planar reference devices and the bottom eight detectors are fabricated on top of micropyramids. (b, e) 10 × 10 PtSi detector array with 21 µm squares fabricated on top of 60 µm pitch micropyramids. (c, f) 10 × 10 PtSi reference detector array of the same size as the detectors on the micropyramids. (d, g) 10 × 10 PtSi detector array with a large fill-factor of 58 µm squares with 60 µm pitch.

The final step to create the monolithically integrated PtSi detector arrays was to create the electrical contacts which combine all 100 detectors together. The sample was cleaned with 1165 solvent at 95˚ C for 5 minutes, then rinsed with acetone, methanol, and IPA, and then dried with nitrogen gas. A dehydration bake was performed at 110˚ C for 75 seconds, and the wafer was let to cool for 30 seconds. AZ15nXT negative photoresist was then spin coated at 4000 RPM with a ramp rate of 200 RPM/second for 120 seconds, then baked at 110˚ C for 75 seconds, and the wafer was let to cool for 30 seconds. Afterwards, the photoresist was exposed times with a Heidelberg DWL 66+ laser writer to create the square perimeter pattern around each detector array as shown in Fig. 4.4. A post exposure bake at 120˚ C for 60 seconds was necessary, after which the sample was let to cool for 30 seconds. Then, the negative photoresist was developed with 300 MIF for ~3 minutes. A 2-minute O_2 ash then took place, and 5 nm of Cr then 300 nm of Au were deposited with an e-beam evaporator, which filled the small openings in the SiO_2 layer and electrically

connected the 100 detectors. Liftoff of AZ15nXT required the use of NI555 solvent heated to 85˚ C for ~10 minutes. Lastly, the sample was cleaned again with 1165 solvent at 95˚ C for 5 minutes, then rinsed with acetone, methanol, and IPA, and then dried with nitrogen gas. At this stage, the sample appeared as it does in Fig. 4.5.

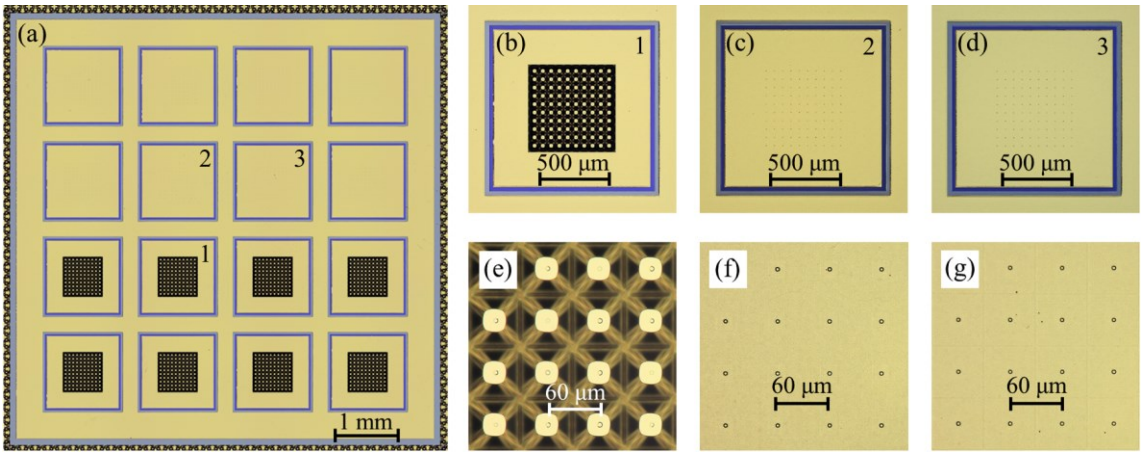

Figure 4.5. Microscope images showing the fabrication step for MWIR PtSi detectors corresponding to Fig. 4.1(f) after the 5 nm of Cr and 300 nm of Au were deposited. (a) An entire die is shown, where the top eight detectors are planar reference devices and the bottom eight detectors are fabricated on top of micropyramids. (b, e) 10 × 10 PtSi detector array with 21 µm squares fabricated on top of 60 µm pitch micropyramids. (c, f) 10 × 10 PtSi reference detector array of the same size as the detectors on the micropyramids. (d, g) 10 × 10 PtSi detector array with a large fill-factor of 58 µm squares with 60 µm pitch.

After fabrication, the samples were diced into individual dies and prepared for characterization by packaging. The packaging process involves mounting the dies in ceramic chip carriers using a two-part thermally conductive epoxy, suitable for temperature-dependent measurements. The dies are mounted on specialized chip carriers that feature a hole in the center, allowing light to pass through the package and reach the detectors for back-side illumination (BSI). An example die in a chip carrier is shown in Fig. 4.6(e). The epoxy is cured on a hotplate at 100° C for ~30-60 minutes. Once the die is mounted to the ceramic chip carrier, the individual detectors are wire bonded, establishing

electrical connections between the device and the testing equipment. After packaging, the micropyramidal detectors and the reference detectors were ready for characterization.

The key innovation was the deposition of a 3-D metallic mirror on the sidewalls of the truncated micropyramids [103, 363], enabling efficient photon concentration onto the photodetectors. The design offers several advantages such as an improved photon collection from a wider area, trapping of the photons inside the truncated micropyramids resulting in resonant optical properties, and leveraging multiple light propagation directions in the detector region. This increases the optical path length and, consequently, enhances the absorption probability and boosts the QE of the photodetectors. The 3-D mirror configuration in Fig. 4.6(a, c) builds upon the previously suggested concept of utilizing back-reflectors, which was implemented in more conventional planar MWIR photodetector FPAs, as illustrated in Fig. 4.6(b, d) [5, 44].

4.3. MWIR Micropyramidal Photodetector Characterization

The MWIR micropyramidal photodetectors and their planar reference devices were then characterized by utilizing the experimental setups shown in Fig. 4.6. This characterization includes analysis of the spectral response measurements (to optically determine the detector's barrier height) and QE measurements (to calculate the detector's QE spectrum and subsequently the enhancement obtained through integration with micropyramids). These characterization setups were not designed by me, but by collaborators at the Air Force Research Laboratory (AFRL) [5].

The PtSi Schottky barrier photodetectors were illuminated through the polished back surface of the substrate as seen in Fig. 4.6(a-d) with MWIR radiation concentrated

toward the small bases of the micropyramids, where partial photon absorption occurred in the PtSi regions. As shown in Fig. 4.6(e), the photoresponse spectra were measured using a Vertex 80v Fourier transform infrared spectrometer (FTIR) by Bruker paired with an Agilent 4156C semiconductor parameter analyzer and a Keithley 428 current amplifier. The photodetector array was illuminated inside an LN_2 cooled dewar with a germanium (Ge) window to minimize ambient noise. The QE was measured using the same dewar but illuminated with a 1000°C Infrared Systems Development Corp. IR-563/301 cavity blackbody where a chopper, Keithley 428 current amplifier, and a Stanford Research Systems SR850 DSP lock-in amplifier were implemented as shown in Fig. 4.6(f). The chopper's frequency is matched with the lock-in amplifier. These QE measurements were calibrated against the incident photon flux, allowing direct comparison between the 10 × 10 photodetector array integrated with micropyramids and the reference array fabricated on the same Si wafer. In both these setups, the detectors were kept between 78K and 80K.

The dewar contains an LN_2 reservoir connected to a cold finger, which is used to cool the sample below ambient temperature. An indium shim is placed to ensure good thermal conductivity between the cold finger and the chip carrier. The chip carrier fits into a pressure-mounted socket with pins in-contact with the chip carrier in order to read out from different locations on the chip carrier, which were wire bonded to specific detector arrays for characterization. A cold shield is used to block unwanted light from reaching the detector. Once the chip carrier with the die is mounted, the dewar was vacuum sealed and cooled for low-temperature measurements. The temperature was measured with a LakeShore 335 temperature controller.

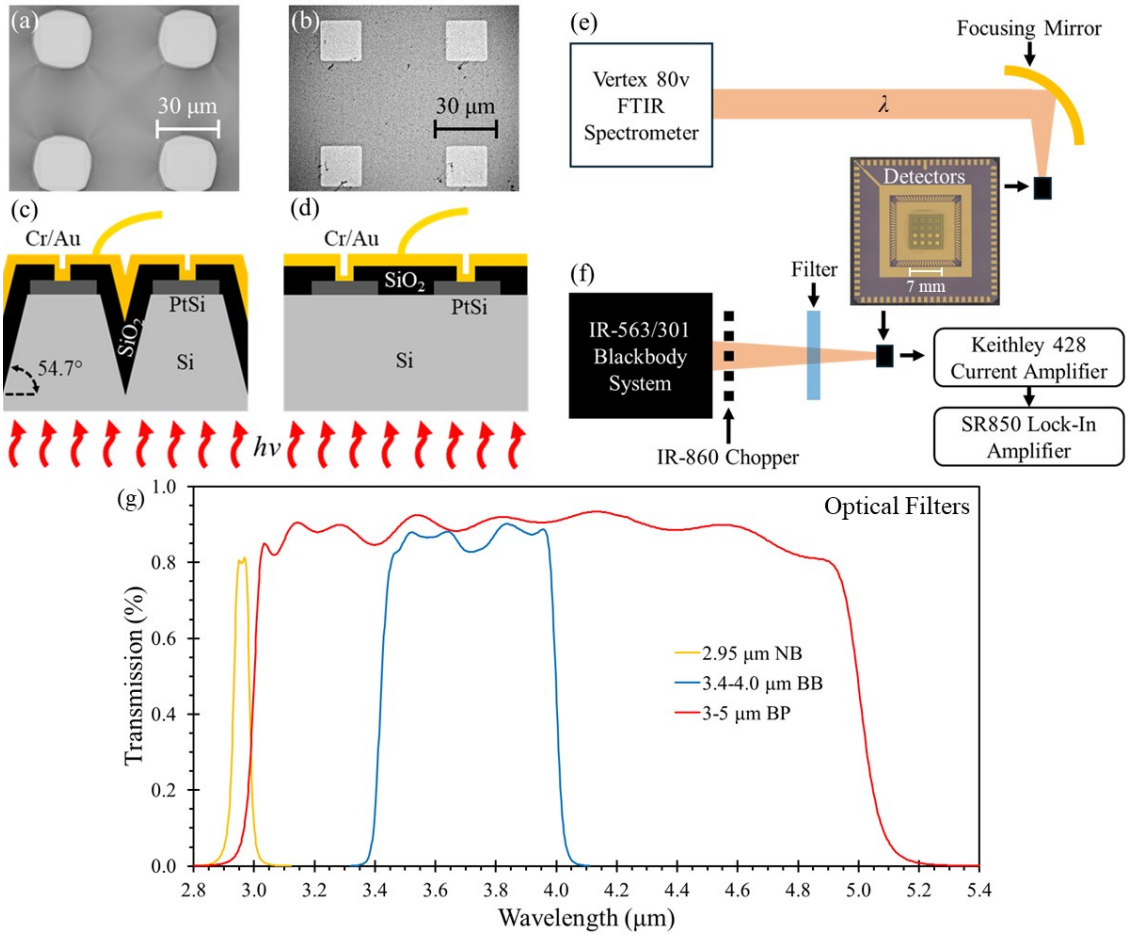

Figure 4.6. (a) Top-down microscope image and (c) corresponding cross-sectional view depicting monolithic integration of Si micropyramid arrays with MWIR PtSi/p-Si Schottky barrier photodetectors. These detectors have 21 μm square mesas fabricated on the small bases of the micropyramids. (b, d) Complimentary images depicting planar reference devices with identical photodetector mesa size. The device diagrams in (c, d) illustrate that, in both cases, the 5 nm thick Cr layer with 300 nm thick Au layer is electrically connected to the ~2 nm thick PtSi layer (n-contact) via a tiny ~3 μm opening in the 300 nm thick SiO_2 layer. (e) Measurement setup for the photoresponse spectra using a Vertex 80v Fourier transform infrared spectrometer (FTIR) by Bruker. (f) Measurement setup for determining the quantum efficiency (QE) of PtSi Schottky barrier detectors with a calibrated blackbody system heated to 1000° C. (g) Plot showing the transmission characteristics of the three optical filters used in the QE setup shown in (f).

Analysis of the measured spectral response data to verify that PtSi on p-type Si was indeed fabricated is shown in Fig. 4.7 for the four detectors in the center of the die seen in Figs 4.2-4.5(a). This analysis was conducted for numerous devices across several dies, but the results shown here are specifically for the die seen in those figures. In order to optically determine the barrier height, the spectral response measurements were normalized to unity.

Afterwards, the barrier height was determined by generating Fowler plots shown in the insets, which involves plotting the square root of the photon response R multiplied by the photon energy hv on the y-axis against the photon energy hv on the x-axis. The optically determined barrier heights for the 10 × 10 detector arrays with 21 μm mesa size as seen in Fig. 4.7(a-c) were $\varphi_B = 0.240 \pm 0.002$ eV, while the barrier height for the 10 × 10 detector array with large 58 μm mesa size as seen in Fig. 4.7(d) was $\varphi_B = 0.235 \pm 0.002$ eV. These values and their estimated errors were determined by averaging the 11 barrier heights obtained at different voltages, as seen in the insets of Fig. 4.7. The aforementioned barrier heights agree with published experimental values around $\varphi_B = 0.24$ eV [346-349], confirming that PtSi Schottky barrier detectors were indeed fabricated.

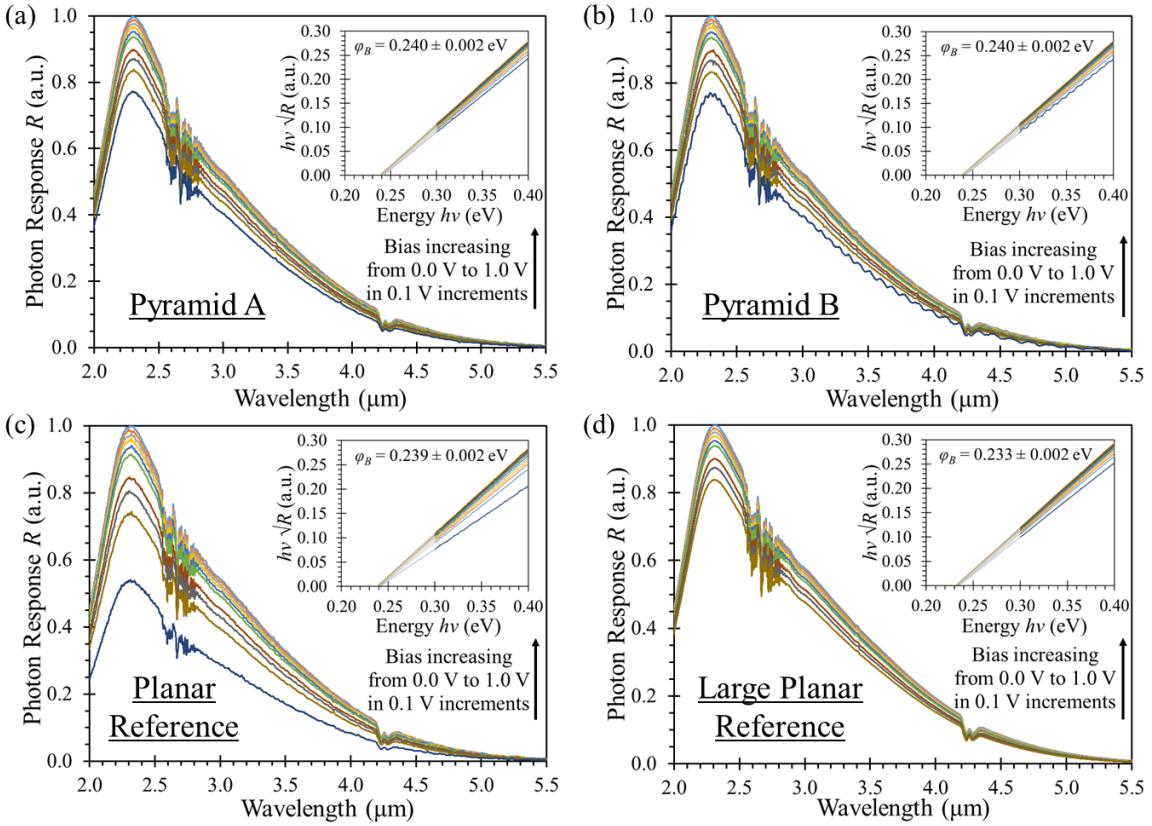

Figure 4.7. Spectral response plots for the four 10 × 10 detector arrays in the center of the dies shown in Figs 4.2(a)-4.5(a) measured at 80 K in reverse bias with a Ge window installed on the dewar, where the inset shows the corresponding Fowler plots used to optically determine the PtSi barrier height.

However, the discrepancy between φ_B for the 21 µm PtSi detectors compared to the 58 µm PtSi detectors warrants a more in-depth view. When plotting the respective barrier height against voltage in Fig. 4.8(a), the expected decrease with bias due to the Schottky imaging force is seen [11, 347, 349]. A further comparison between the dark current density plots shown in Fig. 4.8(b) display the corresponding expected increase in dark current with a lower barrier height [11, 346, 350, 351]. Numerous different factors impact the potential reasons for these differences between the 21 µm detector arrays and the 58 µm detector array. It could be attributed to the lack of etching away excess Pt with *Aqua regia* after the annealing step, which would reduce the QE and increase the dark current [5, 346]. Additionally, the fact 100 detectors were combined together in parallel could contribute to these differences [352].

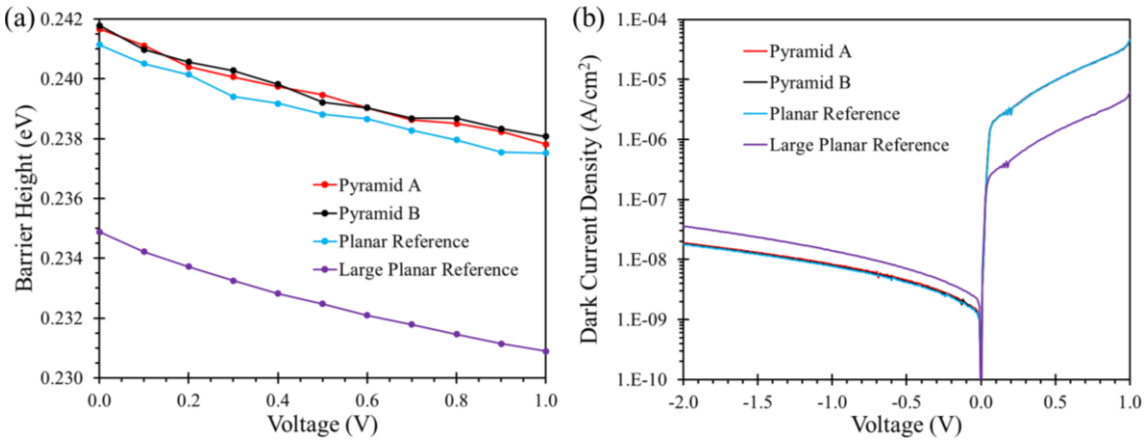

Figure 4.8. (a) Barrier height as a function of voltage and (b) dark current density as a function of voltage for the four 10 × 10 detector arrays in the center of the dies shown in Figs 4.2(a)-4.5(a) measured at 80 K in reverse bias with a Ge window installed on the dewar. These devices all were fabricated on the same Si wafer and were all exposed to the same annealing conditions, yet the large planar reference device shows different barrier height values.

Furthermore, the lower barrier height for the 58 µm detectors and the corresponding increase in dark current density could be due to a difference in the area-to-perimeter ratios (A/P) between the small and large detector mesas. For the 21 µm square mesas, $A/P = 5.25$,

while for the 58 μm square mesas, A/P = 14.5 [353, 354]. A low area-to-perimeter ratio indicates an increase in carrier recombination due to the high electric fields near the outsides of the mesa. In a larger detector, the electric field distribution across the junction is less uniform. This non-uniformity can result in areas where the electric field is weaker, leading to a lower effective barrier height in certain regions of the detector [353-355]. Carrier recombination also contributes to the gradual slope, or "soft" response, of the reverse I-V behavior [353-356]. Recombination due to the perimeter can be mitigated by the use of a p-n guard ring around the perimeter of the detector mesas [349, 356-359]. Upon reviewing the literature on size effects specifically for PtSi Schottky barriers, the only size effect articles found were for n-type Si, which actually indicated a barrier height increase with larger detector size; opposite to the case shown in this work [351, 360]. Perhaps the effects discussed by H. Efeoğlu, A. Turut, and M. Gül for PtSi fabricated on n-type Si wafers has an opposite effect for p-type Si wafer, but studying size effects of small PtSi detectors fabricated on p-type Si wafers is outside the scope of my research. Therefore, it was decided to not compare the QE of the large reference detector array to the QE of the micropyramidal detector array, and only compare the same size detector arrays because this comparison removes all the aforementioned concerns.

QE is the characterization parameter necessary to determine the enhancement capability of detectors integrated with micropyramids as compared to a conventional planar device because this parameter allows us to directly and quantitatively compare the difference in device performance and, thus, the increase in photoresponse due to integration with micropyramids. The spectral response measurement technique shown in Fig. 4.6(e) resulted in a curve with arbitrary units on the y-axis instead of QE. The straightforward

method to measure the QE spectra would be to measure it for a device with known QE in order to calibrate the measurement setup, then measure the QE of the test devices directly. This method presents several challenges. First, spectrally calibrated detectors are scarce, particularly for infrared wavelengths beyond 2 μm [5]. Second, the measurement's accuracy depends heavily on the precision of the initial calibration of the reference detector. Lastly, the FTIR output is usually focused onto the detector (as seen in Fig. 4.6(e)) to increase the SNR. This increases the risk of misalignment between the reference detector and the detector being tested. These problems were avoided by using a calibrated blackbody source to determine the number of photons incident on the detector [5, 30]. Therefore, the ratio of the electrical output divided by the optical input can be determined.

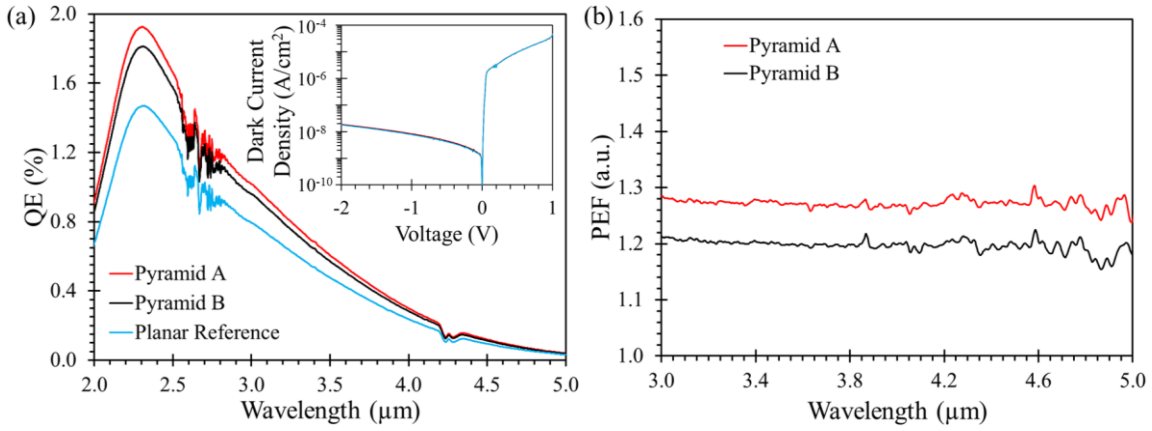

Figure 4.9. (a) Comparison of the QE spectra from two 10 × 10 micropyramidal photodetector arrays, shown by the red and black curves, to the corresponding 10 × 10 planar reference photodetector array fabricated on the same Si wafer, shown by the blue curve. The detector mesas were 21 μm squares with ~2 nm thick PtSi. The insert shows that the dark current density-voltage (I-V) relationships in these three cases were identical. (b) PEF spectra showing ~1.25× signal enhancement due to the micropyramids. This PEF spectra were smaller, potentially due to edge leakage current effects. This is apparent in Fig. 4.2(e) where the corners of the mesa on the micropyramid are over the edge of the micropyramid.

In order to obtain the QE over a spectral range, the QE was measured by using the setup shown in Fig. 4.6(f) with bandpass filters over narrow bands and with the chip carrier in the dewar placed 20 cm away from the blackbody source. These QE measurements were

calibrated against the incident photon flux by the blackbody source, enabling the calculation of relative scaling factors to scale the spectral response measurements to meaningful units of QE in percent on the *y*-axis. The incident photon flux on the detector Φ can be determined from the setup's geometry [5, 30]. This allowed for direct comparison between the 10 × 10 photodetector array integrated with micropyramids and the reference array fabricated on the same Si wafer.

Specifically, the QE spectrum was determined by the following analysis. The measured QE over a narrow range is determined by which optical filter was used (shown in Fig. 4.6(g)), and is related to the incident flux of photons from the blackbody source by $QE_{meas} = I_{ph}/qA\Phi$ where Φ is the incident photon flux, A is the area of the detector, I_{ph} is the photocurrent, and q is the charge of an electron [5, 30]. The measured QE over a narrow range, and the QE spectrum over the entire wavelength range of interest are related by the following equations:

$$QE(\lambda) = MR_r(\lambda) \tag{3}$$

$$M = QE_{meas}\frac{\int_0^\infty T_f}{\int_0^\infty T_f\, R_r(\lambda)} \tag{4}$$

where $QE(\lambda)$ is the quantum efficiency spectrum, M is the scaling factor, $R_r(\lambda)$ is the spectral response curve, T_f is the transmission of the optical filter, and QE_{meas} is the measured quantum efficiency over the optical filter's bandwidth [5]. $R_r(\lambda)$ is known by using the setup in Fig. 4.6(e), QE_{meas} is known by using the setup in Fig. 4.6(f), and T_f is known from Fig 4.6(g). Therefore, the scaling factor M can be calculated in order to scale $R_r(\lambda)$ to $QE(\lambda)$. By averaging the QE spectra for 10 different reverse biases from 0.1 V to 1.0 V in 0.1 V increments for 3 different optical filters (30 total), the QE shown in Fig. 4.9(a) was obtained. Through dividing the QE of the micropyramid devices by the QE

obtained for the same size planar reference devices, the power enhancement factor (PEF) was calculated and is shown in Fig. 4.9(b).

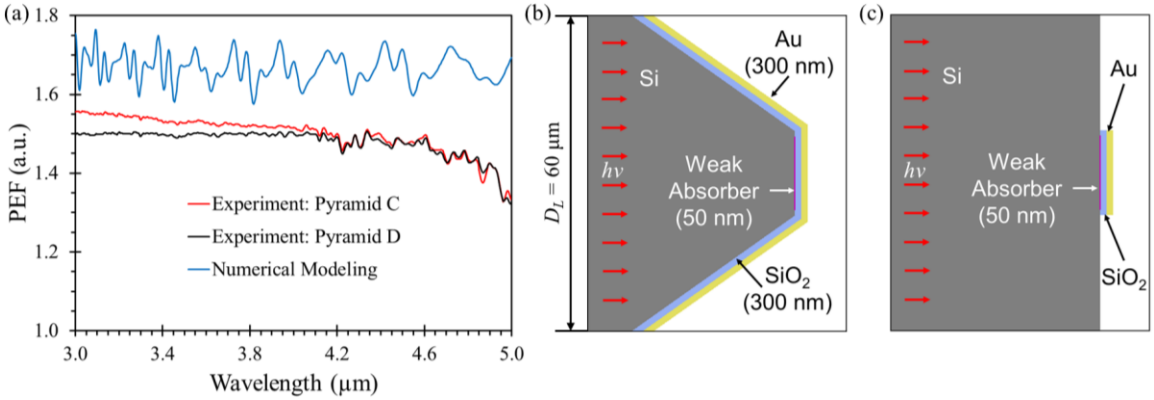

Figure 4.10. (a) By using this same process for the previous die shown in Fig. 4.9, PEF spectra showing ~1.5× signal enhancement due to these micropyramids were obtained. This is in relatively close agreement with what numerical modeling predicts at PEF ≈ 1.7× signal enhancement, shown by the blue curve. This device doesn't have the issue of the mesa hanging over the edge, and therefore gave larger PEF ≈ 1.5×. The numerical modeling curve was calculated by dividing the absorption spectra of the detector integrated with a micropyramid shown in (b) by the absorption spectra of a planar detector shown in (c).

PEF spectra in Fig. 4.9(b) shows only ~1.25× signal enhancement due to monolithic integration of PtSi MWIR photodetectors with micropyramids. This enhancement factor is smaller than expected, potentially due to edge leakage current effects. By taking a look back at the mesa fabrication shown in Fig. 4.2(e), it is clear that some corners of the PtSi mesa fabricated on the micropyramid are over the edge of the micropyramid. Furthermore, upon repeating the device characterization protocol previously described, higher experimental PEF at ~1.5× were obtained for another set of devices fabricated on the same Si wafer. These results are seen in Fig. 4.10(a). The experimentally obtained PEF of ~1.5× is in relatively close agreement with numerical modeling predictions, where the average PEF is ~1.7× and reaches up to ~1.8×, as shown by the blue curve. This device seems to not have the issue of the mesa hanging over the edge, and therefore gave larger PEF of ~1.5×. The numerical modeling curve is calculated by dividing the absorption spectra of

the micropyramid integrated detector obtained via the modeling scenario in Fig. 4.10(b) by the absorption spectra of a planar detector obtained via the modeling scenario in Fig. 4.10(c).

Overall, the goal to fabricate truncated Si micropyramidal arrays, integrate them with PtSi Schottky barrier photodetectors, and conduct optical testing of these devices in comparison with reference planar photodetectors of the same size was a success. This comparison was aimed at evaluating the signal enhancement achieved by the proposed micropyramid designs and showed that the experimental PEF is ~1.5× which agrees with the numerical modeling PEF of ~1.7×. The QE of conventional planar Si-based photodetectors is limited by Si's indirect band gap, leading to low absorption and inefficient photocarrier collection. However, the light-concentrating properties of truncated Si micropyramids has the potential for increased absorption, improved QE, and enhanced photoresponse not limited by the results presented in this study. Another advantage is that the size of the photodetector mesa positioned near the top of the truncated micropyramid can be reduced compared to standard planar devices, which may lead to lower thermal noise in the proposed devices and potentially allow for higher operating temperatures [94-99, 102-104]. In order to further improve the PEFs, another idea based on using silicon-on-insulator (SOI) wafers was developed. This is covered in the next section.

4.4. Silicon-on-Insulator Micropyramids: Further Signal Enhancement

Utilizing a silicon-on-insulator (SOI) Si wafer to fabricate Si micropyramids presents a novel way to further enhance the SNR by creating a resonator cavity inside the micropyramid. A SOI wafer has an insulating SiO_2 layer sandwiched between Si layers

that can be manufactured such that the SiO_2 layer is at a specific depth and with a precise thickness required for a particular use case. In the 3-D FDTD numerical modeling, this SiO_2 layer is always 2 μm thick and is always exactly at the location of the large base D_L.

In order to clarify the mechanism behind the photoresponse increase due to integration with truncated micropyramids, 3-D FDTD numerical modeling of the EM fields were performed for both configurations – with and without the SiO_2 layer as seen in Fig. 4.11. First, to gain insight into the resonance characteristics with the SiO_2 layer, a smaller truncated micropyramid was initially selected with D_L = 15 μm and D_S = 9 μm, compared to those used in the experimental studies (D_L = 60 μm and D_S = 22 μm). In the model, the truncated Si micropyramid has a 300 nm thick SiO_2 layer with a 300 nm thick Au layer, as shown in Fig. 4.11(b,c). To simulate the relatively low absorption in the PtSi Schottky barrier photodetectors, a simplified model was used where a slightly absorbing InSb layer with 50 nm thickness was placed at the interface between the small base D_S of the truncated Si micropyramid and the 300 nm thick SiO_2 layer. This InSb layer absorbs ~1.5% of the incident light with a single pass and is a square absorber with 8 μm lateral dimensions. These dimensions are 1 μm smaller than D_S to account for realistic fabrication capabilities. The InSb layer was encapsulated by an absorption monitor to quantify how much power was absorbed in this layer. An analogous method was applied to calculate the power absorbed in a planar reference structure with the same detector area, similar to what is depicted in Fig. 4.10(c). The 3-D FDTD numerical modeling was conducted using PML BCs on the left and right edges and periodic BCs on the top and bottom, with the resulting EM field maps at λ = 4.84 μm shown in Fig 4.11(d,e). In each scenario, the plane wave source was positioned within the Si slab, with the waves propagating from left to right.

Due to the fact that the detector's photoresponse is proportional to the power absorbed, the PEF was calculated for both the SOI micropyramid case shown in Fig. 4.11 (b,d) and the all-Si micropyramid case shown in Fig. 4.11 (c,e). The PEF spectra were obtained by calculating the absorption spectra with a truncated micropyramid and dividing them by the absorption spectra of the planar reference structure. The resulting PEF spectra in Fig. 4.11(a) are presented for two micropyramid designs: the red curve corresponds to a design utilizing a SOI wafer, while the blue curve represents a monolithic all-Si design.

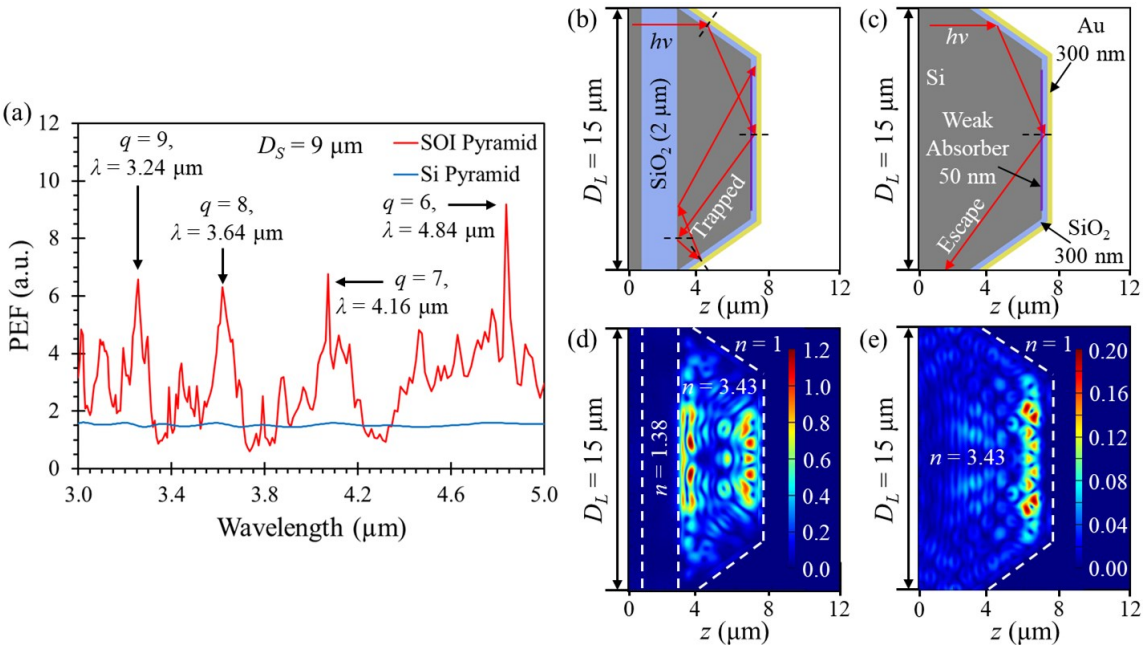

Figure 4.11. The optical absorption characteristics of two micropyramids monolithically integrated with weak absorbers are depicted via ray tracing and 3-D FDTD numerical modeling EM field maps. In both cases the Si micropyramids have identical dimensions where D_L = 15 μm and D_S = 9 μm. (a) The PEF spectra were obtained by calculating the absorption spectra with a micropyramid (as shown in (b) and (c)) and dividing them by the absorption spectra of the planar reference structure (as depicted in Fig 4.10(c)). The resulting PEF spectra are presented for two designs: the red curve corresponds to a design utilizing a silicon-on-insulator (SOI) wafer, while the blue curve represents a monolithic all-Si structure. (b, d) Ray tracing diagram and corresponding EM field map for a SOI micropyramid. (c, e) Ray tracing diagram and corresponding EM field map for an all-Si micropyramid. Both are coated with a 300 nm thick SiO_2 layer and a 300 nm thick Au layer. To model the absorption behavior of PtSi Schottky barrier photodetectors, a simplified approach was used, with a weakly absorbing square structure (8 μm in size, 50 nm thick) positioned at the interface between the small base of the micropyramid and the SiO_2 layer. The Au mirror was included to enhance MWIR radiation absorption [363].

The all-Si PEF spectrum maintains a nearly constant value of PEF ≈ 1.7 over a broad spectral range. This aligns reasonably well with the experimentally observed value of PEF ≈ 1.5 and the numerical modeling value of PEF ≈ 1.7 due to the large D_L = 60 μm and D_S = 22 μm truncated micropyramid illustrated in Fig. 4.10. The relatively low PEF values calculated for the all-Si truncated micropyramids can be attributed to two main factors. First, rays exit the truncated micropyramid after reflecting off the Au mirror, as depicted in Fig. 4.11(c) where light is shown to escape from the truncated micropyramid. Second, rays significantly away from the center of the truncated micropyramid cannot reach the detector itself. Together, these factors limit the buildup of the EM field near the micropyramid's small base D_S, as seen by the EM field maps at λ = 4.84 μm in Fig. 4.11(e).

The EM field enhancement in the detector can be substantially increased by utilizing an improved design where micropyramids are fabricated with a SOI wafer, as shown in Fig. 4.11(b, d). Ray tracing demonstrates that, with a 2 μm thick SiO_2 layer at the large base of the micropyramid, rays are confined within the truncated micropyramid due to total internal reflection with the low-index n = 1.38 SiO_2 layer. This configuration leads to a resonant EM field amplification by nearly an order of magnitude at both truncated micropyramid bases, where Fig. 4.11(d) depicts the peak wavelength of λ = 4.84 μm. Consequently, the SOI-based design yields significantly enhanced absorption, shown by the red curve in Fig. 4.11(a) with PEF resonance peaks surpassing the absorption levels of the planar reference devices by almost an order of magnitude. However, the SOI design warrants a deeper look because of this clear resonance behavior.

The red curve in Fig. 4.11(a) shows strong absorption peaks as a result of introducing an additional oxide layer because of the resonance cavity that is formed. The

resonance wavelengths can be compared to classical Fabry-Pérot resonances described by $\lambda_q = 2nL/q$ where the index of refraction $n = 3.43$ for Si, q is the longitudinal modal number, and L is the length of the resonator cavity which is also the height of the truncated micropyramid determined geometrically by $L = \sqrt{2}*(D_L-D_S)/2$. In this case, $L = 4.24$ μm. The situation in these cases are more complicated due to reflections introduced by the micropyramid's sidewalls and, therefore, cannot be fully explained by classical Fabry-Pérot resonances. However, this comparison gives insight into the origin of these resonance peaks. In the case where $D_L = 15$ μm and $D_S = 9$ μm, Fig. 4.11(a) shows four resonance peaks corresponding to four longitudinal modal numbers: $q = 6$ with $\lambda = 4.84$ μm, $q = 7$ with $\lambda = 4.16$ μm, $q = 8$ with $\lambda = 3.64$ μm, and $q = 9$ with $\lambda = 3.24$ μm. The wavelengths where resonance peaks are expected by theory are nearly exactly where the resonance peaks form in the numerical modeling results, demonstrating that this comparison to classical Fabry-Pérot resonances has merit. The regions surrounding these peaks still give high PEF ≈ 4 and still display some resonance behavior, albeit with lesser order modes most likely from the micropyramid's sidewalls.

Furthermore, this resonance behavior is also apparent in larger truncated SOI micropyramids with $D_L = 30$ μm and $D_S = 18$ μm, as shown in Fig. 4.12. In order to clarify the mechanism behind the photoresponse increase due to integration with truncated micropyramids, 3-D FDTD numerical modeling of the EM fields were performed for both configurations – with and without the SiO_2 layer. The 3-D FDTD numerical model has identical parameters as previously described for the $D_L = 15$ μm and $D_S = 9$ μm case. It is worth noting that for $D_L = 30$ μm and $D_S = 18$ μm, the 50 nm thick square weak absorber layer has 17 μm lateral dimensions. These dimensions are 1 μm smaller than D_S to account

for realistic fabrication capabilities. The resulting EM field maps at $\lambda = 3.24$ μm are shown in Fig 4.12(b, c). The resulting PEF spectra in Fig. 4.12(a) are presented for two micropyramid designs: the red curve corresponds to a design utilizing a SOI wafer, while the blue curve represents a monolithic all-Si design.

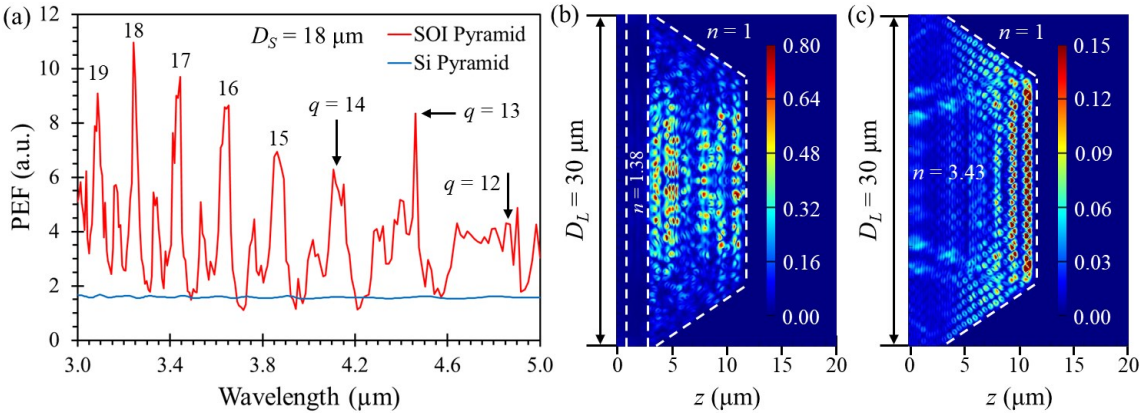

Figure 4.12. The optical absorption characteristics of two micropyramids monolithically integrated with weak absorbers are depicted via ray tracing and 3-D FDTD numerical modeling EM field maps. In both cases the Si micropyramids have identical dimensions where $D_L = 30$ μm and $D_S = 18$ μm. (a) The PEF spectra were obtained by calculating the absorption spectra with a micropyramid (as shown in (b) and (c)) and dividing them by the absorption spectra of the planar reference structure (as depicted in Fig 4.10(c)). The resulting PEF spectra are presented for two designs: the red curve corresponds to a design utilizing a silicon-on-insulator (SOI) wafer, while the blue curve represents a monolithic all-Si structure. (b) EM field map for a SOI micropyramid. (c) EM field map for an all-Si micropyramid. Both are coated with a 300 nm thick SiO_2 layer and a 300 nm thick Au layer. To model the absorption behavior of PtSi Schottky barrier photodetectors, a simplified approach was used, with a weakly absorbing square structure (17 μm in size, 50 nm thick) positioned at the interface between the small base of the micropyramid and the SiO_2 layer. The Au mirror was included to enhance MWIR radiation absorption.

The all-Si PEF spectrum again maintains a nearly constant value of PEF ≈ 1.7 over a broad spectral range, shown by the blue curve in Fig. 4.12(a). This aligns well with the experimentally observed value of PEF ≈ 1.5 and the numerical modeling value of PEF ≈ 1.7 due to the large $D_L = 60$ μm and $D_S = 22$ μm truncated micropyramid illustrated in Fig. 4.10. The EM field enhancement in the detector can be substantially increased by utilizing an improved design where micropyramids are fabricated with a SOI wafer, as shown in

Fig. 4.12(b). This configuration leads to an enhanced PEF of up to 11× at λ = 3.24 μm, where the EM field maps in Fig. 4.12(b, c) depict the fields at this wavelength.

The red curve in Fig. 4.12(a) shows strong absorption peaks as a result of introducing an additional oxide layer because of the resonance cavity that is formed. The resonance wavelengths can be compared to classical Fabry-Pérot resonances described by $\lambda_q = 2nL/q$ where the index of refraction n = 3.43 for Si, q is the longitudinal modal number, and L is the length of the resonator cavity which is also the height of the truncated micropyramid determined geometrically by $L = \sqrt{2}*(D_L-D_S)/2$. In this case, L = 8.49 μm. The situation in these cases are more complicated due to reflections introduced by the micropyramid's sidewalls and, therefore, cannot be fully explained by classical Fabry-Pérot resonances. However, this comparison gives insight into the origin of these resonance peaks. In the case where D_L = 30 μm and D_S = 18 μm, Fig. 4.12(a) shows eight resonance peaks corresponding to eight longitudinal modal numbers: q = 12 with λ = 4.84 μm, q = 13 with λ = 4.47 μm, q = 14 with λ = 4.16 μm, q = 15 with λ = 3.88 μm, q = 16 with λ = 3.64 μm, q = 17 with λ = 3.43 μm, q = 18 with λ = 3.24 μm, and q = 19 with λ = 3.07 μm. Once again, the wavelengths where resonance peaks are expected by theory are nearly exactly where the resonance peaks form in the numerical modeling results, demonstrating that this comparison to classical Fabry-Pérot resonances has merit. The regions surrounding these peaks give still high PEF of ~4× and still display some resonance behavior, albeit with lesser order modes most likely from the micropyramid's sidewalls.

It is clear from the D_L = 15 μm case shown in Fig. 4.11 and the D_L = 30 μm case shown in Fig. 4.12 that the resonance peaks for moderately truncated SOI micropyramids arise due to multiple reflections which occur at SiO_2 layer near D_L and at the Au layer near

D_S. To conclude this analysis, it is only natural to compare the experimental results shown in section 4.3 with 3-D FDTD numerical modeling for the same geometric configuration. The resonance behavior shown in Fig. 4.11 and Fig. 4.12 is also apparent in larger truncated SOI micropyramids with D_L = 60 μm and D_S = 22 μm, as shown in Fig. 4.13. In order to clarify the mechanism behind the photoresponse increase due to integration with truncated micropyramids, 3-D FDTD numerical modeling of the EM fields were performed for both configurations – with and without the SiO_2 layer. The 3-D FDTD numerical model has identical parameters as previously described for the D_L = 15 μm and D_S = 9 μm case. It is worth noting that for D_L = 60 μm and D_S = 22 μm, the 50 nm thick square weak absorber layer has 21 μm lateral dimensions: identical to the experiment. These dimensions are 1 μm smaller than D_S to account for realistic fabrication capabilities. The resulting EM field maps at λ = 3.84 μm are shown in Fig 4.13(b, c). The resulting PEF spectra in Fig. 4.13(a) are presented for two micropyramid designs: the red curve corresponds to a design utilizing a SOI wafer, while the blue curve represents a monolithic all-Si design.

The all-Si PEF spectrum again maintains a nearly constant value of PEF ≈ 1.7 over a broad spectral range, shown by the blue curve in Fig. 4.13(a), which agrees with the experimentally observed value of PEF ≈ 1.5 due to the large D_L = 60 μm and D_S = 22 μm truncated micropyramid illustrated in Fig. 4.10. The EM field enhancement in the detector can be substantially increased by utilizing an improved design where micropyramids are fabricated with a SOI wafer, as shown in Fig. 4.13(b). This configuration leads to an enhanced PEF of up to 9× at λ = 3.84 μm, where the EM field maps in Fig. 4.13(b, c) depict the fields at this wavelength.

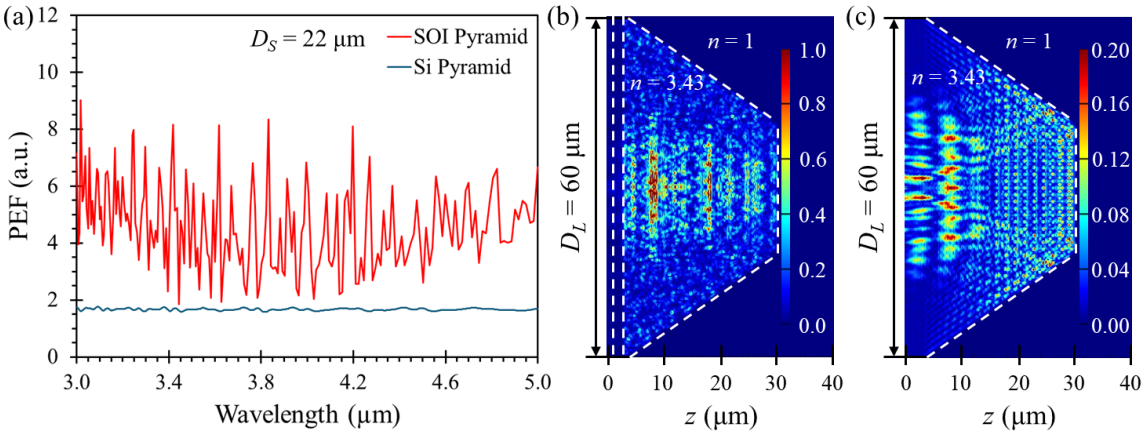

Figure 4.13. The optical absorption characteristics of two micropyramids monolithically integrated with weak absorbers are depicted via ray tracing and 3-D FDTD numerical modeling EM field maps. In both cases the Si micropyramids have identical dimensions where D_L = 60 µm and D_S = 22 µm. (a) The PEF spectra were obtained by calculating the absorption spectra with a micropyramid (as shown in (b) and (c)) and dividing them by the absorption spectra of the planar reference structure (as depicted in Fig 4.10(c)). The resulting PEF spectra are presented for two designs: the red curve corresponds to a design utilizing a silicon-on-insulator (SOI) wafer, while the blue curve represents a monolithic all-Si structure. (b) EM field map for a SOI micropyramid. (c) EM field map for an all-Si micropyramid. Both are coated with a 300 nm thick SiO_2 layer and a 300 nm thick Au layer. To model the absorption behavior of PtSi Schottky barrier photodetectors, a simplified approach was used, with a weakly absorbing square structure (21 µm in size, 50 nm thick) positioned at the interface between the small base of the micropyramid and the SiO_2 layer. The Au mirror was included to enhance MWIR radiation absorption.

The red curve in Fig. 4.13(a) shows strong absorption peaks as a result of introducing an additional oxide layer because of the resonance cavity that is formed. The resonance wavelengths can loosely be compared to classical Fabry-Pérot resonances described by $\lambda_q = 2nL/q$ where the index of refraction n = 3.43 for Si, q is the longitudinal modal number, and L is the length of the resonator cavity which is also the height of the truncated micropyramid determined geometrically by $L = \sqrt{2}*(D_L\text{-}D_S)/2$. In this case, L = 26.87 µm. However, the situation is significantly more complicated due to a large number of reflections introduced by the micropyramid's sidewalls and, therefore, cannot be fully explained by classical Fabry-Pérot resonances. However, this comparison gives insight into the origin of these resonance peaks as seen in the D_L = 15 µm and D_L = 30 µm cases shown in Fig. 4.11 and Fig. 4.12, respectively. In the case where D_L = 60 µm and D_S = 22 µm, the

classical Fabry-Pérot resonances described by $\lambda_q = 2nL/q$ predict twenty-five longitudinal modal numbers ranging from $q = 37$ with $\lambda = 4.98$ μm to $q = 61$ with $\lambda = 3.03$ μm. Therefore, what initially may look like a noisy mess in Fig. 4.13(a) can be attributed to resonances between the SiO_2 layer near the large base D_L and the small base D_S, and large contributions from the micropyramid's sidewalls.

Similar peaks were previously observed for Si microcones in an air environment [25], where it was also noted that certain peaks exhibited omnidirectional resonance such that the same spectral position was maintained across a wide range of incidence angles and for both polarizations of incoming light. This omnidirectional behavior is unattainable in planar structures but can be possible in truncated microcones because of their 3-D geometry. A similar effect may also occur in truncated Si micropyramids fabricated in SOI wafers, though this intriguing possibility warrants further investigation by studying the locations of the resonance peaks with increasing angle-of-incidence. Omnidirectional resonance is a valuable feature for creating multispectral MWIR imaging devices, enabling improved photon collection across a wide range of incidence angles. The integration of Si micropyramidal arrays with photodetectors, either monolithically or heterogeneously, has the potential to raise the operating temperature of MWIR FPAs. Additionally, it is worth noting that the proposed 3-D micropyramid mirror designs [97, 99, 103] fabricated in SOI wafers can also be heterogeneously integrated with photodetectors made from materials with superior absorption characteristics and higher QE in the MWIR range, such as photovoltaic (PbSe, HgTe, HgSe, and colloidal quantum dots) [361] and photoconductor [6, 362] based photodetectors.

4.5. Conclusions

The primary goal of this research was to enhance MWIR photodetectors by reducing the dark current noise and increasing the signal, thereby increasing the signal-to-noise ratio (SNR). To do this, truncated Si micropyramidal arrays with 60 μm pitch were fabricated, integrated with MWIR photodetectors, and optical testing was performed to compare their performance with reference planar photodetectors of the same dimensions. This comparison was done to assess the signal enhancement achieved through the micropyramid-based designs. Determining the QE of these devices was essential for this analysis. Defined as the ratio of electrical output to optical input, QE for conventional planar Si-based photodetectors is limited by Si's indirect band gap, resulting in low absorption and inefficient photocarrier collection. In contrast, the light-focusing properties of the truncated Si micropyramids, when integrated with photodetectors, shows promise for increasing the absorption, thereby improving the QE and enhancing the photoresponse. Additionally, the photodetector mesa size near the top of the truncated micropyramid can be minimized compared to standard planar devices, which could reduce thermal noise and potentially allow for higher operating temperatures [94-99, 102-104, 363].

In order to evaluate the performance enhancement capability of micropyramids integrated with MWIR detectors, silicon-platinum silicide (PtSi/p-Si) Schottky barrier photodetectors were monolithically integrated with truncated Si micropyramid arrays. To further increase the photoresponse, layers of SiO_2 and Au mirror reflectors were deposited on top of the truncated micropyramids housing the photodetectors. The key innovation involved applying a 3-D metallic mirror onto the sidewalls of the truncated micropyramids [103, 363], which enabled effective photon concentration on the photodetectors. This

design offers several advantages: enhanced photon collection over a broader area, effective trapping of photons within the truncated micropyramids to create resonant optical effects, and the utilization of multiple light propagation paths within the detector. Together, these factors extend the optical path length, thereby increasing the likelihood of photon absorption and improving the photodetectors' QE. The 3-D mirror setup builds on earlier concepts of back-reflectors used in traditional planar MWIR photodetector FPAs, as shown in Fig. 4.6(b, d) [5, 44]. This configuration achieved ~1.5× signal enhancement over planar reference devices without truncated micropyramids across a broad MWIR spectral range. These results align well with the 3-D FDTD numerical modeling calculations, which predicted an average PEF of ~1.7× with up to a ~1.8× signal enhancement in similar configurations. The initially expected strong absorption peaks were actually not pronounced as a result of photons escaping from inside the micropyramids back to the bulk Si wafer.

In order to further enhance the PEFs, an approach involving silicon-on-insulator (SOI) wafers was introduced to trap the photons inside the micropyramid. The fabrication of Si micropyramids on an SOI wafer offers a novel method to enhance the SNR by creating a resonant cavity within the micropyramid structure. An SOI wafer includes an insulating SiO_2 layer embedded between Si layers, engineered to be at a precise depth and thickness suitable for specific applications. In the 3-D FDTD modeling, this SiO_2 layer aligns exactly with the large base of the truncated micropyramid. With the purpose of clarifying how integration with truncated micropyramids enhances the photoresponse, 3-D FDTD numerical modeling of the EM fields was conducted for both micropyramid configurations—with and without the SiO_2 layer. It was demonstrated that significantly

stronger absorption of MWIR radiation can be achieved in truncated SOI micropyramids fabricated in the top Si layer of SOI wafers due to resonance inside the micropyramid. The 3-D FDTD numerical modeling calculations indicate that light trapped inside these micropyramidal structures have resonance effects leading to an order of magnitude higher absorbed power compared to planar reference devices of the same detector size. The resonance peaks are enhanced by PEF ≈ 9-11× for different micropyramid pitches due to the Fabry-Pérot resonances caused by mirror reflections at the bases of the micropyramid. Such configurations could potentially address the long-standing issue of low QE in metal-silicide Schottky barrier photodetectors. Furthermore, these structures may exhibit omnidirectional resonance characteristics such that the same spectral position was maintained across a wide range of incidence angles and for both polarizations of incoming light [25].

Overall, this chapter focused on the experimental fabrication and testing of monolithically integrated PtSi detectors with truncated Si micropyramids, as well as a novel way to further improve these detectors. It covered the fabrication of monolithically integrated MWIR PtSi/p-Si Schottky barrier photodetectors directly on top of the truncated Si micropyramids. This was done to experimentally determine if reducing the dimensions of the photodetectors reduces the dark current, while the light collection efficiency can be improved with light-concentrating truncated micropyramids, in order to maintain or enhance the SNR to increase the operating temperature of MWIR FPAs. Furthermore, a detailed analysis of the truncated micropyramid FPA was conducted through characterizing the fabricated devices' spectral response and QE in order to determine the enhancement obtained through integration with truncated micropyramids. Lastly, a novel way to further

enhance the SNR through utilizing a SOI wafer to create a resonator cavity was discussed and demonstrated increased absorption of up to 11× compared to a planar reference device of the same size.

These results do not represent the limits of this technology. Rather, they underscore the adaptability of Si anisotropic wet etching as a flexible approach for creating innovative structures that enhance MWIR FPAs. This research establishes that micropyramidal Si photonics offers a highly customizable optoelectronic platform for improving SNR characteristics and raising the operating temperature of MWIR FPAs. Future efforts could focus on the fabrication and experimental validation of these proposed SOI structures. This would allow for a direct demonstration of the imaging capabilities of these devices in the MWIR range relative to standard cameras.

CHAPTER 5: NUMERICAL MODELING THE OPTICAL PROPERTIES OF LITTROW RETROREFLECTORS

5.1. Grating Concept and Polar Angle Performance

As explained in section 1.5, Littrow retroreflectors are essentially diffraction gratings which are often designed to operate at grazing angles of incidence. Therefore, the advantages of Littrow retroreflectors come from their thin film designs, enabling their fabrication on wide areas of flat and curved surfaces. The well-known diffraction grating equation, $\sin \Theta_r - \sin \Theta_{in} = m\lambda/\Lambda$, where Θ_{in} is the angle of incidence, Θ_r is the angle of diffraction, λ is the wavelength of light, Λ is the periodicity of the diffraction grating, and m is the diffraction order, represents a zero-order approximation to understanding retroreflector performance of Littrow retroreflectors. Indeed, for $m = -1$ and $\Theta_r = -\Theta_{inc} = \Theta$ the grating equation simplifies to the Littrow configuration: $2 \sin \Theta = \lambda/\Lambda$. This means that, only for this angle of incidence, the diffracted beam propagates in the exact reciprocal direction. In this work, $\lambda = 633$ nm was selected corresponding to the wavelength of a HeNe laser to enable simple experimental testing of such retroreflectors. This wavelength is also where most metals, such as Au, experience plasmonic resonant properties, therefore indicating that interesting new physics can be involved in their retroreflection properties. By selecting to optimize the performance at $\Theta \approx 70°$, it was estimated that the grating period should be around $\Lambda \approx 338$ nm, which is a relatively short period but it is still within the fabrication capabilities of electron beam lithography. At the same time, the grating

equation also reveals the main limitation of Littrow retroreflectors. In fact, a small deviation from the optimal angle of incidence leads to the same deviation (but in the opposite direction from the optimal angle) for the diffracted beam, which means that Littrow retroreflectors are not proper retroreflectors in a rigorous sense. On a trade-off, this combination of fabrication simplicity with a somewhat imperfect performance still makes Littrow retroreflectors attractive for practical applications. However, the design of these structures should go far beyond a simplified grating equation to explain the broadband operation of these structures for both polarizations of incident light.

The grating concept is based on periodicity, and these grating properties are introduced by the top layer of the full 3-D retroreflector structure illustrated in Fig. 5.1. This top layer is represented by a 2-D slot array fabricated in a metallic thin film. The simplest 1-D analog of such 2-D slot array is a stripe array illustrated in Fig. 1.32(a).

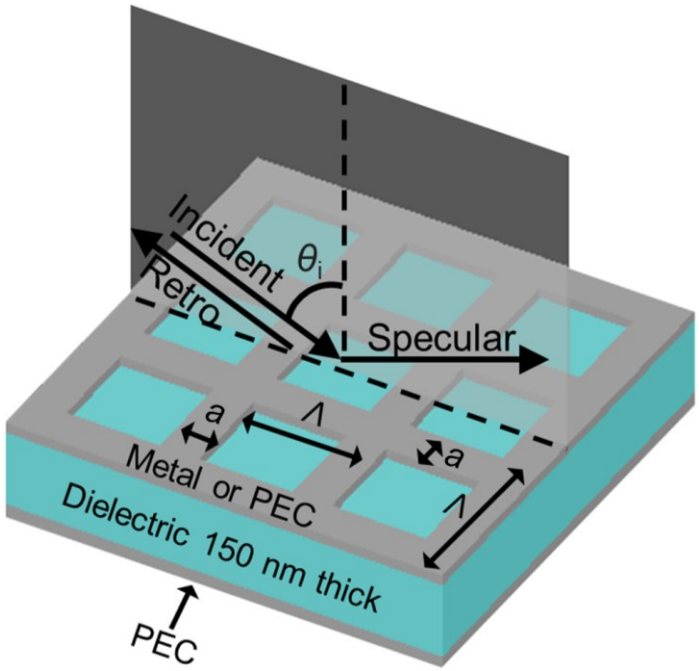

Figure 5.1. Sketch illustrating the 3-D geometry of the retroreflector structure, as well as the experimental geometry. It shows the main parameters such as the period (Λ) and width of the metallic stripes (a) in the surface square slot array. Plane waves are incident at an angle of Θ_{in}. A specularly reflected zero-order beam and diffracted beam corresponding to m = -1 in the grating equation are illustrated.

5.2. Suppression of the Specular Beam

The polar angular performance described in the previous section is a common property of different gratings with a given period and various profiles of grooves. It is important to note that the other diffracted beams corresponding to m numbers different from $m = -1$ are prohibited by the grating equation for the given parameters, so the intensity of the incident plane waves is split between the retroreflected and specular beams, as illustrated in Fig. 5.1. In addition, some part of the intensity can be absorbed by the metallic layers. However, the grating equation does not answer the question regarding the efficiency of the retroreflector. It can be suggested that suppression of the specular beam can increase the intensity of the retroreflected beam.

Suppression of the specular beam around $\lambda = 633$ nm and $\Theta \approx 70°$ can be achieved by the introduction of additional thin layers in the design of the retroreflector structure. Specifically, it can be achieved by using a thin dielectric layer (d) and refractive index (n) separating the top slot array from the bottom metal mirror, as illustrated in Fig. 5.1. This mirror is labeled as PEC because, in the numerical calculations of the EM fields described below, a perfect electric conductor model (PEC) was used to represent this layer. The basic idea is to split the incident beam into two specular reflections, where one is introduced by the metallic fraction of the top slot array and the other is introduced by transmission into the dielectric layer due to openings between the metal stripes. The transmitted beam is reflected by the bottom metallic mirror and directed towards the top metallic slot array. If the phase shift between these two beams is close to π, both beams would interfere destructively therefore suppressing the specular beam.

This design concept looks simple from the first sight since it requires calculating the path difference between these two beams and setting it to be equal to $2\pi(1/2+n)$, where $n = 0,1,2\ldots$ There is, however, one factor which complicates this approach. Along with the path difference, the phase shift acquired at the metallic layers of the structure needs to be considered. At the bottom mirror it is π, but at the top slot array it requires a separate analysis. The issue is that, at the metallized sections of the top slot array, the tangential components of the electric field intensity must vanish both above and below the interface whereas within the openings between the metal stripes, the tangential components of both electric and magnetic fields must be continuous. This means that the phase shift acquired at the top slot array depends on the metal filling factor $f = a/\Lambda$ and on the polarization of the incident light, TE or TM. To solve this problem analytically, a special mathematical approach was developed in Ref. [225] to approximate the properties of such top slot arrays. This enabled the calculation of the retroreflected beam's efficiencies in the whole parameter space for a simplified 1-D lattice of stripes.

The results of Ref. [225], represented in Fig. 1.32, play an important role in the numerical modeling work. Although they were obtained for somewhat different parameters of the system ($\Lambda = 960$ nm, $\lambda = 1550$ nm, $n = 1.444$ and $\Theta \approx 54°$) in a simplified 1-D case, they show the main generic problem of such designs. Inspection of Fig. 1.32 shows that the optimal areas in the parameter space required for achieving efficient retroreflection at TE and TM polarizations have a limited overlap. Indeed, the highly efficient performance of the TE polarization is favored at smaller $f \approx 0.045$ values, whereas the highly efficient performance of the TM polarization is favored at much larger $f \approx 0.45$ values which cannot be combined in the same structure. The selection of the optimal f values for TE and TM

polarizations is driven by the requirement to reduce the retroreflector's sensitivity to variations in the thickness of the dielectric slab [225]. The situation is, however, quite different if maximizing the combined retroreflector performance of both polarizations with the same structure was desired. In the latter case, the values of d and f should be deliberately selected to provide such an overlap between the different polarizations, and Fig. 1.32 clearly indicates this situation for a near-infrared 1-D lattices of metallic stripes with dielectric layer of thickness d = 0.25 - 0.4 μm and with metal fill factors f = 0.3 - 0.5. This opens up the possibility for sufficient retroreflection efficiency of both polarizations for the same points (d, f) in 2-D parameter space. For each polarization, the efficiency can be reduced below 100%, but the combined performance in both polarizations can be still quite reasonable. This result from analytical theory encouraged us to investigate such situations numerically in a more realistic 3-D case based on the exact solution to Maxwells' equations performed for different models of the top slot array. Considering the shorter wavelength of λ = 633 nm with a slightly higher dielectric layer index of n = 1.6 in the designs, the thickness of the dielectric layer was selected to be d = 150 nm.

5.3. Describing the Model in 3-D FDTD Numerical Modeling Software

3-D FDTD numerical modeling of the far-field EM fields for the structure illustrated in Fig. 5.1 was performed using Ansys/Lumerical 3-D FDTD photonic software. An adjustable grid with cell sizes of ~1 nm were used to represent different layers of the structure. The unit cell was represented by a square with 338 nm sides containing metallic stripes with the a/2 width at the edges and with the square slot in the middle. The modeling

was performed for a slot array with a sufficiently large number of periods (>40) to approximate the case of large-scale arrays.

The first task was to estimate the range of stripes widths (a) which provided maximal retroreflection efficiency for both polarizations simultaneously for the same structure. To this end, numerical modeling of the top metal slot array was needed and a PEC model as a zero-order approximation was selected. In the PEC model, the metal is optically lossless and the tangential components of the electric field are zero at the boundary. This means that both the metallic interfaces, the top slot array and the bottom mirror, are lossless and therefore depict the upper limit of the retroreflector's efficiency without considering absorption losses.

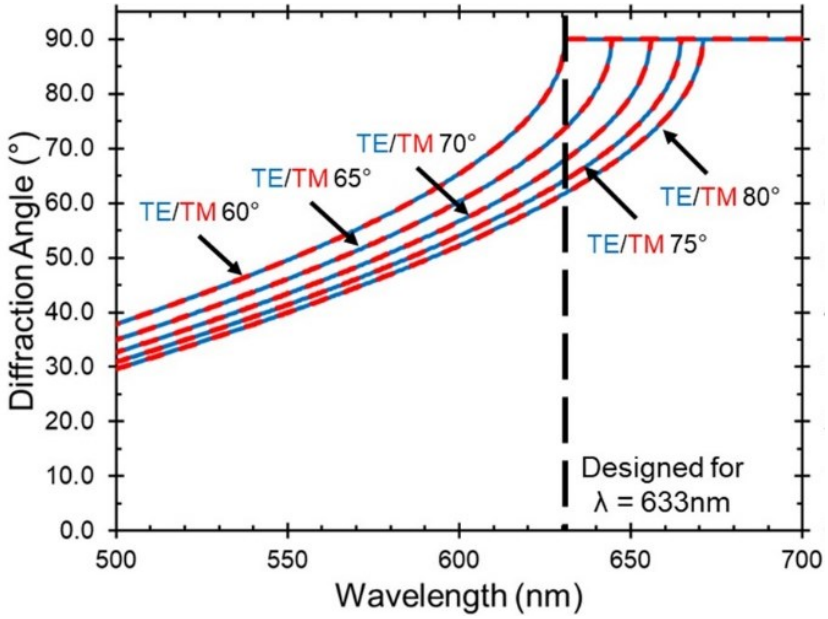

Figure 5.2. Wavelength dependence of the diffraction angle calculated for several angles of incidence in the 60 - 80° range. The dependencies coincide for TE and TM polarizations of incident light. The design wavelength λ = 633 nm is shown by the vertical dashed line.

One more important option offered by Ansys/Lumerical's 3-D FDTD numerical modeling software is the ability to separately calculate the total intensity of the diffracted (m = -1) and specular beams for arbitrary angles of incidence represented by Θ_{in}. As

discussed previously, deviation of Θ_{in} from 70° leads to the corresponding changes in the direction of the diffracted beam and the software automatically monitors the total intensity of the diffracted beam irrespective of its direction.

For a 1-D array of metal stripes, the relationship between the incidence and diffraction angles is represented by the grating equation, $\sin \Theta_r - \sin \Theta_{in} = m\lambda/\Lambda$. The wavelength dependencies of the diffraction angles calculated by Ansys/Lumerical's FDTD numerical modeling software for a 3-D retroreflecting structure at several angles of incidence are shown in Fig. 5.2. These dependencies were calculated in the plane of incidence perpendicular to the stripes of the array. The TE and TM dependencies coincide for each angle of incidence, Θ_{in} = 60, 65, 70, 75, 80°. The design wavelength λ = 633 nm is indicated by the vertical dashed line. For each curve, the diffraction angle is determined by its intersection with this vertical dashed line. The wavelength where each curve reaches Θ_r = 90° level indicates a condition where diffracted beam appears at a grazing angle to the surface of the structure.

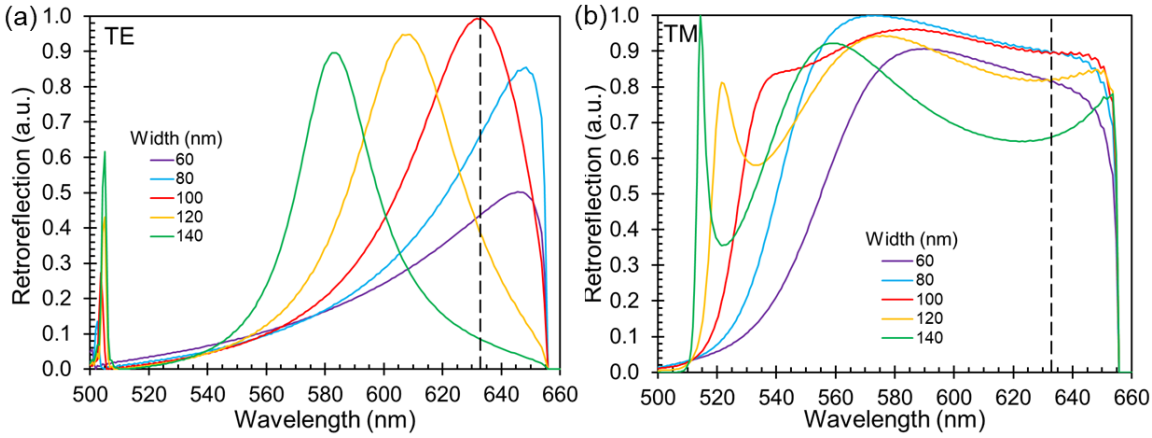

Figure 5.3. Retroreflection spectra normalized to the intensity of the incident beam. The spectra were calculated for (a) TE and (b) TM polarizations incident at Θ_{in} = 70° for different stripe widths, a = 60, 80, 100, 120, and 140 nm. The vertical dashed line shows the design wavelength of λ = 633 nm.

The next step was to study the intensity of the retroreflected beam under different conditions. As shown in Fig. 5.3, this was achieved by calculating the retroreflection spectra at $\Theta_{in} = 70°$ for slot arrays with different widths of the stripes, $a = 60$, 80, 100, 120, and 140 nm. These dependencies show the TM retroreflection response was sufficiently strong and spectrally broad in the $\lambda = 550$ - 650 nm range for all stripe widths. Additionally, the TE response displayed strong retroreflection peaks with spectral widths of ~40 nm, where the peak's position shifted to shorter wavelengths with increasing stripe width a. Lastly, the strongest retroreflection for both TE and TM polarizations at the design wavelength of $\lambda = 633$ nm can be achieved at $a = 100$ nm. The results displayed in Fig. 5.3 establish that highly efficient Littrow retroreflector performance can be achieved with a PEC model in both polarizations where the optimized stripe width a is around 100 nm with a period of $\Lambda = 338$ nm.

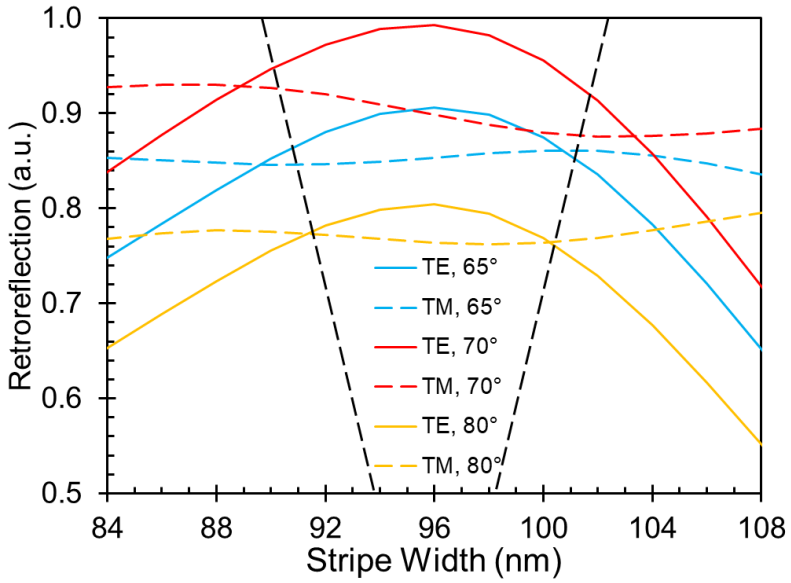

Figure 5.4. Intensity of the diffracted (m = -1) beam normalized to the intensity of the incident beam calculated at different angles of incidence, $\Theta_{in} = 65°$, 70°, and 80° for TE and TM polarizations.

One more task was to investigate the tolerance of the proposed design to variations in the stripe width a, which can be treated as a fabrication tolerance of the proposed design. This was studied by calculating the ratio of the retroreflection intensity to the intensity of the incident light. The results of such 3-D FDTD numerical modeling simulations for different angles of incidence, Θ_{in} = 65°, 70°, and 80°, at two different polarizations are presented in Fig. 5.4. Only at Θ_{in} = 70° does the direction of the diffracted beam reciprocate the direction of incidence, making it a perfect retroreflector. Furthermore, the diffracted beam is referred to as a "retroreflected" beam considering that its direction is relatively close to the direction of incidence for small deviations from the optimal value of Θ_{in} = 70°.

Fig. 5.4 illustrates the dependence of the normalized retroreflected intensity on the stripe width a of the slot array in the PEC model. Analysis of this figure indicates that this design provides extremely efficient (>0.9) retroreflection for both polarizations simultaneously around the optimal value of a = 96 nm. Additionally, the TM retroreflection response demonstrates sufficiently high and almost constant efficiency in the entire range of stripe widths, a = 84 - 108 nm. Furthermore, the TE retroreflection response peaks at a value of a = 96 nm, but the peak is rather wide, which means that this design can tolerate significant stripe width variations in the a = 92 - 100 nm range, as schematically illustrated by the black dashed lines. These results show that optimal performance is expected at a value of a = 96 nm in the 3-D model, which corresponds to a f = 0.28 value in the 1-D stripe lattice considered in Ref. [225]. The main conclusion is that there is some consistency with the predictions of the 1-D model, but the efficiency of such 3-D retroreflectors at optimized parameters (>0.9) is surprisingly high and therefore is a very

encouraging result for further studies. In the rest of this Chapter, the stripe width value of $a = 96$ nm was selected.

5.4. Azimuthal Dependence

The 3-D Littrow retroreflectors can be compared to the simplest 1-D model only in the case where light is incidence along the symmetry directions of the 2-D top slot array, as schematically illustrated in Fig. 5.1. In this case, light is incidence is perpendicular to the stripes of the slot array. In practice, however, the incident light can be provided along arbitrary azimuthal directions represented by the azimuthal angle ϕ, as schematically illustrated in Fig. 5.5.

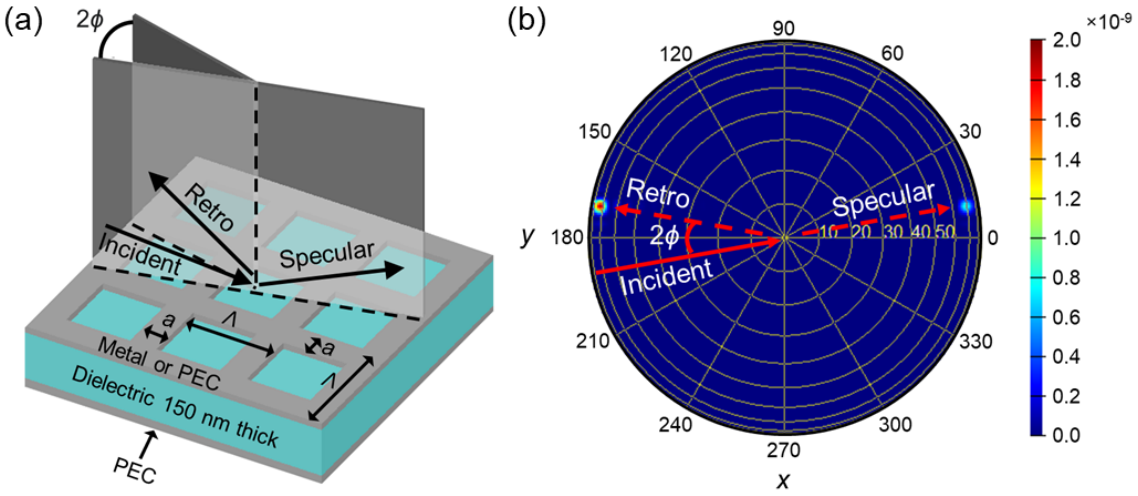

Figure 5.5. (a) Diagram depicting the azimuthal performance of the Littrow retroreflector, showing light incident in a plane rotated by angle ϕ relative to the symmetry plane passing through x-axis. (b) Polar plot showing both the polar and azimuthal angles for the incident, specular, and diffracted beams. The diffracted beam is indicated as retro in this plot [369].

It is seen that the azimuthal behavior of the Littrow retroreflector is also imperfect. Rotating the plane of incidence by angle ϕ from the symmetry planes causes the same rotation of the diffracted beam, but in the opposite direction. As a result, the directions of the incident and diffracted beam differ by 2ϕ, as illustrated in Fig. 5.5(b). This plot shows

that, as expected, the incident and specular beam belong to the same plane, but the diffracted beam, termed “retro” in this polar plot, lies in the plane rotated by 2ϕ. It also shows that diffracted beam intensity dominates over the specular beam. Therefore, such a structure can perform as a standard retroreflector only in highly symmetrical cases where light is incident perpendicular to the stripes. These cases are repeated with 90° periodicity, but the performance at arbitrary azimuthal directions require further studies.

The spectral responses of the retroreflector calculated at a polar angle of incidence Θ_{in} = 70° and different azimuthal angles of incidence, ϕ = 0°, 5°, 10°, and 15° are represented for TE and TM polarizations in Figs. 5.6(a) and 5.6(b), respectively. The 3-D FDTD numerical modeling simulation results indicate that the spectral response remains relatively broad and that the peak of the response shifts to shorter wavelengths with increasing azimuthal angle ϕ. The intensity of the diffracted beam drops from a level greater than 0.9 at ϕ = 0° to a level of ~0.3 at ϕ = 15° for both polarizations at the design wavelength of λ = 633 nm. This means that such retroreflectors can tolerate rotation of the incidence plane by ~15° to each side from the symmetry plane.

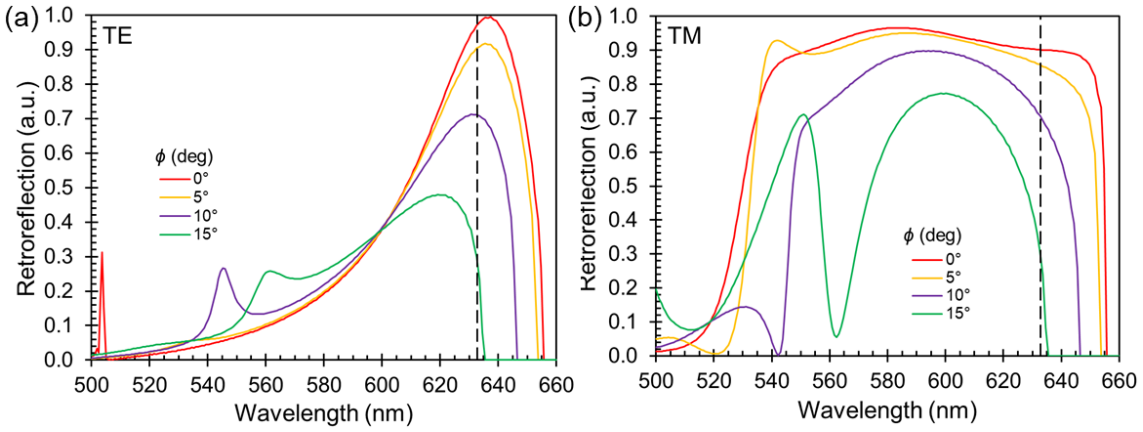

Figure 5.6. Retroreflection spectra normalized to the intensity of the incident beam and calculated for (a) TE and (b) TM polarizations at a polar incidence angle of Θ_{in} = 70° and for different azimuthal angles ϕ = 0°, 5°, 10°, and 15°, measured from the symmetry plane. The design wavelength of λ = 633 nm is shown by the vertical dashed line.

5.5. Transition from PEC Model to Real Metals: Au, Ag, Al, and Cu

The Littrow retroreflector's performance represented in Fig. 5.4 is surprisingly good. At optimal conditions, the intensity of the retroreflected beam exceeds 90% for both polarizations. This is a very encouraging result considering the fundamental problem of obtaining highly efficient performance for both TE and TM polarizations simultaneously in a 1-D lattice of stripes [225]. It should be noted, however, that this modeling completely neglected absorption losses from the bottom mirror and, more importantly, from the slot array because a PEC model was used to represent the metallic layers. Therefore, this approach (a similar approach was used in [225]) can be viewed only as a zero-order approximation to the problem and more realistic metal models considering absorption losses must be used for a more accurate representation of how this retroreflector would perform.

As a next iteration, an approach based on using the real and imaginary parts of the refractive index known for bulk metals such as Au, Ag, Al, and Cu obtained from the software's material library was used. It should be noted that this approach is also only an approximation to a real situation because the bulk values of the refractive index were applied to slot arrays with small thicknesses. However, this approximation enabled the absorption losses to be included. The thickness of such slot arrays made from various metals was varied in the 3-D FDTD numerical modeling between 20 - 70 nm. Thinner slot arrays below 20 nm were not included in the analysis because the scattering strength of these metallic stripes are less, which reduces their retroreflection capability. In addition, plasmon excitations in metallic stripes with such nanoscale thicknesses are affected by quantum confinement properties that require a more detailed knowledge about the behavior

of the refractive index in such thin films. On the other hand, the retroreflection response of arrays with thicknesses larger than 70 nm are also reduced, as the numerical modeling results indicate. For these reasons, this study was limited to the 20 - 70 nm range of metal thicknesses.

Retroreflection properties of Au arrays. In Fig. 5.7, the dependence of the retroreflection spectra on the thicknesses of the Au slot array is shown with 10 nm increments in the thickness. The calculations were performed for a polar incidence angle of $\Theta_{in} = 70°$ and an azimuthal angle of $\phi = 0°$ for TE and TM polarizations as shown in Figs. 5.7(a) and 5.7(b), respectively. These plots demonstrate that the TM retroreflection response is sufficiently strong at ~0.6 level and the response is broadband over a λ = 600 - 650 nm range for all stripe thicknesses in the 20 - 70 nm range. Additionally, the TE retroreflection response displays a spectral peak where the width increases from ~15 nm up to ~60 nm for increasing metal thickness, with the position of the maximum shifting to shorter wavelengths. Furthermore, the strongest retroreflection at the design wavelength of λ = 633 nm can be achieved for the slot array with 30 nm thickness.

Generally, the results show that the strongest combined TE/TM retroreflection response is determined primarily by the retroreflection response of the TE polarization. For an Au slot array, this can be achieved at the thickness of 30 nm. Retroreflection can be obtained for both polarizations with the same structure, but with somewhat reduced efficiencies at ~0.25 for TE and TM ~0.6 for TM compared to the predictions from the simplified PEC model illustrated in Fig. 5.3. This is generally an expected result considering that some part of the incident intensity is absorbed in the Au slot array.

It is interesting to note that the retroreflection thickness dependence shown in Fig. 5.7 is similar to the previously studied stripe width dependence in the PEC model, illustrated in Fig. 5.3. For both cases, the optimized response is determined by the shift of the TE response to shorter wavelengths with an increase in the amount of metal present. The difference is that in Fig. 5.7, the volumetric fraction of Au was increased to keep the same area fill factor *f*, whereas in Fig. 5.3 the area fill factor was increased in a simplified PEC model.

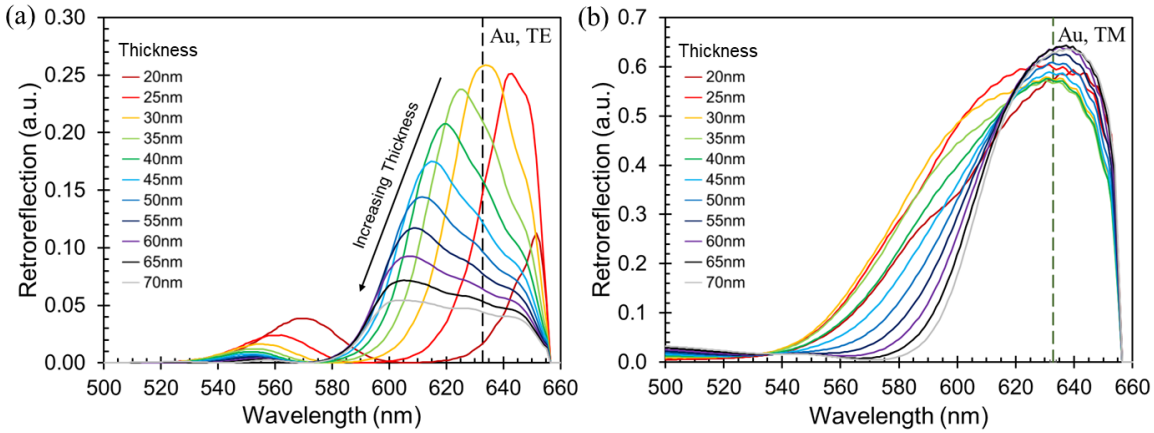

Figure 5.7. Retroreflection spectra normalized to the intensity of the incident beam for an Au slot array. Retroreflection calculated for (a) TE and (b) TM polarizations of incident light at $\Theta_{in} = 70°$ for thicknesses in the 20 - 70 nm range. The vertical dashed line represents the design wavelength of $\lambda = 633$ nm.

Retroreflection properties of Ag slot arrays in comparison with Au arrays. In Fig. 5.8, the dependence of the retroreflection spectra on the thicknesses of an Ag slot array with 10 nm increments is shown. The results display similar trends to those illustrated in Fig. 5.7 for an Au slot array. However, there are some differences in the retroreflection performance of the 3-D structures with Au and Ag top slot arrays. The first is positive for Ag retroreflectors showing more robust performance for the TE polarization with a better efficiency of ~0.3 and a broader spectral response. Potentially, the TE peak can be even stronger for thinner slot arrays at the design wavelength, but this requires additional studies

which go beyond the scope of this dissertation. However, the TM response is approximately two times weaker at ~0.3 for retroreflectors with an Ag slot array compared to the Au slot array. As a trade-off, one can conclude that despite some differences, the overall performance of retroreflectors with Ag and Au slot arrays are comparable in terms of their retroreflection efficiencies obtainable for both polarizations at the designed wavelength.

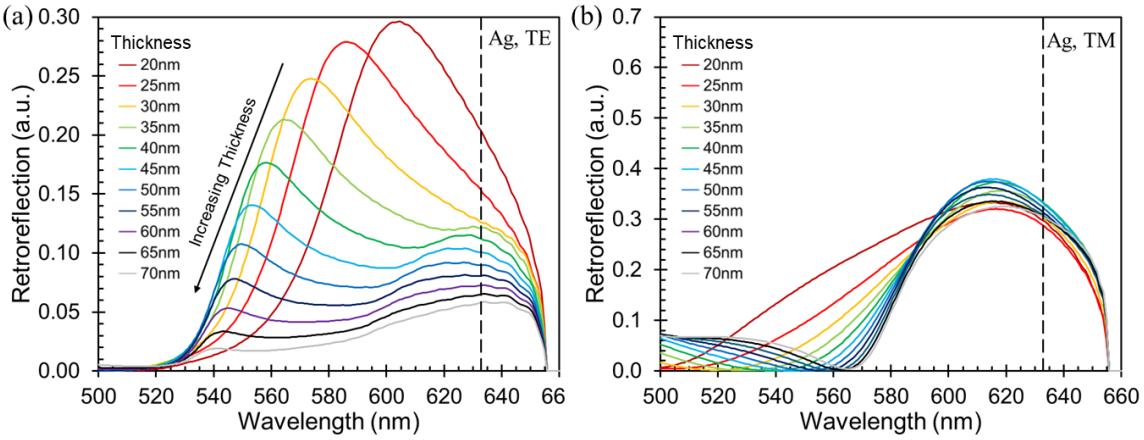

Figure 5.8. Retroreflection spectra normalized to the intensity of the incident beam for an Ag slot array. Retroreflection calculated for (a) TE and (b) TM polarizations of incident light at $\Theta_{in} = 70°$ for thicknesses in the 20 - 70 nm range. The vertical dashed line represents the design wavelength of $\lambda = 633$ nm.

Retroreflection properties of Cu slot arrays in comparison with Au arrays. In Fig. 5.9, the dependence of the retroreflection spectra on the thicknesses of a Cu slot array with 10 nm increments is shown. The results in Fig. 5.9 illustrate similar trends to those illustrated in Fig. 5.7 for Au slot arrays. However, there are some differences in the retroreflection performance of 3-D structures with Au and Cu top slot arrays. Both of the spectral responses for TE and TM polarizations are found to be weaker for Cu slot arrays compared to Au arrays. The maximal response for the TE polarization is obtained with a 30 nm thickness of the Cu slot array like in the Au case, but with two times less efficiency at ~0.15. The maximal response for the TM polarization is also reduced compared to the

Au case at ~0.4. The overall performance of retroreflectors with Cu slot arrays is worse compared to Au or Ag arrays in terms of their efficiencies available at both polarizations at the design wavelength.

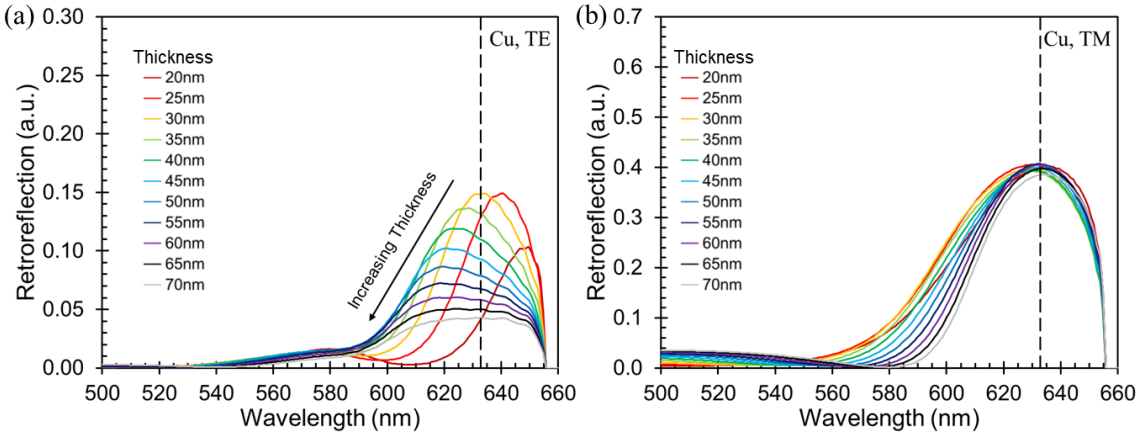

Figure 5.9. Retroreflection spectra normalized on the intensity of the incident beam for a Cu slot array calculated at (a) TE and (b) TM polarizations of incident light for Θ_{in} = 70° with the thicknesses in the 20 - 70 nm range. The design wavelength of λ = 633 nm is shown by the vertical dashed line.

Retroreflection properties of Al slot arrays in comparison with Au arrays. In Fig. 5.10, the dependence of the retroreflection spectra on the thicknesses of an Al slot array with 10 nm increments is shown. The results in Fig. 5.10 illustrate similar trends to those illustrated in Figs. 5.7-5.9 for other metals. However, there are some peculiarities in the retroreflection performance of 3-D structures with Au top slot arrays compared to other metals. The spectral response for the TE polarization is spectrally broad, but it is rather weak at ~0.15, and the maximal response can be obtained for thin arrays with thicknesses around 20 nm. The spectral response for the TM polarization is not strong at ~0.4, but the maximal response can be obtained for thick arrays with thicknesses around 70 nm. As a trade-off, one can conclude that the overall performance of retroreflectors with Al slot arrays is worse compared to that for Au and Ag arrays in terms of their efficiencies available for both polarizations at the design wavelength.

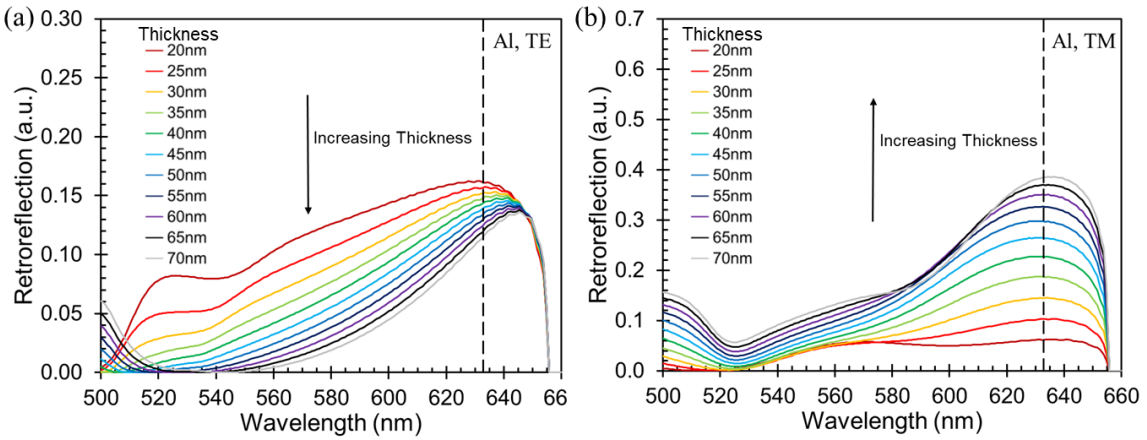

Figure 5.10. Retroreflection spectra normalized on the intensity of the incident beam for an Al slot array calculated at (a) TE and (b) TM polarizations of incident light for $\Theta_{in} = 70°$ with the thicknesses in the 20 - 70 nm range. The design wavelength of λ = 633 nm is shown by the vertical dashed line.

5.6. From Bulk Metal to Real Au Thin Films

The innovation of the modeling done in this section is related to the use of experimentally measured index values for thin metallic films instead of bulk metal values used in the previous section. This modeling takes into account the plasmon size confinement effects that may play a role in such structures. Furthermore, the thickness of the slot array usually has the minimal size among other dimensions of the stripes. Therefore, if these size confinement effects for plasmons play some part in the experimentally studied optical properties of the uniform thin metallic films, they would be automatically incorporated in the retroreflector performance of the slot arrays made from these metals, and these properties could be accurately accessed by this 3-D FDTD numerical modeling.

The metal used for this analysis was Au due to several reasons. First, Au arrays showed one of the best performances compared to Ag, Cu, and Al when using the bulk index data, as shown in the previous section. Second, there exists extensive literature regarding the spectral dependencies of the real and imaginary index values for Au thin

films with thicknesses including 11.7, 21, 25, 44, 53, and 117 nm [264, 305, 306]. These thicknesses fall exactly into the range where an interesting evolution of retroreflection properties is expected based on the results obtained using bulk index values. In addition, the results for retroreflectors formed by slot arrays in real physical thin films can be directly compared to that calculated with bulk index values. Such a comparison can reveal the role of plasmonic confinement effects in real physical thin films. Third, Au slot arrays can be fabricated by electron beam lithography. The advantage of Au over other metals is that this technology is well established, and Au structures cannot be easily oxidized so they can be used in optical experiments for a sufficiently long time.

Retroreflection properties of Au arrays with the experimental index values. In Fig. 5.11, the dependency of the retroreflection spectra on the thicknesses of the Au slot arrays are presented for experimentally measured index values from literature. These results are shown by the solid lines for thicknesses of 11.7, 21, 25, 44, 53, and 117 nm. To compare these results with the modeling based on bulk Au index values, the calculations were performed by using bulk index values for the same thicknesses of the slot arrays. These are shown by the dashed lines with the same colors used for the same thicknesses in order to facilitate easy comparison with the results obtained for real Au thin films.

There is generally a qualitative agreement between the solid and dashed curves in Fig. 5.11 which indicates that the bulk index approximation is quite reasonable for describing the properties of retroreflectors due to real physical metal thin films. At the same time, there are some differences which point potentially towards the role of quantum confinement effects for plasmons in such retroreflectors. The TM retroreflection response spectra show similar behavior for the solid and dashed curves with sufficiently strong (~0.6

level) and broadband (600 - 650 nm) peaks at intermediate thicknesses in the 25 - 53 nm range with reduced peaks at 11.7 nm and 117 nm thicknesses.

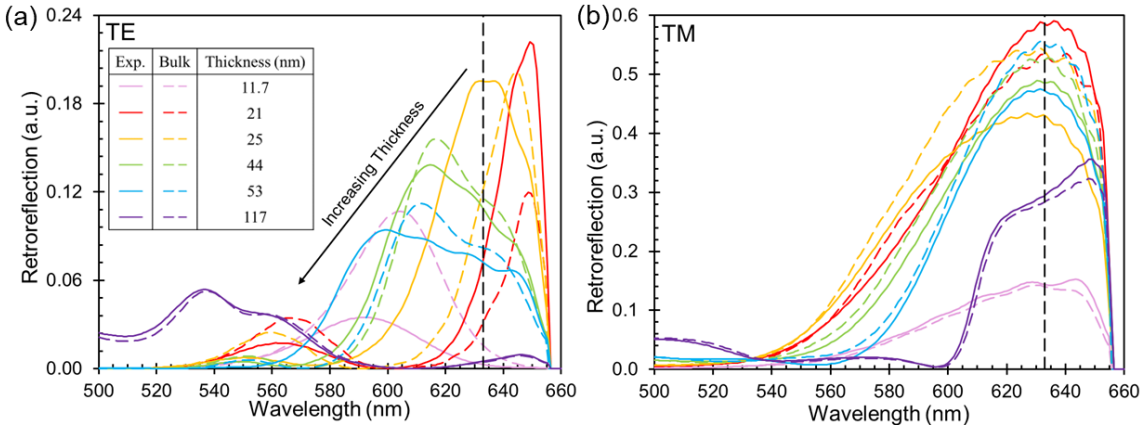

Figure 5.11. Retroreflection spectra normalized to the intensity of the incident beam for an Au slot array with thicknesses of 11.7, 21, 25, 44, 53, and 117 nm. Calculations for real Au thin films with experimentally determined index values are shown by solid curves whereas similar calculations for the bulk Au index values for the same thicknesses are shown by dashed lines. The results were obtained at (a) TE and (b) TM polarizations of incident light at $\Theta_{in} = 70°$. The design wavelength of $\lambda = 633$ nm is shown by the vertical dashed line.

Additionally, the TE response is much more complicated and quite intriguing. At the smallest thickness of 11.7 nm, the peak in the dashed pink curve calculated with bulk index values is more than two times stronger than the corresponding peak in a solid curve calculated for real physical index values. This trend is reversed for 21 nm thick Au, shown by the red curves, indicating potentially enhanced plasmonic response in real metal thin films. Furthermore, for 25 nm thick Au, the magnitudes of the peaks in the corresponding dashed and solid curves are approximately equal. Finally, at larger thicknesses of 44, 53, and 117 nm, the peaks in the dashed curves only slightly exceed the corresponding peaks in the solid curves. This supports the conclusion that, in the limit of sufficiently thick slot arrays, their optical properties can be fairly accurately described by their bulk indices.

The general conclusion of this comparison is that retroreflectors containing slot arrays formed by real Au thin films are not so different from their counterparts described

by bulk index values. However, they perform better for the critical TE polarization with intermediate thicknesses between 21 - 25 nm. The performance of such retroreflectors based on the real physical parameters of thin Au films is limited to a ~0.2 level for the TE polarization and to a ~0.6 level for the TM polarization. However, such retroreflection performance can be achieved in the same structure at both polarizations simultaneously.

Another interesting question appears around the role of absorption on the optical losses of such retroreflectors. The absorption was calculated by subtracting the total intensity of the retroreflected beam and the specular beam from the intensity of the incident beam. In Fig. 5.12, the absorption spectra are presented using the same colors for the same thicknesses as in Fig. 5.11. The results for experimentally determined thin films parameters are shown by solid lines for 11.7, 21, 25, 44, 53, and 117 nm thicknesses. To compare these results with the numerical modeling based on bulk Au index values, calculations of the absorption spectra were performed using bulk index values for the same thicknesses of the slot arrays.

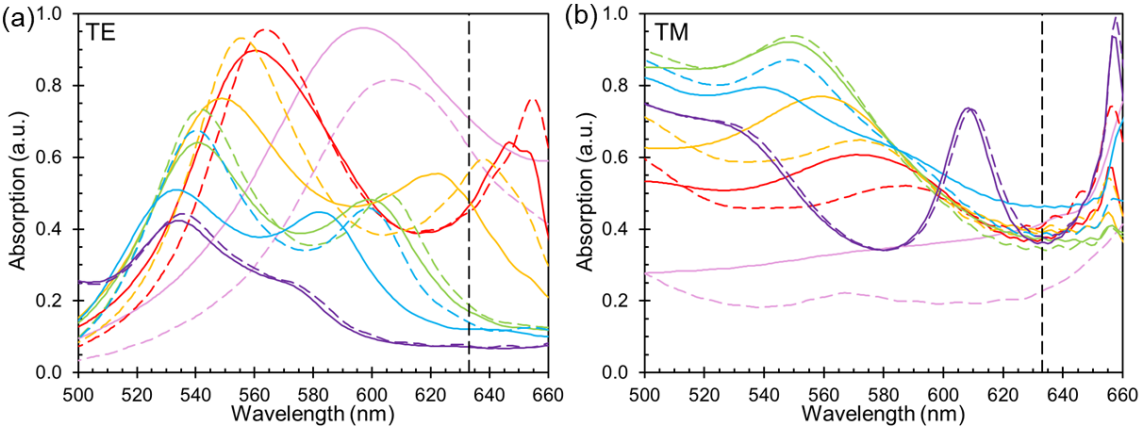

Figure 5.12. Absorption spectra normalized to the intensity of the incident beam for an Au slot array for thin films with thicknesses of 11.7, 21, 25, 44, 53, and 117 nm indicated by the same colors as in Fig. 5.11. Calculations for real Au thin films with experimentally determined index values are shown by solid curves whereas similar calculations for the bulk Au index values for the same thicknesses of the slot arrays are shown by dashed lines. The results were obtained at (a) TE and (b) TM polarizations of incident light at $\Theta_{in} = 70°$. The design wavelength of $\lambda = 633$ nm is shown by the vertical dashed line.

5.7. Conclusions and Guidance for Fabrication

The studies performed in this Chapter show that, although plasmonic Littrow retroreflectors are not ideal, they can still provide quite reasonable response in both polarizations of incident light. This is especially evident in the case of using a PEC model, often used for analyzing the operation of nanoplasmonic structures without taking into account absorption. In this limit, the retroreflector structures were designed with ~0.9 efficiencies for both TE and TM polarizations simultaneously. In this regard, these results build upon earlier work [225] performed for a 1-D lattice of stripes, but it developed the idea for a 3-D Littrow retroreflector geometry. It showed that, in this idealized PEC model, high performance structures can operate at both polarizations.

Guidelines were also developed for designing and fabricating such retroreflectors based on parameters such as the angle of incidence and operation wavelength. A methodology was developed to optimize the stripe width, and as well as the operation of such retroreflectors in the cases when their top array is fabricated from different metals including Au, Ag, Cu, and Al.

The most interesting development in this Chapter was the proposal to use experimentally measured refractive index values for thin Au films with different thicknesses to study and optimize the performance for real physical retroreflector devices. This modeling was proposed and developed for the first time to the best of our knowledge in this work. It revealed some interesting features of Au slot array Littrow retroreflectors. In particular, it was shown that there is a potential involvement of plasmonic enhancement mechanisms caused by their confinement in the metal stripes of the arrays. It was demonstrated that, as expected due to absorption in real physical structures, the

performance of such Au Littrow retroreflectors is worse compared to the predictions of the lossless PEC model, but it still reached ~0.2 and ~0.6 efficiency levels for TE and TM polarizations, respectively, with the same structure simultaneously.

The optimized performance at wavelengths in the vicinity of λ = 633 nm was calculated for top metal layers with thicknesses in the 20 - 40 nm range. However, the thickness dependence can vary for different metals such as Ag, Al, and Cu. The choice of the design wavelength in this work was partly related to plasmon-enhanced resonant properties of thin metallic stripes forming the slot array, as well as simple optical testing of the proposed structures. Applications in the visible regime include laser mirrors and optical phase conjugation in microscopy and imaging [367, 368]. It should be noted, however, that such structures can be easily redesigned for operation at longer wavelengths, and the fabrication of such structures can be performed by a variety of direct-write additive manufacturing methods which employ materials such as metals, composites, and ceramics. Furthermore, these manufacturing methods offer several benefits, including reduced build times, minimal waste, and lower production costs. The plasmonic resonant properties can also be shifted to longer wavelengths due to the quantum confinement effects. This work creates a great opening for designing efficient flat retroreflectors for various applications in different spectral ranges including traffic control recognitions, collision avoidance and other systems.

CHAPTER 6: SUMMARY OF THE MAIN RESULTS AND CONCLUSIONS

In Chapter 2, anisotropic wet etching with 25% TMAH was proven to be an effective and versatile method for the large-scale fabrication of mesophotonic structures in Si. This process offers several key advantages for creating 3-D light-concentrating structures for Si photonics applications. Notably, it enables the rapid production of extensive arrays of regular or inverted micropyramids, provides control over the sidewall angle of light concentrators based on mask orientation on (100) wafers, and results in smooth sidewall surfaces at a 54.74° angle, reducing optical scattering losses. Si anisotropic wet etching is thus an ideal approach for the efficient and economical fabrication of light concentrators, offering precise control over the geometry of structures with remarkable uniformity across entire Si wafers. This uniformity is attributed to the self-terminating nature of the etching process, achieved by the convergence of (111) planes in 3-D structures when Triton X-100 is added to slow down the SiO_2 undercutting rate.

Although Si anisotropic wet etching is well-studied in MEMS applications, the self-terminating nature of Si anisotropic etching has not been fully explored, despite its ability to produce smooth, truncated micropyramidal arrays with highly uniform characteristics—ideal for integration with detector and emitter arrays in optoelectronic devices. In this dissertation, various methods for controlling the geometry of micropyramidal arrays were examined, particularly focusing on (100) wafers etched in TMAH with Triton X-100 as a surfactant. By aligning photoresist patterns along the <110> crystalline direction and

incorporating Triton X-100, highly uniform arrays of Si micropyramids or microvoids, were formed within minutes. These arrays demonstrate perfect periodicity, reproducible geometry, and nearly atomically smooth surfaces—qualities unmatched by other fabrication techniques.

In Chapter 3, the optical properties of truncated Si micropyramids were investigated by using 3-D FDTD simulations with two types of boundary conditions. With periodic boundary conditions, the diffraction and interference patterns of these micropyramid arrays were analyzed, observing the Talbot effect and generating Talbot images that were directly visualized and experimentally validated. This effect suggests a potential application of truncated Si micropyramid arrays for Talbot lithography in 3-D photolithography. With perfectly matched layer boundary conditions, the light-focusing capabilities of these micropyramid arrays in the MWIR spectral range were explored, noting a significant intensity increase—up to an order of magnitude—due to subwavelength light concentration. These arrays demonstrated mesoscale interference effects that enhance subwavelength light focusing, with potential applications as contact superlenses, similar to high-index microspheres, for imaging at close distances. In theory, even tighter light focusing could be achieved using analogous micropyramidal structures with deeply subwavelength dimensions, which would leverage photonic nanojets or photonic funnels to enhance photon collection, signal-to-noise ratio, and operational temperature in MWIR photodetectors. This research demonstrated the unique optical properties of truncated Si micropyramidal arrays with 54.74˚ sidewall angles, specifically their ability to concentrate light to near-wavelength-scale dimensions. This property holds significant potential for enhancing photon collection across wide angles in MWIR FPAs, offering opportunities to

reduce pixel size—and therefore thermal noise—while preserving optical signal integrity. Other fabricated arrays could serve similar roles in various optical applications.

Additionally, these truncated Si micropyramids could act as contact microlenses to enhance the light extraction efficiency and directivity from localized sources in high-index semiconductor substrates. This capability offers a scalable alternative to traditional hemispherical superlenses, which are less suited for large-scale integration. This work demonstrated that these Si micropyramidal arrays can boost single-photon extraction by an order of magnitude, with highly directional output, making them valuable for quantum photonic integrated circuits. Furthermore, integrating these arrays with LED arrays could improve the efficiency and directionality of infrared scene projectors, showcasing the broad applicability of this technology in advanced optoelectronic systems. These results emphasize that the potential of this technology extends well beyond current applications. The versatility of Si anisotropic wet etching allows for the creation of diverse, innovative structures for light concentration, diffraction gratings, and other optical devices.

In Chapter 4, the primary objective of this research to enhance the performance of MWIR photodetectors by reducing dark current noise and increasing signal, ultimately improving the signal-to-noise ratio (SNR) was discussed. To achieve this, truncated Si micropyramidal arrays with 60 μm pitch were fabricated and integrated with silicon-platinum silicide (PtSi/p-Si) Schottky barrier photodetectors, where SiO_2 and Au mirror reflectors were incorporated to enhance photon concentration. These devices were tested and compared against planar photodetectors of the same dimensions to evaluate the signal enhancement provided by the micropyramid design. A key innovation involved adding a 3-D metallic mirror to the sidewalls of the micropyramids, enabling efficient photon

concentration on the photodetectors. This 3-D mirror design builds on previous back-reflector concepts used in planar MWIR photodetector FPAs. Quantum efficiency measurements were essential in this analysis, given that conventional planar Si-based photodetectors are limited by silicon's indirect band gap, which restricts absorption and photocarrier collection. The light-focusing properties of the truncated micropyramids, however, offer promise for increasing the absorption, improving the quantum efficiency, and enhancing the photoresponse. Additionally, the reduced photodetector mesa size in the micropyramid design may help lower thermal noise and potentially allow for higher operating temperatures. Experimentally, the MWIR photodetectors monolithically integrated with truncated Si micropyramids achieved a PEF ≈ 1.5 across a broad MWIR spectrum, aligning well with 3-D FDTD modeling predictions of a PEF ≈ 1.7.

It should be noted that this dissertation is concentrated mainly on signal enhancement due to integration of photodetectors with micropyramids. The noise factor was not studied in detail experimentally because photodetectors with the same mesa size should have the same noise and, for this reason, the signal-to-noise ratio should be increased due to integration with micropyramids by the same factor as the signal. In future work, to address performance enhancement of the micropyramidal photodetectors, it would be desirable to directly measure the signal-to-noise ratio and specific detectivity of the fabricated devices, $D^* = (A\Delta f)^{1/2}/\mathrm{NEP}$, where A is the area of the photodetector mesa, Δf is the bandwidth, and NEP is the noise-equivalent power.

To further boost the enhancement obtained with truncated micropyramids, a silicon-on-insulator wafer design was introduced to create resonant cavities within the micropyramids, trapping photons and enhancing absorption. This design traps photons to

create resonant optical effects, and leverages multiple light propagation paths within the detector, increasing the optical path length and improving the quantum efficiency. In the 3-D FDTD simulations, the SOI structure showed significant resonance effects, resulting in an absorbed power up to 11× higher than planar devices of the same detector size, with resonance peaks enhanced due to Fabry-Pérot resonances. This approach could address the low quantum efficiency in metal-silicide Schottky barrier detectors and potentially offers omnidirectional resonance characteristics where spectral performance is maintained over a wide range of incidence angles. All fabrication techniques developed in this dissertation for Si slabs should be completely transferrable to SOI wafers. It seems to be a highly promising direction for developing practical applications of the proposed technologies and devices.

This chapter detailed the fabrication and experimental testing of monolithically integrated PtSi detectors with truncated Si micropyramids, as well as an innovative approach for further improvement using SOI-based resonator cavities. The devices' spectral response and QE were evaluated, observing that truncated micropyramids significantly enhanced light collection and SNR, potentially enabling higher operating temperatures in MWIR FPAs. Additionally, the SOI approach demonstrated up to 11× absorption enhancement compared to planar reference devices, suggesting a path forward for further improving MWIR photodetector performance. These findings demonstrate the versatility of Si anisotropic wet etching for creating novel structures that improve MWIR FPA functionality. This research establishes micropyramidal Si photonics as a flexible, highly customizable platform to enhance SNR and operational temperatures of MWIR FPAs. Future work could focus on fabricating and experimentally validating SOI-based

structures, enabling direct comparison of imaging performance with standard MWIR cameras.

In Chapter 5, plasmonic Littrow retroreflectors designed for λ = 633 nm were discussed. This chapter demonstrated that, while plasmonic Littrow retroreflectors may not be ideal, they can still deliver a satisfactory response for both TE and TM polarizations of incident light. By using a PEC model, which simplifies the analysis by neglecting absorption losses, the retroreflector structures resulted in an efficiency of ~0.9 for both polarizations simultaneously, extending previous work on 1-D stripe lattices to a 3-D Littrow retroreflector geometry. This idealized model highlights the potential of achieving high-performance retroreflection in both polarizations.

Furthermore, design guidelines were established for optimizing these retroreflectors based on factors like incidence angle and operating wavelength. The study also developed a method for optimizing stripe width and explored the performance of retroreflectors fabricated from various metals, such as Au, Ag, Cu, and Al. A key advancement in this chapter was the use of experimentally measured refractive indices of thin Au films with varying thicknesses to evaluate and optimize real-world retroreflector performance. This novel modeling approach revealed that plasmonic enhancement mechanisms could arise from the confinement of light within the metal stripes. As expected, the efficiency of Au Littrow retroreflectors in real-world conditions is lower than that predicted by the idealized PEC model due to absorption, yet they can still achieve efficiencies of ~0.2 for TE and ~0.6 for TM polarization simultaneously. An optimal performance was observed at wavelengths near 633 nm for Au layers with thicknesses of 20 - 40 nm, though this optimal thickness varies for different metals. The choice of design

wavelength aligns with plasmon-enhanced resonant properties and facilitates optical testing.

Potential applications include laser mirrors and optical phase conjugation for microscopy and imaging. Importantly, these structures can be adapted for longer wavelengths and manufactured via direct-write additive methods, which use materials like metals, composites, and ceramics, offering advantages in speed, waste reduction, and cost. The research in this Chapter opens up new possibilities for designing efficient flat retroreflectors across various spectral ranges, with potential applications in areas such as traffic control, collision avoidance, and other optical systems.

In conclusion, this dissertation is devoted to issues related to design, modeling, and testing of novel micro and nanophotonic devices. During this period, a part of my activity was devoted to gathering inverse scattering microwave data used for advanced imaging of hidden and other objects [370-373]. Although this work was not included in this dissertation, it became a part of my preparation and training which significantly expanded the arsenal of methods which I will use in my future research. In particular, the devices designed and tested in my dissertation in the infrared regime can find applications in different spectral ranges, including the microwave regime.

REFERENCES

[1] A. Rogalski, “Progress in focal plane array technologies,” *Prog. Quant. Electron.* 36(2-3), 342–473 (2012), doi: 10.1016/j.pquantelec.2012.07.001.

[2] C. L. Tan and H. Mohseni, “Emerging technologies for high performance infrared detectors,” *Nanophoton.* 7(1), 169–197 (2017), doi: 10.1515/nanoph-2017-0061.

[3] P. B. Catrysse and T. Skauli, “Pixel scaling in infrared focal plane arrays,” *Appl. Opt.* 52(7), C72–C77 (2013), doi: 10.1364/ao.52.000c72.

[4] C. J. Reyner, G. Ariyawansa, B. Claflin, J. M. Duran, and G. J. Grzybowski, “Approaches to low-cost infrared sensing,” *Appl. Opt.* 60(25), G162–G169, (2021), doi: 10.1364/ao.427969.

[5] J. Duran, “Silicon-based infrared photodetectors for low-cost imaging applications,” Ph.D. thesis (University of Dayton, 2019).

[6] M. C. Gupta, J. T. Harrison, and M. T. Islam, “Photoconductive PbSe thin films for infrared imaging,” *Mater. Adv.* 2(10), 3133–3160 (2021), doi: 10.1039/d0ma00965b.

[7] G. Ariyawansa, J. Duran, C. Reyner, and J. Scheihing, “InAs/InAsSb Strained-Layer Superlattice Mid-Wavelength Infrared Detector for High-Temperature Operation,” *Micromachines* 10(12), 806 (2019), doi: 10.3390/mi10120806.

[8] S. Gunapala *et al*., "High operating temperature T2SL digital focal plane arrays for earth remote sensing instruments," *Proc. SPIE 11741, Infrared Tech. and Appl. XLVII*, 117410U (2021); doi: 10.1117/12.2589648.

[9] G. Vergara *et al*., “Monolithic uncooled IR detectors of polycrystalline PbSe: a real alternative,” *Proc. SPIE 6542, Infrared Tech. and Appl. XXXIII* 654220, (2007), doi: 10.1117/12.719189.

[10] Committee on Developments in Detector Technologies, *National Research Council* (2010), http://www.nap.edu/catalog/12896.html.

[11] S. M. Sze and K. K. Ng, “Physics of Semiconductor Devices,” 3rd ed., *Wiley-Interscience* (2007).

[12] E. Mikheeva *et al*., “CMOS-compatible all-dielectric metalens for improving pixel photodetector arrays,” *APL Photon.* 5(11), 116105 (2020), doi: 10.1063/5.0022162.

[13] H. Hou, Y. Zhang, Z. Luo, P. Zhang, and Y. Zhao, “Design and fabrication of monolithically integrated metalens for higher effective fill factor in long-wave infrared detectors,” *Opt. and Lasers in Eng.* 150, 106849 (2022), doi: 10.1016/j.optlaseng.2021.106849.

[14] F. Li *et al*., “HgCdTe mid-Infrared photo response enhanced by monolithically integrated meta-lenses,” *Sci. Rep.* 10, 6372 (2020), doi: 10.1038/s41598-020-62433-w.

[15] K-K Choi, "Metastructures for VLWIR SLS detectors," *Proc. SPIE 11407, Infrared Tech. and Appl. XLVI*, 114070K (2020), doi: 10.1117/12.2555954.

[16] S. Zhang *et al*., “Solid-Immersion Metalenses for Infrared Focal Plane Arrays,” *Appl. Phys. Lett.* 113(11), 111104 (2018), doi: 10.1063/1.5040395.

[17] C.-M. Kang *et al*., “Substrate-Independent Broad-Band Immersion Microlens Arrays with a High Coupling Efficiency for Infrared Focal Plane Arrays,” *ACS Appl. Electron. Mater.* 4(4), 1910–1920 (2022), doi: 10.1021/acsaelm.2c00109.

[18] A. Soibel *et al*., “High operating temperature nBn detector with monolithically integrated microlens,” *Appl. Phys. Lett.* 112(4), 041105 (2018), doi: 10.1063/1.5011348.

[19] S. Donati, G. Martini, and M. Norgia, “Microconcentrators to recover fill-factor in image photodetectors with pixel on-board processing circuits,” *Opt. Exp.* 15(26), 18066-18075 (2007), doi: 10.1364/oe.15.018066.

[20] M. Garín, R. Fenollosa, R. Alcubilla, L. Shi, L. F. Marsal, and F. Meseguer, “All-silicon spherical-Mie-resonator photodiode with spectral response in the infrared region,” *Nat. Commun.* 5, 3440 (2014), doi: 10.1038/ncomms4440.

[21] F. Abolmaali, A. Brettin, A. Green, N. I. Limberopoulos, A. M. Urbas, and V. N. Astratov, “Photonic jets for highly efficient mid-IR focal plane arrays with large angle-of-view,” *Opt. Exp.* 25(25), 31174-31185 (2017), doi: 10.1364/oe.25.031174.

[22] K. W. Allen *et al*., “Increasing sensitivity and angle-of-view of mid-wave infrared detectors by integration with dielectric microspheres,” *Appl. Phys. Lett.* 108(24), 241108 (2016), doi: 10.1063/1.4954190.

[23] B. Desiatov, I. Goykhman, N. Mazurski, J. Shappir, J. Khurgin, and U. Levy, "Plasmonic enhanced silicon pyramids for internal photoemission Schottky detectors in the near-infrared regime," *Optica* 2(4), 335-338 (2015), doi: 10.1364/optica.2.000335.

[24] H.-J. Syu, H.-C. Chuang, M.-J. Lin, C.-C. Cheng, P.-J. Huang, and C.-F. Lin, "Ultra-broadband photoresponse of localized surface plasmon resonance from Si-based pyramid structures," *Photon. Res.* 7(10), 1119–1126 (2019), doi: 10.1364/prj.7.001119.

[25] B. Jin *et al*., "Microconical silicon mid-IR concentrators: spectral, angular and polarization response," *Opt. Exp.* 28(19), 27615-27627 (2020), doi: 10.1364/oe.398014.

[26] J. R. Janesick, "Scientific Charge-Coupled Devices," *SPIE Press*, (2001).

[27] B. Burke, P. Jorden, and P. Vu, "CCD Technology," *Exp. Astron.* 19, 69–102 (2005), doi: 10.1007/s10686-005-9011-4.

[28] M. Casalino, L. Sirleto, L. Moretti, M. Gioffrè, G. Coppola, and I. Rendina, "Silicon resonant cavity enhanced photodetector based on the internal photoemission effect at 1.55μm: Fabrication and characterization," *Appl. Phys. Lett.* 92(25), 251104 (2008), doi: 10.1063/1.2952193.

[29] J. M. Mooney, "Infrared optical absorption of thin PtSi films between 1 and 6 μm," *J. Appl. Phys.* 64(9), 4664–4667 (1988), doi: 10.1063/1.341248.

[30] J. D. Vincent, "Fundamentals of Infrared Detector Operation and Testing," 1st ed. *Wiley-Interscience* (1990).

[31] A. Rogalski, "Infrared Detectors," 2nd ed., *CRC Press* (2010).

[32] P. Norton, "HgCdTe infrared detectors", *Opto-Electron. Rev.* 10(3), 159–174 (2002).

[33] O. Gravrand, L. Mollard, C. Largeron, N. Baier, and E. Deborniol, "Study of LWIR and VLWIR Focal Plane Array Developments: Comparison Between p-on-n and Different n-on-p Technologies on LPE HgCdTe," *J. Electron. Mater.* 38(8), 1733–1740 (2009), doi: 10.1007/s11664-009-0795-2.

[34] D. Wu *et al*., "High numerical aperture microlens arrays of close packing," *Appl. Phys. Lett.* 97(3), 031109 (2010), doi: 10.1063/1.3464979.

[35] A. Tripathi, T. V. Chokshi, and N. Chronis, "A high numerical aperture, polymer-based, planar microlens array," *Opt. Exp.* 17(22), 19908-19918 (2009), doi: 10.1364/OE.17.019908.

[36] P. Nussbaum, R. Völkel, H. P. Herzig, M. Eisner, and S. Haselbeck, "Design, fabrication and testing of microlens arrays for sensors and microsystems," *Pure Appl. Opt.* 6(6), 617-636 (1997), doi: 10.1088/0963-9659/6/6/004.

[37] R. F. Schmitsdorf and W. Mönch, “Influence of the interface structure on the barrier height of homogeneous Pb/n-Si(111) Schottky contacts,” *Eur. Phys. J.* 7(3), 457–466 (1999), doi: 10.1007/s100510050634.

[38] E. G. Colgan, “Activation energy for Ni_2Si and NiSi formation measured over a wide range of ramp rates,” *Thin Solid Films* 279(1–2), 193–198 (1996), doi: 10.1016/0040-6090(95)08013-9.

[39] S. Khanna, A. Noor, S. Neeleshwar, and M. S. Tyagi, “Electrical Characterization of Chromium/4H-SiC Schottky Barrier Diodes,” *Inter. J. Eng. Sci. and Tech.* 2(3), 220–226 (2010).

[40] D. Mangelinck, J. Y. Dai, J. S. Pan, and S. K. Lahiri, “Enhancement of thermal stability of NiSi films on (100)Si and (111)Si by Pt addition,” *Appl. Phys. Lett.* 75(12), 1736–1738 (1999), doi: 10.1063/1.124803.

[41] G. Majni, F. D. Valle, and C. Nobili, “Growth kinetics of NiSi on (100) and (111) silicon,” *J. Phys. D: Appl. Phys.* 17(5), L77–L81 (1984), doi: 10.1088/0022-3727/17/5/002.

[42] D. Deduytsche, C. Detavernier, R. L. Van Meirhaeghe, and C. Lavoie, “High-temperature degradation of NiSi films: Agglomeration versus $NiSi_2$ nucleation,” *J. Appl. Phys.* 98(3), 033526 (2005), doi: 10.1063/1.2005380.

[43] A. S. Zuruzi, D. Z. Chi, and D. Mangelinck, “Nitrogen enhanced thermal stability of nickel monosilicide,” *Physica Status Solidi A* 214(5), 1600710 (2017), doi: 10.1002/pssa.201600710.

[44] J. Duran and A. Sarangan, “Schottky-Barrier Photodiode Internal Quantum Efficiency Dependence on Nickel Silicide Film Thickness,” *IEEE Photon. J.* 11(1), 1–15 (2019), doi: 10.1109/jphot.2018.2886556.

[45] H. Lee, M. Li, J. Oh, and H.-D. Lee, “A Study of the Dependence of Effective Schottky Barrier Height in Ni Silicide/n-Si on the Thickness of the Antimony Interlayer for High Performance n-channel MOSFETs,” *J. Semi. Tech. and Sci.* 15(1), 41–47 (2015), doi: 10.5573/jsts.2015.15.1.041.

[46] M. I. Stockman, “Nanoplasmonics: past, present, and glimpse into future,” *Opt. Exp.* 19(22), 22029-22106 (2011), doi: 10.1364/OE.19.022029.

[47] J. B. Pendry, “Negative refraction makes a perfect lens,” *Phys. Rev. Lett.* 85(18-30), 3966-3969 (2000), doi: 10.1103/PhysRevLett.85.3966.

[48] V. G. Veselago, “Formulating Fermat's principle for light traveling in negative refraction materials,” *Phys. Usp.* 45, 1097–1099 (2002), doi: 10.1070/pu2002v045n10abeh001223.

[49] A. Boardman, “Pioneers in metamaterials: John Pendry and Victor Veselago,” *J. Opt.* 13(2), 020401 (2011), doi: 10.1088/2040-8978/13/2/020401.

[50] A. A. Yanik, M. Huang, O. Kamohara, A. Artar, T. W. Geisbert, J. H. Connor, and H. Altug, “An optofluidic nanoplasmonic biosensor for direct detection of live viruses from biological media,” *Nano Lett.* 10(12), 4962–4969 (2010), doi: 10.1021/nl103025u.

[51] K. W. Allen, N. Farahi, Y. Li, N. I. Limberopoulos, D. E. Walker Jr., A. M. Urbas, and V. N. Astratov, “Overcoming the diffraction limit of imaging nanoplasmonic arrays by microspheres and microfibers,” *Opt. Exp.* 23(19), 24484-24496 (2015), doi: 10.1364/OE.23.024484.

[52] V. N. Astratov, N. I. Limberopoulos, and A. Urbas, “Super-resolution microscopy methods and systems enhanced by dielectric microspheres or microcylinders used in combination with metallic nanostructures,” US patent 9835870 (2017), available at https://patents.justia.com/patent/9835870.

[53] V. N. Astratov, A. V. Maslov, A. Brettin, K. F. Blanchette, Y. E. Nesmelov, N. I. Limberopoulos, D. E. Walker Jr., and A. M. Urbas, “Contact microspherical nanoscopy: from fundamentals to biomedical applications,” *Proc. SPIE Vol. 10077*, 100770S (2017), doi: 10.1117/12.2251869.

[54] V. N. Astratov *et al*., “Resolution Enhancement in Microspherical Nanoscopy by Coupling of Emission to Plasmonics Metasurfaces,” *ICTON* (2019), doi: 10.1109/icton.2019.8840556.

[55] T. Chen, S. Li, and H. Sun, “Metamaterials Application in Sensing,” *Sensors* 12(3), 2742-2765 (2012), doi: 10.3390/s120302742.

[56] I. V. Minin, O. V. Minin, and Y. E. Geints, “Localized EM and photonic jets from non-spherical and non-symmetrical dielectric mesoscale objects: Brief review,” *Annalen der Physik* 527(7–8), 491–497 (2015), doi: 10.1002/andp.201500132.

[57] Z. Chen, A. Taflove, and V. Backman, “Photonic nanojet enhancement of backscattering of light by nanoparticles: a potential novel visible-light ultramicroscopy technique,” *Opt. Exp.* 12(7), 1214-1220 (2004), doi: 10.1364/OPEX.12.001214.

[58] X. Li, Z. Chen, A. Taflove, and V. Backman, “Optical analysis of nanoparticles via enhanced backscattering facilitated by 3-D photonic nanojets,” *Opt. Exp.* 13(2), 526-533 (2005), doi: 10.1364/OPEX.13.000526.

[59] A. Darafsheh, “Photonic nanojets and their applications,” *J. Phys. Photon.* 3(2), 022001 (2021), doi: 10.1088/2515-7647/abdb05.

[60] V. Pacheco-Peña, I. V. Minin, O. V. Minin, and M. Beruete, “Comprehensive analysis of photonic nanojets in 3D dielectric cuboids excited by surface plasmons,” *Annalen der Physik* 528(9–10), 684–692 (2016), doi: 10.1002/andp.201600098.

[61] A. V. Maslov and V. N. Astratov, “Resolution and Reciprocity in Microspherical Nanoscopy: Point-Spread Function Versus Photonic Nanojets,” *Phys. Rev. Appl.* 11(6), 064004 (2019), doi: 10.1103/physrevapplied.11.064004.

[62] A. V. Itagi and W. A. Challener, "Optics of photonic nanojets," *J. Opt. Soc. Am. A* 22(12), 2847-2858 (2005), doi: 10.1364/JOSAA.22.002847.

[63] V. Yakovlev and B. Luk’yanchuk, “Multiplexed nanoscopic imaging,” *Laser Phys.* 14, 1065–71 (2004).

[64] A. Heifetz, S.-C. Kong, A. V. Sahakian, A. Taflove, and V. Backman, “Photonic Nanojets,” *J. Comput. Theor. Nanosci.* 6(6), 1979-1992 (2009), doi: 10.1166/jctn.2009.1254.

[65] S. Lecler, Y. Takakura, and P. Meyrueis, “Properties of a three-dimensional photonic jet,” *Opt. Lett.* 30(19), 2641-2643 (2005), doi: 10.1364/OL.30.002641.

[66] A. Heifetz, J. J. Simpson, S.-C. Kong, A. Taflove, and V. Backman, "Subdiffraction optical resolution of a gold nanosphere located within the nanojet of a Mie-resonant dielectric microsphere," *Opt. Exp.* 15(25), 17334-17342 (2007), doi: 10.1364/OE.15.017334.

[67] Y. E. Geints, E. K. Panina, and A. A. Zemlyanov, “Collective Effects in the Formation of an Ensemble of Photonic Nanojets by an Ordered Microassembly of Dielectric Microparticles,” *Atmo. Ocean. Opt.* 32(3), 289–295 (2019), doi: 10.1134/s1024856019030084.

[68] Y. E. Geints, A. A. Zemlyanov, and E. K. Panina, “Peculiarities of the formation of an ensemble of photonic nanojets by a micro-assembly of conical particles,” *Quant. Electron.* 49(3), 210–215 (2019), doi: 10.1070/qel16868.

[69] Y. E. Geints, E. K. Panina, and A. A. Zemlyanov, "Comparative analysis of key parameters of "photonic nanojets" from axisymmetric nonspherical microparticles," *Proc. SPIE 10833, 24th Intern. Symposium on Atmo. and Ocean Opt.: Atmo. Phys.*, 1083312 (2018), doi: 10.1117/12.2503311.

[70] Yu. E. Geints, A. A. Zemlyanov, and E. K. Panina, “Microaxicon-generated photonic nanojets,” *J. Opt. Soc. Am. B* 32(8), 1570–1570 (2015), doi: 10.1364/josab.32.001570.

[71] V. V. Kotlyar and S. S. Stafeev, "Modeling the sharp focus of a radially polarized laser mode using a conical and a binary microaxicon," *J. Opt. Soc. Am. B* 27(10), 1991-1997 (2010), doi: 10.1364/JOSAB.27.001991.

[72] S. A. Degtyarev, A. P. Porfirev, and S. N. Khonina, "Photonic nanohelix generated by a binary spiral axicon," *Appl. Opt.* 55(12), B44-B48 (2016), doi: 10.1364/AO.55.000B44.

[73] C.-Y. Liu, "Photonic jets produced by dielectric micro cuboids," *Appl. Opt.* 54(29), 8694-8699 (2015), doi: 10.1364/AO.54.008694.

[74] J. Martin, J. Proust, D. Gérard, J.-L. Bijeon, and J. Plain, “Intense Bessel-like beams arising from pyramid-shaped microtips,” *Opt. Lett.* 37(7), 1274 (2012), doi: 10.1364/ol.37.001274.

[75] M. J. Mendes, I. Tobías, A. Martí, and A. Luque, "Near-field scattering by dielectric spheroidal particles with sizes on the order of the illuminating wavelength," *J. Opt. Soc. Am. B* 27(6), 1221-1231 (2010), doi: 10.1364/JOSAB.27.001221.

[76] L. Han, Y. Han, G. Gouesbet, J. Wang, and G. Gréhan, "Photonic jet generated by spheroidal particle with Gaussian-beam illumination," *J. Opt. Soc. Am. B* 31(7), 1476-1483 (2014), doi: 10.1364/JOSAB.31.001476.

[77] L. Han, Y. Han, J. Wang, and Z. Cui, "Internal and near-surface electromagnetic fields for a dielectric spheroid illuminated by a zero-order Bessel beam," *J. Opt. Soc. Am. A* 31(9), 1946-1955 (2014), doi: 10.1364/JOSAA.31.001946.

[78] C. B. Lin, Z.-H. Huang, and C.-Y. Liu, "Formation of high-quality photonic nanojets by decorating spider silk," *Opt. Lett.* 44(3), 667-670 (2019), doi: 10.1364/OL.44.000667.

[79] L. Yue, O. V. Minin, Z. Wang, J. N. Monks, A. S. Shalin, and I. V. Minin, "Photonic hook: a new curved light beam," *Opt. Lett.* 43(4), 771-774 (2018), doi: 10.1364/OL.43.000771.

[80] Z. Hengyu, C. Zaichun, C. T. Chong, and H. Minghui, "Photonic jet with ultralong working distance by hemispheric shell," *Opt. Exp.* 23(5), 6626-6633 (2015), doi: 10.1364/OE.23.006626.

[81] C.-Y. Liu and C.-J. Chen, “Characterization of photonic nanojets in dielectric microdisks,” *Physica E* 73, 226-234 (2015), doi: 10.1016/j.physe.2015.06.005.

[82] D. McCloskey, J. J. Wang, and J. F. Donegan, "Low divergence photonic nanojets from Si_3N_4 microdisks," *Opt. Exp.* 20(1), 128-140 (2012), doi: 10.1364/OE.20.000128.

[83] D. McCloskey, K. E. Ballantine, P. R. Eastham, and J. F. Donegan, "Photonic nanojets in Fresnel zone scattering from non-spherical dielectric particles," *Opt. Exp.* 23(20), 26326-26335 (2015), doi: 10.1364/OE.23.026326.

[84] Y. E. Geints and A. A. Zemlyanov, “Modeling spatially localized photonic nanojets from phase diffraction gratings,” *J. Appl. Phys.* 119(15), 153101 (2016), doi: 10.1063/1.4946846.

[85] C.-Y. Liu, O. V. Minin, and I. V. Minin, “First experimental observation of array of photonic jets from saw-tooth phase diffraction grating,” *EPL* 123(5), 54003 (2018), doi: 10.1209/0295-5075/123/54003.

[86] I. V. Minin and O. V. Minin. "Photonics of isolated dielectric particles of arbitrary 3D shape–a new direction of optical information technologies," *Vestnik NSU* 12(4), 59-70 (2014).

[87] I. V. Minin, G. V. Shuvalov, and O. V. Minin, “All-dielectric asymmetrical metasurfaces based on mesoscale dielectric particles with different optical transmissions in opposite directions through full internal reflection,” *Frontier Research and Inno. in Optoelectron. Tech. and Industry*; CRC Press (2018).

[88] S. Ge *et al*., “Novel Bilayer Micropyramid Structure Photonic Nanojet for Enhancing a Focused Optical Field,” *Nanomat.* 11(8), 2034 (2021), doi: 10.3390/nano11082034.

[89] A. Darafsheh, “Optical super-resolution and periodical focusing effects by dielectric microspheres,” Ph.D. thesis (University of North Carolina at Charlotte, 2013).

[90] B. S. Luk’yanchuk, R. Paniagua-Domínguez, I. Minin, O. Minin, and Z. Wang, "Refractive index less than two: photonic nanojets yesterday, today and tomorrow [Invited]," *Opt. Mater. Exp.* 7(6), 1820-1847 (2017), doi: 10.1364/OME.7.001820.

[91] J. Zhu and L. L. Goddard. “All-dielectric concentration of electromagnetic fields at the nanoscale: the role of photonic nanojets,” *Nanoscale Adv.* 1(12), 4615-4643 (2019), doi: 10.1039/C9NA00430K.

[92] Xu A. Zhang, I-T. Chen, and C.-H. Chang, “Recent progress in near-field nanolithography using light interactions with colloidal particles: from nanospheres to three-dimensional nanostructures,” *Nanotech.* 30(5), 352002 (2019), doi: 10.1088/1361-6528/ab2282.

[93] M. Hasan and J. J. Simpson, "Photonic nanojet-enhanced nanometer-scale germanium photodiode," *Appl. Opt.* 52(22), 5420-5425 (2013), doi: 10.1364/AO.52.005420.

[94] G. W. Bidney *et al*., "Anisotropic Wet Etching of Si as a Fabrication Tool Enabling 3-D Microphotonics Structures and Devices," *NAECON*, 146-149 (2021), doi: 10.1109/NAECON49338.2021.9696393.

[95] G. W. Bidney *et al*., “Focusing and Diffraction of Light by Periodic Si Micropyramidal Arrays,” *arXiv* (University of North Carolina at Charlotte, 2023), doi: 10.48550/arXiv.2309.15073.

[96] G. W. Bidney *et al*., “Light Manipulation with Si Mesoscale Structures for Applications in IR Photodetector and Photoemitter Arrays,” *RAPID*, 1-2 (2023), doi: 10.1109/rapid54473.2023.10264719.

[97] G. W. Bidney, J. M. Duran, G. Ariyawansa, I. Anisimov, K. W. Allen and V. N. Astratov, "MWIR Photodetector Arrays Enhanced by Integration with Si Micropyramidal Structures," *RAPID*, 1-2 (2023), doi: 10.1109/RAPID54473.2023.10264769.

[98] G. W. Bidney *et al*., “Ni-silicide schottky barrier micropyramidal photodetector array,” *NAECON*, 116-118 (2021), doi: 10.1109/naecon49338.2021.9696408.

[99] G. W. Bidney, J. M. Duran, G. Ariyawansa, I. Anisimov, K. W. Allen, and V. N. Astratov, “Photodetector Focal Plane Arrays Integrated with Silicon Micropyramidal Structures in MWIR,” *arXiv* (University of North Carolina at Charlotte, 2023), doi: 10.48550/arXiv.2309.15077.

[100] V. N. Astratov, A. Brettin, N. I. Limberopoulos, and A. Urbas, “Photodetector Focal Plane Array systems and methods based on microcomponents with arbitrary shapes,” U.S. patent 10,585,238 (2020), available at https://patents.justia.com/patent/10585238.

[101] V. N. Astratov, K. W. Allen Jr., N. I. Limberopoulos, A. Urbas, and J. M. Duran, “Photodetector focal plane array systems and methods,” U.S. patent 9,362,324 (2016), available at https://patents.google.com/patent/US9362324B1/en.

[102] G. W. Bidney *et al*., “Monolithic integration of photodetector focal plane arrays with micropyramidal arrays in mid-wave infrared,” *Proc. SPIE 12006, Si. Photon. XVII*, 1200609 (2022); doi: 10.1117/12.2610304.

[103] V. N. Astratov, G. W. Bidney, I. Anisimov, J. M. Duran, and G. Ariyawansa, “Photodetector Focal Plane Arrays with Enhanced Detection Capability,” Pub. No. US20240243158A1, published 07/18/2024.

[104] G. W. Bidney *et al*., "Fabrication of 3-D light concentrating microphotonic structures by anisotropic wet etching of silicon," *Proc. SPIE 12012, Adv. Fab. Tech. for Micro/Nano Opt. and Photon. XV*, 120120B (2022); doi: 10.1117/12.2610426.

[105] A. Brettin, N. I. Limberopoulos, I. Anisimov, A. M. Urbas, and V. N. Astratov, “Microconical arrays as novel light-concentrating structures for enhancing sensitivity, angle-of-view, and reducing dark current of mid-IR FPAs,” *NAECON*, 496–498 (2019), doi: 10.1109/NAECON.2018.8556800.

[106] B. Jin *et al*., “Light-harvesting microconical arrays for enhancing infrared imaging devices: Proposal and demonstration”, *Appl. Phys. Lett.* 119(5), 051104 (2021), doi: 10.1063/5.0054760.

[107] F. Abolmaali, A. Brettin, A. Green, N. I. Limberopoulos, A. M. Urbas, and V. N. Astratov, “Photonic jets for highly efficient mid-IR focal plane arrays with large angle-of-view,” *Opt. Exp.* 25(25), 31174–31185 (2017), doi: 10.1364/OE.25.031174.

[108] F. Abolmaali, “Focusing, imaging and resonance properties of microphotonics structures and devices”, Ph.D. thesis (University of North Carolina at Charlotte, 2018).

[109] B. Jin *et al*., "Design of Si Micro-Cone Light Concentrators for Heterogeneous Integration with MWIR FPAs," *ICTON* (2020), doi: 10.1109/ICTON51198.2020.9203159.

[110] B. Jin *et al*., "High-index micro-cones for focusing and concentrating light in MWIR focal plane arrays," *NAECON*, 665-668 (2019), doi: 10.1109/NAECON46414.2019.9057919.

[111] B. Jin *et al*., “Light-concentrating microcone array for improving performance of infrared imaging devices,” *NAECON*, 119-122 (2021), doi: 10.1109/naecon49338.2021.9696394.

[112] B. Jin *et al*., "Light-harvesting microconical arrays integrated with photodetector FPAs for enhancing infrared imaging devices," *Proc. SPIE*

12004, Int. Opt.: Dev., Mater., and Tech. XXVI, 120040X (2022); doi: 10.1117/12.2609883.

[113] A. Brettin, F. Abolmaali, N. I. Limberopoulos, A. Green, I. Anisimov, A. M. Urbas, and V. N. Astratov, "Towards fabrication of mid-IR FPAs with enhanced sensitivity and reduced dark current by using integration with microspherical arrays", *NAECON,* 533-535 (2018), doi: 10.1109/NAECON.2018.8556727.

[114] F. Abolmaali, N. I. Limberopoulos, A. M. Urbas and V. N. Astratov, "Design and optimization of focal plane arrays integrated with dielectric microspheres," *NAECON and OIS,* 258-261 (2016), doi: 10.1109/NAECON.2016.7856808.

[115] H. F. Talbot, "Facts relating to optical science," *The London, Edinburgh, and Dublin Phil. Mag. and J. of Sci.* 9(56), 401–407 (1836), doi: 10.1080/14786443608649032.

[116] L. Rayleigh, "On copying diffraction-gratings and on some phenomena connected therewith," *The London, Edinburgh, and Dublin Phil. Mag. and J. of Sci.* 11(67), 196–205 (1881), doi: 10.1080/14786448108626995.

[117] Z. Zhang *et al*., "Distance and depth modulation of Talbot imaging via specified design of the grating structure," *Opt. Exp.* 30(7), 10239 (2022), doi: 10.1364/oe.449807.

[118] E. Ye, A. H. Atabaki, N. Han, and R. J. Ram, "Miniature, sub-nanometer resolution Talbot spectrometer," *Opt. Lett.* 41(11), 2434–2437 (2016), doi: 10.1364/OL.41.002434.

[119] S. De Nicola, P. Ferraro, G. Coppola, A. Finizio, G. Pierattini, and S. Grilli, "Talbot self-image effect in digital holography and its application to spectrometry," *Opt. Lett.* 29(1), 104-106 (2004), doi: 10.1364/OL.29.000104.

[120] H. L. Kung, A. Bhatnagar, and D. A. B. Miller, "Transform spectrometer based on measuring the periodicity of Talbot self-images," *Opt. Lett.* 26(21), 1645–1647 (2001), doi: 10.1364/OL.26.001645.

[121] S. Rasouli, S. Hamzeloui, and D. Hebri, "Colorful radial Talbot carpet at the transverse plane," *Opt. Exp.* 27(13), 17435–17448 (2019), doi: 10.1364/OE.27.017435.

[122] N. Guérineau, E. Di Mambro, J. Primot, and F. Alves, "Talbot experiment re-examined: study of the chromatic regime and application to spectrometry," *Opt. Exp.* 11(24), 3310-3319 (2003), doi: 10.1364/OE.11.003310.

[123] J. Zhu, S. Hu, P. Zhou, and J. Yu, "Experimental study of Talbot imaging moiré -based lithography alignment method," *Opt. and Lasers in Eng.* 58, 54–59 (2014), doi: 10.1016/j.optlaseng.2014.01.028.

[124] H.-s. Kim, W. Li, M. C. Marconi, W. S. Brocklesby, and L. Juschkin, "Restorative Self-Image of Rough-Line Grids: Application to Coherent EUV Talbot Lithography," *IEEE Photon. J.* 8(3), 1-9 (2016), doi: 10.1109/JPHOT.2016.2553847.

[125] P. J. P. Chausse, E. D. Le Boulbar, S. D. Lis, and P. A. Shields, "Understanding resolution limit of displacement Talbot lithography," *Opt. Exp.* 27(5), 5918–5930 (2019), doi: 10.1364/OE.27.005918.

[126] L. Wang, F. Clube, C. Dais, H. H. Solak, and J. Gobrecht, "Sub-wavelength printing in the deep ultra-violet region using Displacement Talbot Lithography," *Microelectron. Eng.* 161, 104–108 (2016), doi: 10.1016/j.mee.2016.04.017.

[127] U. D. Zeitner, L. Stuerzebecher, T. Harzendorf, F. Fuchs, and D. Michaelis, "Submicrometer pattern generation by diffractive mask-aligner lithography," *Proc. SPIE 8249, Adv. Fab. Tech. for Micro/Nano Opt. and Photon. V,* 82490Q (2012), doi: 10.1117/12.909806.

[128] R. Ezaki, Y. Mizutani, N. Ura, T. Uenohara, Y. Makiura, and Y. Takaya, "Fabrication of three-dimensional high-aspect-ratio structures by oblique-incidence Talbot lithography," *Opt. Exp.* 28(24), 36924–36935 (2020), doi: 10.1364/OE.410965.

[129] H. Sun, T. Liu, J. Chen, and P. Sun, "Displacement measurement using Talbot effect," *Proc. SPIE 11209, Eleventh Intern. Con. on Info. Opt. and Photon. (CIOP),* 112090Z (2019), doi: 10.1117/12.2543190.

[130] G. S. Spagnolo, D. Ambrosini, and D. Paoletti, "Displacement measurement using the Talbot effect with a Ronchi grating," *J. Opt. A: Pure Appl. Opt.* 4(6), S376–S380 (2002), doi: 10.1088/1464-4258/4/6/383.

[131] S. Agarwal and C. Shakher, "In-plane displacement measurement by using circular grating Talbot interferometer," *Opt. and Lasers in Eng.* 75, 63–71 (2015), doi: 10.1016/j.optlaseng.2015.06.011.

[132] J. Luo, J. Bai, J. C. Zhang, C. L. Hou, K. W. Wang, and X. Y. Hou, "Long focal-length measurement using divergent beam and two gratings of different periods," *Opt. Exp.* 22(23), 27921–27931 (2014), doi: 10.1364/OE.22.027921.

[133] J. C. Bhattacharya, “Measurement of the refractive index using the Talbot effect and a moire technique,” *Appl. Opt.* 28(13), 2600–2604 (1989), doi: 10.1364/AO.28.002600.

[134] J. C. Bhattacharya, “Talbot interferometry in the measurement of the refractive indices of a doubly refracting crystal,” *Appl. Opt.* 40(10), 1658–1662 (2001), doi: 10.1364/AO.40.001658.

[135] B. Yuan, H.-M. Yan, and X.-Q. Cao, “A new subdivision method for grating-based displacement sensor using imaging array,” *Opt. and Lasers in Eng.* 47(1), 90–95 (2009), doi: 10.1016/j.optlaseng.2008.07.013.

[136] A. Mikš and P. Pokorný, “Diffraction by perfect and imperfect amplitude grating,” *Appl. Opt.* 59(30), 9368–9375 (2020), doi: 10.1364/AO.401606.

[137] S. Teng, T. Zhou, and C. Cheng, “Influence of the size of the grating on Talbot effect,” *Optik* 119(14), 695–699 (2008), doi: 10.1016/j.ijleo.2007.04.011.

[138] M. Aymerich, D. Nieto, and M. T. Flores-Arias, “Laser-based surface multistructuring using optical elements and the Talbot effect,” *Opt. Exp.* 23(19), 24369–24382 (2015), doi: 10.1364/OE.23.024369.

[139] G. Ye *et al*., “Design and development of an optical encoder with sub-micron accuracy using a multiple-tracks analyser grating,” *Rev. Sci. Instrum.* 88(1), 015003 (2017), doi: 10.1063/1.4973726.

[140] C.-F. Kao and M.-H. Lu, “Optical encoder based on the fractional Talbot effect,” *Opt. Commun.* 250(1-3), 16–23 (2005), doi: 10.1016/j.optcom.2005.02.006.

[141] C.-F. Kao, H.-L. Huang, and S.-H. Lu, “Optical encoder based on Fractional-Talbot effect using two-dimensional phase grating,” *Opt. Commun.* 283(9), 1950–1955 (2010), doi: 10.1016/j.optcom.2009.12.057.

[142] P. Zhou and J. H. Burge, “Analysis of wavefront propagation using the Talbot effect,” *Appl. Opt.* 49(28), 5351 (2010), doi: 10.1364/ao.49.005351.

[143] M.-S. Kim, T. Scharf, C. Menzel, C. Rockstuhl, and H. P. Herzig, “Phase anomalies in Talbot light carpets of self-images,” *Opt. Exp.* 21(1), 1287-1300 (2013), doi: 10.1364/oe.21.001287.

[144] I.-H. Lee, S. C. Park, and S.-D. Lee, “Submicro-pillars and holes from the depth-wise Talbot images of a conical phase mask,” *Opt. Exp.* 23(20), 25866–25873 (2015), doi: 10.1364/oe.23.025866.

[145] C.-H. Chang *et al*., "From Two-Dimensional Colloidal Self-Assembly to Three-Dimensional Nanolithography," *Nano Lett.* 11(6), 2533–2537 (2011), doi: 10.1021/nl2011824.

[146] E. C. Darmaev *et al*., "Optical Texture Super-Lattices Produced by Talbot Effect at Superimposed Gratings," *Annalen der Physik* 535(3), 2200543 (2023), doi: 10.1002/andp.202200543.

[147] A. Isoyan *et al*., "Talbot lithography: Self-imaging of complex structures," *J. Vac. Sci. Tech. B* 27(6), 2931–2937 (2009), doi: 10.1116/1.3258144.

[148] J. Frühauf, "Shape and Functional Elements of the Bulk Silicon Microtechnique: A Manual of Wet-Etched Silicon Structures," (2005), ISBN-13: 978-3540221098.

[149] K. M. Gupta and N. Gupta, "Advanced Semiconducting Materials and Devices," *Switzerland: Springer International Publishing* (2016).

[150] P. Pal, V. Swarnalatha, A. V. N. Rao, A. K. Pandey, H. Tanaka, and K. Sato, "High speed silicon wet anisotropic etching for applications in bulk micromachining: a review," *Micro and Nano Syst. Lett.* 9(4), (2021), doi: 10.1186/s40486-021-00129-0.

[151] X. Duan, "Microfabrication Using Bulk Wet Etching with TMAH," M.S. thesis (McGill University, 2005).

[152] M. M. Smiljanić, Ž. Lazić, B. Radjenović, M. Radmilović-Radjenović, and V. Jović, "Evolution of Si Crystallographic Planes-Etching of Square and Circle Patterns in 25 wt % TMAH," *Micromach.* 10(2), 102 (2019), doi: 10.3390/mi10020102.

[153] H. Lu, H. Zhang, M. Jin, T. He, G. Zhou, and L. Shui, "Two-Layer Microstructures Fabricated by One-Step Anisotropic Wet Etching of Si in KOH Solution," *Micromach.* 7(2), 19 (2016), doi: 10.3390/mi7020019.

[154] A. Ashok and P. Pal, "Silicon micromachining in 25 wt% TMAH without and with surfactant concentrations ranging from ppb to ppm," *Microsyst. Tech.* 23, 47–54 (2015), doi: 10.1007/s00542-015-2699-9.

[155] K. B. Sundaram, A. Vijayakumar, and G. Subramanian, "Smooth etching of silicon using TMAH and isopropyl alcohol for MEMS applications," *Microelec. Eng.* 77(3–4), 230–241 (2005), doi: 10.1016/j.mee.2004.11.004.

[156] L. Wang, C. Song, J. Wang, F. Xiao, W. Zhang, and L. Cao, "A wet etching approach for the via-reveal of a wafer with through silicon vias," *Microelec. Eng.* 179, 31–36 (2017), doi: 10.1016/j.mee.2017.04.025.

[157] S. S. Kumar and R. Mukhiya, “CMOS Compatible Wet Bulk Micromachining for MEMS Applications,” *IntechOpen* (2019), doi: 10.5772/intechopen.88487.

[158] K. P. Rola, “Anisotropic etching of silicon in KOH + Triton X-100 for 45° micromirror applications,” *Microsyst. Tech.* 23, 1463–1473 (2016), doi: 10.1007/s00542-016-3103-0.

[159] M. Elwenspoek, “On the Mechanism of Anisotropic Etching of Silicon,” *J. Electrochem. Soc.* 140(7), 2075–2080 (1993), doi: 10.1149/1.2220767.

[160] S. Purohit, V. Swarnalatha, A. K. Pandey, and P. Pal, “Wet anisotropic etching characteristics of Si{111} in NaOH-based solution for silicon bulk micromachining,” *Micro and Nano Syst. Lett.* 10, 21 (2022), doi: 10.1186/s40486-022-00162-7.

[161] X. Chen, R. S. Patel, J. A. Weibel, and S. V. Garimella, “Coalescence-induced jumping of multiple condensate droplets on hierarchical superhydrophobic surfaces,” *Sci. Rep.* 6, 18649 (2016), doi: 10.1038/srep18649.

[162] H. Seidel, L. Csepregi, A. Heuberger, and H. Baumgärtel, “Anisotropic Etching of Crystalline Silicon in Alkaline Solutions: I . Orientation Dependence and Behavior of Passivation Layers,” *J. Electrochem. Soc.* 137(11), 3612–3626 (1990), doi: 10.1149/1.2086277.

[163] K. Biswas and S. Kal, “Etch characteristics of KOH, TMAH and dual doped TMAH for bulk micromachining of silicon,” *Microelec. J.* 37(6), 519–525 (2006), doi: 10.1016/j.mejo.2005.07.012.

[164] Y. Fan, P. Han, P. Liang, Y. Xing, Z. Ye, and S. Hu, “Differences in etching characteristics of TMAH and KOH on preparing inverted pyramids for silicon solar cells,” *Appl. Surf. Sci.* 264, 761–766 (2013), doi: 10.1016/j.apsusc.2012.10.117.

[165] O. Tabata, R. Asahi, H. Funabahi, K. Shimaoka, and S. Sugiyama, “Anisotropic etching of silicon in TMAH solutions,” *Sensors and Actuators A: Physical* 34(1), 51–57 (1992), doi: 10.1016/0924-4247(92)80139-t.

[166] W. K. Choi, J. T. L. Thong, P. Luo, Y. Bai, C. M. Tan, and T. H. Chua, “Formation of pyramids at surface of TMAH etched silicon,” *Appl. Surf. Sci.* 144–145, 472–475 (1999), doi: 10.1016/s0169-4332(98)00842-3.

[167] C. Zhou et al., “Friction-induced selective etching on silicon by TMAH solution,” *RSC Adv.* 8(63), 36043–36048 (2018), doi: 10.1039/c8ra07064d.

[168] V. Swarnalatha, A. V. Narasimha Rao, and P. Pal, “Effective improvement in the etching characteristics of Si{110} in low concentration TMAH solution,” *Micro Nano Lett.* 13(8), 1085–1089 (2018), doi: 10.1049/mnl.2017.0610.

[169] W. K. Choi, J. T. L. Thong, P. Luo, C. M. Tan, T. H. Chua, and Y. Bai, “Characterisation of pyramid formation arising from the TMAH etching of silicon,” *Sensors and Actuators A: Physical* 71(3), 238–243 (1998), doi: 10.1016/s0924-4247(98)00193-9.

[170] A. J. Nijdam, J. van Suchtelen, J. W. Berenschot, J. G. E. Gardeniers, and M. Elwenspoek, “Etching of silicon in alkaline solutions: a critical look at the {111} minimum,” *J. Crystal Growth* 198–199, 430–434 (1999), doi: 10.1016/s0022-0248(98)01032-x.

[171] I. Zubel and I. Barycka, “Silicon anisotropic etching in alkaline solutions I. The geometric description of figures developed under etching Si (100) in various solutions,” *Sensors and Actuators A: Physical* 70(3), 250–259 (1998), doi: 10.1016/s0924-4247(98)00141-1.

[172] M. Kramkowska and I. Zubel, “Silicon anisotropic etching in KOH and TMAH with modified surface tension,” *Proc. Eur. XXIII con.*, 774–777 (2009), doi: 10.1016/j.proche.2009.07.193.

[173] P. Pal and K. Sato, “A comprehensive review on convex and concave corners in silicon bulk micromachining based on anisotropic wet chemical etching,” *Micro and Nano Syst. Lett.* 3(6), (2015), doi: 10.1186/s40486-015-0012-4.

[174] P. Pal and S. S. Singh, “A simple and robust model to explain convex corner undercutting in wet bulk micromachining,” *Micro and Nano Syst. Lett.* 1(1), (2013), doi: 10.1186/2213-9621-1-1.

[175] I. Zubel, M. Kramkowska, and K. Rola, “Silicon anisotropic etching in TMAH solutions containing alcohol and surfactant additives,” *Sensors and Actuators A: Physical* 178, 126–135 (2012), doi: 10.1016/j.sna.2012.02.018.

[176] K. P. Rola, K. Ptasiński, A. Zakrzewski, and I. Zubel, “Silicon 45° micromirrors fabricated by etching in alkaline solutions with organic additives,” *Microsyst. Tech*. 20, 221–226 (2014), doi: 10.1007/s00542-013-1859-z.

[177] O. Tabata, “pH-controlled TMAH etchants for silicon micromachining,” *Sensors and Actuators A: Physical* 53(1–3), 335–339 (1996), doi: 10.1016/0924-4247(96)80157-9.

[178] J. T. L. Thong, W. K. Choi, and C. W. Chong, “TMAH etching of silicon and the interaction of etching parameters,” *Sensors and Actuators A: Physical* 63(3), 243–249 (1997), doi: 10.1016/s0924-4247(97)80511-0.

[179] R. H. Murray, “Light-Reflecting device or unit,” U.S. patent 1,625,905 (1927), available at https://patents.google.com/patent/US1625905A/en.

[180] M. L. Biermann, W. S. Rabinovich, R. Mahon, and G. C. Gilbreath, “Design and analysis of a diffraction-limited cat’s-eye retroreflector,” *Opt. Eng.* 41(7), 1655–1661 (2002), doi: 10.1117/1.1483881.

[181] A. Lundvall, F. Nikolajeff, and T. Lindström, “High performing micromachined retroreflector,” *Opt. Exp.* 11(20), 2459–2473 (2003), doi: 10.1364/OE.11.002459.

[182] C. A. Duboc, “Corner reflectors,” Ph.D. thesis, (MIT 1943).

[183] L. Peters, “Passive bistatic radar enhancement devices,” *Proc. Inst. Electr. Eng., Part C* 109(15), 1–10 (1962), doi: 10.1049/pi-c.1962.0001.

[184] J. L. Zurasky, “Cube corner retroreflector test and analysis,” *Appl. Opt.* 15(2), 445–452 (1976), doi: 10.1364/AO.15.000445.

[185] D. Bird, “Design and Manufacture of a Low-Profile Radar Retro-Reflector,” *RTO-MP-SCI-145* (2005).

[186] D. C. O’Brien, G. E. Faulkner, and D. J. Edwards, “Optical properties of a retroreflecting sheet,” *Appl. Opt.* 38(19), 4137–4144 (1999), doi: 10.1364/AO.38.004137.

[187] A. Pesarakloo and M. Khalaj-amirhosseini, “Planar, wide-band omnidirectional retroreflector using metal-only transmitarray structure for TE and TM polarizations,” *Sci. Rep.* 12, 11279 (2022), doi: 10.1038/s41598-022-15540-9.

[188] J. Park and J. Y. Park, “A bulk-micromachined corner cube retroreflector with piezoelectric micro-cantilevers,” *Micro and Nano Syst. Lett.* 1, 7 (2013), doi: 10.1186/2213-9621-1-7.

[189] J. C. Miñano, P. Benítez, and A. Santamaría, “Hamilton-Jacobi equation in momentum space,” *Opt. Exp.* 14(20), 9083-9092 (2006), doi: 10.1364/oe.14.009083.

[190] W. Yang *et al.*, “Angular-Adaptive Reconfigurable Spin-Locked Metasurface Retroreflector,” *Adv. Sci.* 8(21), 2100885 (2021), doi: 10.1002/advs.202100885.

[191] A. M. H. Wong, P. Christian, and G. V. Eleftheriades, “Binary Huygens’ Metasurfaces: Experimental Demonstration of Simple and Efficient Near-Grazing Retroreflectors for TE and TM Polarizations,” *IEEE Trans. on Antennas and Prop.* 66(6), 2892–2903 (2018), doi: 10.1109/tap.2018.2816792.

[192] R. K. Luneburg, “Mathematical Theory of Optics,” *Brown University*, 189–213 (1944).

[193] R. K. Luneburg and M. Herzberger, “Mathematical Theory of Optics,” *Berkeley Univ. California Press,* (1964).

[194] L. C. Van Atta, “Electromagnetic reflector,” U.S. patent 2,908,002 (1959), available at https://patents.google.com/patent/US2908002A/en.

[195] E. Sharp and M. Diab, “Van Atta reflector array,” *IRE Trans. on Antennas and Prop.* 8(4), 436–438 (1960), doi: 10.1109/TAP.1960.1144877.

[196] C. L. Holloway, M. A. Mohamed, E. F. Kuester, and A. Dienstfrey, “Reflection and transmission properties of a metafilm: with an application to a controllable surface composed of resonant particles,” *IEEE Trans. on Electromag. Comp.* 47(4), 853–865 (2005), doi: 10.1109/TEMC.2005.853719.

[197] R. Leberer and W. Menzel, “A dual planar reflectarray with synthesized phase and amplitude distribution,” *IEEE Trans. on Antennas and Prop.* 53(11), 3534–3539 (2005), doi: 10.1109/TAP.2005.858813.

[198] C. L. Holloway, E. F. Kuester, J. A. Gordon, J. O’Hara, J. Booth, and D. R. Smith, “An Overview of the Theory and Applications of Metasurfaces: The Two-Dimensional Equivalents of Metamaterials,” *IEEE Antennas and Prop. Mag.* 54(2), 10–35 (2012), doi: 10.1109/MAP.2012.6230714.

[199] A. Epstein and G. V. Eleftheriades, “Huygens’ metasurfaces via the equivalence principle: design and applications,” *J. Opt. Soc. Am. B* 33(2), A31-A50 (2016), doi: 10.1364/JOSAB.33.000A31.

[200] V. S. Asadchy, M. Albooyeh, S. N. Tcvetkova, A. Díaz-Rubio, Y. Ra’di, and S. A. Tretyakov, “Perfect control of reflection and refraction using spatially dispersive metasurfaces,” *Phys. Rev. B* 94(7), 075142 (2016), doi: 10.1103/PhysRevB.94.075142.

[201] N. M. Estakhri and A. Alù, “Wave-front Transformation with Gradient Metasurfaces,” *Phys. Rev. X* 6(4), 041008 (2016), doi: 10.1103/PhysRevX.6.041008.

[202] M. Kim, A. M. H. Wong, and G. V. Eleftheriades, “Optical Huygens’ Metasurfaces with Independent Control of the Magnitude and Phase of the

Local Reflection Coefficients," *Phys. Rev. X* 4(4), 041042 (2014), doi: 10.1103/PhysRevX.4.041042.

[203] J. P. S. Wong, M. Selvanayagam, and G. V. Eleftheriades, "Design of unit cells and demonstration of methods for synthesizing Huygens metasurfaces," *Photon. Nanostruct. Fundam. Appl.* 12(4), 360–375 (2014), doi: 10.1016/j.photonics.2014.07.001.

[204] M. Selvanayagam and G. V. Eleftheriades, "Polarization Control Using Tensor Huygens Surfaces*," IEEE Trans. on Antennas and Prop.* 62(12), 6155-6168 (2014), doi: 10.1109/TAP.2014.2359208.

[205] M. Selvanayagam and G. V. Eleftheriades, "Design And Measurement of Tensor Impedance Transmitarrays For Chiral Polarization Control," *IEEE Trans. on Microwave Theory and Tech.* 64(2),414-428 (2016), doi: 10.1109/TMTT.2015.2505718.

[206] M. Selvanayagam and G. V. Eleftheriades, "Discontinuous electromagnetic fields using orthogonal electric and magnetic currents for wavefront manipulation," *Opt. Exp.* 21(12), 14409–14429 (2013), doi: 10.1364/OE.21.014409.

[207] C. Liu *et al.*, "Broadband, High-Efficiency and Wide-Incident-Angle Anomalous Reflection in Groove Metagratings," *Annalen der Physik* 533(9), 2100149 (2021), doi: 10.1002/andp.202100149.

[208] H.-X. Xu, G. Hu, X. Kong, Y. Shao, P. Genevet, and C.-W. Qiu, "Super-reflector enabled by non-interleaved spin-momentum-multiplexed metasurface," *Light Sci. Appl.* 12, 78 (2023), doi: 10.1038/s41377-023-01118-1.

[209] Q. Wang *et al.*, "Retroreflection from a single layer of electromagnetic Helmholtz cavities based on magnetic symmetric dipole modes," *Opt. Exp.* 28(21), 30606-30615 (2020), doi: 10.1364/oe.402675.

[210] [194, 210] Q. Tan *et al.*, "Broadband Spin-Locked Metasurface Retroreflector," *Adv. Sci.* 9(20), 2201397 (2022), doi: https://doi.org/10.1002/advs.202201397.

[211] L. B. Yan *et al.*, "0.2 λ_0 Thick Adaptive Retroreflector Made of Spin-Locked Metasurface," *Adv. Mater.* 30(39), 1802721 (2018), doi: 10.1002/adma.201802721.

[212] A. Arbabi, E. Arbabi, Y. Horie, S. M. Kamali, and A. Faraon, "Planar metasurface retroreflector," *Nat. Photon.* 11, 415–420 (2017), doi: 10.1038/nphoton.2017.96.

[213] N. Ullah, R. Zhao, and L. Huang, “Recent Advancement in Optical Metasurface: Fundament to Application,” *Micromach.* 13(7), 1025 (2022), doi: 10.3390/mi13071025.

[214] A. Pesarakloo and M. Khalaj-Amirhosseini, “Planar metal-only omnidirectional retroreflector using transmitarray and blazed grating for TE and TM polarizations,” *Opt. Exp.* 30(15), 28121–28141 (2022), doi: 10.1364/oe.464369.

[215] N. Yu *et al.*, “Light Propagation with Phase Discontinuities: Generalized Laws of Reflection and Refraction,” *Science* 334(6054), 333–337 (2011), doi: 10.1126/science.1210713.

[216] F. S. Cuesta, G. A. Ptitcyn, M. S. Mirmoosa, and S. A. Tretyakov, “Coherent retroreflective metasurfaces,” *Phys. Rev. Res.* 3(3), L0322025 (2021), doi: 10.1103/physrevresearch.3.l032025.

[217] G. Cao *et al.*, “Polarization-insensitive unidirectional meta-retroreflector,” *Opt. & Laser Tech.* 156, 108497 (2022), doi: 10.1016/j.optlastec.2022.108497.

[218] S. Zhu, Y. Cao, Y. Fu, X. Li, L. Gao, H. Chen, and Y. Xu, “Switchable bifunctional metasurfaces: nearly perfect retroreflection and absorption at the terahertz regime," *Opt. Lett.* 45(14), 3989-3992 (2020), doi: 10.1364/OL.394164.

[219] J. L. Shen, Y. B. Li, H. Li, and T. J. Cui, “Arbitrarily polarized retro-reflections by anisotropic digital coding metasurface,” *J. Phys. D: Appl. Phys.* 52(50), 505401 (2019), doi: 10.1088/1361-6463/ab42b2.

[220] H. Li, W.-B. Lee, C. Zhou, D.-Y. Choi, and S.-S. Lee, “Flat Retroreflector Based on a Metasurface Doublet Enabling Reliable and Angle-Tolerant Free-Space Optical Link,” *Adv. Opt. Mater.* 9(21), 2100796 (2021), doi: 10.1002/adom.202100796.

[221] L.-Z. Yin, J. Zhao, M.-Z. Chong, F.-Y. Han, and P.-K. Liu, “Ultrathin All-Angle Hyperbolic Metasurface Retroreflectors Based on Directed Routing of Canalized Plasmonics,” *ACS Appl. Mater. Interfaces* 14(18), 21605–21612 (2022), doi: 10.1021/acsami.2c00802.

[222] M. Chen, M. Kim, A. M. H. Wong, and G. V. Eleftheriades, “Huygens’ metasurfaces from microwaves to optics: a review,” *Nanophoton.* 7(6), 1207–1231 (2018), doi: 10.1515/nanoph-2017-0117.

[223] P. Christian, “Retroreflective Binary Huygens’ Metasurface,” Master’s thesis, (University of Toronto, 2018).

[224] M. Mansuripur, “Classical optics and its applications,” *Cambridge University Press*, (2002).

[225] P. Honzatko and J. Čtyroký, “Flat metal-dielectric grating with 100% retro-diffraction efficiency: rigorous theory,” *J. Opt.* 23(1), 015601 (2020), doi: 10.1088/2040-8986/abcd01.

[226] W. L. Barnes, A. Dereux, and T. W. Ebbesen, “Surface plasmon subwavelength optics,” *Nature* 424, 824–830 (2003), doi: 10.1038/nature01937.

[227] S. Szunerits, A. Shalabney, R. Boukherroub, and I. Abdulhalim, “Dielectric coated plasmonic interfaces: their interest for sensitive sensing of analyte-ligand interactions,” *Rev. Anal. Chem.* 31(1), 15-28 (2012), doi: 10.1515/revac.2011.120.

[228] H. Shimizu, T. Ogura, T. Maeda, and S. Suzuki, “A Wedge-Shaped Au Thin Film: Integrating Multiple Surface Plasmon Resonance Sensors in a Single Chip and Enhancing the Figure of Merit,” *Front. Nanotechnol.* 3, 724528 (2021), doi: 10.3389/fnano.2021.724528.

[229] R. H. Ritchie, “Plasma Losses by Fast Electrons in Thin Films,” *Phys. Rev.* 106(5), 874–881 (1957), doi: 10.1103/PhysRev.106.874.

[230] T. Ito and S. Okazaki, “Pushing the limits of lithography,” *Nature* 406, 1027-1031 (2000), doi: 10.1038/35023233.

[231] C. L. Haynes and R. P. Van Duyne, “Nanosphere Lithography: A Versatile Nanofabrication Tool for Studies of Size-Dependent Nanoparticle Optics,” *J. Phys. Chem. B* 105(24), 5599-5611 (2001), doi: 10.1021/jp010657m.

[232] P. Mühlschlegel, H.-J. Eisler, O. J. F. Martin, B. Hecht, and D. W. Pohl, “Resonant Optical Antennas,” *Science* 308(5728), 1607-1609 (2005), doi: 10.1126/science.1111886.

[233] C. Ducamp-Sanguesa, R. Herrera-Urbina, M. Figlarz, “Synthesis and characterization of fine and monodisperse silver particles of uniform shape,” *J. Solid State Chem.* 100(2), 272-280 (1992), doi: 10.1016/0022-4596(92)90101-Z.

[234] D. V. Goia and E. Matijević, “Preparation of monodispersed metal particles,” *New J. Chem.* 22(11), 1203-1215 (1998), doi: 10.1039/A709236I.

[235] Y. Sun and Y. Xia, "Shape-Controlled Synthesis of Gold and Silver Nanoparticles," *Science* 298(5601), 2176-2179 (2002), doi: 10.1126/science.1077229.

[236] R. Jin, Y. C. Cao, E. Hao, G. S. Métraux, G. C. Schatz, and C. A. Mirkin, "Controlling anisotropic nanoparticle growth through plasmon excitation," *Nature* 425(6957), 487-90 (2003), doi: 10.1038/nature02020.

[237] R. Malureanu and A. Lavrinenko, "Ultra-thin films for plasmonics: a technology overview," *Nanotechnol. Rev.* 4(3), 259-275 (2015), doi: 10.1515/ntrev-2015-0021.

[238] B. Hecht, H. Bielefeldt, L. Novotny, Y. Inouye, and D. W. Pohl, "Local Excitation, Scattering, and Interference of Surface Plasmons," *Phys. Rev. Lett.* 77(9), 1889–1892 (1996), doi: 10.1103/PhysRevLett.77.1889.

[239] J. Pendry, "Playing Tricks with Light," *Science* 285(5434), 1687–1688 (1999), doi: 10.1126/science.285.5434.1687.

[240] D. L. Mills and E. Burstein, "Polaritons: the electromagnetic modes of media," *Rep. Prog. Phys.* 37(7), 817-926 (1974), doi: 10.1088/0034-4885/37/7/001.

[241] S. Zou and G. C. Schatz, "Silver nanoparticle array structures that produce giant enhancements in electromagnetic fields," *Chem. Phys. Lett.* 403(1-3), 62-67 (2005), doi: 10.1016/j.cplett.2004.12.107.

[242] S. G. Rodrigo, F. J. García-Vidal, and L. Martín-Moreno, "Influence of material properties on extraordinary optical transmission through hole arrays," *Phys. Rev. B* 77(7), 075401 (2008), doi: 10.1103/physrevb.77.075401.

[243] J. Parsons, E. Hendry, C. P. Burrows, B. Auguié, J. R. Sambles, and W. L. Barnes, "Localized surface-plasmon resonances in periodic nondiffracting metallic nanoparticle and nanohole arrays," *Phys. Rev. B* 79(7), 073412 (2009), doi: 10.1103/physrevb.79.073412.

[244] J. J. Mock, M. Barbic, D. R. Smith, D. A. Schultz, and S. Schultz, "Shape effects in plasmon resonance of individual colloidal silver nanoparticles," *J. Chem. Phys.* 116(15), 6755-6759 (2002), doi: 10.1063/1.1462610.

[245] W. A. Murray and W. L. Barnes, "Plasmonic Materials," *Adv. Mater.* 19(22), 3771-3782 (2007), doi: 10.1002/adma.200700678.

[246] W. A. Murray, J. R. Suckling, and W. L. Barnes, "Overlayers on Silver Nanotriangles: Field Confinement and Spectral Position of Localized Surface Plasmon Resonances," *Nano Lett.* 6(8), 1772-1777 (2006), doi: 10.1021/nl060812e.

[247] A. D. Humphrey and W. L. Barnes, “Plasmonic surface lattice resonances on arrays of different lattice symmetry,” *Phys. Rev. B* 90(7), 075404 (2014), doi: 10.1103/physrevb.90.075404.

[248] F. Wang and Y. R. Shen, “General Properties of Local Plasmons in Metal Nanostructures,” *Phys. Rev. Lett.* 97(20), 206806 (2006), doi: 10.1103/physrevlett.97.206806.

[249] V. G. Kravets, A. V. Kabashin, W. L. Barnes, and A. N. Grigorenko, “Plasmonic Surface Lattice Resonances: A Review of Properties and Applications,” *Chem. Rev.* 118(12), 5912–5951 (2018), doi: 10.1021/acs.chemrev.8b00243.

[250] K. L. Kelly, E. Coronado, L. L. Zhao, and G. C. Schatz, “The Optical Properties of Metal Nanoparticles: The Influence of Size, Shape, and Dielectric Environment,” *J. Phys. Chem. B* 107(3), 668−677 (2003), doi: 10.1021/jp026731y.

[251] U. Kreibig and M. Vollmer, “Optical Properties of Metal Clusters,” *Springer* (1995).

[252] H. Ditlbacher *et al*., “Fluorescence imaging of surface plasmon fields,” *Appl. Phys. Lett.* 80(3), 404–406 (2002), doi: 10.1063/1.1435410.

[253] E. Kretschmann and H. Raether, “Radiative Decay of Non Radiative Surface Plasmons Excited by Light,” *Z. Naturforsch. A* 23(12), 2135–2136 (1968), doi: 10.1515/zna-1968-1247.

[254] A. Otto, “Exitation of nonradiative surface plasma waves in silver by the method of frustrated total reflection,” *Z. Physik* 216, 398-410 (1968), doi: 10.1007/BF01391532.

[255] R. H. Ritchie, E. T. Arakawa, J. J. Cowan, and R. N. Hamm, “Surface-Plasmon Resonance Effect in Grating Diffraction,” *Phys. Rev. Lett.* 21(22-25), 1530–1533 (1968), doi: 10.1103/PhysRevLett.21.1530.

[256] R. W. Wood, “On a Remarkable Case of Uneven Distribution of Light in a Diffraction Grating Spectrum,” *Proc. Phys. Soc. London* 18(1), 269-275 (1902), doi: 10.1088/1478-7814/18/1/325.

[257] H. Raether, “Surface Plasmons on Smooth and Rough Surfaces and on Gratings,” *Springer* (1988).

[258] J. Moreland, A. Adams, and P. K. Hansma, "Efficiency of light emission from surface plasmons," *Phys. Rev. B* 25(4), 2297–2300 (1982), doi: 10.1103/PhysRevB.25.2297.

[259] P. T. Worthing and W. L. Barnes, "Efficient coupling of surface plasmon polaritons to radiation using a bi-grating," *Appl. Phys. Lett.* 79(19), 3035–3037 (2001), doi: 10.1063/1.1414294.

[260] C. Yang *et al*., "Angle Robust Reflection/Transmission Plasmonic Filters Using Ultrathin Metal Patch Array," *Adv. Opt. Mater.* 4(12), 1981–1986 (2016), doi: 10.1002/adom.201600397.

[261] V. G. Kravets, F. Schedin, A. V. Kabashin, and A. N. Grigorenko, "Sensitivity of collective plasmon modes of gold nanoresonators to local environment," *Opt. Lett.* 35(7), 956–956 (2010), doi: 10.1364/ol.35.000956.

[262] W. L. Barnes, "Particle plasmons: Why shape matters," *Am. J. Phys.* 84(8), 593–601 (2016), doi: 10.1119/1.4948402.

[263] M. B. Ross, C. A. Mirkin, and G. C. Schatz, "Optical Properties of One-, Two-, and Three-Dimensional Arrays of Plasmonic Nanostructures," *J. Phys. Chem. C* 120(2), 816–830 (2016), doi: 10.1021/acs.jpcc.5b10800.

[264] G. Rosenblatt, B. Simkhovich, G. Bartal, and M. Orenstein, "Nonmodal Plasmonics: Controlling the Forced Optical Response of Nanostructures," *Phys. Rev. X* 10(1), 011071 (2020), doi: 10.1103/physrevx.10.011071.

[265] B. Lamprecht *et al.*, "Metal Nanoparticle Gratings: Influence of Dipolar Particle Interaction on the Plasmon Resonance," *Phys. Rev. Lett.* 84(20), 4721 (2000), doi: 10.1103/physrevlett.84.4721.

[266] E. Prodan, C. Radloff, N. J. Halas, and P. Nordlander, "A Hybridization Model for the Plasmon Response of Complex Nanostructures," *Science* 302(5644), 419−422 (2003), doi: 10.1126/science.108917.

[267] W. Rechberger, A. Hohenau, A. Leitner, J. R. Krenn, B. Lamprecht, and F. R. Aussenegg, "Optical properties of two interacting gold nanoparticles," *Opt. Commun.* 220(1-3), 137−141 (2003), doi: 10.1016/S0030-4018(03)01357-9.

[268] P. Nordlander, C. Oubre, E. Prodan, K. Li, and M. I. Stockman, "Plasmon Hybridization in Nanoparticle Dimers," *Nano Lett.* 4(5), 899−903 (2004), doi: 10.1021/nl049681c.

[269] N. J. Halas, S. Lal, W.-S. Chang, S. Link, and P. Nordlander, "Plasmons in Strongly Coupled Metallic Nanostructures," *Chem. Rev.* 111(6), 3913−3961 (2011), doi: 10.1021/cr200061k.

[270] L. V. Panina, A. N. Grigorenko, and D. P. Makhnovskiy, “Optomagnetic composite medium with conducting nanoelements,” *Phys. Rev. B* 66(15), 155411 (2002), doi: 10.1103/PhysRevB.66.155411.

[271] V. G. Kravets, F. Schedin, and A. N. Grigorenko, “Extremely Narrow Plasmon Resonances Based on Diffraction Coupling of Localized Plasmons in Arrays of Metallic Nanoparticles,” *Phys. Rev. Lett.* 101(8), 087403 (2008), doi: 10.1103/physrevlett.101.087403.

[272] I. Zorić, M. Zäch, B. Kasemo, and C. Langhammer, “Gold, Platinum, and Aluminum Nanodisk Plasmons: Material Independence, Subradiance, and Damping Mechanisms,” *ACS Nano* 5(4), 2535–2546 (2011), doi: 10.1021/nn102166t.

[273] S. R. K. Rodriguez, M. C. Schaafsma, A. Berrier, and J. Gómez Rivas, “Collective Resonances in Plasmonic Crystals: Size Matters,” *Physica B* 407(20), 4081−4085 (2012), doi: 10.1016/j.physb.2012.03.053.

[274] L. Zhang, F. Zhao, Z. Li, Y. Fang, and P. Wang, “Tailoring of Localized Surface Plasmon Resonances of Core-Shell Au@Ag Nanorods by Changing the Thickness of Ag Shell,” *Plasmonics* 11, 1511-1517 (2016), doi: 10.1007/s11468-016-0204-7.

[275] M. B. Ross and G. C. Schatz, “Aluminum and Indium Plasmonic Nanoantennas in the Ultraviolet,” *J. Phys. Chem. C* 118(23), 12506-12514 (2014), doi: 10.1021/jp503323u.

[276] M. G. Blaber, M. D. Arnold, and M. J. Ford, “A review of the optical properties of alloys and intermetallics for plasmonics,” *J. Phys.: Condens. Matter.* 22(14), 143201 (2010), doi: 10.1088/0953-8984/22/14/143201.

[277] G. H. Chan, J. Zhao, G. C. Schatz, and R. P. Van Duyne, “Localized Surface Plasmon Resonance Spectroscopy of Triangular Aluminum Nanoparticles,” *J. Phys. Chem. C* 112(36), 13958−13963 (2008), doi: 10.1021/jp804088z.

[278] T. W. Ebbesen, H. J. Lezec, H. F. Ghaemi, T. Thio, and P. A. Wolff, “Extraordinary optical transmission through sub-wavelength hole arrays,” *Nature* 391, 667–669 (1998), doi: 10.1038/35570.

[279] K. Yang and M. Li, “The Sensitivity of a Hexagonal Au Nanohole Array under Different Incident Angles,” *Biosensors* 13(6), 654 (2023), doi: 10.3390/bios13060654.

[280] F. J. García de Abajo, “Colloquium: Light scattering by particle and hole arrays,” *Rev. Mod. Phys.* 79(4), 1267–1290 (2007), doi: 10.1103/revmodphys.79.1267.

[281] F. J. Garcia-Vidal, L. Martin-Moreno, T. W. Ebbesen, and L. Kuipers, “Light passing through subwavelength apertures,” *Rev. Mod. Phys.* 82(1), 729–787 (2010), doi: 10.1103/revmodphys.82.729.

[282] M. Born and E. Wolf, “Principles of Optics: Electromagnetic Theory of Propagation, Interference and Diffraction of Light,” 7th ed. *Cambridge University Press* (1999).

[283] M. Valenti *et al*., “Hot Carrier Generation and Extraction of Plasmonic Alloy Nanoparticles,” *ACS Photon.* 4(5), 1146–1152 (2017), doi: 10.1021/acsphotonics.6b01048.

[284] R. Borah and S. W Verbruggen, “Silver–Gold Bimetallic Alloy versus Core–Shell Nanoparticles: Implications for Plasmonic Enhancement and Photothermal Applications,” *J. Phys. Chem. C* 124(22), 12081–12094 (2020), doi: 10.1021/acs.jpcc.0c02630.

[285] R. Borah, R. Ninakanti, S. Bals, and S. W. Verbruggen, “Plasmon resonance of gold and silver nanoparticle arrays in the Kretschmann (attenuated total reflectance) vs. direct incidence configuration,” *Sci. Rep.* 12, 15738 (2022), doi: 10.1038/s41598-022-20117-7.

[286] E. Prodan, A. Lee, and P. Nordlander, “The effect of a dielectric core and embedding medium on the polarizability of metallic nanoshells,” *Chem. Phys. Lett.* 360(3-4), 325–332 (2002), doi: 10.1016/S0009-2614(02)00850-3.

[287] X. Zhou, H. Li, S. Xie, S. Fu, H. Xu, and Z. Liu, “Effects of dielectric core and embedding medium on plasmonic coupling of gold nanoshell arrays,” *Solid State Commun.* 151(14-15), 1049–1052 (2011), doi: 10.1016/j.ssc.2011.04.014.

[288] A. Shiohara, J. Langer, L. Polavarapu, and L. M. Liz-Marzán, “Solution processed polydimethylsiloxane/gold nanostar flexible substrates for plasmonic sensing,” *Nanoscale* 6(16), 9817-9823 (2014), doi: 10.1039/C4NR02648A.

[289] C. Sönnichsen, T. Franzl, T. Wilk, G. von Plessen, J. Feldmann, O. Wilson, and P. Mulvaney, “Drastic Reduction of Plasmon Damping in Gold Nanorods,” *Phys. Rev. Lett.* 88(7), 077402 (2002), doi: 10.1103/PhysRevLett.88.077402.

[290] M. D. Wissert, C. Moosmann, K. S. Ilin, M. Siegel, U. Lemmer, and H.-J. Eisler, “Gold nanoantenna resonance diagnostics via transversal particle plasmon luminescence,” *Opt. Exp.* 19(4), 3686-3693 (2011), doi: 10.1364/OE.19.003686.

[291] P. K. Ghosh, D. T. Debu, D. A. French, and J. B. Herzog, “Calculated thickness dependent plasmonic properties of gold nanobars in the visible to near-infrared light regime,” *PloS One* 12(5), 0177463 (2017), doi: 10.1371/journal.pone.0177463.

[292] C. Saylor, E. Novak, D. Debu, and J. B. Herzog, “Investigation of maximum optical enhancement in single gold nanowires and triple nanowire arrays,” *J. Nanophoton.* 9(1), 093053 (2015), doi: 10.1117/1.JNP.9.093053.

[293] J. B. Herzog, M. W. Knight, Y. Li, K. M. Evans, N. J. Halas, and D. Natelson, “Dark Plasmons in Hot Spot Generation and Polarization in Interelectrode Nanoscale Junctions,” *Nano Lett.* 13(3), 1359-1364 (2013), doi: 10.1021/nl400363d.

[294] J. B. Herzog, M. W. Knight, and D. Natelson, “Thermoplasmonics: Quantifying Plasmonic Heating in Single Nanowires,” *Nano Lett.* 14(2):499-503 (2014), doi: 10.1021/nl403510u.

[295] T. C. Choy, “Effective Medium Theory: Principles and Applications,” 2nd ed., *Oxford Science Publications* (2016).

[296] M. Song, G. Chen, Y. Liu, E. Wu, B. wu, and H. Zeng, “Polarization properties of surface plasmon enhanced photoluminescence from a single Ag nanowire,” *Opt. Exp.* 20(20), 22290-22297 (2012), doi: 10.1364/OE.20.022290.

[297] E. Massa, S. A. Maier, and V. Giannini, “An analytical approach to light scattering from small cubic and rectangular cuboidal nanoantennas,” *New J. Phys.* 15(6), 063013 (2013), doi: 10.1088/1367-2630/15/6/063013.

[298] O. L. Muskens, V. Giannini, J. A. Sánchez-Gil, and J. Gómez Rivas, “Optical scattering resonances of single and coupled dimer plasmonic nanoantennas,” *Opt. Exp.* 15(26), 17736-17746 (2007), doi: 10.1364/OE.15.017736.

[299] M. W. Knight *et al*., “Aluminum Plasmonic Nanoantennas,” *Nano Lett.* 12(11), 6000-6004 (2012), doi: 10.1021/nl303517v.

[300] T. V. Raziman and O. J. F. Martin, “Polarisation charges and scattering behaviour of realistically rounded plasmonic nanostructures,” *Opt. Exp.* 21(18), 21500-21507 (2013), doi: 10.1364/OE.21.021500.

[301] M. Rafiee, S. Chandra, H. Ahmed, and S. J. McCormack, “Optimized 3D Finite-Difference-Time-Domain Algorithm to Model the Plasmonic Properties of Metal Nanoparticles with Near-Unity Accuracy,” *Chemosensors* 9(5), 114 (2021), doi: 10.3390/chemosensors9050114.

[302] A. Said, K. S. R. Atia, and S. S. A. Obayya, "On modeling of plasmonic devices: overview," *J. Opt. Soc. Am. B* 37(11), A163-A174 (2020), doi: 10.1364/josab.399121.

[303] J. Gong, R. Dai, Z. Wang, and Z. Zhang, "Thickness Dispersion of Surface Plasmon of Ag Nano-thin Films: Determination by Ellipsometry Iterated with Transmittance Method," *Sci. Rep.* 5, 9279 (2015), doi: 10.1038/srep09279.

[304] D. Gaspar *et al.*, "Influence of the layer thickness in plasmonic gold nanoparticles produced by thermal evaporation," *Sci. Rep.* 3, 1469 (2013), doi: 10.1038/srep01469.

[305] L. Gao, F. Lemarchand, and M. Lequime, "Comparison of different dispersion models for single layer optical thin film index determination," *Thin Solid Films* 520(1), 501–509 (2011), doi: 10.1016/j.tsf.2011.07.028.

[306] D. I. Yakubovsky, A. V. Arsenin, Y. V. Stebunov, D. Yu. Fedyanin, and V. S. Volkov, "Optical constants and structural properties of thin gold films," *Opt. Exp.* 25(21), 25574-25587 (2017), doi: 10.1364/oe.25.025574.

[307] M. Hernandez-Raya, "Higher Definition Mid-Wave Infrared Scene Projectors via Shrinking Pixel Pitch," Ph.D. thesis (University of Delaware 2020).

[308] V. K. Malyutenko, V. V. Bogatyrenko, and O. Y. Malyutenko, "Bulk silicon as photonic dynamic infrared scene projector," *Appl. Phys. Lett.* 102(13), (2013), doi: 10.1063/1.4800936.

[309] P. Campbell and M. A. Green, "Light trapping properties of pyramidally textured surfaces," *J. Appl. Phys.* 62(1), 243–249 (1987), doi: 10.1063/1.339189.

[310] H.-P. Wang, D. Periyanagounder, A.-C. Li, and J.-H. He, "Fabrication of Silicon Hierarchical Structures for Solar Cell Applications," *IEEE Access* 7, 19395-19400 (2019), doi: 10.1109/ACCESS.2018.2885169.

[311] P. Helin, M. Mita, T. Bourouina, G. Reyne, and H. Fujita, "Self-Aligned Micromachining Process for Large-Scale, Free-Space Optical Cross-Connects," *J. Lightwave Tech.* 18(12), 1785–1791 (2000), doi: 10.1109/50.908730.

[312] Y.-J. Yang, B.-T. Liao and W.-C. Kuo, "A novel 2 × 2 MEMS optical switch using the split cross-bar design," *J. Micromech. Microeng.* 17(5), 875–882 (2007), doi: 10.1088/0960-1317/17/5/005.

[313] H.-L. Hsiao, H.-C. Lan, C. C. Chang, C.-Y. Lee, S.-P. Chen, C.-H. Hsu, S.-F. Chang, Y.-S. Lin, F.-M. Kuo, J.-W. Shi, and M.-L. Wu, "Compact and passive-

alignment 4-channel × 2.5-Gbps optical interconnect modules based on silicon optical benches with 45° micro-reflectors," *Opt. Exp.* 17(16), 24250–24260 (2009), doi: 10.1364/OE.17.02425.

[314] B. Tang, K. Sato, D. Zhang, and Y. Cheng, "Fast Si (100) etching with a smooth surface near the boiling temperature in surfactant-modified tetramethylammonium hydroxide solutions," *Micro & Nano Lett.* 9(9), 582-584 (2014), doi: 10.1049/mnl.2014.0214.

[315] D. T. Norton *et al*., "512 × 512 individually addressable MWIR LED Arrays Based on Type-II InAs/GaSb Superlattices," *IEEE J. of Quant. Electron* 49(9), 753-759 (2013), doi: 10.1109/JQE.2013.2272878.

[316] M. Hollenbach *et al*., "Wafer-scale nanofabrication of telecom single-photon emitters in silicon," *Nat. Comm.* 13(1), 7683 (2022), doi: 10.1038/s41467-022-35051-5.

[317] J. T. Winthrop and C. R. Worthington, "Theory of Fresnel Images. I. Plane Periodic Objects in Monochromatic Light," *J. Opt. Soc. Am.* 55(4), 373–381 (1965), doi: 10.1364/JOSA.55.000373.

[318] R. F. Edgar, "The Fresnel Diffraction Images of Periodic Structures," *Optica Acta: Intern. J. Opt.* 16(3), 281–287 (1969), doi: 10.1080/713818186.

[319] A. V. Veluthandath and G. S. Murugan, "Photonic Nanojet Generation Using Integrated Silicon Photonic Chip with Hemispherical Structures," *Photonics* 8(12), 586 (2021), doi: 10.3390/photonics8120586.

[320] Y. Chen *et al*., "Ultrahigh Quality Factor Photonic Nanojets Generated by Truncated Microtoroid Structures," *IEEE Photonics J.* 13(4), 2700106 (2021), doi: 10.1109/JPHOT.2021.3100136.

[321] C.-Y. Liu, W.-Y. Chen, Y. E. Geints, O. V. Minin, and I. V. Minin, "Simulation and experimental observations of axial position control of a photonic nanojet by a dielectric cube with a metal screen," *Opt. Lett.* 46(17), 4292-4295 (2021), doi: 10.1364/OL.431807.

[322] D. Chen *et al*., "Photon-trapping-enhanced avalanche photodiodes for mid-infrared applications," *Nat. Phot.* 17(7), 594-600 (2023), doi: 10.1038/s41566-023-01208-x.

[323] M. R. Lien, N. Wang, J. Wu, A. Soibel, S. D. Gunapala, H. Wang, and M. L. Povinelli, "Resonant Grating-Enhanced Black Phosphorus Mid-Wave Infrared Photodetector," *Nano Lett.* 22(21), 8704−8710 (2022), doi: 10.1021/acs.nanolett.2c03469.

[324] V. Zwiller and G. Björk, “Improved light extraction from emitters in high refractive index materials using solid immersion lenses,” *J. Appl. Phys.* 92(2), 660–665 (2002), doi: 10.1063/1.1487913.

[325] A. W. Schell, T. Neumer, and O. Benson, “Numerical analysis of efficient light extraction with an elliptical solid immersion lens,” *Opt. Lett.* 39(16), 4639-4642 (2014), doi: 10.1364/OL.39.004639.

[326] T. M. Babinec, B. J. Hausmann, M. Khan, Y. Zhang, J. R. Maze, P. R. Hemmer, and M. Lončar, “A diamond nanowire single-photon source,” *Nat. Nanotechnol.* 5(3), 195–199 (2010), doi: 10.1038/nnano.2010.6.

[327] J. Claudon *et al*., “A highly efficient single-photon source based on a quantum dot in a photonic nanowire,” *Nat. Photon.* 4(3), 174–177 (2010), doi: 10.1038/nphoton.2009.287.

[328] C. Santori, D. Fattal, J. Vučković, G. S. Solomon, and Y. Yamamoto, “Indistinguishable photons from a single-photon device,” *Nature* 419(6907), 594–597 (2002), doi: 10.1038/nature01086.

[329] N. Somaschi *et al* ., “Near-optimal single-photon sources in the solid state,” *Nat. Photon.* 10(5), 340–345 (2016), doi: 10.1038/nphoton.2016.23.

[330] A. I. Kuznetsov, A. E. Miroshnichenko, M. L. Brongersma, Y. S. Kivshar, and B. Luk’yanchuk, “Optically resonant dielectric nanostructures,” *Science* 354(6314), 846–855 (2016), doi: 10.1126/science.aag2472.

[331] S. Mignuzzi, S. Vezzoli, S. A. R. Horsley, W. L. Barnes, S. A. Maier, and R. Sapienza, “Nanoscale Design of the Local Density of Optical States,” *Nano Lett.* 19(3), 1613–1617 (2019), doi: 10.1021/acs.nanolett.8b04515.

[332] S. Noda, M. Fujita, and T. Asano, “Spontaneous-emission control by photonic crystals and nanocavities,” *Nat. Photon.* 1(8), 449–458 (2007), doi: 10.1038/nphoton.2007.141.

[333] P. Lodahl, S. Mahmoodian, and S. Stobbe, “Interfacing single photons and single quantum dots with photonic nanostructures,” *Rev. Mod. Phys.* 87, 347–400 (2015), doi: 10.1103/RevModPhys.87.347.

[334] S. G. Bishop, J. K. Cannon, H. B. Yağci, R. N. Clark, J. P. Hadden, W. Langbein, and A. J. Bennet, “Evanescent-field assisted photon collection from quantum emitters under a solid immersion lens,” *New J. Phys.* 24(10), 103027 (2022), doi: 10.1088/1367-2630/ac9697.

[335] X. Cheng *et al*., "Additive GaN Solid Immersion Lenses for Enhanced Photon Extraction Efficiency from Diamond Color Centers," *ACS Photon.* 10(9), 3374−3383 (2023), doi: 10.1021/acsphotonics.3c00854.

[336] R. Uppu, L. Midolo, X. Zhou, J. Carolan, and P. Lodahl, "Quantum-dot-based deterministic photon-emitter interfaces for scalable photonic quantum technology," *Nat. Nanotechnol.* 16(12), 1308–1317 (2021), doi: 10.1038/s41565-021-00965-6.

[337] H. Lee, T. Chen, J. Li, O. Painter, and K. J. Vahala, "Ultra-low-loss optical delay line on a silicon chip," *Nat. Commun.* 3, 867 (2012), doi: 10.1038/ncomms1876.

[338] W. H. P. Pernice, C. Schuck, O. Minaeva, M. Li, G. N. Goltsman, A. V. Sergienko, and H. X. Tang, "High-speed and high-efficiency travelling wave single-photon detectors embedded in nanophotonic circuits," *Nat. Commun.* 3, 1325 (2012), doi: 10.1038/ncomms2307.

[339] Y. Tian *et al*., "Experimental demonstration of a reconfigurable electro-optic directed logic circuit using cascaded carrier-injection micro-ring resonators," *Sci. Rep.* 7, 6410 (2017), doi: 10.1038/s41598-017-06736-5.

[340] S. Gyger *et al*., "Reconfigurable photonics with on-chip single-photon detectors," *Nat. Commun.* 12(1), 1408 (2021), doi: 10.1038/s41467-021-21624-3.

[341] M. Hollenbach, Y. Berencén, U. Kentsch, M. Helm, and G. V. Astakhov, "Engineering telecom single-photon emitters in silicon for scalable quantum photonics," *Opt. Exp.* 28(18), 26111-26121 (2020), doi: 10.1364/OE.397377.

[342] D. B. Higginbottom *et al*., "Optical observation of single spins in silicon," *Nature* 607(7918), 266–270 (2022), doi: 10.1038/s41586-022-04821-y.

[343] Y. Baron *et al*., "Detection of Single W-Centers in Silicon," *ACS Photon.* 9(7), 2337–2345 (2022), doi: 10.1021/acsphotonics.2c00336.

[344] Z. Wang, M. Chen, and W. Zhang, "Sub-50 nm control of light at 405 nm with planar Si nanolens," *Opt. Exp.* 30(6), 9904-9912 (2022), doi: 10.1364/OE.453588.

[345] K. Li, E. Simmons, A. Briggs, L. Nordin, J. Xu, V. Podolskiy, and D. Wasserman, "Subdiffraction Limited Photonic Funneling of Light," *Adv. Opt. Mater.* 8(24), 2001321 (2020), doi: 10.1002/adom.202001321.

[346] V. W. L. Chin, J. W. V. Storey, and M. A. Green, “Characteristics of p-type PtSi Schottky diodes under reverse bias,” *J. Appl. Phys.* 68(8), 4127–4132 (1990), doi: 10.1063/1.346254.

[347] V. W. L. Chin, J. W. V. Storey, and M. A. Green, “Bias and thickness dependence of the infra-red PtSi/*p*-Si Schottky diode studied by internal photoemission,” *Solid-State Electron.* 39(2), 277-280 (1996), doi: 10.1016/0038-1101(95)00130-1.

[348] A. Tanabe, K. Konuma, N. Teranishi, S. Tohyama, and K. Masubuchi, “Influence of Fermi-level pinning on barrier height inhomogeneity in PtSi/*p*-Si Schottky contacts,” *J. Appl. Phys.* 69(2), 850–853 (1991), doi: 10.1063/1.347321.

[349] W.-S. Wang, C. Ho, and T.-M. Chuang, “Investigation of PtSi/p-Si Schottky barrier height using *I-V-T* technique,” *Mat. Chem. & Phys.* 51(1), 88-91 (1997), doi: 10.1016/S0254-0584(97)80273-8.

[350] J. Fu, Z. Guo, C. Nie, F. Sun, G. Li, S. Feng, and X. Wei, “Schottky infrared detectors with optically tunable barriers beyond the internal photoemission limit,” *The Innovation* 5(3), 100600 (2024), doi: 10.1016/j.xinn.2024.100600.

[351] H. Efeoğlu, A. Turut, and M. Gül, “An experimental study: Dependence of Schottky diode parameters on Schottky contact area size,” *Opt. Mat.* 142, 114038 (2023), doi: 10.1016/j.optmat.2023.114038.

[352] I. Ohdomari and K. N. Tu, “Parallel silicide contacts,” *J. Appl. Phys.* 51(7), 3735-3739 (1980), doi: 10.1063/1.328160.

[353] M. Wittmer, “Conduction mechanism in PtSi/Si Schottky diodes,” *Phys. Rev. B* 43(5-15), 4385 (1991), doi: 10.1103/PhysRevB.43.4385.

[354] A. Y. C. Yu, and E. H. Snow, “Surface Effects on Metal-Silicon Contacts,” *J. Appl. Phys.* 39(7), 3008–3016 (1968), doi: 10.1063/1.1656723.

[355] V. W. L. Chin, J. W. V. Storey, and M. A. Green, “Diffusion effects in *p*-type PtSi Schottky diodes under reverse bias,” *J. Appl. Phys.* 69(6) 3601-3604 (1991), doi: 10.1063/1.348505.

[356] M. J. McNutt, "Edge leakage control in platinum-silicide Schottky-barrier diodes used for infrared detection," *IEEE Electron Device Lett.* 9(8), 394-396 (1988), doi: 10.1109/55.755.

[357] T. L. Lin, J. S. Park, S. D. Gunapala, E. W. Jones, and H. M. Del Castillo, "Doping-spike PtSi Schottky infrared detectors with extended cutoff

wavelengths," *IEEE Trans. on Electron Devices* 42(7), 1216-1220 (1995), doi: 10.1109/16.391201.

[358] J.-H. Wu, R.-S. Chang, and G.-J. Horng, "Microstructure, electrical, and optical properties of evaporated PtSi/p-Si(100) Schottky barriers as high quantum efficient infrared detectors," *Thin Solid Films* 466(1-2), 314-319 (2004), doi: 10.1016/j.tsf.2004.03.016.

[359] G.-J. Horng, C.-Y. Chang, T. Chang, C. Ho, and C.-S. Wu, "Microstructure effects of quantum efficiency in PtSi/p-Si(100) Schottky barrier detector," Mat. Chem. & Phys. 68(1-3), 17-21 (2001), doi: 10.1016/S0254-0584(00)00350-3.

[360] H. Efeoğlu, A. Turut, and M. Gül, "Thermal sensitivity and current-voltage-temperature characteristics in Pt/epitaxy *n*-Si/n^+Si structures as a function of Schottky contact area," *J. Vac. Sci. Technol. B* 40(5), 052208 (2022), doi: 10.1116/6.0002030.

[361] J. Qiu *et al*., "High-Performance Uncooled Mid-Infrared Detector Based on a Polycrystalline PbSe/CdSe Heterojunction," *ACS Appl. Mater. & Inter.* 15(20), 24541-24548 (2023), doi: 10.1021/acsami.3c01538.

[362] S. Jost, "Identifying the physical mechanisms of polycrystalline lead salt photoconductors," *J. Appl. Phys.* 132(6), 064503 (2022), doi: 10.1063/5.0098505.

[363] G. W. Bidney, J. M. Duran, G. Ariyawansa, I. Anisimov, J. R. Hendrickson, and V. N. Astratov, "Micropyramidal Si Photonics–A Versatile Platform for Detector and Emitter Applications," *Laser Photon. Rev.* 2400922 (2024), doi: 10.1002/lpor.202400922.

[364] S. Yang and V. N. Astratov, "Spectroscopy of coherently coupled whispering-gallery modes in size-matched bispheres assembled on a substrate," *Opt. Lett.* 34(13), 2057-2059 (2009), doi: 10.1364/OL.34.002057.

[365] A. D. Bristow *et al*., "Polarization Conversion in the Reflectivity Properties of Photonic Crystal Waveguides," *IEEE J. Quant. Electron.* 38(7), 880-884 (2002), doi: 10.1109/JQE.2002.1017601.

[366] A. D. Bristow *et al*., "Defect states and commensurability in dual-period $Al_xGa_{1-x}As$ photonic crystal waveguides," *Phys. Rev. B* 68(3), 033303 (2003), doi: 10.1103/PhysRevB.68.033303.

[367] V. N. Astratov *et al*., "Roadmap on Label-Free Super-Resolution Imaging," *Laser Photon. Rev.* 17(12), 2200029 (2023), doi: 10.1002/lpor.202200029.

[368] V. N. Astratov, Label-Free Super-Resolution Microscopy (Springer, 2019).

[369] G. W. Bidney, I. Anisimov, D. E. Walker, G. Ariyawansa and V. N. Astratov, "Hybrid Photonic-Plasmonic Littrow Retroreflectors," *RAPID* 1-2 (2024), doi: 10.1109/RAPID60772.2024.10646995.

[370] T. Le, V. A. Khoa, M. V. Klibanov, L. H. Nguyen, G. W. Bidney, and V. N. Astratov, "Numerical Verification of the Convexification Method for a Frequency-Dependent Inverse Scattering Problem with Experimental Data," *J. Appl. Ind. Math.* 17, 908–927 (2023), doi: 10.1134/S199047892304018X.

[371] M. V. Klibanov *et al*., "Convexification Inversion Method for Nonlinear SAR Imaging with Experimentally Collected Data," *J. Appl. Ind. Math.* 15, 413-436 (2021), doi: 10.1134/S1990478921030054.

[372] V. A. Khoa *et al*., "An inverse problem of a simultaneous reconstruction of the dielectric constant and conductivity from experimental backscattering data," *Inverse Problems in Sci. and Eng.* (2020), doi: 10.1080/17415977.2020.1802447.

[373] V. A. Khoa *et al*., "Convexification and experimental data for a 3D inverse scattering problem with the moving point source," *Inverse Problems* 36(8), 085007 (2020), doi: 10.1088/1361-6420/ab95aa.

APPENDIX A: PUBLICATIONS SO FAR

Patents:

[1] V. N. Astratov, G. W. Bidney, I. Anisimov, J. M. Duran, and G. Ariyawansa, "Photodetector Focal Plane Arrays with Enhanced Detection Capability," Pub. No. US20240243158A1, published 07/18/2024.

Journal Articles:

[1] G. W. Bidney, J. M. Duran, G. Ariyawansa, I. Anisimov, J. R. Hendrickson, and V. N. Astratov, "Micropyramidal Si Photonics–A Versatile Platform for Detector and Emitter Applications," *Laser Photon. Rev.* 2400922 (2024), doi: 10.1002/lpor.202400922.

[2] T. Le, V. A. Khoa, M. V. Klibanov, L. H. Nguyen, G. W. Bidney, and V. N. Astratov, "Numerical Verification of the Convexification Method for a Frequency-Dependent Inverse Scattering Problem with Experimental Data," *J. Appl. Ind. Math.* 17, 908–927 (2023), doi: 10.1134/S199047892304018X.

[3] B. Jin, A. Brettin, G. W. Bidney *et al*., "Light-harvesting microconical arrays for enhancing infrared imaging devices: Proposal and demonstration," *Appl. Phys. Lett.* 119(5), 051104 (2021), doi: 10.1063/5.0054760.

[4] M. V. Klibanov, V. A. Khoa, A. V. Smirnov, L. H. Nguyen, G. W. Bidney *et al*., "Convexification Inversion Method for Nonlinear SAR Imaging with Experimentally Collected Data," *J. Appl. Ind. Math.* 15, 413-436 (2021), doi: 10.1134/S1990478921030054.

[5] B. Jin, G. W. Bidney *et al*., "Microconical silicon mid-IR concentrators: spectral, angular and polarization response," *Opt. Exp.* 28(19), 27615-27627 (2020), doi: 10.1364/oe.398014.

[6] V. A. Khoa, G. W. Bidney *et al*., "An inverse problem of a simultaneous reconstruction of the dielectric constant and conductivity from experimental backscattering data," *Inverse Problems in Sci. and Eng.* (2020), doi: 10.1080/17415977.2020.1802447.

[7] V. A. Khoa, G. W. Bidney *et al*., "Convexification and experimental data for a 3D inverse scattering problem with the moving point source," *Inverse Problems* 36(8), 085007 (2020), doi: 10.1088/1361-6420/ab95aa.

Conference Proceedings:

[1] G. W. Bidney, I. Anisimov, D. E. Walker, G. Ariyawansa and V. N. Astratov, "Hybrid Photonic-Plasmonic Littrow Retroreflectors," *RAPID* 1-2 (2024), doi: 10.1109/RAPID60772.2024.10646995.

[2] G. W. Bidney, J. M. Duran, G. Ariyawansa, I. Anisimov, and V. N. Astratov, "The World of Microphotonic Arrays Enabled by Anisotropic Wet Etching of Silicon," *CLEO*, Technical Digest Series, paper ATh1J.6 (2024).

[3] G. W. Bidney, I. Anisimov, D. E. Walker, G. Ariyawansa, J. M. Duran, and V. N. Astratov, "Plasmonic Littrow Retroreflectors," *CLEO*, Technical Digest Series, paper JTh2A.59 (2024).

[4] G. W. Bidney, J. M. Duran, G. Ariyawansa, I. Anisimov, K. W. Allen, and V. N. Astratov, "Photodetector Focal Plane Arrays Integrated with Silicon Micropyramidal Structures in MWIR," *arXiv* (University of North Carolina at Charlotte, 2023), doi: 10.48550/arXiv.2309.15077.

[5] G. W. Bidney *et al*., "Focusing and Diffraction of Light by Periodic Si Micropyramidal Arrays," *arXiv* (University of North Carolina at Charlotte, 2023), doi: 10.48550/arXiv.2309.15073.

[6] G. W. Bidney *et al*., "Light Manipulation with Si Mesoscale Structures for Applications in IR Photodetector and Photoemitter Arrays," *RAPID* 1-2 (2023), doi: 10.1109/rapid54473.2023.10264719.

[7] G. W. Bidney, J. M. Duran, G. Ariyawansa, I. Anisimov, K. W. Allen and V. N. Astratov, "MWIR Photodetector Arrays Enhanced by Integration with Si Micropyramidal Structures," *RAPID*, 1-2 (2023), doi: 10.1109/RAPID54473.2023.10264769.

[8] G. W. Bidney *et al*., "Monolithic integration of photodetector focal plane arrays with micropyramidal arrays in mid-wave infrared," *Proc. SPIE 12006, Si. Photon. XVII*, 1200609 (2022), doi: 10.1117/12.2610304.

[9] G. W. Bidney *et al*., "Fabrication of 3-D light concentrating microphotonic structures by anisotropic wet etching of silicon," *Proc. SPIE 12012, Adv. Fab. Tech. for Micro/Nano Opt. and Photon. XV*, 120120B (2022), doi: 10.1117/12.2610426.

[10] B. Jin A. Brettin, G. W. Bidney *et al*., "Light-harvesting microconical arrays integrated with photodetector FPAs for enhancing infrared imaging devices," *Proc. SPIE 12004, Int. Opt.: Dev., Mater., and Tech. XXVI*, 120040X (2022), doi: 10.1117/12.2609883.

[11] B. Jin, G. W. Bidney *et al*., "Label-free cellphone microscopy with submicron resolution through high-index contact ball lens for in vivo melanoma diagnostics and other applications," *Proc. SPIE 11972, Label-free Biomedical Imaging and Sensing (LBIS)*, 119720F (2022), doi: 10.1117/12.2609911.

[12] G. W. Bidney *et al*., "Anisotropic Wet Etching of Si as a Fabrication Tool Enabling 3-D Microphotonics Structures and Devices," *NAECON*, 146-149 (2021), doi: 10.1109/NAECON49338.2021.9696393.

[13] G. W. Bidney *et al*., "Ni-silicide schottky barrier micropyramidal photodetector array," *NAECON*, 116-118 (2021), doi: 10.1109/naecon49338.2021.9696408.

[14] B. Jin, G. W. Bidney, I. Anisimov, N. I. Limberopoulos, A. V. Maslov, and V. N. Astratov, "High-resolution label-free cellphone microscopy using contact ball lenses," *NAECON*, 356-358 (2021), doi: 10.1109/NAECON49338.2021.9696405.

[15] B. Jin, A. Brettin, G. W. Bidney *et al*., "Light-concentrating microcone array for improving performance of infrared imaging devices," *NAECON*, 119-122 (2021), doi: 10.1109/naecon49338.2021.9696394.

[16] B. Jin, G. W. Bidney *et al*., "Design of Si Micro-Cone Light Concentrators for Heterogeneous Integration with MWIR FPAs," *ICTON* (2020), doi: 10.1109/ICTON51198.2020.9203159.

[17] G. W. Bidney *et al*., "Improving Cellphone Microscopy Imaging with Contact Ball Lenses," *NAECON*, 672-674 (2019), doi: 10.1109/NAECON46414.2019.9058104.

[18] B. Jin, G. W. Bidney *et al*., "High-index micro-cones for focusing and concentrating light in MWIR focal plane arrays," *NAECON*, 665-668 (2019), doi: 10.1109/NAECON46414.2019.9057919.

[19] V.N. Astratov, F. Abolmaali, A. Brettin, G.W. Bidney *et al.*, "Resolution Enhancement in Microspherical Nanoscopy by Coupling of Emission to Plasmonics Metasurfaces," *ICTON* (2019), doi: 10.1109/icton.2019.8840556.